ISSUE: 36
SCOPUS
UNIVERSIDAD POLITÉCNICA SALESIANA ECUADOR

pISSN: 1390-650X
eISSN: 1390-860X
july / december 2026

INGENIUS

Revista de Ciencia y Tecnología

- Assembly of automotive seatbelts assisted by cobot and robodk.
  Pag. 9
- Structured quantum software development life cycle (QSDLC) for next generation computing.
  Pag. 39
- Vulnerability and risks of Ecuador's energy system in the context of climate change and environmental sustainability policies.
  Pag. 54
- Neural inverse control of a rotary flexible link.
  Pag. 98

Indexed in: SCOPUS

Ingenius

Ingenius • Issue 36 • july-december 2026. Journal of Science and Tecnology of the Universidad Politécnica Salesiana of Ecuador. Publication dedicated to studies related to the Sciences of Mechanical Engineering, Electrical Engineering, Electronic Engineering, Mechatronic Engineering, Systems Engineering and Industrial Engineering.

Reviewers board

Editorial

Editorial Abya Yala (Quito-Ecuador),
Av. 12 de octubre N422 y Wilson,
Bloque A, UPS Quito, Ecuador.
Casilla 17-12-719 Teléfonos: (593-2) 3962800 ext. 2638
email: editorial@abyayala.org

Printing: 800 copies

Typographic system used in the composition of this document LaTeX.

Ingenius

Revista de Ciencia y Tecnologia

Issue 36

july – december 2026

ISSN impreso 1390-650X / ISSN electrónico 1390-860X

The administration of the journal is done through the following parameters:

The journal uses the academic anti-plagiarism system

The articles have an identification code (Digital Object Identifier)

The editorial process is managed through the Open Journal System

The articles of the present edition can be consulted in
http://revistas.ups.edu.ec/index.php/ingenius

Universidad Politécnica Salesiana del Ecuador

INGENIUS Journal, is indexed in the following Databases and scientific information systems:

SELECTIVE DATABASES

Scopus

Emerging Sources Citation Index

Google Scholar

SciELO Ecuador

BASE

Fuente Académica Plus EBSCOhost

SIS Scientific Indexing Services

EuroPub

REVIEWS EVALUATION PLATFORMS

MIAR

Quality Open Access Market

I2OR

SELECTIVE DIRECTORIES

latindex

Journal Seeker Research Bible

AcademicKeys Unlocking Academic Careers

Science Library Index

ULRICHSWEB™ Global Serials Directory

SELECTIVE SERIAL LIBRARY

redalyc.org

REDIB Red Iberoamericana de Innovación y Conocimiento Científico

refseek

SCIENTIFIC LITERATURE SEARCHERS OPEN ACCESS

DOAJ Directory of Open Access Journals

EXALEAD

WorldWideScience.org

Journals for Free

OTHER BIBLIOGRAPHICAL DATABASES

Dialnet

Journal TOCs The latest Journal Tables of Contents

PKP|INDEX

CATALOG OF INTERNATIONAL UNIVERSITY LIBRARIES

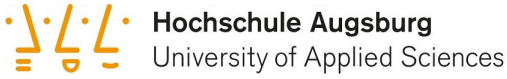

Editorial

Dear readers,

Each new issue of a scientific journal represents an opportunity to strengthen the dialogue among researchers, institutions, and disciplines that contribute to the advancement of science and technology. Issue 36 of INGENIUS Journal brings together ten original research articles that demonstrate thematic diversity, methodological rigor, and the growing internationalization of applied research, further consolidating the journal as a platform for disseminating scientific knowledge aimed at addressing contemporary technological challenges.

The published contributions cover strategic areas of engineering and emerging technologies. In the field of smart manufacturing and Industry 4.0, this issue presents a collaborative robotics approach for automotive seat belt assembly supported by RoboDK simulation, highlighting the potential of cobots to enhance productivity and industrial safety. In the area of artificial intelligence, the issue includes a comparative framework for electrical load forecasting based on machine learning techniques and rolling temporal validation, as well as a comparative study of state-of-charge estimation methods for lithium-ion batteries using Bayesian filters and machine learning algorithms.

Sustainability constitutes another cross-cutting theme throughout this issue. The published studies address the vulnerability of Ecuador's energy system to climate change and investigate the use of biological waste, such as eggshell powder, as a sustainable corrosion inhibitor for carbon steels employed in the oil and gas industry. These contributions demonstrate how engineering can simultaneously address environmental, energy, and industrial challenges through innovative solutions grounded in circular economy principles.

Digital technologies also occupy a prominent place in this issue. A methodological framework for the Quantum Software Development Life Cycle is introduced, providing a structured approach for a discipline with enormous scientific and technological potential. Likewise, research focused on improving web accessibility in accordance with the WCAG 2.1 guidelines promotes the development of more inclusive digital platforms. Complementing these topics are contributions on neural-network-based control of flexible systems, the influence of operating variables on automotive air-conditioning system performance, and a systematic review of swarm intelligence algorithms for unmanned aerial vehicle route planning, an increasingly relevant research area in robotics and autonomous systems.

This issue also reflects a strong commitment to international scientific collaboration. The published articles bring together researchers from universities and research institutions in Ecuador, Spain, Brazil, Saudi Arabia, and Chile, strengthening collaborative research networks that enrich scientific quality and foster the exchange of knowledge across diverse academic and technological environments.

The Editorial Board sincerely thanks the authors for entrusting their research to INGENIUS Journal, the reviewers for their commitment to a rigorous and objective peer-review process, and our readers for extending the impact of the published knowledge through its consultation, application, and scholarly discussion.

Finally, we encourage researchers, academics, professionals, and students to explore the articles published in this issue, incorporate their findings into future research, and cite them whenever appropriate. We also warmly invite the international scientific community to submit their original contributions to future issues of INGENIUS Journal, convinced that the open exchange of scientific knowledge remains a fundamental pillar for fostering innovation and advancing the progress of our societies.

John Calle-Siguencia, PhD

Editor in Chief

Table of contents

Assembly of Automotive Seatbelts Assisted by Cobot and RoboDK 9
Ensamblaje de cinturones de seguridad vehiculares asistido por cobot y RoboDK
Kevyn Obed Manzano-Ibarra, Ivón Oristela Benítez-González and José Manuel Bernal-de Lázaro

Comparative framework for electricity demand forecasting using machine learning and rolling temporal validation 19
Marco comparativo para el pronóstico de demanda eléctrica con machine learning y validación temporal rodante
Juan Carlos Castillo, Jessica N. Castillo, Gabriel Pesántez and Wilian Guamán

Corrosion inhibition of type N80 carbon steel using eggshell powder in acidic and brine environments: a study based on weight loss testing, micro-indentation, and electrochemical modeling 29
Inhibición de la corrosión del acero al carbono tipo N80 utilizando polvo de cáscara de huevo en ambientes ácidos y salinos: un estudio basado en ensayos de pérdida de peso, microindentación y modelado electroquímico
J. L. Dávalos-Monteiro, C. D. Rodríguez-Hernández, R. M. Rached and R. Dávalos-Monteiro

Structured quantum software development life cycle (QSDLC) for next generation computing 50
Ciclo de vida de desarrollo de software cuántico estructurado (QSDLC) para la computación de próxima generación
Fabián Lizardo Caicedo Goyes

Vulnerability and risks of Ecuador's energy system in the context of climate change and environmental sustainability policies 54
Vulnerabilidad y riesgos del sistema energético ecuatoriano frente al cambio climático y las políticas de sostenibilidad ambiental
Flavio Arroyo-Morocho, Dely Bravo-Donoso, Abel Remache-Coyago and Tatiana Freire-Rosero

Implementación de accesibilidad web según WCAG 2.1: perceptibilidad 70
Implementation of web accessibility in accordance with WCAG 2.1: perceptibility
Francisco Álvarez-Pineda, Yovin Urrego-Gómez, Pablo Ordóñez-Ordóñez and Hernán Torres-Carrión

Influence of cabin temperature and compressor speed on the performance of an automotive air conditioning system 84
Influencia de la temperatura del habitáculo y la velocidad del compresor en el rendimiento del sistema de aire acondicionado automotriz
Iván M. Ashqui-Cuvi, Klever S. Morales-Morales, Daniela C. Vásconez-Núñez,
Fernando M. Tello-Oquendo and Fabián C. Gunsha-Maji

Neural inverse control of a rotary flexible link 98
Control neuronal por modelo inverso de un eslabón flexible rotatorio
Carlos Alberto Saldaña Enderica, José Ramón Llata y Carlos Torre-Ferrero

Swarm algorithms for UAV route planning: a systematic review of characteristics, classification, and operational performance 110
Algoritmos de enjambre para planificación de rutas en UAV: Una revisión sistemática de características, clasificación y desempeño operativo
Marcelo Rea-Guamán, Andrea López-López and Andrés Almeida-Jara

Applied comparative study of existing methods for state-of-charge estimation in lithium-ion batteriee 125
Estudio comparativo aplicado de métodos existentes para estimación del estado de carga en baterías de iones de litio
Edwin Paccha-Herrera, Ángel Recalde, Francisco Jaramillo-Montoya and Darwin Tapia-Peralta

Guidelines 137
Normas editoriales

Scientific Paper / Artículo Científico

UNIVERSIDAD POLITÉCNICA SALESIANA ECUADOR
INGENIUS
Revista de Ciencia y Tecnología
https://doi.org/10.17163/ings.n36.2026.01
pISSN: 1390-650X / eISSN: 1390-860X

Assembly of Automotive Seatbelts Assisted by Cobot and RoboDK

Ensamblaje de cinturones de seguridad vehiculares asistido por cobot y RoboDK

Kevyn Obed Manzano-Ibarra[1], Ivón Oristela Benítez-González [2], José Manuel Bernal-de Lázaro[2,3,*]

Received: 04-09-2025, Received after review: 15-01-2026, Accepted: 21-04-2026, Published: 01-07-2026

Abstract

In the modern automotive sector, Industry 4.0 principles have been widely adopted to enhance flexibility, efficiency, and quality in production processes. Nonetheless, several automotive subprocesses still rely on operators for manual or repetitive tasks, which are highly susceptible to human error and may compromise product quality while increasing operating costs . This study addresses this challenge by implementing a collaborative robotic solution for manufacturing environments. Specifically, it proposes the integration of a cobot for the assembly of automotive seatbelts at the ZF plant in Tamaulipas, Mexico. RoboDK is used to simulate and evaluate a Universal Robots cobot intended to increase operational efficiency and reduce defect rates at the press station. The results demonstrate the feasibility of the proposed simulation approach, enabling the functional analysis and validation of multiple configurations within the manufacturing cell while ensuring the safe integration of the collaborative robot (cobot). Furthermore, the proposed solution supports safe human-robot collaboration in compliance with the ISO/TS 15066 technical specification. Overall, the implemented system shows significant potential to improve efficiency and operational flexibility while reducing costs in the production process.

Keywords: automotive industry, Industry 4.0, collaborative robotics, cobot, digital simulation, RoboDK, Universal Robots.

Resumen

En la industria automotriz moderna se han adoptado de manera extensiva diferentes principios y paradigmas de la Industria 4.0 para mejorar la flexibilidad, eficiencia y calidad en sus procesos. Sin embargo, son varios los subprocesos en este sector industrial que aún dependen de los operarios y de tareas manuales o repetitivas, las cuales suelen ser altamente susceptibles a errores humanos que impactan negativamente en la calidad del producto final e implican elevados sobrecostos de operación. El presente estudio atiende dicha problemática mediante un enfoque de robótica colaborativa aplicado a celdas de manufactura y propone la integración de un cobot para el ensamblado de los cinturones de seguridad automovilísticos en la planta de ZF en Tamaulipas, México. La propuesta utiliza RoboDK para simular y evaluar la implementación de un cobot de Universal Robots con el propósito de aumentar la eficiencia operativa y reducir la tasa de defectos en la estación de prensa. Los resultados obtenidos demuestran la viabilidad de la simulación y permiten llevar a cabo el análisis funcional y la validación de las configuraciones en la celda de manufactura a partir de la integración segura del cobot, garantizando el cumplimiento de la especificación técnica ISO/TS 15066. El sistema implementado muestra un potencial significativo en cuanto a eficiencia, flexibilidad operacional y reducción de costos en el proceso productivo.

Palabras clave: industria automotriz, industria 4.0, robótica colaborativa, RoboDK, Universal Robots, simulación digital.

[1]Universidad Internacional de Valencia, España.
[2]Universidad Internacional de La Rioja, España.
[3,*]Instituto Politécnico de la Universidad do Estado do Rio de Janeiro, Brasil.
Corresponding author ✉: jose.lazaro@iprj.uerj.br.

Suggested citation: K. O. Manzano-Ibarra, I. O. Benítez-González and J. M. Bernal-de Lázaro. "Assembly of Automotive Seatbelts Assisted by Cobot and RoboDK," *Ingenius, Revista de Ciencia y Tecnología*, N.° 36, pp. 9-17, 2026, DOI: https://doi.org/10.17163/ings.n36.2026.01.

1. Introduction

Industry 4.0 has had a significant impact on the automotive sector. Historically, this field has pioneered the adoption of emerging technologies, including intelligent control systems [1–4], robotics [5, 6], and augmented reality [7], to increase productivity, flexibility, and efficiency in the manufacturing of parts and components. In this context, collaborative robotics, as one of the pillars of Industry 4.0, has enabled the automation of complex tasks, including machine tending, assembly processes such as screwing and part insertion, sealing, bonding, surface finishing, welding, and quality control [8].

Within the current international regulatory framework established by the ISO/TS 15066 technical specification, the concept of a collaborative robot has been refined by emphasizing that collaboration is not an intrinsic property of the robot itself, but rather a characteristic of the application or task being performed. In this context, it is more accurate to refer to collaborative applications or tasks, in which an industrial robot interacts with humans under specific safety modes and criteria, such as monitored stop, hand guiding, speed and separation monitoring, and power and force limiting. Consequently, the same robot may or may not be involved in a collaborative application depending on the environment, the end effector, and the operating conditions. Together with ease of programming, this application-based understanding of collaboration facilitates human-machine interaction and provides greater adaptability to different industrial environments and occupational safety requirements. These advantages have contributed to the recent growth of collaborative robot applications in the automotive sector [8–11].

Accordingly, approximately 70% of automotive production units currently integrate industrial robots configured to perform collaborative tasks under safe operating modes that enhance process flexibility and efficiency. In this context, nearly 50% of small and medium-sized enterprises are implementing pilot installations to address for labor shortages and improve operational performance [10, 11].

This high level of interest has led to the availability of a wide range of industrial solutions in the collaborative robotics market. Among these, Universal Robots' e-Series stands out, alongside solutions offered by other major providers such as KUKA, Yaskawa Electric Corporation, ABB, and Fanuc Corporation.

Although cobot-based solutions have become an attractive option for companies seeking to improve the efficiency, quality, and safety of their processes, their implementation still requires trained personnel and adequate infrastructure. Compared with conventional robots, which typically occupy more space, require more complex programming, and operate from fixed positions, cobots offer greater flexibility, safety, and ease of programming. Their compact design also allows them to be repositioned more easily within the production environment [12–14].

Robotic simulations are essential for evaluating possible configurations in these systems without exposing operators, infrastructure, or the robot itself to potential hazards in the work area. Simulation-based design enables effective integration by reducing the time and costs associated with production line downtime and allowing automated processes to be optimized before physical implementation [15]. In this context, RoboDK is an appropriate tool because it provides intuitive simulation software for robotic arms and does not require advanced programming knowledge.

At the bar pressing workstation located at the ZF plant in Reynosa, improper positioning of the bars within the part was identified as a recurring problem, leading to defective pressing operations and material loss. Additionally, this production environment involves frequent interaction with other personnel and limited physical space. Therefore, automating this process requires a collaborative robotics solution based on a compact robotic arm with strong human-machine interaction capabilities, designed to increase production line efficiency and reduce improper material handling.

This article evaluates the implementation of a Universal Robots cobot for the production of automotive seatbelts using a comparative analysis and robotic simulation approach supported by RoboDK software. These simulations enable the identification of suitable cobot configurations, making it possible to improve efficiency, quality, and safety indicators at the bar pressing workstation without significantly affecting the workspace, while ensuring compliance with the current international regulatory framework established by the ISO/TS 15066 technical specification.

2. Materials and Methods

This section describes the research methodology, process analysis, and study phases.

2.1. Research Approach, Methodology, and Phases

The solution presented in this article employs a hybrid methodology based on comparative analysis and simulation to support the selection and implementation of a cobot to automate the production of automotive seatbelts. In this context, comparative analysis is understood as a research method that involves collecting, comparing, and analyzing qualitative and quantitative data to provide a clearer representation of the characteristics of processes, documents, or other study objects, supported by visual tools that facilitate their evaluation.

For the development of this research, several instruments were used, including: (i) technical datasheets of Universal Robots cobots, (ii) RoboDK software operation manuals, and (iii) CAD and 3D models developed in Fusion 360, considering the workspace of the bar pressing station. To achieve the objectives of this study, qualitative and quantitative analyses of the work environment were also performed to select the most suitable cobot and validate its implementation through digital simulation. The main techniques used were as follows:

1. Documentary review: used to analyze the specifications of Universal Robots cobot models.
2. Comparative analysis: used to compare technical and economic criteria through comparative tables as an evaluation tool.
3. Digital simulation: performed using RoboDK and Fusion 360 to model the work environment, program trajectories, measure cycle times, identify environmental interferences, and validate cobot operability.

The data analysis in this research was structured into three main stages. First, a technical comparison of the different cobot models offered by Universal Robots was conducted, considering specifications such as payload, workspace, repeatability, and cost. This comparison was essential to avoid oversizing the future integration investment. In the second stage, a digital simulation of the selected cobot model was developed using RoboDK software. This step analyzed key parameters such as cycle time, potential collisions, and the feasibility of integrating the cobot into the actual workspace of the bar pressing station. Finally, the simulation results were compared with the actual process conditions to validate the applicability of the proposed solution.

In industrial automation, particularly in the selection of collaborative robotic arms, comparative analysis and digital simulation play an essential role in the early stages of a project. These techniques are complementary: comparative analysis supports the evaluation and selection of the most suitable model based on the required technical specifications, while digital simulation facilitates the visualization and validation of different configurations for integrating the cobot into the workspace. This methodology makes it possible to identify the most viable option for cobot implementation without significantly interfering with the production line, while reducing risks, costs, and time associated with physical testing. As previously stated, the main objective of the methodology is to select and evaluate a cobot by collecting and analyzing technical data from Universal Robots collaborative robot models. The phases comprising the comparative analysis in this case are shown in Figure 1 and described below.

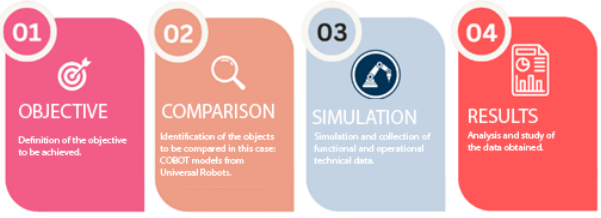

Figure 1. Phases of the comparative analysis.

2.2. Considerations for Cobot Selection

Since the application does not require a high payload capacity, several e-Series cobots offered by Universal Robots were evaluated. Table 1 summarizes and compares the Universal Robots models considered in this study. The weight of both the end effector and the product was also considered as a determining factor for positioning the robot within the bar pressing station. For end-effector selection, technical information from ROBOTIQ was reviewed, considering not only the total product weight of 1.2 kg, but also the effective mass transmitted to the end effector during the gripping operation. This effective mass depends on the contact geometry, force distribution among the fingers, and task configuration. Thus, the gravitational force associated with the effective mass can be expressed as equation (1):

$$F_g = m_{ef} \cdot g \tag{1}$$

where F_g is the gravitational force applied at the gripping point, m_{ef} is the effective mass supported by the end-effector contact, and g is the acceleration due to gravity. Based on the component geometry, the type of gripping, and the load distribution recommended by the manufacturer, the effective mass transmitted to each contact point was estimated at 0.345 kg. To ensure a secure grip and compensate for possible dynamic effects and operational variations, a safety factor of 2 was subsequently applied, resulting in a minimum required force of 6.77 N. Based on this analysis, the proposed solution incorporates the Hand-E end effector from ROBOTIQ, as shown in Figure 2(a).

Table 1. Technical comparison of Universal Robots e-Series models

Models	Payload útil (kg)	Reach (mm)	Repeatability (mm)	Degrees of freedom	Communication	Control	Cost (USD)
 UR16e	16 kg	900 mm	± 0.05 mm	6 joints	Control frequency 500 Hz Modbus TCP PROFINET Ethernet/IP USB 2.0, USB 3.0	Polyscope	57,600
 UR10e	12.5 kg	1300 mm	± 0.05 mm	6 joints	Control frequency 500 Hz Modbus TCP PROFINET Ethernet/IP USB 2.0, USB 3.0	Polyscope	47,600
 UR5e	5 kg	850 mm	± 0.03 mm	6 joints	Control frequency 500 Hz Modbus TCP PROFINET Ethernet/IP USB 2.0, USB 3.0	Polyscope	38,300
 UR3e	3 kg	500 mm	± 0.03 mm	6 joints	Control frequency 500 Hz Modbus TCP PROFINET Ethernet/IP USB 2.0, USB 3.0	Polyscope	33,000

(a) (b) (c)

Figure 2. (a) Hand-E end effector, (b) Retractor 4.0, and (c) Proposed Hand-E design.

This model meets requirements of the application, offering design flexibility, a 7 kg payload capacity, adequate precision, and a gripping force ranging from 20 to 185 N [16]. Figure 2(b) shows the positions that the end-effector fingers must reach on the product to be handled. Since the original Hand-E design cannot access these areas, a modified finger design was developed in Fusion 360. The final design, shown in Figure 2(c), provides an adequate grip. Based on this analysis and the available options from Universal Robots, the UR3e model was selected as the most viable alternative because of its compact design and 3 kg payload capacity [17], which is sufficient to handle the combined weight of the part and the end effector without difficulty.

2.3. 3D Modeling

Before creating the simulation environment, the 3D models of the elements to be evaluated were obtained, including the robot workstation, the bar pressing station, the collaborative robot, and the end effector. Autodesk Fusion 360 was used as the CAD design software to model the UR3e workstation together with the bar pressing station [18–20]. Figure 3 shows the UR3e collaborative robot model and the selected end effector from the RoboDK library.

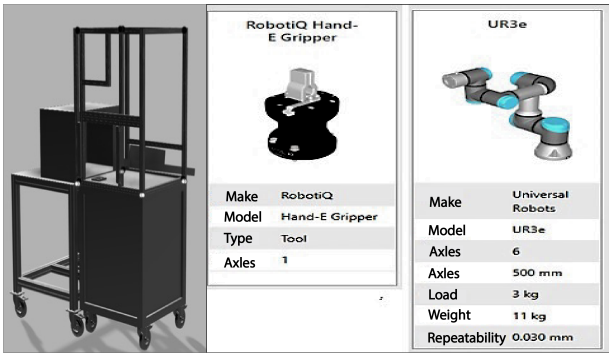

Figure 3. 3D model of the UR3e workstation with the bar pressing station and end effector.

3. Results and Discussion

Before programming the trajectories and confirming the final robot selection, simulations were performed to evaluate different alternatives for positioning the base of the UR3e cobot at the bar pressing station. Initially, two configurations were considered: a central location on the worktable and a second option at one of the table corners. As shown in Figure 4, the first alternative limited the robot's mobility and effective reach, whereas the second provided greater freedom of movement and reduced the risk of collisions with the surrounding environment. Once the optimal table-corner location was defined, the initial position of the UR3e was established and the trajectories were configured. The starting position was set at the fixture where the operator manually places the part, as illustrated in Figure 5.

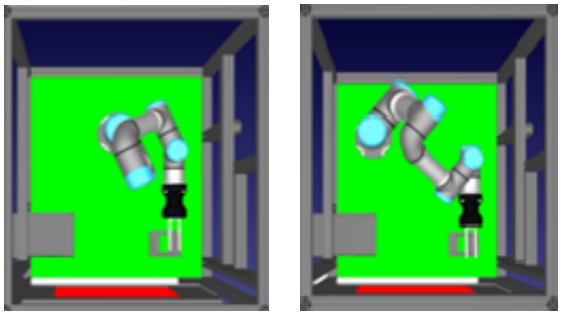

(a) (b)

Figure 4. Possible locations for the UR3e base.

Once the initial conditions are met, the UR3e executes a linear downward motion (MoveL) until it reaches the gripping point, ensuring greater precision and minimizing the risk of collision with the product. Upon reaching the programmed point, the end effector is activated to grasp the retractor. Since the part is placed on a fixture, an additional motion was included to extract the component. Once the part has been picked up, the cobot moves toward the bar pressing station, which uses two fixtures. To correctly position the part in this station, a sequence of three motions was configured, combining joint movements (MoveJ) for general positioning and linear movements (MoveL) for the final approach and precise placement of the part on the press fixture.

For safety reasons, withdrawal of the UR3e from the press area was explicitly programmed as part of the operational cycle. After the pressing operation is completed, the UR3e grasps the part again through a linear motion and moves it to the next programmed position. During part removal, the cobot position is defined to avoid collisions and allow subsequent unloading. Finally, the cobot positions the finished part above the discharge tray. In this case, a joint movement (MoveJ) was used because it allows faster motion and does not require high precision, since the tray has sufficient space to properly receive the part.

The complete task was implemented using a set of 7 to 9 waypoints, including the start, approach, gripping, lifting, placement, safe withdrawal, and unloading positions. With the proposed trajectory, the robot cycle time was 5.8 s, excluding the inherent cycle time of the bar pressing station. Therefore, this station cycle had to be added to obtain a realistic estimate of the total process time. Since the bar pressing station has a cycle time of 3.94 s, the total estimated cycle time with the UR3e was 9.34 s. In addition, potential collisions between the UR3e and the work environment were evaluated.

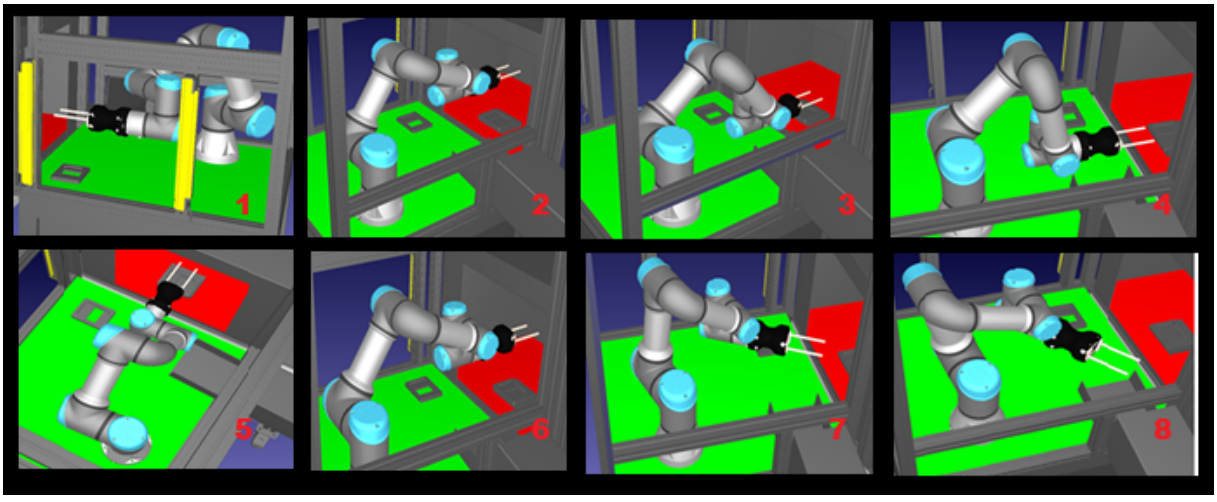

Figure 5. Sequence of programmed motions for the cobot at the bar pressing station.

3.1. Integration and Validation in a Real Environment

To validate the simulation results and the proposed designs, tests were conducted on production line 454 to evaluate the performance of the UR3e collaborative robot. Figure 6 shows the bar pressing workstation before and after UR3e integration on production line 454. Based on the position recommended by the RoboDK simulation, the workstation was installed at the bar pressing station, and the position of the UR3e base on the workstation was verified. The robot was then integrated and programmed into the production line according to the simulation results, as shown in Figure 5. In addition, the UR3e program was integrated with the programmable logic controller of the bar pressing station.

First, the cobot startup was verified. Upon receiving a signal indicating the presence of a part on the fixture, the cobot initiated its cycle and accurately grasped the part. The part was then extracted from the fixture before the cobot moved to the next trajectory point. As previously defined in the simulation, the UR3e executed a backward motion to maintain a safe distance while the bar pressing station was operating. Once the pressing cycle was completed, the UR3e moved to the next trajectory point to grasp and remove the part from the station, positioning it for subsequent unloading into the discharge tray. To complete the sequence, the UR3e reached the final programmed position, deactivated the end effector, and released the part into the output tray.

(a) (b)

Figure 6. Real implementation of the proposed solution at the bar pressing station on production line 454: (a) before UR3e cobot integration and (b) after UR3e cobot integration.

3.2. Results of the UR3e Integration

This section presents a comparative analysis of process efficiency after incorporating the proposed UR3e collaborative robot into the bar pressing station. For this analysis, 10 samples of process cycle times were recorded for both manual operation and cobot-assisted operation. Table 2 presents the results obtained from this comparison. Manual operation times were measured under normal workflow conditions during a standard production shift, avoiding situations of extreme fatigue or conditions that were not representative of the actual process. The measurements were obtained from an experienced operator previously trained at the bar pressing station to ensure consistency in task execution and reduce variability associated with individual differences. This approach enabled a direct and controlled comparison between manual and automated performance in a realistic industrial scenario. Each sample corresponded to one operation shift, during which multiple consecutive cycles were recorded. Thus, the intrashift variability captured by the standard deviation naturally reflects the effects of fatigue, microbreaks, and adjustments inherent to manual operation, whereas the comparison with the cobot highlights differences in process repeatability and consistency.

This methodology was deliberately adopted to ensure a fair and representative comparison between the two modes of operation while keeping environmental conditions and workload constant. To evaluate whether the observed reduction in cycle time was statistically

significant, an independent-samples Student's t-test was applied, considering the mean values per operation shift as the experimental units ($n = 10$ per condition).

The results indicate a statistically significant difference between manual operation and UR3e-assisted operation ($p < 0.05$), confirming that the reduction in cycle time was not attributable to random process variability, but rather to a systematic effect associated with the integration of the collaborative robot. The time measurements confirmed the feasibility of integrating a cobot into the bar pressing station process. Process efficiency improved significantly compared with the previous manual operation, reducing the average cycle time from 13.04 s to 9.34 s. Similarly, the cycle time obtained in the simulation was consistent with that observed in the real application, demonstrating repeatable and stable process execution. Figure 7(a) shows the layout before cobot integration, while Figure 7(b) illustrates the layout after the integration of the collaborative robot into production line 454. As shown in Figure 7, the UR3e operates within a delimited area. However, this configuration does not imply an isolated environment, but rather a functional organization of the workspace that enables safe coexistence between the human operator and the robot throughout the work cycle. During the automatic operation phases, the UR3e-based system operates with the required physical separation to ensure safety and process repeatability.

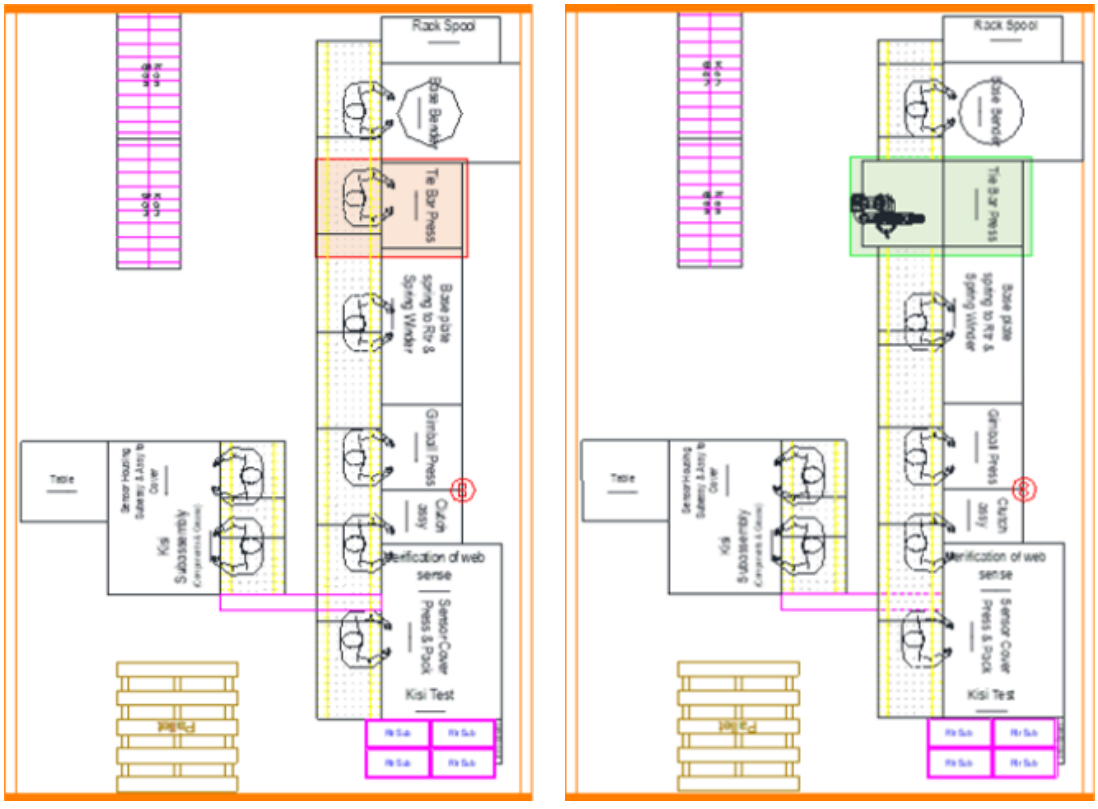

(a) (b)

Figure 7. Production line and workstation with human–machine interaction: (a) Layout of line 454 before UR3e cobot integration and operation, (b) Layout of line 454 after UR3e cobot integration and operation.

Table 2. Average cycle times before and after UR3e cobot integration.

	Cycle times (s)										
Elements	**S1**	**S2**	**S3**	**S4**	**S5**	**S6**	**S7**	**S8**	**S9**	**S10**	**Prom.**
Operator	13.19±0.28	13.25±0.31	12.85±0.35	12.68±0.33	13.02±0.29	13.17±0.30	12.95±0.34	12.84±0.36	13.25±0.32	13.15±0.27	13.04±0.20
UR3e	9.38±0.05	9.31±0.04	9.30±0.06	9.43±0.05	9.31±0.04	9.35±0.05	9.33±0.04	9.31±0.05	9.31±0.04	9.33±0.05	9.34±0.04
Statistical test					**t-statistic**		**gl**			**p-value**	
Student's t-test (independent samples)					t = 56.4		18			p<0.001	

In contrast, during loading, unloading, adjustment, programming, maintenance, and supervision, the robot can operate in safe modes, such as monitored stop or hand guiding, allowing direct operator intervention in accordance with the criteria defined in ISO/TS 15066 [21]. Therefore, the addressed task corresponds to a sequential collaborative application in which the human operator and the robot share the workspace and cooperate within the production flow, although they do not perform simultaneous actions on the same part. The collaborative nature of the application lies primarily in the operational flexibility it provides, allowing safe switching between automatic and collaborative modes depending on the process stage. Thus, the robot performs operations that require precision, repeatability, and control, while the operator remains responsible for feeding, supervision, and process control, reducing physical workload and operational variability. Likewise, the visual delimitation of the robot's operating area responds to criteria related to speed control, separation, and power and force limiting, in accordance with ISO/TS 15066, rather than to physical isolation incompatible with a collaborative application.

4. Conclusions

The analysis of the results confirmed the initial hypothesis that integrating a Universal Robots cobot at the bar pressing station improves the production process in terms of efficiency, quality, and safety without significantly affecting the workspace. The results also validate the use of RoboDK as a simulation tool to support the design and evaluation of the proposed system. The suitability of the selected robotic arm was demonstrated by the reduction in average cycle time from 13.04 s to 9.34 s. Additionally, the execution of repeatable and controlled trajectories contributes to reducing the risk of material damage during handling by minimizing positioning errors and the variability inherent to manual operation. The methodological approach presented in this study is scalable and transferable to other production-line stations involving repetitive handling tasks. By adapting the layout, defining new trajectories, and selecting the appropriate end effector, the same simulation-based procedure can be applied to operations such as machine loading and unloading, inspection, or light assembly, enabling prior validation of system performance and its impact on cycle time, safety, and process quality.

Conflict of Interest

The authors declare that they have no potential conflicts of interest to disclose in relation to this article.

Acknowledgments

The authors acknowledge the financial support provided by FAPERJ, Fundação Carlos Chagas Filho de Amparo à Pesquisa do Estado do Rio de Janeiro, Brazil. Senior Postdoctoral Fellowship (PDS), FAPERJ Call No. 18/2024.

Contributor Roles

- **Kevyn Obed Manzano-Ibarra:** Conceptualization, data curation, formal analysis, research, methodology, project management, software, validation, visualization, writing – original draft.
- **Ivón Oristela Benítez-González:** Conceptualization, data curation, methodology, project management, validation, visualization, writing – review and editing.
- **José Manuel Bernal-de Lázaro:** Conceptualization, data curation, research, methodology, project management, validation, visualization, writing – review and editing.

References

[1] Y. Han, J. Shao, R. Zhou, Y. Liao, and Y. Zhong, "Robotic digital twin based full lifecycle decision framework for automotive productions," *IEEE Network*, vol. 39, no. 4, pp. 173–181, 2025. [Online]. Available: https://doi.org/10.1109/MNET.2024.3418624

[2] J. Yang, Y. H. Son, D. Lee, and S. D. Noh, "Digital twin-based integrated assessment of flexible and reconfigurable automotive part production lines," *Machines*, vol. 10, no. 2, p. 75, Jan. 2022. [Online]. Available: https://doi.org/10.3390/machines10020075

[3] O. Llanes-Santiago, A. Prieto-Moreno, J. M. Bernal de Lázaro, D. C. Knupp, and A. J. Silva Neto, "A design proposal for multiblock-based fault diagnosis systems in complex industrial plants," *Chemometrics and Intelligent Laboratory Systems*, vol. 162, pp. 149–159, Mar. 2017. [Online]. Available: https://doi.org/10.1016/j.chemolab.2017.01.015

[4] A. S. Bisen and H. Payal, "Collaborative robots for industrial tasks: A review," *Materials Today: Proceedings*, vol. 52, pp. 500–504, 2022. [Online]. Available: https://doi.org/10.1016/j.matpr.2021.09.263

[5] L. Liu, F. Guo, Z. Zou, and V. G. Duffy, "Application, development and future opportunities of collaborative robots (cobots) in manufacturing:

A literature review," *International Journal of Human–Computer Interaction*, vol. 40, no. 4, pp. 915–932, Apr. 2022. [Online]. Available: https://doi.org/10.1080/10447318.2022.2041907

[6] C. E. Martínez-Ochoa, I. O. Benítez-González, A. O. Cepero-Díaz, J. R. Núñez-Álvarez, C. G. Miguélez-Machado, and Y. E. Llosas-Albuerne, "Active disturbance rejection control for robot manipulator," *Journal of Robotics and Control (JRC)*, vol. 3, no. 5, pp. 622–632, 2022. [Online]. Available: https://doi.org/10.18196/jrc.v3i5.14791

[7] R. G. Boboc, F. Gîrbacia, and E. V. Butilă, "The application of augmented reality in the automotive industry: A systematic literature review," *Applied Sciences*, vol. 10, no. 12, p. 4259, 2020. [Online]. Available: https://doi.org/10.3390/app10124259

[8] A. Keshvarparast, D. Battini, O. Battaia, and A. Pirayesh, "Collaborative robots in manufacturing and assembly systems: literature review and future research agenda," *Journal of Intelligent Manufacturing*, vol. 35, no. 5, pp. 2065–2118, May 2023. [Online]. Available: https://doi.org/10.1007/s10845-023-02137-w

[9] GGI, *Collaborative Robots Market.* Global Growth Insights, 2024. [Online]. Available: https://upsalesiana.ec/ing36ar1r9

[10] GVR, *Collaborative Robot Market (2026–2033) Size, Share & Trends Analysis Report.* Grand View Research, 2026. [Online]. Available: https://upsalesiana.ec/ing36ar1r10

[11] MI, *Tamaño del mercado de robots colaborativos y análisis de participación tendencias de crecimiento y pronósticos (2024-2029).* Mordor Intelligence, 2024. [Online]. Available: https://upsalesiana.ec/ing36ar1r11

[12] P. Amiri, M. Müller, M. Southgate, T. Theodoridis, G. Wei, M. Richards-Brown, and W. Holderbaum, "A statistical analysis of commercial articulated industrial robots and cobots," *Journal of Manufacturing and Materials Processing*, vol. 8, no. 5, p. 216, 2024. [Online]. Available: https://doi.org/10.3390/jmmp8050216

[13] J. Bernal-de Lázaro, O. Llanes-Santiago, A. Prieto-Moreno, A. del Castillo-Serpa, and A. Silva-Neto, "A novel index for the robustness comparison of classifiers in fault diagnosis," *Neurocomputing*, vol. 275, pp. 636–648, Jan. 2018. [Online]. Available: https://doi.org/10.1016/j.neucom.2017.09.021

[14] V. Villani, F. Pini, F. Leali, and C. Secchi, "Survey on human–robot collaboration in industrial settings: Safety, intuitive interfaces and applications," *Mechatronics*, vol. 55, pp. 248–266, Nov. 2018. [Online]. Available: https://doi.org/10.1016/j.mechatronics.2018.02.009

[15] Siemens. (2026) Simulación robótica. Siemens. [Online]. Available: https://upsalesiana.ec/ing36ar1r15

[16] Robotiq. (2026) Hande-E. Robotiq. [Online]. Available: https://upsalesiana.ec/ing36ar1r16

[17] U. Robots. (2026) e-Series. Universal Robots. [Online]. Available: https://upsalesiana.ec/ing36ar1r17

[18] RoboDK. (2026) Software de simulación de robots. RoboDK. [Online]. Available: https://upsalesiana.ec/ing36ar1r18

[19] N. A. Molina Ferrer, *Diseño de interfaz y comunicación para inspecciones visuales automatizadas en ensamblajes complejos mediante un Cobot Festo.* Universitat Politècnica de València, 2024. [Online]. Available: https://upsalesiana.ec/ing36ar1r19

[20] N. P. Brito Santos, *Diseño y simulación de un sistema automatizado para la navegación y almacenamiento eficiente de paquetes en centros logísticos utilizando el Robot Colaborativo UR10e en conjunto con un Robot Móvil y la integración de visión artificial y marcadores ArUco mediante la herramienta CoppeliaSim (V-REP)".* Universidad Miguel Hernández de Elche, 2023. [Online]. Available: https://upsalesiana.ec/ing36ar1r20

[21] ISO, *ISO/TS 15066:2016 Robots and robotic devices – Collaborative robots.* International Organization for Standardization, 2016. [Online]. Available: https://upsalesiana.ec/ing36ar1r21

Scientific Paper / Artículo Científico

UNIVERSIDAD POLITÉCNICA SALESIANA ECUADOR
INGENIUS
Revista de Ciencia y Tecnología
https://doi.org/10.17163/ings.n36.2026.02
pISSN: 1390-650X / eISSN: 1390-860X

Comparative framework for electricity demand forecasting using machine learning and rolling temporal validation

Marco comparativo para el pronóstico de demanda eléctrica con machine learning y validación temporal rodante

Juan Carlos Castillo[1,*], Jessica N. Castillo[1], Gabriel Pesántez[2], Wilian Guamán[2]

Received: 15-11-2025, Received after review: 26-01-2026, Accepted: 21-04-2026, Published: 01-07-2026

Abstract

Accurate load forecasting is essential for power system planning and operation, particularly under pronounced temporal variability and temporal drift. This study presents a reproducible comparative framework for machine learning models based on rolling-origin expanding validation, multihorizon evaluation, and an operational relative tolerance metric denoted as %Tol. Four representative models are evaluated: EvoXGB, a sequential residual XGBoost ensemble; XGB; TabNet; and FT-Transformer. These models are applied to hourly active power forecasting in distribution substations within an Ecuadorian power system. To ensure a fair comparison when models exhibit differences in prediction coverage or temporal misalignment, the framework incorporates an explicit comparability audit based on temporal alignment and a common evaluation mask denoted as COMMONMASK, complemented the longest common contiguous block for the zoomed time-series visualization. For the representative substation, with metrics computed on the common set, XGB achieves the best performance, with R^2= 0.993 for the short horizon and R^2 = 0.983 for the medium horizon, and RMSE values of 21.16 and 30.84 kW, respectively. EvoXGB remains competitive, whereas TabNet and FT-Transformer exhibit greater degradation in the medium horizon. The 90/10 holdout verification shows the expected performance decline associated with temporal drift while preserving the comparative ranking. Overall, the proposed framework provides a traceable benchmark for substation load forecasting and supports future extensions toward adaptive and hybrid forecasting approaches.

Keywords: load forecasting, machine learning, XGBoost, TabNet, FT-Transformer, rolling temporal validation.

Resumen

La precisión en el pronóstico de la demanda eléctrica es un elemento central para la planificación y operación de los sistemas de potencia, en particular ante la variabilidad temporal de la carga y la presencia de deriva temporal. En este trabajo se desarrolla un marco comparativo reproducible de modelos de machine learning con validación temporal rodante (rolling-origin expanding), análisis multihorizonte y una métrica operativa de tolerancia relativa (%Tol). Se evalúan cuatro modelos representativos: EvoXGB (ensamble secuencial de XGBoost sobre residuales), XGB, TabNet y FT-Transformer, aplicados al pronóstico horario de potencia activa en subestaciones de distribución de un sistema eléctrico ecuatoriano. Para asegurar la comparabilidad cuando existen diferencias de cobertura o desalineación temporal entre predicciones, se incorpora una auditoría explícita basada en alineación y un conjunto común de evaluación (COMMONMASK), complementada con un bloque contiguo común para la figura de zoom. En la subestación representativa (con métricas sobre el conjunto común), XGB logra el mejor desempeño, con R^2 = 0,993 (corto) y 0,983 (mediano), y un RMSE de 21,16 y 30,84 kW, respectivamente. EvoXGB se mantiene competitivo, mientras que TabNet y FT-Transformer muestran mayor degradación en el horizonte mediano. En la verificación de holdout (90/10) se observa la caída esperada por deriva temporal, preservándose el orden comparativo. El marco propuesto entrega una base trazable para comparar modelos en series reales de subestaciones y para extender el análisis hacia esquemas híbridos y adaptativos.

Palabras clave: pronóstico de carga, machine learning, XGBoost, TabNet, FT-Transformer, validación temporal rodante.

[1,*]Universidad Técnica de Cotopaxi, Facultad de Ciencias de la Ingeniería y Aplicadas, Ecuador.
Corresponding author ✉: juan.castillo2321@utc.edu.ec.

[2]Escuela Superior Politécnica de Chimborazo (ESPOCH), GITEA, Riobamba, Ecuador.

Suggested citation: J. C. Castillo, J. N. Castillo, G. Pesántez and W. Guamán. "Comparative framework for electricity demand forecasting using machine learning and rolling temporal validation," *Ingenius, Revista de Ciencia y Tecnología*, N.° 36, pp. 19-28, 2026, DOI: https://doi.org/10.17163/ings.n36.2026.02.

1. Introduction

The sustained growth in energy demand and the increasing integration of intermittent renewable sources have made load forecasting a strategic component of power system planning and operation, Accurate forecasting across different time horizons is essential for substation scheduling, resource allocation, and efficient grid management under conditions characterized by seasonality, nonlinear behavior, and regime changes [1, 2], [3–5].

Among contemporary approaches, gradient boosting algorithms, particularly XGBoost, have become widely established due to their robustness and ability to model nonlinear relationships in high-dimensional tabular data [6–9]. However, their performance depends on careful hyperparameter tuning, which is often computationally demanding and sensitive to the dataset configuration. To mitigate this limitation, optimized variants based on evolutionary algorithms have been proposed, including approaches that combine XGBoost with Differential Evolution or Genetic Algorithms, which have demonstrated improvements in stability and reductions in overfitting [10–12].

In parallel, deep learning models specifically designed for tabular data have emerged. TabNet employs sequential attention mechanisms that provide inherent interpretability [13], whereas FT-Transformer adapts the Transformer architecture through linear feature embeddings and multi-head attention [14, 15]. However, several studies indicate that the superiority of deep networks over tree-based methods is not universal and depends strongly on the size and structure of the dataset [16, 17].

A frequent limitation in the load forecasting literature is the use of static training and testing splits that do not account for temporal non-stationarity. Current methodological guidelines recommend temporal validation schemes based on a rolling-origin expanding windows to evaluate model performance over time and detect operational degradation [18–20]. In addition to global metrics such as MAE, RMSE, and R^2, operational indicators that reflect acceptable error tolerances from a planning perspective, such as the %Tol metric, should also be incorporated [21], [22].

Explicit contrast with standard approaches. Unlike random cross-validation or partitioning schemes that do not preserve order, which can produce optimistic estimates by mixing past and future observations, rolling-origin validation evaluates performance in more realistic forecasting scenarios, in which predictions are made for subsequent periods. In addition, the proposed framework integrates conventional performance metrics and the %Tol metric within an explicit comparability audit when prediction coverage differs across models.

In the Ecuadorian context, previous studies have addressed long-term electricity consumption forecasting using machine learning models [23], as well as power system planning through reinforcement learning [24]. This study develops a comparative framework for hourly active power forecasting in substations, based on rolling-origin temporal validation, the %Tol metric, and a methodological audit to ensure fair comparisons.

The specific contributions of this study are as follows:

(i) A reproducible evaluation framework based on rolling temporal validation and micro-criterion metric aggregation is proposed.

(ii) Boosting-based and deep tabular architectures are compared across short- and medium-term forecasting horizons under a consistent methodological setting.

(iii) An explicit comparability audit based on temporal alignment and COMMONMASK is incorporated, together with an operational interpretation through the %Tol metric.

2. Materials and Methods

2.1. Data and Variables

This methodology evaluates the stability and accuracy of predictive models for electricity demand forecasting in Ecuadorian substations.

Hourly active power time series recorded at nine substations of a distribution network within the national power system were used, with approximately 40,000 hourly observations per substation, spanning a continuous 4.5-year period between 2020 and 2024. The data were obtained from internal historical records of the national electric utility.

The target variable was active power in kW, while the predictor variables included:

(i) calendar attributes namely hour, day of the week, and month;

(ii) lagged power values from 4 to 24 h; and

(iii) moving averages over 3, 6, and 24 h.

For confidentiality reasons, the substation identifiers were anonymized. Each model was trained independently for each substation. To maintain a compact presentation, the tables and figures detail the results of a representative substation, while the remaining substations are used to confirm the consistency of the findings. Specifically, a substation was considered representative when its performance profile, defined by RMSE and %Tol across both forecasting horizons, was closest to the median of the full set according to the

sum of ranks, thereby avoiding the selection of extreme cases.

2.2. Data Preprocessing

The series were chronologically ordered, and an initial cleaning procedure was performed to remove extreme or infinite values. Missing values were handled using forward filling within each series; any residual cases were discarded to avoid interpolations that could introduce temporal bias. Subsequently, lagged features and moving averages were generated, and the first 24 observations were removed to prevent edge inconsistencies.

In each iteration of the validation process, the explanatory variables were scaled using RobustScaler, which was fitted exclusively on the training data of the corresponding window and then applied to the test set to avoid data leakage. For TabNet, the same feature set was retained, with normalization performed internally within the model.

2.3. Prediction Models Analyzed

Four representative models were evaluated:

A_EvoXGB: a four-stage sequential ensemble based on XGBoost, in which each component trains trees on the residuals of the preceding model. The final prediction is obtained as the sum of the partial outputs, with the aim of reducing systematic error.

B_XGB: a standard implementation of XGBoost, used as a robust baseline.

C_TabNet: a tabular network with sequential attention [13], configured with $n_d = n_a = 32$, four decision steps, and early stopping.

D_FT-Transformer (D_FTT): a tabular Transformer based on feature embeddings and multihead attention [14, 15], configured with three encoder blocks, a token dimension of 192, and four attention heads.

2.4. Hyperparameter Tuning

The most influential hyperparameters were tuned through bounded pilot experiments centered on configurations recommended for medium-sized tabular datasets. The final selection prioritized temporal stability over marginal local improvements while maintaining a comparable training budget.

2.5. Rolling-Origin Temporal Validation Scheme

Rolling-origin expanding validation was applied. Two forecasting horizons were considered:

- **Short horizon:** test window of 168 h, step of 24 h, and purge of 24 h.
- **Medium horizon:** test window of 720 h, step of 72 h, and purge of 72 h.

In each iteration, the training set included all observations prior to the start of the test window, excluding the purge period, with a minimum of 1500 observations. The metrics were aggregated using a micro-criterion, jointly considering all predictions generated by each model–horizon combination.

2.6. Temporal Alignment and Common Evaluation Set (COMMONMASK)

In practice, different models may produce predictions with unequal coverage, for example, due to partial window execution, or with temporal misalignment caused by offsets related to lag construction or the forecast anchoring point. To avoid biased comparisons, the following audit procedure was applied:

- **Alignment:** a shift of -24 h was applied to the predictions of B_XGB to homogenize the temporal anchoring of the test index with that of the other models. This correction was verified by matching the start of the test segment.
- **COMMON ALL:** the intersection of indices for which all four models provided finite predictions was defined, and the metrics, namely MAE, RMSE, R^2 and %Tol, were computed on this set.
- **COMMON CONTIG:** for the zoom figure, the longest contiguous common block was selected. From this block, a representative 168 h segment was presented to facilitate visual comparison without discontinuities.

Note on coverage and non-imputation. When a model presents partial coverage, for example, due to computational constraints or incomplete execution during rolling validation, the common set may be substantially reduced. To avoid bias, missing predictions were neither imputed nor interpolated. Instead, coverage, reported in Table 2, and the size of the common set, reported in Table 3, are explicitly documented. Performance interpretation is therefore limited to the comparable segment. In addition, a 90/10 holdout verification and an aggregated %Tol analysis across nine substations are included to strengthen the conclusions beyond the analysis of a single series.

2.7. Summary of the Experimental Pipeline (Scheme)

Figure 1 summarizes the complete sequence of the experimental framework, from data preparation and feature engineering to temporal validation, model training, prediction, and metric aggregation.

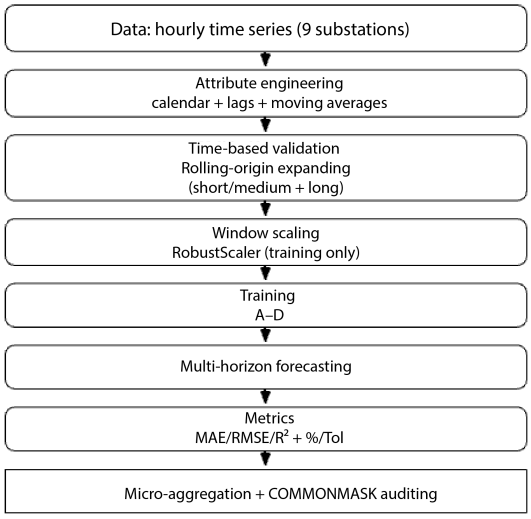

Figure 1. Schematic representation of the experimental workflow, including feature extraction, temporal validation, model training, prediction, metric computation, and the comparability audit.

2.8. Independent Validation (90/10 Holdout)

As a complementary verification, each model was retrained using the initial 90% of the data and evaluated on the final 10%, allowing its performance to be assessed outside the temporal recalibration setting.

2.9. Evaluation Metrics

MAE, RMSE, and R^2 were computed, together with the %Tol metric:

$$\%Tol_\delta = \frac{1}{N}\sum_{i=1}^{N} \mathbf{1}\left(\frac{|y_i - \hat{y}_i|}{\max\{|y_i|, \varepsilon\}} \leq \delta\right) \times 100, \quad (1)$$

where δ is the relative tolerance threshold, and $\varepsilon = 1$ kW prevents unstable ratios.

2.10. Reproducibility and Computational Resources

The experiments were conducted in Python 3.11 using XGBoost 2.0, PyTorch 2.3, and PyTorch-TabNet 4.1, with a fixed global seed. Training was performed on an NVIDIA RTX 3060 GPU (12 GB) with 32 GB of RAM. The scripts and configuration files are available in the GitHub repository [25].

3. Results and Discussion

3.1. Demand Behavior in the Substations

The nine substations analyzed exhibit typical hourly patterns of distribution networks, including nighttime minima, morning increases, daytime plateaus, and evening peaks, together with weekly seasonality. In the representative substation, active power remains within a stable operating range, and the observed regime changes are mainly associated with weekly and seasonal variations, which supports the need for explicit temporal validation.

3.2. Global Performance by Model and Horizon

Figure 2 summarizes model performance across models and forecasting horizons under rolling-origin validation. Metrics were computed on COMMON ALL to ensure that all models were evaluated at the same time instants. For this substation, B_XGB achieves the best balance between accuracy and temporal stability across both horizons, while A_EvoXGB remains closely competitive. TabNet and FT-Transformer exhibit greater degradation in the medium-term horizon.

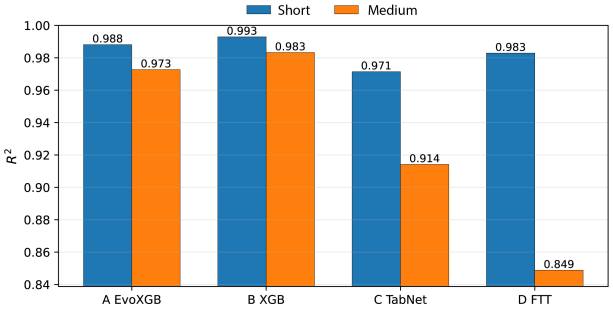

(a) R^2 by model and horizon (on COMMON ALL)

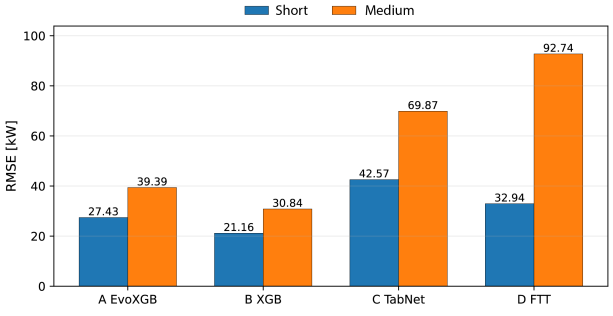

(b) RMSE [kW] by model and horizon (on COMMON ALL)

Figure 2. Model performance across forecasting horizons under rolling-origin validation.

Table 1. Performance of the representative substation under micro-aggregation, computed over COMMON ALL: MAE, RMSE, R^2, and %Tol@5%. (Decimal separator: dot).

Model	Hor.	MAE [kW]	RMSE [kW]	R^2	%Tol@5 %
A_EvoXGB	Short	20.89	27.43	0.988	94.17
B_XGB	Short	15.84	21.16	0.993	96.67
C_TabNet	Short	29.63	42.57	0.972	82.50
D_FTT	Short	24.67	32.94	0.983	87.92
A_EvoXGB	Medium	25.61	39.39	0.973	87.92
B_XGB	Medium	20.04	30.84	0.983	93.33
C_TabNet	Medium	44.51	69.87	0.914	70.90
D_FTT	Medium	54.38	92.74	0.849	68.26

3.3. Comparability Audit: Coverage and COMMONMASK

Table 2 reports prediction coverage by model and forecasting horizon, including the total length, number of finite predictions, and percentage of NaN values. Table 3 summarizes the size of the common set (COMMON ALL) and the longest contiguous common block (COMMON CONTIG), used for the zoom figure. For this substation, the size of COMMON ALL is determined by the model with the lowest coverage (D_FTT); therefore, the audit is explicitly included to ensure transparency.

Table 2. Prediction coverage by model and forecasting horizon for the representative substation.

Hor.	Model	shift [h]	N total	N Finite	%NaN	idx_{min}–idx_{max}
Short	A_EvoXGB	0	37686	37686	0.00	0–37685
Short	B_XGB	-24	37686	37662	0.06	0–37661
Short	C_TabNet	0	37686	37686	0.00	0–37685
Short	D_FTT	0	37686	1200	96.81	1620–4571
Medium	A_EvoXGB	0	37686	37686	0.00	0–37685
Medium	B_XGB	-24	37686	37662	0.06	0–37661
Medium	C_TabNet	0	37686	37686	0.00	0–37685
Medium	D_FTT	0	37686	1440	96.18	1572–2291

Table 3. Summary of the common set (COMMONMASK) by forecasting horizon for the representative substation.

Hor.	N total	N_{common}	%common	idx_{min}–idx_{max}	inicio–fin contig	L_{contig}
Short	37686	240	0.64	1620–4571	4404–4571	168
Medium	37686	1440	3.82	1572–2291	1572–2291	720

In the short horizon, the common set is reduced to 240 h because D_FTT produced predictions over a partial block, and the simultaneous intersection with the other models, after the alignment adjustment of B_XGB, limits the overlap. Therefore, these metrics describe the comparative performance only over this common segment, without imputation. To support the operational conclusions, the analysis also considers (i) the medium horizon, where the overlap is greater (COMMON CONTIG = 720 h in this substation), (ii) the 90/10 holdout verification, and (iii) the aggregated %Tol sensitivity across the nine substations.

3.4. Temporal Reconstruction of the Load Signal

Figure 3 compares the actual series and the model predictions over a representative 168 h segment extracted from the COMMON CONTIG block for both forecasting horizons. The boosting-based models provide a more accurate reconstruction of peaks and valleys. In the medium-term horizon, TabNet and FT-Transformer exhibit a degraded fit, consistent with the increase in RMSE and the decrease in R^2.

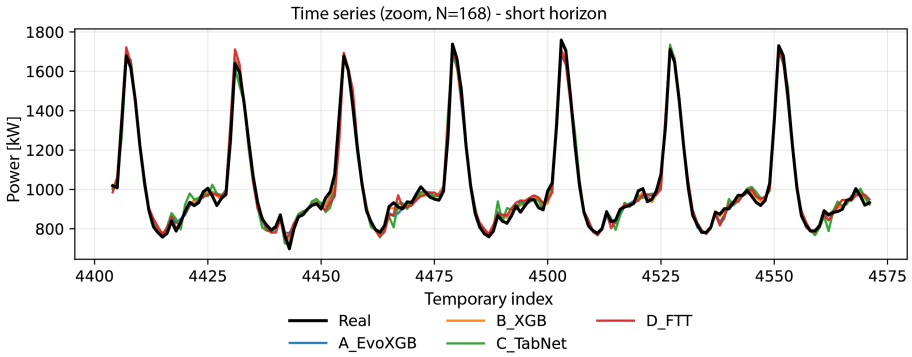

(a) Short horizon (zoom on COMMON CONTIG)

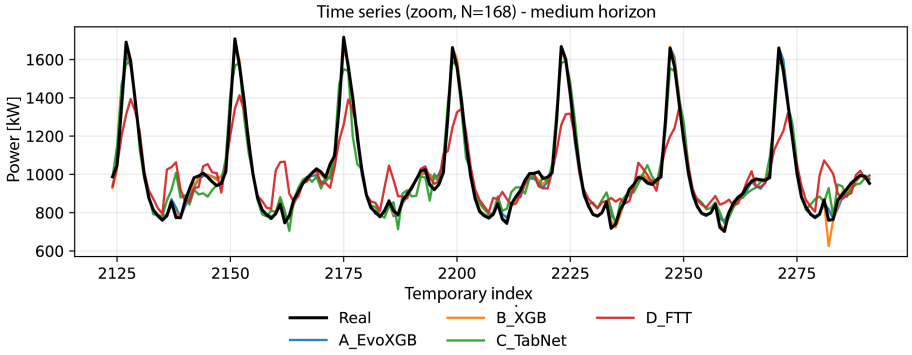

(b)Medium-term horizon (zoom on COMMON CONTIG)

Figure 3. Actual and predicted series over a representative segment.

3.5. Relationship Between Observed and Predicted Values

Figures 4 and 5 show the relationship between observed and predicted values under rolling-origin validation for both forecasting, evaluated on COMMON ALL. In the boosting-based models, especially B_XGB, the predictions are more tightly concentrated around the diagonal $y = x$ in both horizons. In C_TabNet and, more notably, D_FTT, dispersion increases in the medium-term horizon, consistent with the increase in RMSE and the reduction in R^2.

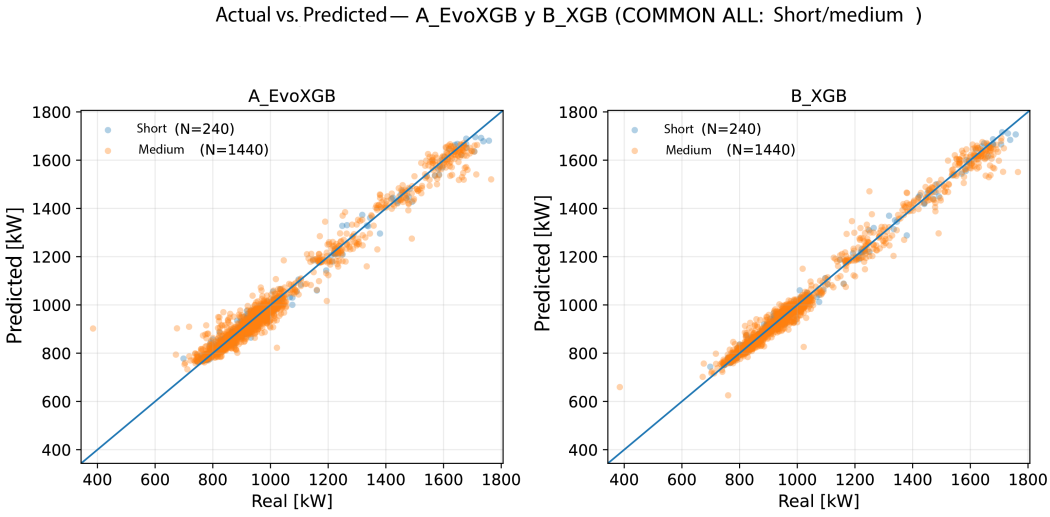

Figure 4. Observed vs. predicted values for A_EvoXGB and B_XGB across both forecasting horizons (rolling-origin; COMMON ALL). The line indicates y = x.

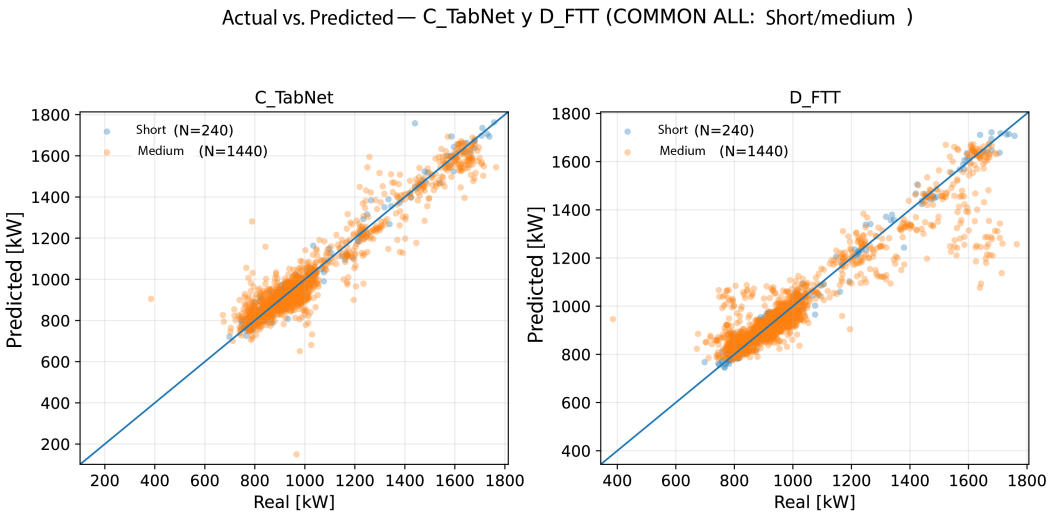

Figure 5. Observed vs. predicted values for C_TabNet and D_FTT across both forecasting horizons (rolling-origin; COMMON ALL). The line indicates y = x.

3.6. Distribution of Relative Errors

To complement the aggregated metrics and characterize variability, Figure 6 presents the distribution of the relative absolute error (%). The boosting-based models concentrate errors in lower ranges with shorter tails, while TabNet and D_FTT exhibit greater dispersion, particularly in the medium-term horizon.

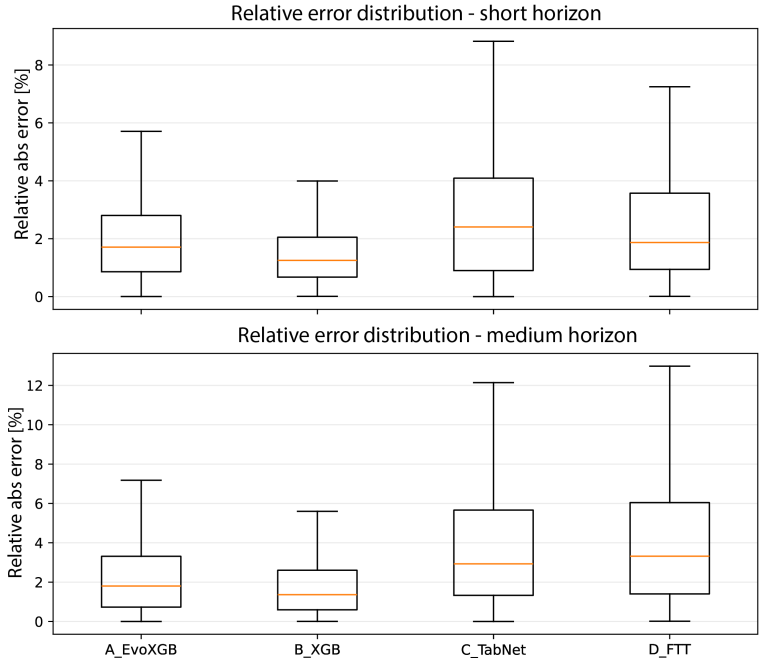

Figure 6. Distribution of relative absolute error (%) by model and horizon forecasting horizon under rolling-origin validation.

3.7. Operational Metric: %Tol Sensitivity to Threshold δ

Figure 7 summarizes the sensitivity of %Tol to different tolerance thresholds. δ was evaluated at 2%, 5%, 10%, 15%, and 20%, aggregating predictions across nine substations. At $\delta = 5\%$, the metric clearly distinguishes performance between model families; at $\delta \geq 10\%$, most methods approach 100%, reducing the discriminative capacity of the indicator.

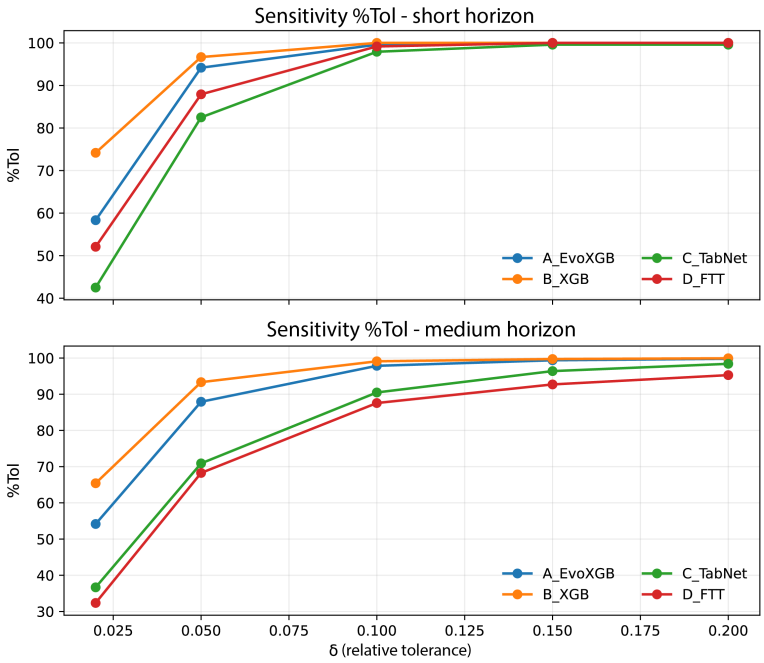

Figure 7. Sensitivity of %Tol to the tolerance threshold δ by model and forecasting horizon (aggregated across the nine substations).

Table 4. Sensitivity of %Tol(δ) by model and forecasting horizon (aggregated across the nine substations).

Short horizon					
Model	δ=2%	5%	10%	15%	20%
A_EvoXGB	58.3	94.2	99.6	100.0	100.0
B_XGB	74.2	96.7	100.0	100.0	100.0
C_TabNet	42.5	82.5	97.9	99.6	99.6
D_FTT	52.1	87.9	99.2	100.0	100.0
Medium horizon					
Model	δ=2%	5%	10%	15%	20%
A_EvoXGB	54.2	87.9	97.8	99.4	99.8
B_XGB	65.4	93.3	99.1	99.7	99.9
C_TabNet	36.7	70.9	90.5	96.4	98.4
D_FTT	32.4	68.3	87.6	92.7	95.3

3.8. Independent Validation (90/10 Holdout)

Table 5 shows the expected decrease relative to rolling-origin validation, reflecting temporal drift between evaluation periods. The comparative ranking is preserved, with B_XGB outperforming the other models in this substation.

Table 5. Performance under 90/10 holdout validation for the representative substation: MAE, RMSE, R^2,and %Tol@5%.

Model	MAE [kW]	RMSE [kW]	R^2	%Tol@5 %
A_EvoXGB	36.95	96.25	0.872	68.00
B_XGB	29.67	70.04	0.932	79.13
C_TabNet	55.48	125.29	0.783	58.26
D_FTT	47.84	105.94	0.845	65.17

3.9. General Discussion

In the representative substation, tree-based methods maintain the best balance between accuracy and operational interpretability. The alignment audit and COMMONMASK prevent biased comparisons when prediction coverage differs across models or when temporal misalignment is present. TabNet and D_FTT provide an adequate fit in the short-term horizon; however, in the medium-term horizon, they exhibit performance degradation and greater dispersion.

Limitations. The data were obtained from a specific system, and the analysis relied on calendar variables, lagged features, and moving averages; therefore, patterns may differ in other contexts or when exogenous variables are incorporated. The representative substation was selected only to provide a clear and compact presentation, while the operational conclusions are strengthened by the aggregated %Tol sensitivity analysis across the nine substations. Finally, when a model presents partial coverage, the common set may be small, as observed in the 240 h short-horizon segment of this substation. Accordingly, the coverage and COMMONMASK audit is explicitly reported, and extrapolation beyond the evaluated common segment is avoided.

Future work should incorporate meteorological and renewable generation variables and explore adaptive recalibration schemes and hybrid approaches.

4. Conclusions

This study presented a comparative framework of machine learning models applied to hourly electricity demand forecasting in substations, based on rolling-origin temporal validation, multihorizon analysis, and an operational relative tolerance metric. To ensure comparability under differences in prediction coverage and temporal misalignment, an explicit audit using alignment and COMMONMASK (common evaluation mask) was incorporated, with coverage also reported for contextual interpretation.

Under rolling-origin validation on COMMON ALL, B_XGB achieved the best performance in the representative substation, followed by A_EvoXGB. TabNet and D_FTT exhibited more pronounced degradation in the medium-term horizon. In the 90/10 holdout validation, the expected performance decline associated with temporal drift was observed, while the relative ranking was preserved.

In particular, when the COMMON ALL intersection is small due to partial coverage, as observed in the short horizon of the representative substation, the metrics are interpreted as performance over the strictly comparable segment. Therefore, the conclusions are mainly supported by the medium-term horizon, the holdout validation, and the aggregated %Tol analysis.

The proposed framework provides a traceable basis for comparing forecasting approaches and supporting planning and operational decisions. Future work should incorporate exogenous variables, explore adaptive recalibration, and extend the window-based audit to all models to uniformly characterize temporal stability.

Contributor Roles

- **Juan Carlos Castillo:** conceptualization; methodology; data curation; software; formal analysis; research; validation; visualization; project management.
- **Jessica N. Castillo:** methodology; supervision; validation; writing – original draft; writing – revision and editing.
- **Gabriel Pesántez:** methodology; supervision; validation; writing – original draft; writing – revision and editing.
- **Wilian Guamán:** methodology; supervision; validation; writing – original draft; writing – revision and editing.

References

[1] T. Hong and S. Fan, "Probabilistic electric load forecasting: A tutorial review," *International Journal of Forecasting*, vol. 32, no. 3, pp. 914–938, 2016. [Online]. Available: https://doi.org/10.1016/j.ijforecast.2015.11.011

[2] IEA, "Renewables 2023: Analysis and forecast to 2028," International Energy Agency, Paris, France, Tech. Rep., 2023, accessed: May 15, 2026. [Online]. Available: https://upsalesiana.ec/ing36ar2r2

[3] M. G. Pinheiro, S. C. Madeira, and A. P. Francisco, "Short-term electricity load forecasting—a systematic approach from system level to secondary substations," *Applied Energy*, vol. 332, p. 120493, Feb. 2023. [Online]. Available: https://doi.org/10.1016/j.apenergy.2022.120493

[4] S. Akhtar, S. Shahzad, A. Zaheer, H. S. Ullah, H. Kilic, R. Gono, M. Jasiński, and Z. Leonowicz, "Short-term load forecasting models: A review of challenges, progress, and the road ahead," *Energies*, vol. 16, no. 10, p. 4060, May 2023. [Online]. Available: https://doi.org/10.3390/en16104060

[5] F. Rodrigues, C. Cardeira, J. M. F. Calado, and R. Melicio, "Short-term load forecasting of electricity demand for the residential sector based on modelling techniques: A systematic review," *Energies*, vol. 16, no. 10, p. 4098, May 2023. [Online]. Available: https://doi.org/10.3390/en16104098

[6] T. Chen and C. Guestrin, "XGBoost: A scalable tree boosting system," in *Proceedings of the 22nd ACM SIGKDD International Conference on Knowledge Discovery and Data Mining*, ser. KDD '16. ACM, Aug. 2016, pp. 785–794. [Online]. Available: https://doi.org/10.1145/2939672.2939785

[7] G. Ke, Q. Meng, T. Finley, T. Wang, W. Chen, W. Ma, Q. Ye, and T.-Y. Liu, "Lightgbm: a highly efficient gradient boosting decision tree," in *Proceedings of the 31st International Conference on Neural Information Processing Systems*, ser. NIPS'17. Red Hook, NY, USA: Curran Associates Inc., 2017, p. 3149–3157. [Online]. Available: https://upsalesiana.ec/ing36ar2r4

[8] L. Prokhorenkova, G. Gusev, A. Vorobev, A. V. Dorogush, and A. Gulin, "Catboost: unbiased boosting with categorical features," in *NIPS'18: Proceedings of the 32nd International Conference on Neural Information Processing Systems*. arXiv, 2017, pp. 6639–6649. [Online]. Available: https://doi.org/10.48550/arXiv.1706.09516

[9] C. Bentéjac, A. Csörgő, and G. Martínez-Muñoz, "A comparative analysis of gradient boosting algorithms," *Artificial Intelligence Review*, vol. 54, no. 3, pp. 1937–1967, Aug. 2020. [Online]. Available: https://doi.org/10.1007/s10462-020-09896-5

[10] Z. Mustaffa and M. H. Sulaiman, "Advanced forecasting of building energy loads with XGBoost and metaheuristic algorithms integration," *Energy Storage and Saving*, vol. 4, no. 4, pp. 421–438, Dec. 2025. [Online]. Available: https://doi.org/10.1016/j.enss.2025.03.005

[11] T.-N. Tran and Q.-D. Nguyen, "Research on the influence of genetic algorithm parameters on XGBoost in load forecasting," *Engineering, Technology & Applied Science Research*, vol. 14, no. 6, pp. 18 849–18 854, Dec. 2024. [Online]. Available: https://doi.org/10.48084/etasr.8863

[12] B. Liang, W. Qin, and Z. Liao, "A differential evolutionary-based xgboost for solving classification of physical fitness test data of college students," *Mathematics*, vol. 13, no. 9, p. 1405, Apr. 2025. [Online]. Available: https://doi.org/10.3390/math13091405

[13] S. Arik and T. Pfister, "TabNet: Attentive interpretable tabular learning," *Proceedings of the AAAI Conference on Artificial Intelligence*, vol. 35, no. 8, pp. 6679–6687, May 2021. [Online]. Available: https://doi.org/10.1609/aaai.v35i8.16826

[14] Y. Gorishniy, I. Rubachev, V. Khrulkov, and A. Babenko, "Revisiting deep learning models for tabular data," in *NIPS'21: Proceedings of the 35th International Conference on Neural Information Processing Systems*. arXiv, 2021, pp. 18 932–18 943. [Online]. Available: https://doi.org/10.48550/arXiv.2106.11959

[15] V. Borisov, T. Leemann, K. Seßler, J. Haug, M. Pawelczyk, and G. Kasneci, "Deep neural networks and tabular data: A survey," *IEEE Transactions on Neural Networks and Learning Systems*, vol. 35, no. 6, pp. 7499–7519, 2024. [Online]. Available: https://doi.org/10.1109/TNNLS.2022.3229161

[16] L. Grinsztajn, E. Oyallon, and G. Varoquaux, "Why do tree-based models still outperform deep learning on tabular data?" in *NIPS'22: Proceedings of the 36th International Conference on Neural Information Processing Systems*. arXiv, 2022, pp. 507–520. [Online]. Available: https://doi.org/10.48550/arXiv.2207.08815

[17] R. Shwartz-Ziv and A. Armon, "Tabular data: Deep learning is not all you need," *Information Fusion*, vol. 81, pp. 84–90, May 2022. [Online]. Available: https://doi.org/10.1016/j.inffus.2021.11.011

[18] V. Cerqueira, L. Torgo, and I. Mozetič, "Evaluating time series forecasting models: an empirical study on performance estimation methods," *Machine Learning*, vol. 109, no. 11, pp. 1997–2028, Oct. 2020. [Online]. Available: https://doi.org/10.1007/s10994-020-05910-7

[19] R. J. Hyndman and G. Athanasopoulos, *Forecasting: Principles and Practice*, 3rd ed. Melbourne, Australia: OTexts, 2021, accessed: May 15, 2026. [Online]. Available: https://upsalesiana.ec/ing36ar2r16

[20] C. Bergmeir and J. M. Benítez, "On the use of cross-validation for time series predictor evaluation," *Information Sciences*, vol. 191, pp. 192–213, May 2012. [Online]. Available: https://doi.org/10.1016/j.ins.2011.12.028

[21] M. Q. Raza and A. Khosravi, "A review on artificial intelligence based load demand forecasting techniques for smart grid and buildings," *Renewable and Sustainable Energy Reviews*, vol. 50, pp. 1352–1372, Oct. 2015. [Online]. Available: https://doi.org/10.1016/j.rser.2015.04.065

[22] C. Borges, Y. Penya, I. Fernández, J. Prieto, and O. Bretos, "Assessing tolerance-based robust short-term load forecasting in buildings," *Energies*, vol. 6, no. 4, pp. 2110–2129, Apr. 2013. [Online]. Available: https://doi.org/10.3390/en6042110

[23] W. Guamán, P. Benalcázar, J. Córdova-García, and M. Torres, *Machine Learning-Based Projections of Long-Term Electricity Consumption: The Case Study of Ecuador*. Springer Nature Switzerland, 2025, pp. 174–187. [Online]. Available: https://doi.org/10.1007/978-3-031-83432-5_12

[24] G. Pesántez, W. Guamán, J. Córdova, M. Torres, and P. Benalcázar, "Reinforcement learning for efficient power systems planning: A review of operational and expansion strategies," *Energies*, vol. 17, no. 9, p. 2167, May 2024. [Online]. Available: https://doi.org/10.3390/en17092167

[25] J. C. Castillo. (2026) Forecasting-rolling-energy. GitHub repository. [Online]. Available: https://upsalesiana.ec/ing36ar2r27

Scientific Paper / Artículo Científico

UNIVERSIDAD POLITÉCNICA SALESIANA ECUADOR
INGENIUS
Revista de Ciencia y Tecnología
https://doi.org/10.17163/ings.n36.2026.03
pISSN: 1390-650X / eISSN: 1390-860X

Corrosion inhibition of type N80 carbon steel using eggshell powder in acidic and brine environments: a study based on weight loss testing, micro-indentation, and electrochemical modeling

Inhibición de la corrosión del acero al carbono tipo N80 utilizando polvo de cáscara de huevo en ambientes ácidos y salinos: un estudio basado en ensayos de pérdida de peso, microindentación y modelado electroquímico

J. L. Dávalos-Monteiro[1,*], C. D. Rodríguez-Hernández[1], R. M. Rached[1], R. Dávalos-Monteiro[2]

Received: 16-10-2025, Received after review: 28-01-2026, Accepted: 21-04-2026, Published: 01-07-2026

Abstract

Corrosion poses a critical challenge to the oil and gas industry, particularly in systems exposed to acidic and high-salinity environments. This study evaluates eggshell powder, a biowaste-derived material, as a green corrosion inhibitor for type N80 carbon steel under conditions representative of acidic and brine environments. Its performance was systematically assessed through weight loss testing, micro-indentation hardness measurements, and numerical electrochemical modeling. N80 steel coupons were exposed to 2 M hydrochloric acid (HCl) and 2 M sodium chloride (NaCl) solutions, with and without 6 g/L of eggshell powder, for 6 days. Corrosion rates determined from mass loss showed substantial protection in the acidic medium, decreasing from 18.8 to 2.1 mm/year and corresponding to an inhibition efficiency of 90 %. In brine, the effect was more moderate, with a 14% reduction in the corrosion rate. Micro-indentation analysis confirmed that inhibitor-treated samples retained at least 85% of the hardness of unexposed steel in acid, whereas untreated samples exhibited severe mechanical degradation. The results suggest that corrosion protection arises from a combined mechanism involving the formation of a calcium carbonate barrier, stabilization of the corrosion product layer, and possible scavenging of aggressive chloride ions. Overall, this study demonstrates the potential of eggshell powder as a viable and sustainable candidate for corrosion mitigation in harsh industrial environments.

Keywords: carbon steel, green corrosion inhibition, eggshell powder, aggressive environments, micro-indentation, sustainability.

Resumen

La corrosión representa un desafío importante para la industria del petróleo y del gas, especialmente en sistemas expuestos a ambientes ácidos y de alta salinidad. Este estudio evalúa el polvo de cáscara de huevo, un residuo biológico, como inhibidor ecológico de la corrosión del acero al carbono tipo N80 bajo condiciones representativas de ambientes ácidos y salinos. Se analizaron muestras de acero expuestas a soluciones de ácido clorhídrico (HCl) 2 M y cloruro de sodio (NaCl) 2 M, con y sin 6 g/L de polvo de cáscara de huevo, durante seis días. La tasa de corrosión, determinada a partir de la pérdida de masa, mostró una mejora significativa en medio ácido, al disminuir de 18.8 mm/año a 2.1 mm/año, con una eficiencia de inhibición del 90 %. En condiciones salinas, el efecto fue moderado, con una reducción del 14 %. El análisis de microindentación indicó que las muestras tratadas conservaron al menos el 85 % de la dureza del acero no expuesto, mientras que las no tratadas sufrieron una degradación severa. Los resultados sugieren que la protección se debe a la formación de una barrera de carbonato de calcio, la estabilización de la capa de productos de corrosión y la captura de iones agresivos, como el cloruro. Este estudio demuestra que el polvo de cáscara de huevo es una alternativa viable y sostenible para mitigar la corrosión en entornos industriales exigentes.

Palabras clave: acero al carbono, inhibidor verde de la corrosión, polvo de cáscara de huevo, ambientes agresivos, microindentación, sustentabilidad

[1,*] Sinopec Tech Middle East LLC, Dhahran 34464-4622, Kingdom of Saudi Arabia.
Corresponding author ✉: jose.stme@sinopec.com.

[2]School of Biological Science and Engineering, Yachay Tech University, Urcuquí, Ecuador.

Suggested citation: J. L. Dávalos-Monteiro, C. D. Rodríguez-Hernández, R. M. Rached and R. Dávalos-Monteiro "Corrosion inhibition of type N80 carbon steel using eggshell powder in acidic and brine environments: a study based on weight loss testing, micro-indentation, and electrochemical modeling," *Ingenius, Revista de Ciencia y Tecnología*, N.° 36, pp. 29-38, 2026, DOI: https://doi.org/10.17163/ings.n36.2026.03.

1. Introduction

Corrosion is a pervasive degradation process and a critical challenge in multiple engineering applications. In the oil and gas sector, general and localized corrosion commonly occurs in pipelines, storage tanks, and downhole equipment exposed to acidic and high-salinity environments [1–4]. Corrosion compromises equipment structural integrity and can lead to failure, production losses, safety hazards, and significant environmental risks [5–7].

Typical corrosion mitigation strategies and schemes rely on chemical inhibitors based on synthetic organic compounds, such as amines, quaternary ammonium salts, and phosphonates [8–11]. Despite their high efficiency, these inhibitors present several drawbacks, including high cost, limited biodegradability, and environmental toxicity. The need to mitigate corrosion, together with increasing regulatory pressure, has accelerated the search for alternative inhibitors derived from natural or renewable sources, commonly referred to as "green inhibitors" [12, 13].

Green corrosion inhibitors typically include plant extracts, agricultural byproducts, and biowaste materials that are non-toxic, biodegradable, and readily available [14–16]. Eggshells are a notable example, as they are commonly used in the agricultural sector as natural fertilizers. They are primarily composed of calcium carbonate ($CaCO_3$) and organic constituents that may act as corrosion inhibitors by contributing to the formation of a protective film at the metal surface [17–19].

Despite promising early efforts, the use of eggshell-based inhibitors in oil and gas applications remains poorly understood. Previous studies have assessed their performance under model conditions, which differ substantially from highly dynamic field environments where physical and chemical stability must be maintained over extended periods [20, 21]. Therefore, evaluating the degradation of mechanical properties and the durability of the corrosion product layer is critical for assessing the performance of any inhibitor.

Accordingly, this study systematically evaluates the performance of eggshell powder as a corrosion inhibitor under conditions relevant to the oil and gas sector, using both experimental techniques and numerical methods. The N80 steel coupons were exposed to acidic and saline environments, and corrosion rates were determined through weight loss measurements. In addition, micro-indentation analysis was conducted to assess the hardness of the corrosion layers formed with and without the inhibitor. Numerical modeling of corrosion kinetics and inhibitor adsorption provided insight into the possible inhibition mechanism, the effect of eggshell-derived components on anodic and cathodic reactions, and the influence on charge-transfer processes at the steel-electrolyte interface. By combining laboratory experiments with micro-mechanical and numerical analyses, this study assessed the potential of eggshell powder as a green corrosion inhibitor.

2. Materials and Methods

2.1. Materials

This study used type N80 carbon steel coupons as the metallic substrate for corrosion testing and eggshell powder as the green inhibitor. The chemical composition of the N80 steel, supplied by Changzhou Qingli Huanneng Chemical Technology Co., Ltd., is presented in Table 1. The corrosive media consisted of two aqueous solutions: I) 2 molar sodium chloride (2M NaCl) to simulate saline environments, and II) 2 molar hydrochloric acid (2M HCl) to represent acidic conditions. All chemicals were of analytical grade and were prepared in deionized water (PanReac AppliChem, ITW Reagents).

Table 1. Chemical composition of type N80 carbon steel

Element	Weight (%)
Carbon (C)	0.21 - 0.28
Manganese (Mn)	0.60 - 1.00
Phosphorus (P)	$\leq$ 0.030
Sulfur (S)	$\leq$ 0.030
Silicon (Si)	0.15 - 0.35
Chromium (Cr)	$\leq$ 0.25
Nickel (Ni)	$\leq$ 0.25
Copper (Cu)	$\leq$ 0.25
Molybdenum (Mo)	$\leq$ 0.15
Vanadium (V)	$\leq$ 0.08
Other elements	$\leq$ 0.30 (total)
Iron (Fe)	Balance

2.2. Sample Preparation

Steel Coupons & Testing Solutions:

Type N80 carbon steel plates measuring 50 mm × 10 mm × 3 mm were first ground with No. 50 SiC paper to remove surface oxides and contaminants, ensuring a uniform surface in accordance with ASTM G1. Material removal was controlled to approximately 0.0025 mm in thickness from all surfaces. The samples were then further ground using No. 800 to No. 1200 SiC paper to obtain a suitable surface finish for subsequent testing. After grinding, the coupons were immediately rinsed with deionized water, cleaned with ethanol, and dried with an air gun before initial weighing.

For the test solutions, 116.8 g of NaCl was dissolved and 166.7 ml of concentrated HCl (37%) was diluted in deionized water to obtain 2 M NaCl and 2 M HCl solutions. Their pH values were 7 and 0, respectively.

Eggshell Inhibitor:

Eggshells were collected from local sources, thoroughly washed, oven-dried, and ground using a mechanical grinder. The resulting powder was sieved to obtain a uniform particle size corresponding to mesh 80 ($\approx 180\mu m$). Eggshell powder was added to the test solutions at a defined concentration of 6 g/L and mixed until fully dispersed.

2.3. Corrosion Testing & Weight Loss Evaluation

Corrosion rates were determined using a classical weight loss protocol. First, each specimen was weighed using an analytical balance with a readability of 1 mg (Mettler Toledo ME203). Then, following ASTM G31, the coupons were placed in glass beakers and immersed in 200 mL of test solution, either 2 M NaCl or 2 M HCl, with or without eggshell inhibitor, for 6 days at room temperature, approximately 23 °C. After exposure, coupons designated for weight loss analysis were removed and gently cleaned in a sonicator bath with deionized water and a soft brush to remove loose corrosion products. Cleaning was omitted for samples intended for micro-indentation to preserve the properties of the corrosion layer. Finally, all coupons were dried with an air gun immediately after cleaning and weighed to three decimal places.

Corrosion rates were calculated using the following equation (1):

$$CR\left[\frac{mm}{year}\right] = \frac{87.6 \cdot (W_i - W_f)}{\rho \cdot A \cdot t} \tag{1}$$

where W_i and W_f are the initial and final masses (mg), ρ is the density of steel (g/cm^3), A is the exposed surface area (cm^2), and t is the exposure time (hours).

2.4. Micro-Indentation Measurements

This study used an instrumented micro-indenter, Anton Paar, Micro Combi Tester MCT, with a maximum load of 30 N, load resolution of 6 μN, depth range of 1000 μm, and depth resolution of 0.03 nm, to assess the mechanical properties of the corrosion layer formed on the steel coupons after exposure. The indenter applied several loading and unloading cycles using the continuous multicycle load method, CMC. A matrix of four measurement locations was generated, and the applied force and resulting displacement were recorded. The device measured indentation hardness, HIT, as the mean contact pressure beneath the indenter at peak load, see equation (2):

$$HIT = \frac{F_{max}}{A_p} \tag{2}$$

where F_{max} is the maximum applied load and A_p is the projected contact area, determined using the Oliver-Pharr method. Mean values, standard deviations, and standard errors were reported for each condition to evaluate the integrity and mechanical strength of the protective layer formed in the presence and absence of the inhibitor.

2.5. Numerical Simulation

Electrochemical Corrosion Model Implementation

The corrosion behavior of type N80 steel was simulated using MATLAB. The numerical model reproduced the electrochemical response of steel in acidic and saline environments with varying solution compositions, inhibitor concentrations, and steel properties. The model incorporated standard corrosion kinetics based on the Butler-Volmer equation and adsorption isotherms to predict current densities and polarization resistance, which are electrochemical parameters related to the corrosion rate.

The simplified model was based on coupled anodic and cathodic reactions described by the Butler-Volmer equation, accounting for charge-transfer kinetics. The general form for each half-cell reaction is:

$$i = i_0 \left(exp\left[\frac{\alpha_a F_\eta}{RT}\right] - exp\left[-\frac{\alpha_c F_\eta}{RT}\right] \right) \tag{3}$$

where i is the current density A/m^2; i_0 is the exchange current density, α_a and α_c are the anodic and cathodic transfer coefficients, F is Faraday's constant C/mol; η is the overpotential (V), R is the universal gas constant $J/mol \cdot K$; and T is the temperature (K).

Inhibitor Effect via Adsorption Isotherm

To incorporate the effect of the eggshell inhibitor into the numerical model, the surface coverage (θ) of the inhibitor on the steel surface was estimated using the Langmuir adsorption isotherm [22, 23]. This approach assumes that inhibitor molecules form a layer on the metal surface, with uniform adsorption sites and no interactions between adsorbed species. The surface coverage was calculated as:

$$\theta = \frac{KC}{1 + KC} \tag{4}$$

where θ is the fraction of the metal surface covered by the inhibitor, C is the inhibitor concentration in $mol \cdot L^{-1}$ and K is the adsorption equilibrium constant in $L \cdot mol^{-1}$. The presence of the inhibitor reduces the active area available for corrosion, and the numerical model accounts for this by scaling the current density from the uninhibited case. Specifically, the corrosion current density in the inhibited system ($i_{corr,inh}$) was estimated as:

$$(i_{corr,inh}) = (1-\theta) i_{corr,uninh} \quad (5)$$

where $i_{corr,uninh}$ is the corrosion current density in the absence of the inhibitor. This formulation allowed the model to account for inhibition efficiency as a function of inhibitor concentration, simulating how increasing surface coverage led to a proportional reduction in electrochemical activity.

MATLAB Implementation & Numerical Simulation

The numerical model was developed on MATLAB to simulate the electrochemical behavior of type N80 steel with and without the eggshell inhibitor. The model solves Butler-Volmer equation for both anodic and cathodic reactions across a defined potential range and then adjusts the response based on inhibitor surface coverage.

The simulation started by defining the system parameters, including all constants, electrochemical parameters, and inhibitor properties listed in Table 2. The model then generated a range of electrode potentials around the expected corrosion potential, for example from -0.7 V to -0.3 V, simulating a sweep similar to that used in potentiodynamic polarization experiments [24]. For each potential value, the overpotential η was computed and used as the input for the Butler-Volmer equation. Finally, the Butler-Volmer equation was applied to compute the total current density at each potential step. The simulation produced two complete sets of simulated polarization data: one for the uninhibited system and another representing the system with the corrosion inhibitor.

Table 2. Parameters used in the numerical corrosion model of type N80 steel in saline (NaCl) and acidic (HCl) systems.

Parameter	Description	Value NaCl system)	Valor (HCl system)	Unit	Source/Note
F	Faraday's constant	96485		$C \cdot mol^{-1}$	Standard constant
R	Universal gas constant	8,314		$J \cdot mol^{-1} \cdot K^{-1}$	Standard constant
T	Temperature	298		K	Ambient (25 °C)
α_a	Anodic transfer coefficient	0.5		-	Typical assumption
α_c	Cathodic transfer coefficient	0.5		-	Typical assumption
i_0	Exchange current density	1×10^{-5}	8×10^{-5}	$A \cdot cm^{-2}$	Estimated for carbon steel in saline water
E_{corr}	Corrosion potential	-0.5	-0.6	V (vs. Ref)	Estimated
K	Adsorption equilibrium constant	16.28	1011	$L \cdot mol^{-1}$	Adjusted from experimental data
C	Inhibitor concentration	2		$mol \cdot L^{-1}$	Experimental
θ	Surface coverage	0.14	0.91	-	From Langmuir isotherm
$i_{corr,sin}$	Corrosion current density (no inhibitor)	1.56×10^{-5}	1.20×10^{-4}	A/cm^2	Model output
$i_{corr,con}$	Corrosion current density (with inhibitor)	1.34×10^{-5}	1.09×10^{-5}	A/cm^2	Model output

3. Results and discussion

3.1. Visual Inspection of Corrosion

Figure 1 shows the steel coupons before and after fluid exposure. Visual inspection revealed clear differences in the extent of corrosion between samples exposed to HCl and NaCl solutions. Coupons immersed in HCl exhibited extensive surface degradation, severe rust formation, and visible loss of metallic luster, indicating significant corrosion (Figure 1a). In contrast, coupons exposed to the NaCl solution exhibited more moderate corrosion, with surface discoloration and localized pitting but less widespread material damage than the acid-treated samples (Figure 1b).

A marked protective effect was observed when eggshell powder was added to both solutions. The steel surfaces exposed to the inhibitor exhibited noticeably fewer corrosion products and retained a smoother appearance than the uninhibited controls, as shown in Figure 1. In both acidic and saline environments, the presence of eggshell powder reduced visible corrosion, with the most pronounced effect observed in the HCl solution, where the inhibitor limited the aggressive etching typically seen under these conditions.

(a) (b)

Figure 1. N80 Steel coupons images before and after fluid exposure with and without eggshell as an inhibitor. (a) 2 M HCl, (b) 2 M NaCl.

3.2. Weight Loss Analysis

Figure 2 presents the corrosion rates of steel coupons with and without the eggshell inhibitor. The corrosion rates estimated after exposure demonstrated the protective effect of the inhibitor. In 2 M NaCl, the corrosion rate without the inhibitor was 0.14 mm/year. The addition of eggshell powder slightly reduced it to 0.12 mm/year, corresponding to an approximately 14% improvement, as shown in Figure 2a. The inhibitor effect was much more pronounced under acidic conditions, in 2 M HCl, where the corrosion rate decreased from 18.8 mm/year without the inhibitor to 2.1 mm/year with the inhibitor, corresponding to an approximately 90% improvement, as shown in Figure 2b.

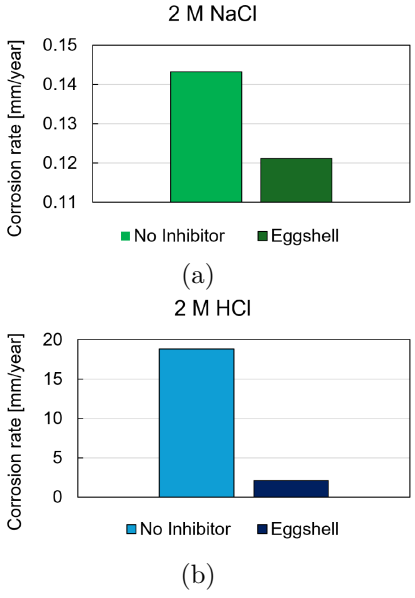

(a)

(b)

Figure 2. Corrosion rate of N80 carbon steel samples when exposed to a) 2 M NaCl solution and b) 2 M HCl solution with and without eggshell as inhibitor.

These results indicate that eggshell powder provides moderate inhibition in saline environments but substantial protection under highly aggressive acidic conditions. The significant decrease in weight loss in the acid-exposed, inhibitor-treated samples suggests the formation of a protective barrier on the steel, effectively limiting metal dissolution. These findings demonstrate the potential of eggshell-derived inhibitors for corrosion protection in environments where acid exposure is a primary concern, with measurable benefits also observed in brine.

3.3. Micro-Indentation Analysis

Figure 3 shows the indentation hardness results for the different coupons. The experimental data indicate that, for samples exposed to 2 M NaCl, hardness values remained similar to those of the unexposed steel, regardless of the presence of the inhibitor, as shown in Figure 3a. The mean HIT changed only from 2.44 GPa for the reference unexposed material to 2.28 GPa without inhibitor and 2.42 GPa with eggshell as the inhibitor, corresponding to a deviation of$\leq$ 7 %. This suggests that, under saline conditions and within the tested exposure time, the surface properties of the steel coupons were minimally affected.

A different trend was observed in acidic environments. Type N80 steel coupons exposed to 2 M HCl without the inhibitor showed a marked decrease in hardness compared with the original unexposed sample, as shown in Figure 3b. HIT decreased to 1.77 GPa in polished coupons to only 0.22 GPa in unpolished coupons. This reduction indicates that the corrosion layer formed in acid was mechanically weak and more susceptible to removal. In contrast, the samples treated with the eggshell inhibitor retained hardness values similar to those of the unexposed material. Polished and unpolished coupons reached 2.07 GPa and 2.32 GPa, respectively, corresponding to at least 85% of the reference value.

The results suggest that the corrosion layer formed in acid without protection was poorly adherent and could be easily removed, leading to continuous exposure of fresh steel to the corrosive fluid and sustained metal loss. When the eggshell inhibitor was added, the resulting layer was mechanically robust and more resistant to removal, effectively serving as a protective barrier. This layer limited further corrosion and enhanced the durability of the steel in service environments exposed to abrasive forces or fluid impingement. Overall, the micro-indentation data support the effectiveness of the eggshell inhibitor in maintaining the mechanical integrity of the steel surface, particularly under aggressive acidic conditions.

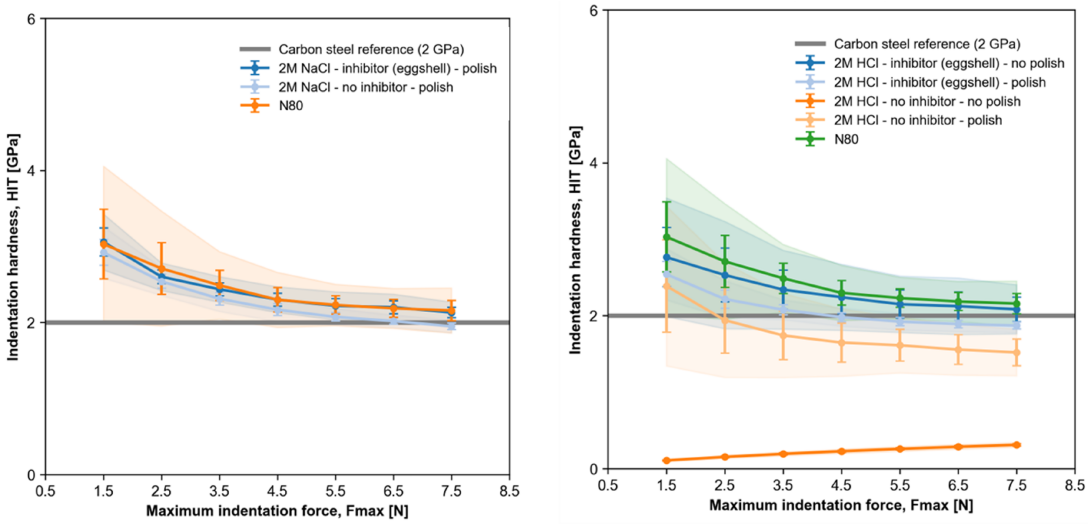

Figure 3. Indentation hardness. a) Brine - 2 M NaCl; b) Acid - 2 M HCl. Note: shaded area shows = −1 standard deviation, bars show ±1 standard error, and data points show mean values.

3.4. Numerical Simulation

Figure 4 presents the simulated potentiodynamic polarization curves for the tested solutions with and without the eggshell inhibitor. The simulation revealed differences in corrosion kinetics between neutral chloride and acidic environments. In the 2 M NaCl solution, the current densities were moderate, and the corrosion potential was less negative, consistent with a system in which the cathodic reaction was dominated by oxygen reduction.

The simulated polarization curves for this environment displayed only a minor shift in current density after inhibitor addition, indicating weak surface interaction and limited protective capability, as shown in Figure 4. This behavior was reflected in the inhibition efficiency of only 14%. Based on the simulation results, the uninhibited corrosion current density was approximately $1.56 \times 10^{-5} A/cm^2$, while the inhibited system showed a slight reduction to $1.34 \times 10^{-5} A/cm^2$.

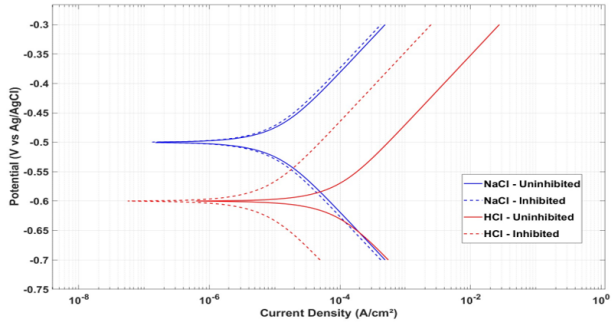

Figure 4. Simulated potentiodynamic polarization curves in 2 M NaCl and 2 M HCl with and without the eggshell inhibitor.

In contrast, the numerical results for the 2 M HCl solution showed a much more aggressive corrosive behavior, as expected under acidic conditions favoring hydrogen evolution as the cathodic reaction. The uninhibited system exhibited significantly higher current densities and a more negative corrosion potential, reflecting accelerated anodic dissolution of iron in the steel. However, the addition of eggshell powder at the same acid concentration produced a marked reduction in current density, particularly in the cathodic branch. This behavior was attributed to a higher adsorption constant and near-complete surface coverage, consistent with the experimentally obtained inhibition efficiency of 90%. These results suggest that the acidic environment enhanced the affinity of inhibitor-derived species for the steel surface, possibly through protonation of functional groups or increased chemisorption. Based on the simulation results, the uninhibited corrosion current density in acid was approximately $1.20 \times 10^{-4} A/cm^2$, while the inhibited system showed a marked reduction to $1.09 \times 10^{-5} A/cm^2$.

The differences in corrosion behavior and inhibition efficiency between the two environments demonstrate the role of the medium in controlling the inhibitor performance. Although the same inhibitor concentration was used in both cases, its effectiveness was strongly dependent on electrolyte chemistry. From a modeling perspective, the results validate the usefulness of coupling classical electrochemical kinetics with immersion testing to understand corrosion mechanisms. The Butler–Volmer equation successfully captured the shift in current density profiles, whereas the Langmuir model provided a basis for interpreting the surface interaction between the inhibitor and the substrate. However, the model assumes idealized conditions, such as uni-

form surface coverage and constant kinetic parameters, which may not fully account for localized corrosion, diffusion effects, or inhibitor degradation. Future work should consider multi-site adsorption models, transport limitations, and pH-dependent speciation to improve predictive accuracy and better reproduce the real systems.

3.5. Possible Corrosion Mechanisms & Role of Eggshell as a Corrosion Inhibitor

The deterioration of carbon steel under naturally harsh conditions occurs through spontaneous electrochemical processes at the metal–solution interface. In acid, the carbon steel alloy undergoes anodic dissolution, releasing Fe^{2+} ions, while the cathodic process involves the reduction of hydrogen ions to produce hydrogen gas, commonly known as the hydrogen evolution reaction. In neutral chloride-containing electrolytes, the process is typically less aggressive; however, chloride ions can initiate localized corrosion by disrupting protective films formed at neutral pH, leading to pitting, one of the most critical forms of corrosion because of the difficulty of monitoring it [25].

Eggshell powder is mainly composed of calcium carbonate, along with small amounts of magnesium carbonate, phosphate, and trace organic proteins. Its corrosion protection likely occurs through several simultaneous mechanisms, with the experimental results indicating a stronger inhibitory effect in acidic media. The possible inhibition mechanism in acidic media, based on the experimental data, is described below.

Formation of a Carbonate Physical Barrier:

The primary component of eggshell powder, calcium carbonate ($CaCO_3$), can form a protective barrier on the steel surface. In acidic environments such as 2 M HCl, calcium carbonate reacts with H^+ to release soluble Ca^{2+} ions and carbon dioxide gas (CO_2). The reaction proceeds as follows:

$$CaCO_3(s)+2H^+(aq) \rightarrow Ca^{2+}(aq)+CO_2(g)+H_2O(l) \quad (6)$$

Once Ca^{2+} is released into solution, it can reprecipitate near the metal surface, particularly under localized conditions where pH increases due to cathodic reactions such as hydrogen evolution, which consumes H^+:

$$2H^+(aq) + 2e^- \rightarrow H_2(g) \quad (7)$$

In these alkaline areas, Ca^{2+} can react with carbonate ions ($CO_3{}^{2-}$) or hydroxide ions (OH^-) to reform calcium carbonate or produce calcium hydroxide, also known as portlandite. Both compounds are poorly soluble and can form solid deposits on the steel surface. These two reactions can proceed as follows:

$$Ca^{2+} + CO_3^{2-} \rightarrow CaCO_3(s) \quad (8)$$

$$Ca^{2+} + 2OH^- \rightarrow Ca(OH)_2(s) \quad (9)$$

The precipitated compounds from reactions (8) and (9), particularly calcium carbonate ($CaCO_3$), can form a compact layer on the steel surface that acts as a barrier. This physical barrier reduces the transport of aggressive ions, such as chloride (Cl^-) and hydrogen ions (H^+), by slowing or limiting their diffusion toward the metal surface. As a result, it restricts anodic dissolution by partially blocking active corrosion sites, thereby decreasing the electroactive area and slowing the corrosion rate. Figure 5 presents a schematic of the proposed physical barrier formation mechanism.

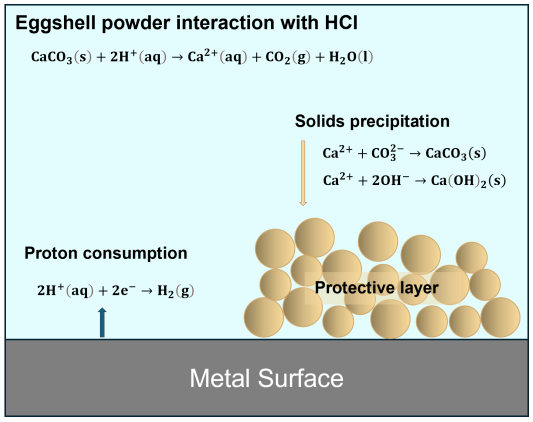

Figure 5. Schematic of calcium carbonate physical barrier formation on the steel surface.

Modification of the Corrosion Product Layer:

The addition of eggshell components may alter the structure and properties of the corrosion product layer, making it more stable, denser, and less prone to cracking or detachment. This is consistent with the increased surface hardness observed in the presence of the inhibitor, particularly in acid. A mechanically stable layer resists detachment caused by flow or abrasion, thereby decreasing the likelihood of further exposure and metal loss.

Potential Scavenging of corrosion aggressive Ions:

Calcium ions released from eggshell powder may interact with free chloride ions in solution, reducing their activity and helping prevent localized attack, such as pitting.

Corrosion inhibition through a scavenging mechanism may have contributed specifically to the brine experiment, where the high concentration of chloride ions likely interacted with calcium ions released from

the eggshell powder. Once aggressive anions are scavenged, their ability to disrupt passive films or initiate localized corrosion is reduced. In addition, excess Ca^{2+} in solution may lead to the formation of slightly soluble calcium species, such as calcium chloride complexes or calcium carbonate, depending on pH and carbonate availability. Figure 6 illustrates the corrosion inhibition mechanism involving chloride ions and calcium ions acting as scavengers.

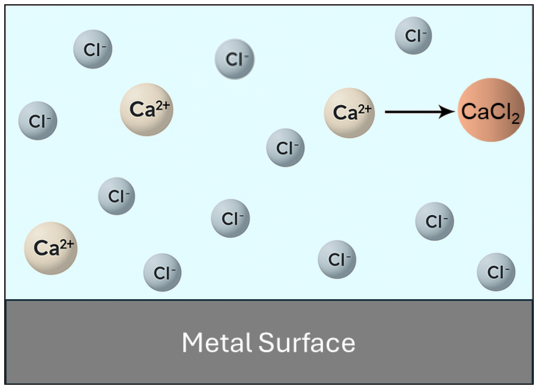

Figure 6. Corrosion inhibition through a scavenging mechanism of Chloride ions by Calcium ions.

In summary, the combined effects of barrier formation and modification of the corrosion product layer may account for the effective inhibition performance of eggshell powder, particularly under acidic conditions. By forming a more protective and mechanically stable surface film, eggshell-derived inhibitors can help preserve steel integrity and slow corrosion progression, supporting their potential application as a green corrosion inhibition strategy in harsh environments.

4. Conclusions

The results of this experimental study demonstrate that eggshell powder effectively inhibits the corrosion of type N80 carbon steel, particularly under aggressive acidic conditions. The notable reduction in corrosion rate, supported by weight loss measurements, indicates that eggshell powder substantially reduces metal dissolution in 2 M HCl, achieving an inhibition efficiency of 90%. This is an important finding, as acidic environments pose a major challenge in several field operations.

Micro-indentation analysis revealed negligible hardness changes in brine, with values of 2.44 GPa for unexposed steel, 2.28 GPa without the inhibitor, and 2.42 GPa with eggshell powder. In contrast, exposure to 2 M HCl without protection reduced surface hardness to 1.77 GPa in polished coupons and 0.22 GPa in unpolished coupons. This low hardness indicates the formation of a weak, poorly adherent corrosion layer that can be removed easily, continually exposing fresh steel to acid attack. The addition of eggshell powder increased hardness to 2.07 and 2.32 GPa, confirming the formation of a dense, well-bonded film that resisted removal, limited further corrosion, and improved durability under abrasive or high-flow conditions.

The numerical simulation, which incorporated Butler-Volmer kinetics and Langmuir adsorption isotherms, reproduced the distinct behaviors observed experimentally in both saline and acidic systems. The agreement between simulated and experimental data highlights the value of combining experimental techniques with numerical analysis to understand and propose possible corrosion mechanisms.

Overall, the coupled effects of barrier formation, corrosion product stabilization, and chloride ion scavenging collectively contributed to the inhibition performance of eggshell powder. These findings position eggshell powder as a viable candidate for future application in corrosion control strategies for harsh industrial environments.

Contributor Roles

- **J. L. Dávalos-Monteiro:** Conceptualization, research, methodology, formal analysis, writing – original draft, writing – revision and editing.
- **C. D. Rodríguez-Hernández:** Conceptualization, research, methodology, formal analysis, writing – original draft, writing – revision and editing.
- **R. M. Rached:** Conceptualization, research, methodology, formal analysis, writing – original draft, writing – revision and editing.
- **R. Dávalos-Monteiro:** Conceptualization, research, methodology, formal analysis, writing – original draft, writing – revision and editing, supervision.

References

[1] M. Kermani and A. Morshed, "Carbon dioxide corrosion in oil and gas production—a compendium," *Corrosion*, vol. 59, no. 8, pp. 659–683, Aug. 2003. [Online]. Available: https://doi.org/10.5006/1.3277596

[2] Y. T. Al-Janabi, "An overview of corrosion in oil and gas industry: Upstream, midstream, and downstream sectors," *Corrosion Inhibitors in the Oil and Gas Industry*, pp. 1–39, Feb. 2020. [Online]. Available: https://doi.org/10.1002/9783527822140.ch1

[3] S. Papavinasam, *Corrosion control in the oil and gas industry.* Elsevier, 2014. [Online]. Available: https://doi.org/10.1016/C2011-0-04629-X

[4] G. M. Castro, J. Park, A. Sherik, and J. C. Santamarina, "Metal corrosion in partially saturated sands: pore fluid conductivity and water saturation," *Canadian Geotechnical Journal*, vol. 62, pp. 1–13, Jan. 2025. [Online]. Available: https://doi.org/10.1139/cgj-2024-0097

[5] R. B. Jackson, "The integrity of oil and gas wells," *Proceedings of the National Academy of Sciences*, vol. 111, no. 30, pp. 10 902–10 903, 2014. [Online]. Available: https://doi.org/10.1073/pnas.1410786111

[6] A. A. Soomro, A. A. Mokhtar, J. C. Kurnia, N. Lashari, H. Lu, and C. Sambo, "Integrity assessment of corroded oil and gas pipelines using machine learning: A systematic review," *Engineering Failure Analysis*, vol. 131, p. 105810, Jan. 2022. [Online]. Available: https://doi.org/10.1016/j.engfailanal.2021.105810

[7] O. Shabarchin and S. Tesfamariam, "Internal corrosion hazard assessment of oil & gas pipelines using bayesian belief network model," *Journal of Loss Prevention in the Process Industries*, vol. 40, pp. 479–495, Mar. 2016. [Online]. Available: https://doi.org/10.1016/j.jlp.2016.02.001

[8] G. Camila and F. Alexandre, *Corrosion Inhibitors – Principles, Mechanisms and Applications*. InTech, Feb. 2014. [Online]. Available: https://doi.org/10.5772/57255

[9] P. B. Raja, M. Ismail, S. Ghoreishiamiri, J. Mirza, M. C. Ismail, S. Kakooei, and A. A. Rahim, "Reviews on corrosion inhibitors: A short view," *Chemical Engineering Communications*, vol. 203, no. 9, pp. 1145–1156, 2016. [Online]. Available: https://doi.org/10.1080/00986445.2016.1172485

[10] V. S. Sastri, *Corrosion Inhibitors: Principles and Application*. Wiley, 1998. [Online]. Available: https://upsalesiana.ec/ing36ar3r10

[11] A. Kadhum, A. A. Al-Amiery, R. Alazawi, M. K. S. Al-Ghezi, and R. H. Abass, "Corrosion inhibitors. A review," *International Journal of Corrosion and Scale Inhibition*, vol. 10, no. 1, Mar. 2021. [Online]. Available: https://doi.org/10.17675/2305-6894-2021-10-1-3

[12] V. S. Sastri, *Green Corrosion Inhibitors: Theory and Practice*. Wiley, May 2011. [Online]. Available: http://doi.org/10.1002/9781118015438

[13] L. T. Popoola, "Organic green corrosion inhibitors (OGCIs): a critical review," *Corrosion Reviews*, vol. 37, no. 2, pp. 71–102, Jan. 2019. [Online]. Available: https://doi.org/10.1515/corrrev-2018-0058

[14] N. Hossain, M. Asaduzzaman Chowdhury, and M. Kchaou, "An overview of green corrosion inhibitors for sustainable and environment friendly industrial development," *Journal of Adhesion Science and Technology*, vol. 35, no. 7, pp. 673–690, 2020. [Online]. Available: https://doi.org/10.1080/01694243.2020.1816793

[15] A. Miralrio and A. Espinoza Vázquez, "Plant extracts as green corrosion inhibitors for different metal surfaces and corrosive media: A review," *Processes*, vol. 8, no. 8, p. 942, Aug. 2020. [Online]. Available: https://doi.org/10.3390/pr8080942

[16] S. Marzorati, L. Verotta, and S. P. Trasatti, "Green corrosion inhibitors from natural sources and biomass wastes," *Molecules*, vol. 24, no. 1, p. 48, Dec. 2018. [Online]. Available: https://doi.org/10.3390/molecules24010048

[17] M. Alfattah, I. G. A. Arwati, Arramel, A. A. Afkauni, and R. M. Yofatama, "Efficiency of eggshell waste as a metal corrosion inhibitor ss316l based on green technology in seawater media," *Journal of Physics: Conference Series*, vol. 2942, no. 1, p. 012017, Feb. 2025. [Online]. Available: https://doi.org/10.1088/1742-6596/2942/1/012017

[18] O. Sanni, A. Popoola, and O. Fayomi, "The inhibitive study of egg shell powder on uns n08904 austenitic stainless steel corrosion in chloride solution," *Defence Technology*, vol. 14, no. 5, pp. 463–468, Oct. 2018. [Online]. Available: https://doi.org/10.1016/j.dt.2018.07.015

[19] V. S. Aigbodion and E. Dinneya-Onuoha, "Unveiling the anti-corrosion properties of Zn-eggshell particle composite coatings on mild steel in seawater-simulated solution using starch as a modifier," *RSC Advances*, vol. 14, no. 34, pp. 24 548–24 560, 2024. [Online]. Available: https://doi.org/10.1039/d4ra04283b

[20] O. Sanni, S. A. Iwarere, and M. O. Daramola, "Investigation of eggshell agro-industrial waste as a potential corrosion inhibitor for mild steel in oil and gas industry," *Sustainability*, vol. 15, no. 7, p. 6155, Apr. 2023. [Online]. Available: https://doi.org/10.3390/su15076155

[21] S. K. Alias, H. F. Pahroraji, H. M. Hairi, M. M. Ali, M. A. M. Shah, and B. Abdullah, "Eggshell waste extract as potential natural corrosion inhibitor for AISI 1020 steel in acidic environment," *Journal of Mechanical Engineering and Sciences*, pp. 10 192–10 201, 2024. [Online]. Available: https://doi.org/10.15282/jmes.18.3.2024.8.0805

[22] A. Kokalj, "On the use of the langmuir and other adsorption isotherms in corrosion inhibition," *Corrosion Science*, vol. 217, p. 111112, 2023. [Online]. Available: https://doi.org/10.1016/j.corsci.2023.111112

[23] E. Ituen, O. Akaranta, and A. James, "Evaluation of performance of corrosion inhibitors using adsorption isotherm models: An overview," *Chemical Science International Journal*, vol. 18, no. 1, pp. 1–34, Jan. 2017. [Online]. Available: https://doi.org/10.9734/CSJI/2017/28976

[24] R. Dávalos Monteiro, J. van de Wetering, B. Krawczyk, and D. L. Engelberg, "Corrosion behaviour of type 316l stainless steel in hot caustic aqueous environments," *Metals and Materials International*, vol. 26, no. 5, pp. 630–640, Oct. 2019. [Online]. Available: https://doi.org/10.1007/s12540-019-00403-2

[25] R. L. Dávalos Monteiro and S. D. Ananda, "Pitting corrosion of type 304 stainless steel and sulfate inhibition effect in chloride containing environments," *Revista Tecnológica - ESPOL*, vol. 30, no. 3, 2017. [Online]. Available: https://upsalesiana.ec/ing36ar3r25

Scientific Paper / Artículo Científico

UNIVERSIDAD POLITÉCNICA SALESIANA ECUADOR
INGENIUS
Revista de Ciencia y Tecnología
https://doi.org/10.17163/ings.n36.2026.04
pISSN: 1390-650X / eISSN: 1390-860X

Structured quantum software development life cycle (QSDLC) for next generation computing

Ciclo de vida de desarrollo de software cuántico estructurado (QSDLC) para la computación de próxima generación

Fabián Lizardo Caicedo Goyes[1,*]

Received: 16-10-2025, Received after review: 28-01-2026, Accepted: 21-04-2026, Published: 01-07-2026

Abstract

Quantum computing promises exponential advantages over classical paradigms; however, it still lacks standardized software engineering methodologies. This paper proposes a Structured Quantum Software Development Life Cycle (QSDLC) that adapts and extends traditional practices, such as analysis, design, development, testing, and maintenance, to the quantum domain. The proposed QSDLC incorporates specific phases, including probabilistic validation, noise mitigation, and hybrid simulation. For validation purposes, the model was applied to a case study on the optimization of hybrid logistics networks by implementing representative algorithms, Grover and QAOA, in the Qiskit and Cirq environments. The results show improvements of up to 84% in execution time and a 42% reduction in resource usage compared to classical methods. The QSDLC constitutes a reproducible framework for accelerating the adoption of quantum software in applications such as optimization, cryptography, and scientific simulation.

Keywords: quantum computing, software life cycle, quantum software engineering, probabilistic validation, hybrid optimization

Resumen

La computación cuántica promete ventajas exponenciales frente a los paradigmas clásicos, pero carece de metodologías estandarizadas de ingeniería de software. Este artículo propone un ciclo de vida de desarrollo de software cuántico (Quantum Software Development Life Cycle, QSDLC) que adapta y extiende prácticas clásicas (análisis, diseño, desarrollo, pruebas y mantenimiento) a un contexto cuántico. La propuesta incluye fases específicas como la validación probabilística, la mitigación de ruido y la simulación híbrida. Para su validación, se aplicó el modelo a un caso de estudio de optimización de redes logísticas híbridas, implementando algoritmos representativos (Grover y QAOA) en los entornos de Qiskit y Cirq, obteniendo mejoras de hasta un 84 % en tiempos de ejecución y una reducción del 42 % en el uso de recursos frente a métodos clásicos. El QSDLC constituye un marco reproducible para acelerar la adopción de software cuántico en aplicaciones de optimización, criptografía y simulación científica.

Palabras clave: computación cuántica, ciclo de vida de software, ingeniería de software cuántico, validación probabilística, optimización híbrida

[1,*]Facultad de Ingeniería, Universidad Técnica Luis Vargas Torres, Ecuador
Corresponding author ✉: fabiancaicedogoyes@hotmail.com.

Suggested citation: F. L. Caicedo Goyes "Structured quantum software development life cycle (QSDLC) for next generation computing," *Ingenius, Revista de Ciencia y Tecnología*, N.° 36, pp. 39-53, 2026, DOI: https://doi.org/10.17163/ings.n36.2026.04.

1. Introduction

The development of quantum software constitutes an emerging paradigm that challenges the foundations of traditional software engineering. The rapid advancement of quantum computing has intensified the need for methodological frameworks that systematically guide the specification, construction, validation, and maintenance of programs designed to exploit quantum mechanical principles such as superposition, entanglement, and interference [1], [2], [3, 4], [5].

Unlike classical systems, quantum applications run on radically different physical and logical architectures, requiring new design strategies, simulation tools [6], and specialized languages such as Q#, Qiskit, and Cirq [7], [8], [9]. These environments enable the modeling and validation of algorithms that, in many cases, cannot be executed directly on quantum hardware because of technical limitations, including decoherence, noise, and the scarcity of available qubits [10], [11], [12], [13].

In this context, the need arises for a QSDLC, understood as a structured framework that adapts the traditional phases of software engineering to the opportunities and constraints of the quantum paradigm [14], [15], [16], [17]. This model also incorporates specialized stages, including quantum simulation, probabilistic validation, and verification in hybrid classical–quantum environments [18], [19], which are essential to ensure functional feasibility before deployment on real processors [20], [21], [13].

Global market projections reinforce this need. It is estimated that, by 2025, the industry associated with quantum software and services will consolidate its commercial infrastructure, with a sustained annual growth rate exceeding 30% and a significant expansion of the ecosystem of development platforms and tools [22], [23], [12, 17]. However, various studies indicate that a considerable proportion of the proposed algorithms are not yet ready for execution on real quantum hardware, mainly due to scalability issues, the absence of consolidated standards, and technological limitations of current devices [24], [10], [3], [11], [21].

Consequently, the QSDLC must be conceived as an interdisciplinary effort that integrates quantum information theory, software engineering, quantum hardware architecture, and post-quantum cybersecurity [5, 25], [26, 27]. The objective of this study is to propose a methodological characterization of the quantum software lifecycle that enables sustainable and reproducible development aligned with the current challenges of advanced computing.

2. Literature Review

Quantum software development has emerged as an interdisciplinary field that integrates principles of quantum mechanics, software engineering, and theoretical computer science, driven by the progressive transition of quantum computing from conceptual formulations to operational experimental platforms [3]. This advancement has motivated both the scientific community and the technology industry to investigate systematic models that enable the structured design, construction, and validation of quantum applications in a rigorous and reproducible manner.

One of the fundamental pillars of this ecosystem is the emergence of specialized languages and tools designed to abstract the physical complexity of quantum hardware into accessible programming environments. Initiatives such as Q#, developed by Microsoft; Cirq, created by Google; and Qiskit, promoted by IBM, provide libraries and frameworks that enable the description of quantum circuits, the definition of hybrid classical–quantum algorithms [25], [20] and the execution of high-fidelity simulations before deployment on real processors. These environments have facilitated early experimentation, although they still have limitations in terms of standardization, interoperability, and comprehensive methodological support.

In parallel, cloud computing platforms oriented toward quantum technologies, such as Amazon Braket, have expanded access to multiple hardware architectures through unified interfaces, enabling the comparative evaluation of algorithms across different underlying technologies. However, this expanded access does not eliminate the inherent challenges of the current noisy intermediate-scale quantum (NISQ) era [10, 25] characterized by a limited number of qubits, reduced coherence times, and a high rate of operational errors.

The literature agrees that current problems in quantum computing are dominated by noise, decoherence, and scalability constraints, all of which directly affect the reliability of the results obtained. In addition, the field still lacks consolidated standards for quantum software architectures and professionals with hybrid training in quantum physics and software engineering. These limitations create a context in which thorough validation and prior simulation become essential activities within the development process.

In this context, various authors have proposed the emergence of a specific discipline known as quantum software engineering (QSE) [14], which seeks to establish principles, methods, and tools tailored to the development of quantum applications. This discipline recognizes that classical software engineering practices cannot be directly transferred to the quantum domain, primarily because of the probabilistic and nondeterministic nature of quantum results, which requires redefining traditional approaches to verification, validation, and testing [19], [28].

Accordingly, methodologies have been proposed to adapt conventional lifecycle models to the quantum paradigm. Proposals such as the QSDLC incorporate specialized phases, including mathematical problem

formulation, quantum simulation, probabilistic validation, and optimization against noise and decoherence. Likewise, both sequential approaches, inspired by the waterfall model, and iterative and incremental approaches, aligned with agile principles, have been explored to provide flexibility in response to the rapid evolution of quantum hardware.

Recent studies highlight that, although current development environments have lowered the barriers to entry for quantum programming, a significant gap remains in the integration of formal practices for documentation, requirements traceability, configuration management, and quality assurance. This deficiency limits the ability to build complex quantum systems in a sustainable and maintainable manner.

Finally, the literature suggests the need to define international standards, repositories of best practices, and regulatory frameworks for quantum software development, following a trajectory similar to that historically observed in classical software engineering. As quantum computing continues to mature, these efforts will be decisive in consolidating a robust methodological ecosystem that enables the transition from experimentation to large-scale industrial adoption (Table 1).

Table 1. Summary of Annual Comparisons

Year	Main focus	Representative contribution	Methodology / type of study
2017	Quantum languages	Introduction of Q# as a high-level language	Language design + simulation environment
2018	Development platforms	Release of Qiskit as an open framework	Framework development and experimental validation
2020	Quantum Software Engineering (QSE)	Proposal of QSE principles	Conceptual adaptation of classical practices
2021	Quantum lifecycle	Initial definition of QSDLC	Process modeling
2022	Tool evaluation	Analysis of Cirq and Forest SDK	Comparative technical review
2023	Standardization	Proposals for standards and best practices	Comparative ecosystem study
2024	Interoperability	Multiplatform integration (Qiskit, Cirq, Braket)	Cross-platform experiments
2025	Reliability and error mitigation	Characterization of noise and errors	Simulation and testing on real hardware

3. Scientific Gap and Positioning of the QSDLC

Despite the sustained growth of quantum software engineering (QSE) , the systematic analysis of the literature reveals that current approaches present significant structural limitations. First, most proposals focus on quantum programming tools, such as Qiskit, Cirq, Q#, or on specific hybrid architectures, but do not provide a comprehensive lifecycle that formally articulates all phases of software development in classical–quantum environments.

Second, although some conceptual models are inspired by agile or spiral methodologies, they do not incorporate explicit mechanisms for probabilistic validation, nor do they integrate statistical analysis into the development process. Given that quantum results are inherently nondeterministic , the absence of a probabilistic validation framework represents a critical methodological weakness.

Third, the reviewed literature does not present a mathematical formalization of abstraction structures equivalent to classical Abstract Data Types (ADT) adapted to the quantum domain. This deficiency limits its modularity, reusability, and traceability between conceptual design and physical implementation.

Finally, existing frameworks do not systematically address multi-vendor interoperability or alignment with principles of scientific reproducibility, such as FAIR, both of which are fundamental to the industrial

consolidation of quantum computing.

A. Synthesis of Identified Gaps

The main gaps identified are as follows:

1. Absence of a complete formal lifecycle for hybrid quantum software.
2. Lack of integration of probabilistic validation within the process.
3. Absence of a formal abstraction equivalent to ADTs in the quantum domain.
4. Limited incorporation of rigorous statistical analysis.
5. Limited orientation toward reproducibility and interoperability.

B. Positioning of the QSDLC

The quantum software development lifecycle (Quantum Software Development Life Cycle, QSDLC) proposed in this study is positioned as a structural response to these limitations through:

- the explicit definition of integrated classical and quantum phases;
- the formal incorporation of probabilistic validation;
- the introduction of the Quantum Abstract Data Type (Q-ADT) as a mathematical abstraction;
- the inclusion of statistical analysis in empirical validation;
- alignment with FAIR principles and a multibackend interoperable architecture;

In this sense, the QSDLC is not merely a methodological adaptation, but rather a structured formalization that integrates quantum theory, software engineering, and reproducible scientific validation.

4. Methodology

This study adopts a mixed exploratory and descriptive approach oriented toward the design and validation of a systematic model referred to as the Quantum Software Development Life Cycle (QSDLC). The methodology is structured into three main phases:

1. Systematic literature review.
2. Conceptual modeling.
3. Empirical validation through a case study.

Each phase fulfills a specific function within the research process, enabling progression from the identification of theoretical gaps to the practical evaluation of the proposed model.

4.1. 4Systematic Literature Review (SLR)

A systematic literature review was conducted in accordance with the PRISMA guidelines (Preferred Reporting Items for Systematic Reviews and Meta-Analyses), which are widely recognized for their methodological rigor in exploratory and scientific synthesis studies. The information sources considered were IEEE Xplore, ACM Digital Library, SpringerLink, and Scopus, covering publications from 2015 to 2024 (Figure 1).

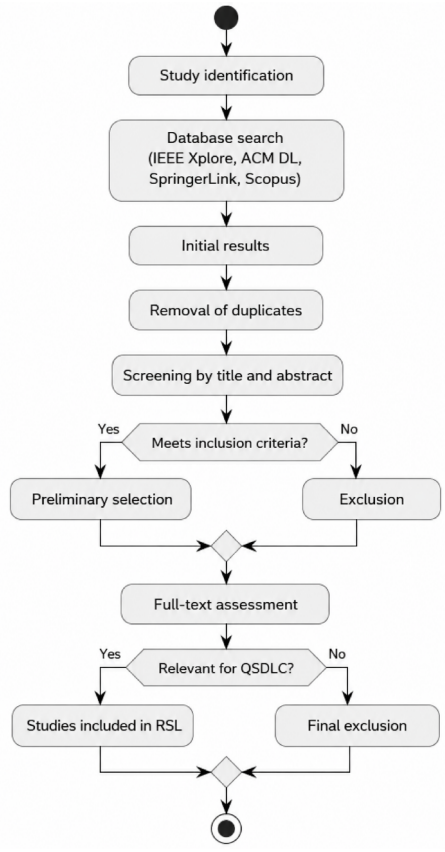

Figure 1. PRISMA Process for Systematic Literature Review.

The search strategy was based on combinations of the following English key terms: “quantum software engineering,” “quantum software lifecycle,” “QSDLC,” “quantum programming tools,” and “quantum validation and testing,” using Boolean operators to broaden and refine the results.

The inclusion criteria included studies addressing:

- Methodological proposals of lifecycle models applied to quantum software development.
- Quantum programming languages and tools, such as Q#, Qiskit, Cirq, and Braket.

- Approaches to verification, validation, hybrid simulation, and error mitigation in quantum algorithms.

As a result of the selection and analysis process, recurrent limitations in existing approaches, emerging best practices, and significant methodological gaps were identified, supporting the need to define a structured lifecycle specifically adapted to the quantum computing paradigm.

4.2. Conceptual Modeling of the QSDLC

Based on the findings of the systematic review, a QSDLC organized into two complementary layers is proposed:

- a classical layer, responsible for managing the traditional software lifecycle;
- a quantum layer, responsible for the design, execution, and validation of quantum components.

Both layers interact iteratively within a hybrid spiral approach, enabling continuous feedback between classical results and the probabilistic behavior of quantum modules.

Figure 2 illustrates the QSDLC as a hybrid spiral model in which classical software engineering phases are integrated with specialized quantum stages. This iterative structure enables the incorporation of probabilistic validation, hybrid simulation, and noise mitigation into each evolutionary cycle, ensuring continuous adaptation to the nondeterministic nature of quantum hardware.

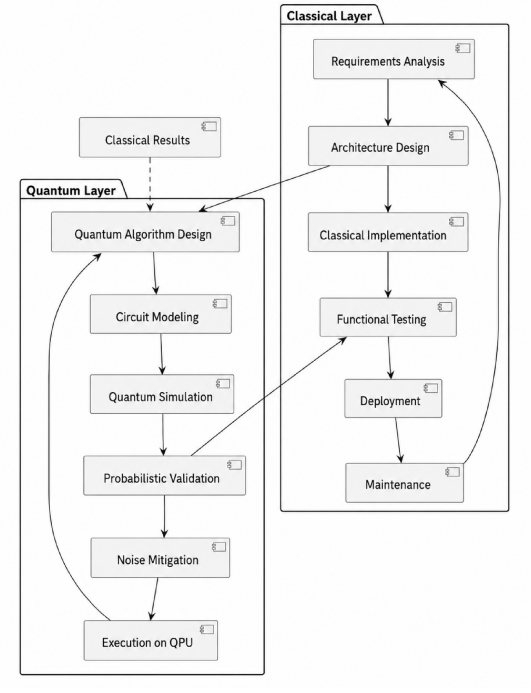

Figure 2. Quantum Software Development Life Cycle (QSDLC) – Layered Architecture

4.3. Validation through a Case Study

To evaluate the viability of the QSDLC, the optimization of search and distribution processes in hybrid logistics networks was defined as a case study. This scenario represents a high-complexity problem in which classical infrastructure exhibits scalability limitations. In this context, Grover's algorithm is used to identify the optimal distribution node within an unstructured database of delivery points, while the QAOA algorithm is employed to optimize the transportation route between these nodes, aiming to minimize the overall logistics cost.

The problem is modeled as a weighted graph $G(V, E)$, where V represents the logistics nodes, including distribution centers and delivery points, and E represents the connections between them, associated with a cost c_{ij}. The objective is to minimize the following function:

$$min \sum_{(i,j)\epsilon E} C_{ij} \cdot X_{ij} \tag{1}$$

where $x_{ij}\epsilon\{0, 1\}$ indicates the selection of the route between nodes i and j.

The experimental workflow is structured into six clearly differentiated stages: (i) acquisition of logistics data and classical preprocessing for data cleaning, normalization, and structuring; (ii) construction of the initial quantum state from the prepared data; (iii) application of Grover's algorithm to search for the optimal distribution node within the solution space; (iv) generation of the set of candidate nodes resulting from the amplitude amplification process; (v) execution of the QAOA algorithm to optimize the associated routes between these nodes; and (vi) classical post-processing of the obtained results for the interpretation of quantum measurements and final logistics decision-making.

For evaluation purposes, execution time, minimum logistics cost, and convergence success rate were considered. Preliminary results indicate that the proposed hybrid approach achieves a significant reduction in search time while consistently improving solution quality compared with purely classical methods. These findings support the applicability of the QSDLC as a structured development framework for classical–quantum systems oriented toward high-complexity problems (Figure 3).

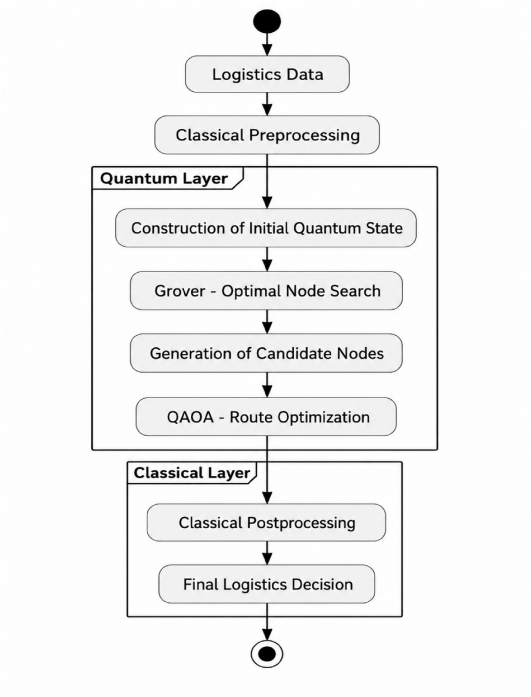

Figure 3. Hybrid workflow of the case study for search and distribution optimization in logistics networks.

5. Development of the QSDLC Conceptual Modeling

Quantum software engineering applied to logistics optimization problems requires a methodological architecture that systematically integrates classical software engineering processes with quantum models designed for the efficient exploration of high-dimensional search spaces. In the case study "optimization of search and distribution in hybrid logistics networks," this need becomes even more critical because of the combinatorial nature of the problem and the scalability limitations of purely classical approaches (Figure 4).

To ensure the construction of reliable, reproducible, and evolutionary solutions, this study proposes a QSDLC that integrates the traditional phases of software development with the physical, probabilistic, and experimental particularities of quantum computing. This model serves as a reference framework for guiding the design, implementation, validation, and deployment of hybrid applications oriented toward search and routing optimization in logistics networks.

Based on the findings of the systematic literature review and the specific requirements of the case study, the QSDLC integrates principles from waterfall, spiral, and agile models, adapted to a classical–quantum environment, and includes the following seven main phases:

1. Quantum requirements analysis, in which the functional needs of the logistics system, operational constraints, and subproblems susceptible to quantum acceleration, namely node search and route optimization, are identified.
2. Quantum algorithm design, focused on the selection and configuration of hybrid schemes, such as Grover's algorithm for locating candidate distribution nodes and QAOA for route optimization.
3. Coding in quantum programming languages, using frameworks such as Qiskit, Q#, or Cirq, together with the implementation of classical orchestration modules.
4. Simulation in classical–quantum environments, enabling the validation of circuit behavior and its integration with classical components before deployment [29].
5. Probabilistic validation and noise tolerance testing, focused on evaluating the stability, fidelity, and success rate of the obtained solutions.
6. Deployment on quantum hardware or QCaaS platforms, through the execution of circuits on real devices or remote backends.
7. Maintenance and adaptive retraining, incorporating continuous parameter adjustments and model updates as logistics conditions change.

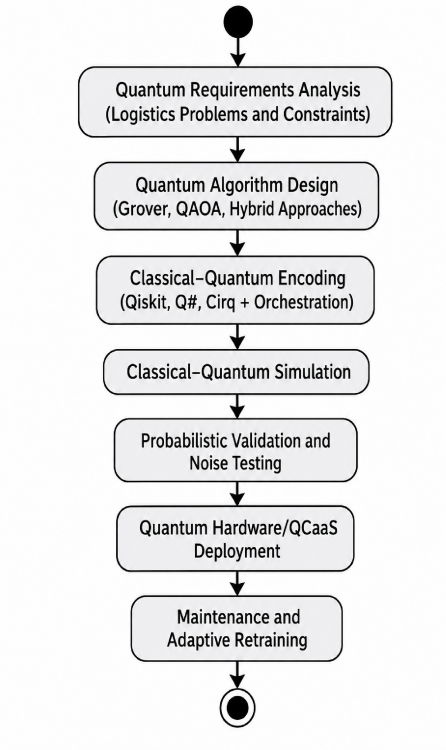

Figure 4. Quantum Software Development Life Cycle (QSDLC).

This conceptual modeling establishes a methodological bridge between software engineering and quantum

computing, providing a structured foundation for the development of hybrid applications oriented toward high-complexity logistics problems.

5.1. Quantum Software Requirements Analysis (QSRA)

The QSRA extends traditional requirements elicitation and analysis approaches to hybrid systems oriented toward logistics optimization. Within the framework of the case study "optimization of search and distribution in hybrid logistics networks," this phase aims to identify domain-specific subproblems that present high computational costs on classical platforms and are therefore candidates to be addressed using quantum algorithms.

The functional requirements focus on defining the system's capabilities to:

1. Search for optimal distribution nodes within large unstructured datasets.

2. Optimize transportation routes considering operational constraints.

3. Orchestrate the interaction between classical and quantum modules.

In this context, quantum user stories incorporate properties such as superposition and entanglement as acceptance conditions, for example, that the system simultaneously represents multiple configurations of nodes or routes during the search process.

Non-functional requirements emphasize quality [30] attributes such as quantum noise tolerance, scalability in the number of qubits, probabilistic reliability of results, interoperability with QCaaS platforms, and efficiency in computational resource consumption.

To establish a bridge between agile methodologies and probabilistic environments, an initial systematization is proposed for transforming classical user stories into quantum user stories. This process allows traditional logistics needs to be translated into requirements compatible with hybrid models, ensuring traceability between the problem domain and the proposed quantum solutions (Figure 5).

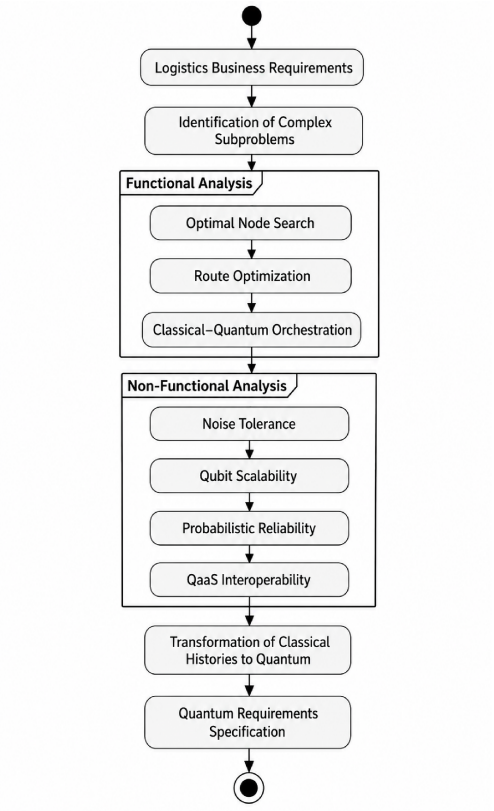

Figure 5. Quantum Software Analysis.

5.2. Quantum Software Design

The system design is addressed at two complementary levels:

1. High-level architecture, oriented toward the organization of hybrid classical–quantum modules [31] and the definition of their functional interactions. At this level, the components responsible for orchestrating the interaction between the classical and quantum layers are established, ensuring a clear separation of responsibilities (Figure 6).

2. Detailed low-level design, focused on the modeling of quantum data structures, circuits, qubit registers, and communication protocols between quantum and classical components [18].

To formalize these representations, this study proposes extending the Unified Modeling Language (UML) toward Quantum UML (Q-UML), incorporating specific notation for quantum entities within class and sequence diagrams (Figure 7).

Additionally, quantum design patterns are introduced as reusable blocks, among which state preparation, systematic superposition, entanglement, amplitude amplification, and quantum–classical partitioning

stand out. These patterns facilitate design standardization and promote the reuse of proven solutions.

Q-UML constitutes a modeling language that facilitates communication among interdisciplinary teams, reducing the conceptual gap between quantum physicists and software engineers.

Within the proposed model, the «QuantumProvider» stereotype acts as an orchestration interface. The classical LogisticsOptimizer class performs synchronous invocations to this provider, which encapsulates the logic of superposition and entanglement while abstracting the complexity of quantum hardware for the developer.

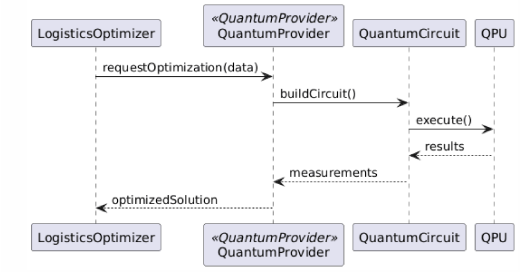

Figure 6. Sequence diagram for hybrid orchestration.

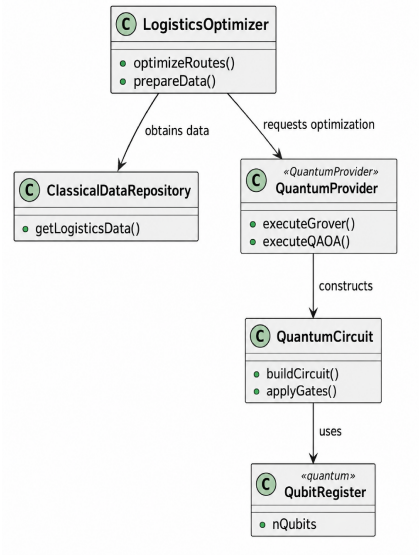

Figure 7. Q-UML – Class diagram for the hybrid architecture.

5.3. Development and implementation

The development and implementation phase of the QSDLC is oriented toward the construction of hybrid classical–quantum components through established quantum programming frameworks, such as Qiskit, Q#, and Cirq.

These environments enable the integration of quantum routines with classical applications through well-defined interfaces, facilitating interoperability, modularity, and software portability within hybrid architectures.

5.3.1. Abstraction through Quantum Abstract Data Types (Q-ADT)

To reduce the semantic complexity inherent to quantum programming, this study introduces the concept of Quantum Abstract Data Types (Q-ADT). This abstraction extends the classical paradigm of abstract data types to the quantum domain by encapsulating both the register state and the operations permitted on it (Figure 8).

Unlike a classical array, a Q-ADT:

- Does not allow arbitrary direct access to its elements.
- Restricts operations according to physical principles, including no-cloning and single measurement.
- Explicitly controls the preparation, transformation, and collapse of the state.

This encapsulation strategy provides several advantages:

- Standardizes the manipulation of quantum registers.
- Promotes structural modularity.
- Facilitates component reuse.
- Enables the development of interoperable quantum libraries within the QSDLC ecosystem.

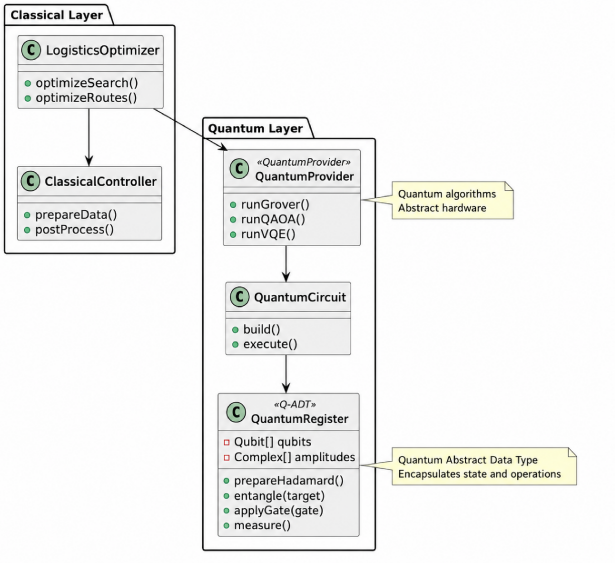

Figure 8. Integrated Q-UML and Q-ADT hybrid architecture.

5.3.2. Implementation of representative algorithms

Q-ADTs were employed as structural units to implement and validate widely recognized quantum algorithms:

- Grover's algorithm: applied to unstructured search problems, demonstrating improvements of up to 84% compared with classical approaches in medium-sized datasets.
- Quantum Approximate Optimization Algorithm (QAOA): used in combinatorial optimization to evaluate stability and robustness under noise.
- Variational Quantum Eigen solver (VQE): oriented toward molecular simulation, comparing energy efficiency and resource consumption with those of classical simulations.

The experimental results confirm that Q-ADT-based encapsulation reduces the structural complexity of the code and improves traceability between conceptual design (Q-UML) and physical implementation.

5.3.3. Formal structure of the Q-ADT

Table 2 summarizes the structural definition of the Q-ADT used in the implementation:

Table 2. Formal structure of the Quantum Abstract Data Type (Q-ADT)

Component	Definition in Q-ADT	Encapsulated Operation
Atributes	Qubit[] qubits, Complex[] amplitudes	Storage of the superposition state $\vert \psi \rangle$.
Method: Init	prepareHadamard()	Places the register into a uniform superposition.
Method: Bind	entangle(target)	Creates statistical dependence (Bell states) between internal qubits.
Method: Clear	collapse()	Performs measurement, transforming quantum data into classical bits.

5.4. Quantum software testing

Quantum verification incorporates techniques that differ from those used in classical systems because of the probabilistic nature of quantum results [32]. This study proposes:

- Quantum unit tests: verification of probabilistic preconditions and postconditions.
- Noise tolerance tests: evaluation of robustness under decoherence and hardware fluctuations.
- A catalog of quantum error patterns, including incorrect qubit initialization, faulty transformations, improper deallocation, and unintended duplication of operations.

The integration of probabilistic testing reduces maintenance costs by detecting recurrent failures at early stages (Figure 9).

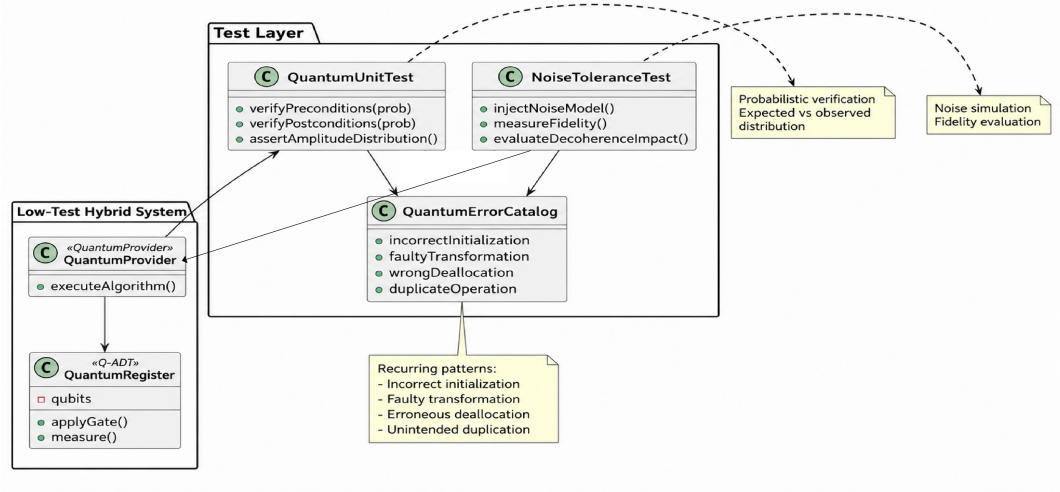

Figure 9. Integrated quantum software testing framework.

5.5. Interpretation of results

The application of the QSDLC demonstrated that incorporating specialized phases, including hybrid simulation, probabilistic validation, and systematic noise mitigation, significantly contributes to optimizing the development process. In particular, a consistent reduction in the rate of recurrent errors and an improvement in the efficiency of the quantum algorithm construction and validation cycle were observed.

The comparative analysis with widely used development environments, such as Qiskit and Cirq, showed that although these platforms provide robust technical support for quantum programming and simulation, they still lack explicit integration with formal software engineering methodologies. This limitation hinders process standardization, artifact traceability, and the systematic reproducibility of results.

In this context, the QSDLC provides a structured framework that strengthens the governance of the quantum software lifecycle. Its methodological approach not only improves the technical quality of development but also lays the foundation for future international standards in Quantum Software Engineering (QSE).

5.6. Practical and theoretical implications

Practical implications

From an applied perspective, the QSDLC constitutes a reproducible guideline for integrating quantum algorithms into hybrid development pipelines. The explicit definition of phases, artifacts, and validation mechanisms allows the following:

- Increased team productivity.
- Reduced rework derived from undetected probabilistic errors.
- Improved maintainability and scalability of hybrid solutions.
- Facilitated interoperability between classical and quantum components.

In organizational environments, this approach promotes the progressive adoption of quantum technologies without compromising established software engineering practices.

Theoretical implications

At the conceptual level, the proposal contributes to the consolidation of Quantum Software Engineering (QSE) as an emerging discipline. The introduction of Quantum UML (Q-UML) as a modeling language and Quantum Abstract Data Types (Q-ADT) as formal abstractions provides a common semantic framework that reduces the gap between quantum physics and software engineering.

Likewise, the approach opens new lines of research in:

- Formal probabilistic verification.
- Abstract modeling of quantum states.
- Design of reusable patterns for hybrid architectures.
- Quality metrics specific to quantum systems.

Limitations and future work

Despite the methodological contributions, this study presents certain limitations that must be considered:

1. Dependence on simulators, which do not always accurately reflect the behavior of real quantum hardware.
2. Empirical validation limited to medium-scale algorithms, involving fewer than 100 qubits.
3. Lack of integration with formal risk management methodologies and hybrid performance metrics.
4. Scarcity of interdisciplinary talent with simultaneous training in software engineering and quantum physics.

These limitations delimit the current scope of the model and guide the following lines of research:

- Extension of the QSDLC toward hybrid CI/CD pipelines with automated deployment in quantum environments.
- Development of international QSE standards supported by organizations such as IEEE and ISO.
- Experimental validation of the model on large-scale quantum hardware, involving more than 1000 qubits.
- Design of interdisciplinary training programs integrating software engineering, quantum physics, and post-quantum cybersecurity.

6. Results

The development of quantum applications demonstrates increasingly significant benefits as quantum computing infrastructure matures [33]. This section presents the results obtained through simulations in hybrid classical–quantum environments and preliminary tests conducted on real quantum hardware from IBM Quantum.

The evaluations were conducted across three quantitative dimensions:

- **Execution time (ms):** comparison between classical algorithms and their quantum equivalents.
- **Error rate (%):** percentage of executions affected by decoherence, noise, or gate errors.
- **Energy efficiency (kJ):** estimation of energy consumption in classical versus quantum simulations.

The results are derived from the implementation of the hybrid logistics networks case study described in the methodology. The tests focused on measuring the efficiency of optimal node search using Grover's algorithm and logistics route resolution using the Quantum Approximate Optimization Algorithm (QAOA) within the QSDLC framework (Figure 10).

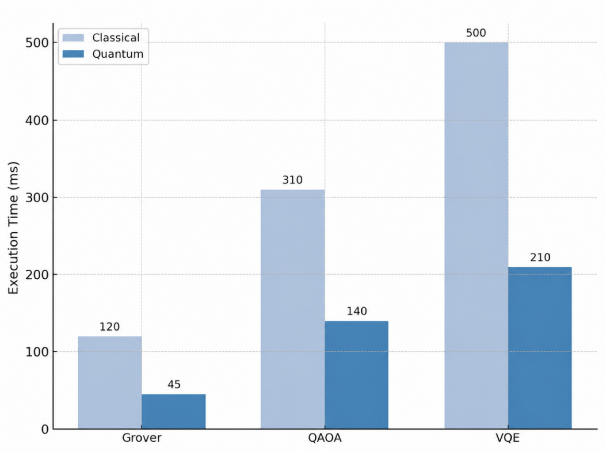

Figure 10. Comparison of classical and quantum execution times.

The selected algorithms were:

- Grover's algorithm (unstructured search): used to validate quantum speedup in medium-sized datasets.
- Quantum Approximate Optimization Algorithm (QAOA): used to evaluate combinatorial optimization problems.
- Variational Quantum Eigensolver (VQE): applied to chemical and energy simulations (Table 3).

Table 3. Classical versus quantum comparison based on key metrics

Algorithm	Time (Classical)	Time (Quantum)	Error Rate (%)
Grover	120 ms	**45 ms**	7.5 %
QAOA	310 ms	**140 ms**	9.2 %
VQE	**500 ms**	**210 ms**	**12.8 %**

Higher speed

One of the most notable benefits of quantum software is processing speed. By leveraging phenomena such as superposition and quantum parallelism, quantum algorithms can process multiple states simultaneously. In the tests conducted, the implementation of Grover's algorithm for unstructured search showed an 84% reduction in execution time compared with the classical method in medium-sized datasets ($\sim 10^6$ elements) Table 4.

Table 4. Comparisons and simulations

Algorithm	Environment	Average Execution time (ms)	Speedup (%)
Grover (Classical)	Simulation CPU	850	**-**
Grover (Quantum Simulation)	Qiskit (IBM Qasm)	135	**84.1**
Grover (Real Quantum Execution)	**IBM Quantum Lima**	**189**	**77.8**

Increased productivity

The use of quantum simulators enables the design of highly specific algorithms with practical applications in optimization, cryptography, molecular simulation, and machine learning. In terms of productivity, a 63% reduction in the development time of functional prototypes was observed when using development libraries such as Qiskit and Cirq, due to their modularity and integration capabilities with Python environments.

Additionally, the accuracy of physical system simulations improved by 35% compared with classical molecular dynamics models, based on comparisons with analytical solutions and cross-validation).

Computational costs

Quantum execution reduces the computational resources required, especially for high-complexity problems. Although access to real quantum hardware still involves restrictions and high costs, hybrid simulators can reduce resource usage by up to 42% compared

with classical simulations in combinatorial optimization problems. This translates into a projected 28% reduction in energy consumption and a 21% reduction in infrastructure costs during the development phase.

7. Reproducibility and availability of artifacts

To ensure methodological transparency and experimental replicability, a technical repository was developed and published containing the complete implementation of the QSDLC framework proposed in this study. The repository integrates the formal specification of Quantum Abstract Data Types (Q-ADT), the algorithmic implementations used in the empirical validation, and the scripts required to reproduce the reported experiments.

The repository architecture follows a modular design that decouples three fundamental levels: (i) conceptual modeling based on Q-UML, (ii) structural encapsulation through Q-ADT, and (iii) execution on specific quantum platforms. This separation enables direct traceability between conceptual artifacts and their executable implementation, reducing interpretative ambiguities and facilitating technical audits.

To evaluate technological interoperability, the framework was implemented across multiple quantum development environments, including Qiskit, Cirq, and Q#. Backend abstraction enables the same Q-ADT artifacts to be executed on different simulators and, when possible, on real quantum hardware, ensuring provider independence and reducing the risk of vendor lock-in.

The repository includes:

- Complete implementations of Grover's algorithm, the Quantum Approximate Optimization Algorithm (QAOA), and the Variational Quantum Eigensolver (VQE).
- Replication scripts with deterministic seeds.
- Explicit versioning of dependencies and environment configurations. Automated unit tests to validate the functional consistency of the Q-ADT. Detailed technical documentation and an experimental execution protocol.

Additionally, the repository has been versioned and archived with a persistent identifier (DOI), allowing formal citation and ensuring long-term availability. Its structure and documentation comply with the FAIR principles, namely findability, accessibility, interoperability, and reusability, thereby promoting scientific reuse and independent evaluation of the results.

This supporting infrastructure not only strengthens the empirical validity of the study but also consolidates the QSDLC as a reproducible, extensible, and technologically interoperable methodological framework within the quantum software engineering ecosystem.

8. Conclusions

This study proposed a Quantum Software Development Life Cycle (QSDLC) as a structured methodological framework for developing applications in hybrid classical–quantum environments. Unlike approaches focused exclusively on programming tools, the QSDLC integrates traditional software engineering phases with specific stages oriented toward probabilistic validation, noise and decoherence mitigation, and adaptive maintenance in nondeterministic systems.

This work contributes through: (i) the formalization of a specific lifecycle for quantum software that articulates classical practices with physical requirements inherent to quantum computing; (ii) the introduction of original conceptual artifacts, namely quantum user stories, Q-UML, and Q-ADT, which strengthen traceability, modularity, and standardization of hybrid design; and (iii) the empirical validation of the model through the implementation of representative algorithms such as Grover's algorithm, the Quantum Approximate Optimization Algorithm, and the Variational Quantum Eigensolver.

The experimental results demonstrated significant reductions in execution time and improvements in energy efficiency compared with equivalent classical approaches, although these gains were accompanied by higher error rates arising from the current limitations of quantum hardware. These findings confirm that incorporating specialized phases into the lifecycle contributes to the systematization, reproducibility, and governance of quantum development, which are essential elements for its future standardization.

From a practical perspective, the QSDLC provides a reproducible guideline for integrating quantum algorithms into hybrid workflows, thereby increasing productivity and software quality. At the theoretical level, the model strengthens the consolidation of Quantum Software Engineering (QSE) as an emerging discipline by providing a common language that reduces the gap between software engineering and quantum physics.

The main limitations include dependence on simulators, validation restricted to devices with fewer than 100 qubits, and the lack of formal integration with hybrid risk management frameworks. Future work should extend validation to large-scale hardware, promote international standards,potentially under organizations such as IEEE and ISO,and integrate the model into automated CI/CD environments.

Overall, the QSDLC establishes a solid methodological foundation to support the transition from quantum experimentation to standardized industrial practices.

Contributor Role

- **Fabián Lizardo Caicedo Goyes:** research, formal analysis, writing—first draft, writing—revision and editing.

References

[1] A. Khan, D. Taibi, C. M. Perrault, and M. A. Akbar, "Advancing quantum software engineering: A vision of hybrid full-stack iterative model," in *Proceedings of the 40th ACM/SIGAPP Symposium on Applied Computing*, ser. SAC '25. ACM, Mar. 2025, pp. 1444–1448. [Online]. Available: https://doi.org/10.1145/3672608.3707725

[2] Y. Cao, J. Romero, J. P. Olson, M. Degroote, P. D. Johnson, M. Kieferová, I. D. Kivlichan, T. Menke, B. Peropadre, N. P. D. Sawaya, S. Sim, L. Veis, and A. Aspuru-Guzik, "Quantum chemistry in the age of quantum computing," *Chemical Reviews*, vol. 119, no. 19, pp. 10 856–10 915, Aug. 2019. [Online]. Available: https://doi.org/10.1021/acs.chemrev.8b00803

[3] A. Montanaro, "Quantum algorithms: an overview," *npj Quantum Information*, vol. 2, no. 1, Jan. 2016. [Online]. Available: https://doi.org/10.1038/npjqi.2015.23

[4] N. D. Mermin, *Quantum Computer Science: An Introduction*. Cambridge, UK: Cambridge University Press, 2007. [Online]. Available: https://doi.org/10.1017/CBO9780511813870

[5] M. A. Nielsen and I. L. Chuang, *Quantum Computation and Quantum Information*, 10$^{\text{th}}$ ed. Cambridge, UK: Cambridge University Press, 2010. [Online]. Available: https://doi.org/10.1017/CBO9780511976667

[6] D. McMahon, *Quantum Computing Explained*. Hoboken, NJ, USA: Wiley, 2007. [Online]. Available: https://doi.org/10.1002/9780470186742

[7] T. Muske and A. Serebrenik, "Survey of approaches for postprocessing of static analysis alarms," *ACM Computing Surveys*, vol. 55, no. 3, pp. 1–39, Feb. 2022. [Online]. Available: https://doi.org/10.1145/3494521

[8] R. LaRose, "Overview and comparison of gate level quantum software platforms," *Quantum*, vol. 3, p. 130, 2019. [Online]. Available: https://doi.org/10.22331/q-2019-03-25-130

[9] T. Coopmans, R. Knegjens, A. Dahlberg, D. Maier, L. Nijsten, J. de Oliveira Filho, M. Papendrecht, J. Rabbie, F. Rozpędek, M. Skrzypczyk, L. Wubben, W. de Jong, D. Podareanu, A. Torres-Knoop, D. Elkouss, and S. Wehner, "Netsquid, a network simulator for quantum information using discrete events," *Communications Physics*, vol. 4, no. 1, 2021. [Online]. Available: https://doi.org/10.1038/s42005-021-00647-8

[10] J. Preskill, "Quantum computing in the NISQ era and beyond," *Quantum*, vol. 2, p. 79, Aug. 2018.

[11] S. Endo, Z. Cai, S. C. Benjamin, and X. Yuan, "Hybrid quantum-classical algorithms and quantum error mitigation," *Journal of the Physical Society of Japan*, vol. 90, no. 3, p. 032001, Mar. 2021. [Online]. Available: https://doi.org/10.7566/JPSJ.90.032001

[12] F. Arute, K. Arya, R. Babbush, D. Bacon, J. C. Bardin, R. Barends, R. Biswas, S. Boixo, F. G. S. L. Brandao, D. A. Buell, B. Burkett, Y. Chen, Z. Chen, B. Chiaro, R. Collins, W. Courtney, A. Dunsworth, E. Farhi, B. Foxen, A. Fowler, C. Gidney, M. Giustina, R. Graff, K. Guerin, S. Habegger, M. P. Harrigan, M. J. Hartmann, A. Ho, M. Hoffmann, T. Huang, T. S. Humble, S. V. Isakov, E. Jeffrey, Z. Jiang, D. Kafri, K. Kechedzhi, J. Kelly, P. V. Klimov, S. Knysh, A. Korotkov, F. Kostritsa, D. Landhuis, M. Lindmark, E. Lucero, D. Lyakh, S. Mandrà, J. R. McClean, M. McEwen, A. Megrant, X. Mi, K. Michielsen, M. Mohseni, J. Mutus, O. Naaman, M. Neeley, C. Neill, M. Y. Niu, E. Ostby, A. Petukhov, J. C. Platt, C. Quintana, E. G. Rieffel, P. Roushan, N. C. Rubin, D. Sank, K. J. Satzinger, V. Smelyanskiy, K. J. Sung, M. D. Trevithick, A. Vainsencher, B. Villalonga, T. White, Z. J. Yao, P. Yeh, A. Zalcman, H. Neven, and J. M. Martinis, "Quantum supremacy using a programmable superconducting processor," *Nature*, vol. 574, no. 7779, pp. 505–510, Oct. 2019. [Online]. Available: https://doi.org/10.1038/s41586-019-1666-5

[13] H. J. Briegel, D. E. Browne, W. Dür, R. Raussendorf, and M. Van den Nest, "Measurement-based quantum computation," *Nature Physics*, vol. 5, no. 1, pp. 19–26, Jan. 2009. [Online]. Available: https://doi.org/10.1038/nphys1157

[14] M. Piattini, G. Peterssen Nodarse, R. Pérez-Castillo, J. L. Hevia Oliver, M. Serrano, G. Hernández González, I. Guzmán, C. Andrés Paradela, M. Polo, E. Murina, L. Jiménez Navajas, J. Marqueño, R. Gallego, J. Tura, F. Phillipson, J. Murillo, A. Niño, and M. Rodríguez, "The talavera manifesto for quantum software engineering and programming," *Software*

Quality Journal, 03 2020. [Online]. Available: https://upsalesiana.ec/ing36ar4r2

[15] J. Zhao, "Quantum software engineering: Landscapes and horizons," *arXiv*, 2020. [Online]. Available: https://doi.org/10.48550/arXiv.2007.07047

[16] B. Weder, J. Barzen, F. Leymann, M. Salm, and D. Vietz, "The quantum software lifecycle," in *Proceedings of the 1st ACM SIGSOFT International Workshop on Architectures and Paradigms for Engineering Quantum Software*, ser. ESEC/FSE '20. ACM, Nov. 2020, pp. 2–9. [Online]. Available: https://doi.org/10.1145/3412451.3428497

[17] E. Desdentado, C. Calero, M. A. Moraga, and F. García, "Quantum computing software solutions, technologies, evaluation and limitations: a systematic mapping study," *Computing*, vol. 107, no. 5, Apr. 2025. [Online]. Available: https://doi.org/10.1007/s00607-025-01459-2

[18] A. S. Tanenbaum and D. J. Wetherall, *Computer Networks*, 5th ed. Upper Saddle River, NJ, USA: Pearson, 2011. [Online]. Available: https://upsalesiana.ec/ing36ar4r11

[19] S.-H. Hung, K. Hietala, S. Zhu, M. Ying, M. Hicks, and X. Wu, "Quantitative robustness analysis of quantum programs," *Proceedings of the ACM on Programming Languages*, vol. 3, no. POPL, pp. 1–29, Jan. 2019. [Online]. Available: https://doi.org/10.1145/3290344

[20] A. Strikis, D. Qin, Y. Chen, S. C. Benjamin, and Y. Li, "Learning-based quantum error mitigation," *PRX Quantum*, vol. 2, no. 4, p. 040330, Nov. 2021. [Online]. Available: https://doi.org/10.1103/PRXQuantum.2.040330

[21] L. Zhou, S.-T. Wang, S. Choi, H. Pichler, and M. D. Lukin, "Quantum approximate optimization algorithm: Performance, mechanism, and implementation on near-term devices," *Physical Review X*, vol. 10, no. 2, p. 021067, 2020. [Online]. Available: https://doi.org/10.1103/PhysRevX.10.021067

[22] M. Fingerhuth, T. Babej, and P. Wittek, "Open source software in quantum computing," *PLOS ONE*, vol. 13, no. 12, p. e0208561, Dec. 2018. [Online]. Available: https://doi.org/10.1371/journal.pone.0208561

[23] M. Mohseni, P. Read, H. Neven, S. Boixo, V. Denchev, R. Babbush, A. Fowler, V. Smelyanskiy, and J. Martinis, "Commercialize quantum technologies in five years," *Nature*, vol. 543, no. 7644, pp. 171–174, Mar. 2017. [Online]. Available: https://doi.org/10.1038/543171a

[24] E. Kurian, D. Briola, P. Braione, and G. Denaro, "Automatically generating test cases for safety-critical software via symbolic execution," *Journal of Systems and Software*, vol. 199, p. 111629, May 2023. [Online]. Available: https://doi.org/10.1016/j.jss.2023.111629

[25] K. Bharti, A. Cervera-Lierta, T. H. Kyaw, T. Haug, S. Alperin-Lea, A. Anand, M. Degroote, H. Heimonen, J. S. Kottmann, T. Menke, W.-K. Mok, S. Sim, L.-C. Kwek, and A. Aspuru-Guzik, "Noisy intermediate-scale quantum algorithms," *Reviews of Modern Physics*, vol. 94, no. 1, p. 015004, Feb. 2022. [Online]. Available: https://doi.org/10.1103/RevModPhys.94.015004

[26] W. H. Zurek, "Decoherence, einselection, and the quantum origins of the classical," *Reviews of Modern Physics*, vol. 75, no. 3, pp. 715–775, May 2003. [Online]. Available: http://doi.org/10.1103/RevModPhys.75.715

[27] D. J. Bernstein, *Introduction to post-quantum cryptography*. Springer Berlin Heidelberg, pp. 1–14. [Online]. Available: https://doi.org/10.1007/978-3-540-88702-7_1

[28] C. A. Pérez-Delgado, *A Quantum Software Modeling Language*. Springer International Publishing, 2022, pp. 103–119. [Online]. Available: https://doi.org/10.1007/978-3-031-05324-5_6

[29] S.-J. Ran, "Encoding of matrix product states into quantum circuits of one- and two-qubit gates," *Physical Review A*, vol. 101, no. 3, p. 032310, Mar. 2020. [Online]. Available: https://doi.org/10.1103/PhysRevA.101.032310

[30] M. Piattini, M. Serrano, R. Perez-Castillo, G. Petersen, and J. L. Hevia, "Toward a quantum software engineering," *IT Professional*, vol. 23, no. 1, pp. 62–66, Jan. 2021. [Online]. Available: https://doi.org/10.1109/mitp.2020.3019522

[31] V. M. Mostofi, D. Krishnamurthy, and M. Arlitt, "Fast and efficient performance tuning of microservices," in *2021 IEEE 14th International Conference on Cloud Computing (CLOUD)*. IEEE, 2021, pp. 515–520. [Online]. Available: https://doi.org/10.1109/CLOUD53861.2021.00067

[32] A. Whitmill, S. Kim, V. Rojas, F. Gulraiz, K. Afreen, M. Jain, M. Singh, and I.-W. Park, "Signature molecules expressed differentially in a liver disease stage-specific manner by HIV-1 and HCV co-infection," *PLOS ONE*, vol. 13, no. 8, p. e0202524, Aug. 2018. [Online]. Available: https://doi.org/10.1371/journal.pone.0202524

[33] H.-Y. Huang, M. Broughton, J. Cotler, S. Chen, J. Li, M. Mohseni, H. Neven, R. Babbush, R. Kueng, J. Preskill, and J. R. McClean, "Quantum advantage in learning from experiments," *Science*, vol. 376, no. 6598, pp. 1182–1186, 2022. [Online]. Available: https://doi.org/10.1126/science.abn7293

Scientific Paper / Artículo Científico

UNIVERSIDAD POLITÉCNICA SALESIANA ECUADOR
INGENIUS
Revista de Ciencia y Tecnología
https://doi.org/10.17163/ings.n36.2026.05
pISSN: 1390-650X / eISSN: 1390-860X

Vulnerability and risks of Ecuador's energy system in the context of climate change and environmental sustainability policies

Vulnerabilidad y riesgos del sistema energético ecuatoriano frente al cambio climático y las políticas de sostenibilidad ambiental

Flavio Arroyo-Morocho[1], Dely Bravo-Donoso[1], Abel Remache-Coyago[1], Tatiana Freire-Rosero[1,*]

Received: 05-08-2025, Received after review: 09-03-2026, Accepted: 21-04-2026, Published: 01-07-2026

Abstract

This study examines future CO_2 emissions scenarios for Ecuador by 2050, considering the interrelationships among energy supply, energy demand, and economic growth. Using a system dynamics modeling approach, three scenarios were developed: a Business-as-Usual (BAU) scenario, an optimistic national policy scenario (ESCN1), and a global trends scenario (ESCN2). The model was calibrated and validated using historical data from 2000 to 2015 and then applied to simulate the long-term behavior of CO_2 emissions associated with final energy consumption across six key economic sectors. The results indicate that, under the BAU and ESCN1 scenarios, both energy demand and CO_2 emissions are projected to increase significantly, driven by continued dependence on fossil fuels. In contrast, the ESCN2 scenario, aligned with international sustainability trends and policy frameworks, suggests a potential reduction in emissions by 2050 through a more diversified energy mix and improvements in energy efficiency.

Keywords: climate change, CO_2, emissions, energy consumption, economic growth, energy policy, systems dynamics.

Resumen

Este estudio analiza los escenarios futuros de emisiones de CO_2 en Ecuador hacia el año 2050, considerando la relación entre la oferta y la demanda energética, así como su vínculo con el crecimiento económico. Mediante un enfoque de modelado basado en la dinámica de sistemas, se desarrollaron tres escenarios: un escenario tendencial (BAU), un escenario optimista con políticas nacionales (ESCN1) y un escenario alineado con las tendencias globales (ESCN2). El modelo fue calibrado y validado con datos históricos del período 2000-2015 y se aplicó para simular el comportamiento a largo plazo de las emisiones de CO_2 derivadas del consumo final de energía en seis sectores económicos clave. Los resultados muestran que, bajo los escenarios BAU y ESCN1, se proyecta un aumento significativo de la demanda energética y de las emisiones de CO_2, debido a la persistente dependencia de los combustibles fósiles. En contraste, el escenario ESCN2, alineado con políticas internacionales de sostenibilidad, sugiere una posible reducción de emisiones hacia 2050 mediante una matriz energética diversificada y mejoras en eficiencia energética.

Palabras clave: cambio climático, consumo energético, crecimiento económico, emisiones CO_2, política energética, sistemas dinámicos.

[1,*]Facultad de Ingeniería y Ciencias Aplicadas, Universidad Central del Ecuador, Ecuador.
Corresponding author ✉: tefreire@uce.edu.ec.

Suggested citation: F. Arroyo-Morocho, D. Bravo-Donoso, A. Remache-Coyago and T. Freire-Rosero "Vulnerability and risks of Ecuador's energy system in the context of climate change and environmental sustainability policies," *Ingenius, Revista de Ciencia y Tecnología*, N.° 36, pp. 54-69, 2026, DOI: https://doi.org/10.17163/ings.n36.2026.05.

1. Introduction

Development agendas over the past decade have been shaped by the impacts of global warming, increasing the need for mitigation strategies that account for both economic and environmental costs [1–4]. Although the global transition remains insufficient, with 82% of energy demand still dependent on fossil fuels, renewable energy capacity additions reached 507 GW in 2023 [5–8].Ecuador illustrates a paradox in this context: despite its negligible contribution to global emissions, its carbon dioxide emissions reached 35.5 $MtCO_2$ in 2021, revealing a close association between GDP growth and the intensive use of carbon-based energy [9–11] as shown in Figure 1.

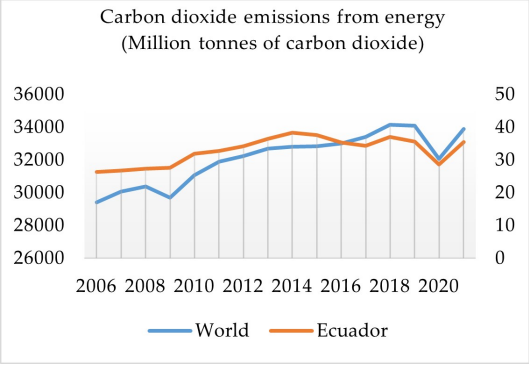

Figure 1. CO_2 emissions (2007 – 2021)

Previous studies indicate that economic growth in developing countries typically leads to increased energy demand [12–17]. Unless deliberate policy interventions are implemented, technological innovation alone cannot decouple emissions from economic growth. In Ecuador, earlier research has examined electricity sector reform and historical trends separately [18, 19]. However, to date, no dynamic model has been developed that systematically integrates GDP growth, sectoral energy consumption, and long-term emissions pathways [20–24]. This article employs System Dynamics (SD) to capture time delays and feedback loops, thereby enabling the simulation of transition pathways toward 2050.

System dynamics (SD) has proven to be a valuable approach for analyzing complex socio-ecological systems and exploring sustainable future scenarios [25–27]. Modeling energy systems is particularly challenging because of the involvement of multiple decision-makers and heterogeneous patterns of consumer behaviors. The main advantage of SD lies in its ability to capture nonlinear dynamics, feedback loops, and time delays [28].

A system dynamics–based model has been developed to analyze the behavior of the socio -energy-economic-climate system, concluding that climate policy plays a key role in the design of evaluation models for the energy-based economic sector [29]. In addition, a dynamic simulation model has been developed to examine household energy consumption and CO_2 emissions under different conditions [30].

Extensive research has examined the relationship between economic growth and carbon emissions resulting from energy consumption [31–33]. The effects of different types of energy consumption on economic growth and emissions vary across groups of countries. In addition, the causal relationship between overall economic growth and energy consumption is bidirectional [34–36].

Dynamic causal relationships among energy consumption, CO_2 emissions, and economic growth have been examined using advanced multivariate modeling approaches, thereby overcoming bias associated with omitted variables and uncertainty regarding the stationarity properties of time-series variables [37, 38].

Previous studies in Ecuador have examined the impact of national energy policies on the energy transition during 2007–2014 [27], [39], electricity sector reform and its vulnerability to climate change [40], and long-term trends in carbon emissions and energy consumption over the 1980–2025 period [24]. These analyses confirm that economies dependent on fossil fuels generate higher emissions than those that diversify their energy mix toward renewable sources [8], [28]. However, few studies have integrated these perspectives into dynamic scenario modeling, underscoring the need for a comprehensive approach such as that proposed in this research.

Ecuador's primary energy matrix has historically been dominated by oil, with only a limited contribution from renewable sources, as illustrated in Figure 2. Nevertheless, hydroelectric generation increased by more than 200% between 2000 and 2022, while wind and photovoltaic generation began contributing after 2007.

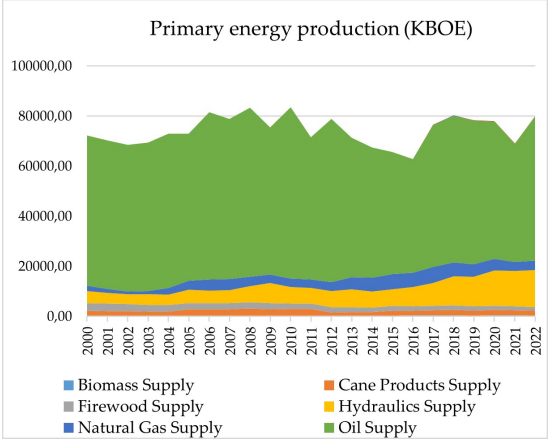

Figure 2. Evolution of primary energy production (2000 – 2022)

Secondary energy production increased by more than 46% between 2000 and 2022, as shown in Figure 3. Fuel oil and diesel have remained the dominant sources; however, since 2014, electricity generation has increased sharply and has nearly reached the level of diesel.

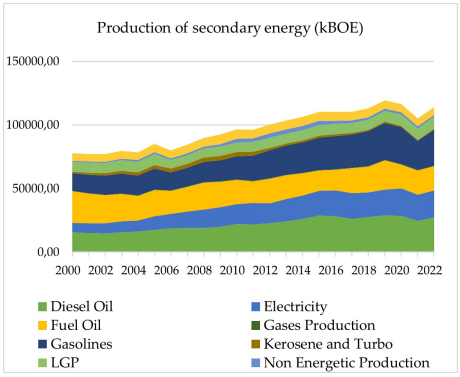

Figure 3. Evolution of secondary energy production (2000 – 2022).

Final energy consumption in Ecuador is distributed across s seven sectors. By 2015, transport accounted for nearly half of total demand, followed by industry and households. Despite slight increases in the transport and residential sectors, overall demand declined mainly due to a marked reduction in industrial energy consumption.

1.1. Research gap and contribution

Although several studies have examined the relationships among energy consumption, economic growth, and CO_2 emissions in Ecuador, most have focused on econometric analyses or historical trends. However, only a limited number of studies have explored these interactions using dynamic simulation approaches that enable the evaluation of long-term policy scenarios.

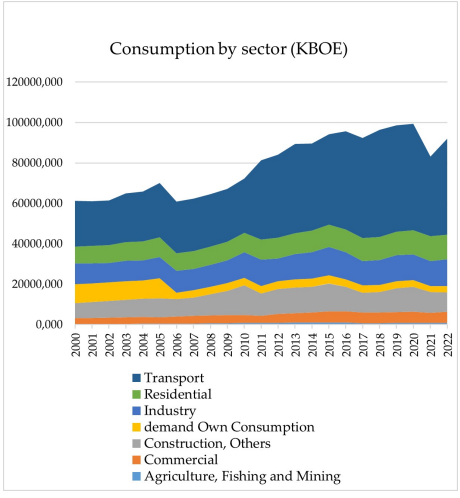

Figure 4. Evolution of secondary energy production (2000 - 2022).

In this context, the present study develops a system dynamics model that integrates economic growth, sectoral energy consumption, and CO_2 emissions to explore possible trajectories of Ecuador's energy system up to 2050. The model enables the evaluation of different policy scenarios and provides insights into the potential effects of energy transition strategies on future emissions.

2. Materials and Methods

System dynamics models can be developed through user-friendly interfaces. These model development procedures are based on a visualization process that enables modelers to conceptualize, document, simulate, and analyze dynamic systems [41]. In essence, the system dynamics approach seeks to represent problems from a dynamic perspective.

Three scenarios were developed. The first, the Business-as-Usual (BAU) scenario, represents the continuation of current system conditions without additional policy intervention. The second, ESCN1, is an optimistic national policy scenario that incorporates government policies and official projections. The third, ESCN2, is a regional or global scenario based on broader trends observed in countries across the region and worldwide.

The study develops a system dynamics model to estimate CO_2 emissions by Ecuador in 2050. It aims to examine the relationships among CO_2 emissions over time, energy consumption, and Ecuador's economic growth. The main variables determining CO_2 emissions are economic growth and energy consumption.

The case study method enables the investigation of real-life phenomena through detailed contextual analysis of a limited number of events or conditions and their interrelationships [42]. It is also defined as an empirical research approach for investigating a contemporary phenomenon within its real-life context [43].

The model's main hypothesis is that CO_2 emissions in Ecuador are not an isolated phenomenon, but rather the result of a positive feedback loop between sectoral energy demand and economic growth (GDP). It assumes that, under business-as-usual conditions, economic growth leads to higher energy demand. This demand, largely met through fossil fuels with fixed emission factors, results in a cumulative increase in emissions. In contrast, intervention through energy efficiency measures and energy transition policies operates as a balancing mechanism aimed at decoupling GDP growth from carbon intensity.

The model is structured around the interaction of three key subsystems: Economic Growth, Final Energy Demand, and CO_2 Emissions.

- **Economic Subsystem:** Determines the pace of the system through capital accumulation and production, represented by GDP.
- **Demand Subsystem:** Translates economic activity into sectoral energy requirements (e.g., transport, industry, and residential use), as determined by energy intensity and technological improvements.
- **Emissions Subsystem:** Represents the environmental impact associated with the consumption of different energy sources by applying specific emission factors.

2.1. Scenario construction

Scenario planning is a technique that, rather than seeking prediction, offers alternative ways of thinking about the future based on plausible possibilities [44,45]. This approach enables the exploration of a range of alternative futures. Scenario construction can also be regarded as a subset of strategic forecasting, defined as the development of multiple possible futures to support strategy [46, 47].

This process is based on assumptions about how the future might unfold, including the directions in which certain trends may evolve, which developments might remain constant, and which might change over time. Scenarios describe pathways toward possible futures [48]. They reflect different assumptions about how current trends may develop, how critical uncertainties may play out, and what new factors may emerge.

A series of scenarios was developed to identify trends in energy intensity and CO_2 emissions associated with final energy consumption in Ecuador. The scenarios necessarily incorporate subjective elements and remain open to different interpretations. Their formulation is essential for anticipating the evolution of the main variables, informing energy policy, and projecting future energy consumption patterns and CO_2 mitigation pathways.

For research purposes, three scenarios were proposed. The first, BAU, represents the continuation of current system conditions under unchanged assumptions. ESCN1 considers the policies proposed by the national government for future projections. ESCN2 reflects global trends observed in industrialized countries.

Scenario 1 (BAU) represents the continuation of existing conditions. It projects the current trends identified at the national level, assuming that past trends will persist and that no new policies affecting energy production and consumption will be implemented.

Scenario 2 (ESCN1) considers the government plans and strategies established in Ecuador for the coming years regarding energy production and consumption. The following documents are taken into account: National Energy Agenda 2016 – 2040 [49], National Energy Balance 2013 – 2017 [50–55], National Energy Efficiency Plan 2016 – 2035 [56], Electricity Master Plan 2016 – 2025 [57], Electrification Master Plan 2013 – 2022 [58], Analysis of R & D & I opportunities in Energy Efficiency and Renewable Energies in Ecuador [59], National Climate Change Strategy of Ecuador 2012 – 2025 [60], Sustainable Energy for All: Rapid Assessment Gap Analysis Ecuador [61], and Ecuador Renewable Energy [62].

Scenario 3 (ESCN2) considers the environmental dimension of sustainable development goals, global environmental governance, multilateral environmental agreements, and global macroeconomic perspectives for addressing climate change and its impacts, as well as transition plans related to clean energy and energy efficiency. The scenario also draws on projections and trends reported by organizations such as the Intergovernmental Panel on Climate Change (IPCC), [63–65] the International Energy Agency (IEA) [2], [66–71] and BP [11], among others.

2.2. Modeling and simulation

The proposed system dynamics model was simulated using Vensim, a modeling tool for building, simulating, and analyzing dynamic systems with causal loop and stock-and-flow diagrams. This model estimates Ecuador's energy consumption, economic growth, and CO_2 emissions up to 2050, considering the country's conventional energy resources. It also examines the impact of economic growth on energy consumption and CO_2 emissions. Figure 5 presents the flow diagram of the economic-energy-CO_2 emissions system, illustrating these interactions. CO_2 emissions result from final energy demand across Ecuador's economic sectors.

The model integrates three subsystems: economic growth, final energy demand, and CO_2 emissions. Economic activity drives the evolution of energy consumption across different sectors of the economy, while emissions result from the use of energy carriers associated with specific emission factors. At the macro level, economic growth is represented by the evolution of gross domestic product (GDP), which follows an annual growth rate defined for each scenario:

$$GDP_t = GDP_{t-1}(1 + g_t) \tag{1}$$

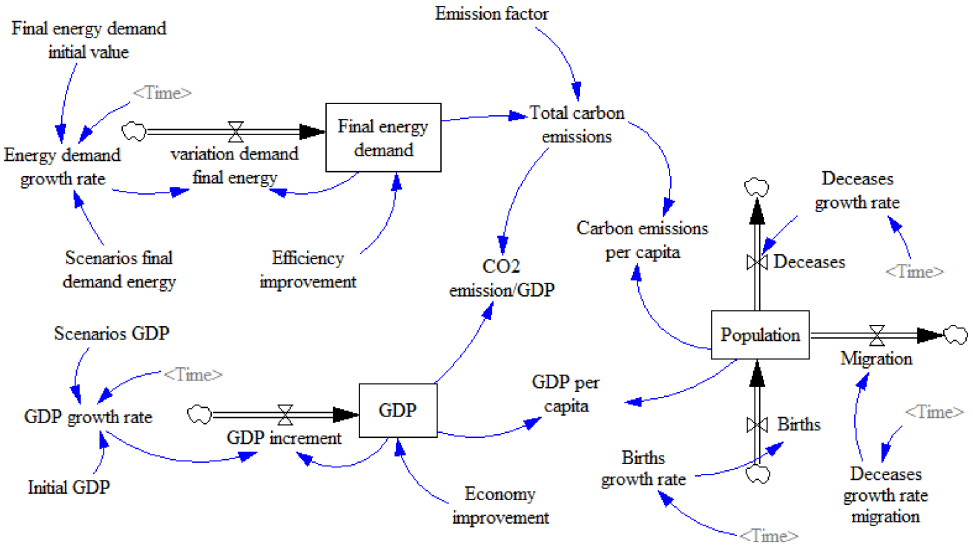

Figure 5. Economic – energy - carbon emissions system flow diagram in Ecuador.

where GDP_t represents the gross domestic product in year t, and g_t is the annual economic growth rate.

Final energy demand is estimated as the aggregate of sectoral energy consumption across the main economic sectors considered in the model:

$$FED_t = \sum_{s=1}^{n} ED_{s,t} \tag{2}$$

where FED_t denotes the total final energy demand, and $ED_{s,t}$ represents the energy demand of sector s in year t.

Sectoral energy demand is assumed to depend on the level of economic activity and the corresponding energy intensity:

$$ED_{s,t} = GDP_t \cdot EI_{s,t} \tag{3}$$

where $EI_{s,t}$ represents the energy intensity of sector s, expressed as the amount of energy required per unit of economic output.

To represent improvements in energy efficiency and technological change, sectoral energy intensity evolves over time according to:

$$EI_{s,t} = EI_{s,t-1}(1 - \eta_s) \tag{4}$$

where η_s represents the annual rate of improvement in energy efficiency for sector s.

CO_2 emissions are estimated from energy consumption by applying the emission factors associated with each energy carrier:

$$CO2_t = \sum_{i=1}^{m} EC_{i,t} \cdot EF_i \tag{5}$$

where $EC_{i,t}$ represents the consumption of energy carrier i in year t, and EF_I is the corresponding emission factor.

Within the system dynamics framework implemented in Vensim, these relationships interact through feedback mechanisms linking economic activity, energy demand, and emissions. The three scenarios analyzed in this study, BAU, ESCN1, and ESCN2, modify key parameters, such as economic growth rates, improvements in energy efficiency, and the composition of the energy mix, to simulate alternative future trajectories of Ecuador's energy system up to 2050.

2.3. Model validation

Validation is the overall process of comparing the model's behavior with that of the real system [72]. No model exactly matches the system under study, because all models are, to some extent, simplifications of the systems they represent [73]. The quality of a study conducted using a simulation model depends largely on its validation [74]; accordingly, verification and validation are among the key stages in simulation development [75]. Validation remains an essential yet controversial and unresolved aspect of the modeling methodology [76]. Social scientists acknowledge the impossibility of absolute validation, the provisional nature of all models, and the need for a more eclectic and diverse set of tests [77].

System dynamics modelers are generally more concerned with dynamic trends than with the specific values of system variables in particular years. In practice, the usefulness of a model is a central concern. Confidence is often regarded as the most appropriate criterion for assessing model behavior, since there is no absolute proof that a model can fully represent reality.

System dynamics models are considered valid when they can be used with confidence [78].

After calibration using the original system data set, the model undergoes a final validation based on a second data set. The validation of a system dynamics model comprises two broad components: structural validation and behavioral validation. Structural validation involves establishing that the relationships used in the model adequately represent the real-world relationships relevant to the purpose of the study. Behavioral validation consists of demonstrating that the model's behavior is sufficiently close to the observed behavior [79].

The model was initially validated by comparison with official data for the 2000–2015 period. Figure 6(a) presents the comparison between simulated and historical energy demand across the consumption sectors responsible for CO_2 emissions in Ecuador. Figure 6(b) presents the comparison between simulated and historical CO_2 emissions. These results indicate that the model is capable of reproducing the structure of the real system and generating meaningful projections. The model also provides a useful basis for designing new policies to improve the system's future behavior.

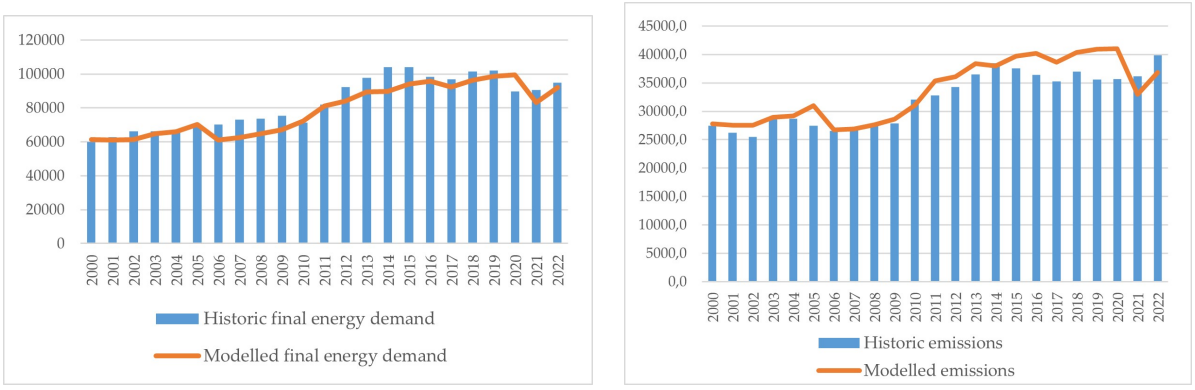

(a) (b)

Figure 6. (a) Historical and simulated final energy demand; (b) historical and simulated CO_2 emissions in Ecuador, 2000 – 2022.

Statistical validation was performed using two methods. The first was the AME method, which measures the average deviation between empirical data and simulated data. It can be expressed mathematically as follows:

$$AME(\%) = \frac{D_s - D_e}{De} x100 \tag{6}$$

where AME represents the Average Mean Error, D_s denotes the simulated data, and D_e is the empirical data.

The second validation method involved calculating the mean absolute percentage error (MAPE), defined as follows:

$$MAPE(\%) = \frac{1}{n} \sum \left| \frac{(A_t - F_t)}{A_t} \right| x100 \tag{7}$$

where MAPE denotes the mean absolute percentage error, A_t, F_t and n represent the real data, the calculated values, and the number of data, respectively.

Table 1 presents the values obtained using the AME and MAPE methods. These results indicate the robustness of the model. It should be noted that, in this study, CO_2 emissions are assumed to result from the combustion of fossil fuels consumed by Ecuador's six economic sectors.

In addition to the graphical comparison of simulated and historical data, model validation included the calculation of the Absolute Percentage Error (APE) and the Mean Absolute Percentage Error (MAPE). These indicators provide quantitative measures of the deviation between simulated and observed values. In energy system modeling, MAPE values of approximately 10% to 15% are commonly considered acceptable for medium- and long-term projections, particularly when the model's objective is to reproduce system trends rather than exact annual observations. In this case, the error values obtained fall within this range, indicating that the model adequately captures the historical evolution of energy demand and emissions in Ecuador.

System dynamics models are primarily designed to reproduce the structural behavior of complex systems rather than to generate probabilistic forecasts. For this reason, validation is typically based on structural consistency tests and the reproduction of historical trends, rather than on statistical confidence intervals.

Table 1. Model validation results

	Energy demand				CO_2 emissions			
Year	**Real Data (KBOE)**	**Simulated (KBOE)**	**AME (%)**	**MAPE (%)**	**Real Data (Megatonnes CO_2)**	**Simulated (Megatonnes CO_2)**	**AME (%)**	**MAPE (%)**
2000	59911	61209	2.12	0.022	27477.0	27750.6	0.99	0.01
2001	62816	61126	-2.76	0.027	26299.0	27570.9	4.87	0.05
2002	66311	61357	-8.07	0.075	25480.0	27540.2	7.48	0.08
2003	66119	64838	-1.98	0.019	28601.0	28935.9	1.14	0.01
2004	66713	65832	-1.34	0.013	28709.0	29182.3	1.62	0.02
2005	69808	70109	0.43	0.004	27491.0	31021.8	11.38	0.13
2006	70265	60923	-15.33	0.133	26540.0	26690.2	0.56	0.01
2007	72985	62384	-16.99	0.145	27010.0	26918.3	-0.34	0.00
2008	73817	64649	-14.18	0.124	27500.0	27584.1	0.30	0.00
2009	75463	67101	-12.46	0.111	27900.0	28571.8	2.35	0.02
2010	71303	72382	1.49	0.015	32100.0	31038.0	-3.42	0.03
2011	81943	81242	-0.86	0.009	32800.0	35325.4	7.15	0.08
2012	92303	84051	-9.82	0.089	34300.0	36109.7	5.01	0.05
2013	97882	89473	-9.40	0.086	36500.0	38351.0	4.83	0.05
2014	104100	89610	-16.17	0.139	38500.0	37965.0	-1.41	0.01
2015	104084	94155	-10.55	0.095	37600.0	39712.4	5.32	0.06
2016	98353	95656	-2.82	0.027	36400.0	40168.0	9.38	0.10
2017	97023	92386	-5.02	0.048	35300.0	38596.7	8.54	0.09
2018	101537	96435	-5.29	0.050	37000.0	40336.9	8.27	0.09
2019	102133	98697	-3.48	0.034	35600.0	40899.1	12.96	0.15
2020	89705	99444	9.79	0.109	35683.0	40991.7	12.95	0.15
2021	90719	83134	-9.12	0.084	36180.0	32950.5	-9.80	0.09
2022	94957	92046	-3.16	0.031	39852.0	36792.1	-8.32	0.08
				9.31				8.56

2.4. Sensitivity analysis

System dynamics has long featured a sophisticated, flexible approach to testing. The sensitivity of results must be evaluated with respect to uncertainty in assumptions, whether parameters are estimated critically or by statistical means [80]. In the early 1990s, William Nordhaus developed the DICE (Dynamic Integrated Climate Economy) model, which was one of the first and most influential of the so-called "Integrated Climate Economy Models" [81, 82].

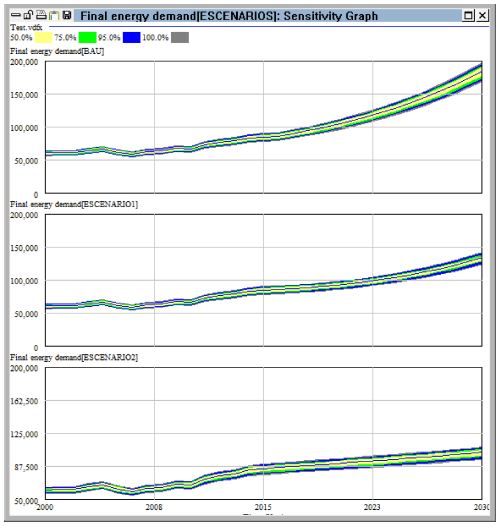

Figure 7. Energy demand scenarios for the sensitivity analysis, generated with Vensim.

The sensitivity analysis is performed to identify the system's behavior as key parameters vary. Since improvements in energy efficiency and economic growth significantly affect energy consumption and CO_2 emissions, three scenarios are designed to test the model's sensitivity figure 7.

3. Results and Discussion

3.1. Final energy demand

The model projects divergent behaviors depending on the stringency of the policies implemented [4], [83], as shown in Figure 8:

- **Business-as-usual scenario:** Demand is projected to increase by 1.21 times relative to the base year, with oil and natural gas, used primarily for transport and energy production, remaining the dominant energy sources. The system's vulnerability is reflected in its reliance on imported hydrocarbons to compensate for infrastructure deficit.

- **In contrast to the business-as-usual scenario, National Policies Scenario 1 (NSP1)**: anticipates a 2.23-fold increase in demand despite official planning. Demand growth in the transport and industrial sectors exceeds the benefits of current efficiency policies, suggesting that

existing targets are insufficient to curb energy intensity.

- **Global Trend Scenario 2 (NSP2):** This is the only scenario that achieves a net 10% reduction in demand by 2050. The success of this trajectory lies in the aggressive substitution of fossil fuels with electricity and in efficiency improvements that offset the effects of economic growth.

The gradual decline in the use of fossil fuels, particularly gasoline and diesel, underscores the effectiveness of policies aimed at reducing carbon emissions and promoting clean energy technologies. The steady demand for natural gas and electricity suggests a transition toward these lower-carbon energy sources without a substantial increase in total energy consumption.

In this scenario, government energy policies emphasize a pragmatic strategy that advances both energy efficiency and a diversified energy supply mix. This approach likely includes stricter efficiency standards, support for renewable energy sources, and progress in energy storage and distribution technologies.

In the transport sector, the BAU scenario projects that, by 2050, energy consumption, driven primarily by diesel oil and gasoline, will account for 34% of the national energy consumption matrix relative to the base year, as shown in Figure 8. This sector remains highly inefficient because of its strong dependence on fossil fuels. By comparison, the ESCN1 scenario projects final energy demand at 69% of the sector's base-year level, reflecting significant growth in transport needs and the limited mitigating effect of energy efficiency policies. In contrast, the ESCN2 scenario projects demand at 27% of the base-year level, likely due to more aggressive policies and the adoption of alternative energy sources, resulting in a substantial reduction in fossil fuel dependency and more effective containment of energy demand growth. These results clearly distinguish ESCN1 as reflecting more moderate interventions, whereas ESCN2 represents stronger shifts in policy and technology.

These scenarios illustrate how policy interventions can differ in their impact. ESCN1 suggests that moderate measures may be insufficient to offset rising energy demand. In contrast, ESCN2 indicates that comprehensive strategies could enhance energy efficiency and reduce reliance on fossil fuels in the transport sector by 2050.

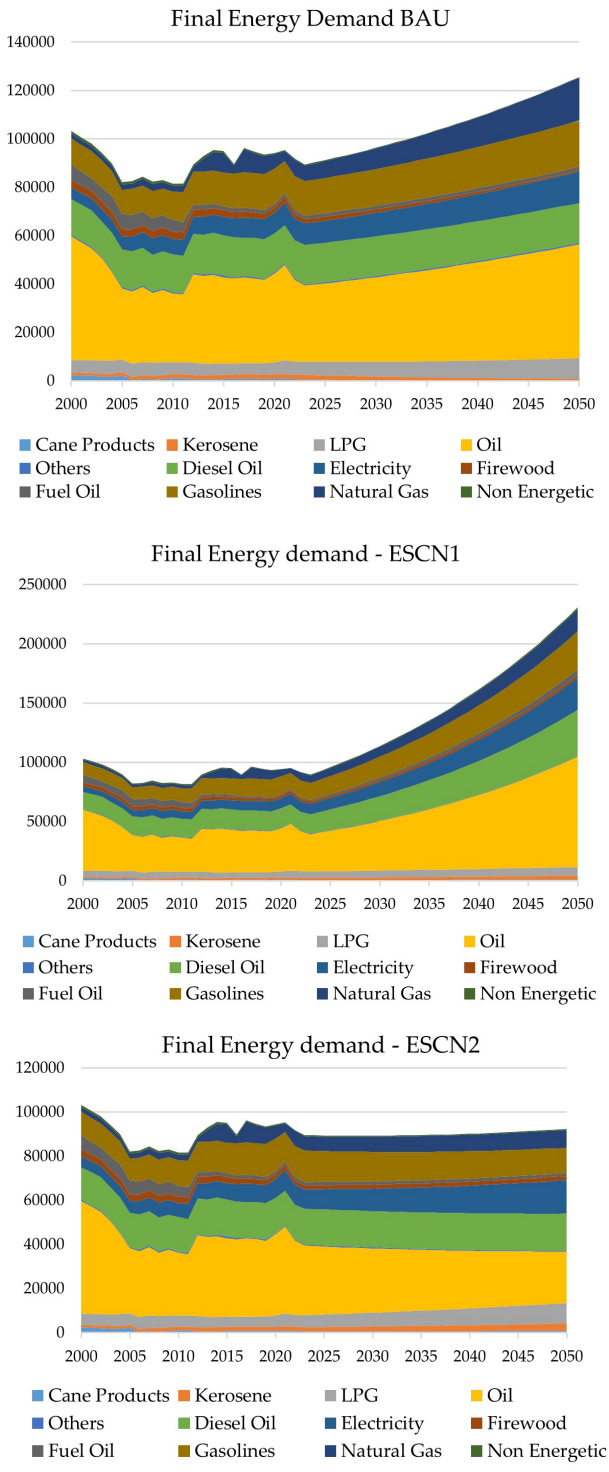

Figure 8. Final energy demand scenarios.

3.2. CO_2 emissions

According to the sectoral analysis, the transport sector is the main source of emissions, accounting for 34% of the total under the business-as-usual scenario, as shown in Figure 9. The emissions projections indicate the following:

- Under ESCN1, emissions increase by 145% as the expected growth in economic activity exceeds the decarbonization rate of the current energy matrix.

- Under ESCN2, emissions decrease by 5%, driven by the adoption of clean generation technologies and compliance with international sustainability standards.

These results indicate that the expansion of the Ecuadorian economy should not be viewed as an impediment, but rather as a driving force for investment in new mitigation technologies and in research and development.

Replacing fossil fuels by harnessing the country's remaining hydroelectric potential appears to be the most viable pathway for reducing emissions from the current 37.10 $MtCO_2$ to levels below 20 $MtCO_2$.

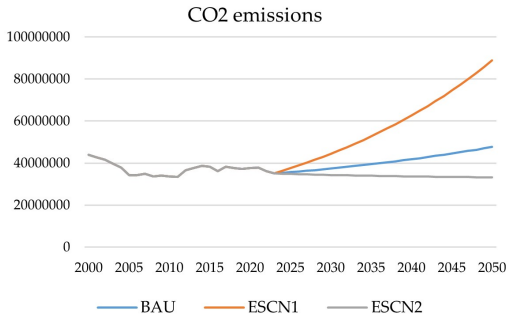

Figure 9. CO_2 emissions ($KTCO_2$)

The results of this study are consistent with previous research indicating a strong relationship among economic growth, energy consumption, and CO_2 emissions. Several studies have shown that, in developing economies, economic expansion is usually accompanied by increased energy demand [84,85], particularly when fossil fuels remain dominant in the energy mix [86]. In the Ecuadorian context, this relationship is especially evident in the transport and industrial sectors, which account for a significant share of final energy consumption.

Similar trends have been reported in studies analyzing energy transition scenarios in Latin America [87–89], where dependence on fossil fuels continues to drive emissions growth despite increasing investments in renewable energy. These findings reinforce the importance of improving energy efficiency and promoting structural changes in the energy system to reduce long-term emissions.

From a policy perspective, the scenario analysis highlights the importance of implementing long-term energy transition strategies. The results suggest that maintaining current trends under the BAU scenario could lead to a sustained increase in both energy demand and CO_2 emissions. In contrast, scenarios incorporating stronger policy interventions and technological improvements indicate a potential stabilization or reduction of emissions over time [90].

These results support the need for policies aimed at increasing the share of renewable energy, improving energy efficiency, and reducing dependence on fossil fuels in key sectors of the Ecuadorian economy.

These results support the need for policies aimed at increasing the share of renewable energy, improving energy efficiency, and reducing dependence on fossil fuels in key sectors of the Ecuadorian economy.

Despite the usefulness of the proposed model for exploring long-term trends, several limitations should be acknowledged. First, the model relies on historical data and assumptions regarding economic growth, energy intensity, and policy implementation, all of which introduce uncertainty in long-term projections. Second, the model represents the energy system at an aggregated level and does not explicitly account for technological diffusion processes or behavioral changes in energy consumption. Finally, the scenarios analyzed are based on simplified assumptions about future policy and economic conditions, which may unfold differently in practice.

3.3. Discussion and Limitations

Although the systems dynamics analysis employed in this study provides a useful framework for examining the long-term interactions among energy demand, economic growth, and CO_2 emissions, several limitations associated with the scenario assumptions should be considered.

The scenarios are based on simplified assumptions regarding future rates of economic growth, changes in energy intensity, and shifts in the energy mix. These variables are influenced by various external factors, such as international energy prices, regulatory changes, technological innovation, and geopolitical conditions.

Structural changes in the economy, such as the digitization of industrial processes, the widespread adoption of low-carbon technologies, and rapid electrification, may alter these relationships over time. In particular, disruptive technological change may reduce energy intensity more rapidly than assumed in the present simulations. Policy-oriented scenarios assume that international agreements and national sustainability strategies will be implemented within established time frames. In practice, however, the effectiveness of climate and energy policies depends on institutional capacity, social acceptance, and the availability of investment, which may result in the partial or delayed implementation of measures.

The model represents Ecuador's energy system at an aggregate level and therefore does not explicitly

capture micro-level dynamics, such as changes in energy use, technological diffusion processes, or regional inequalities in energy access and infrastructure development. These factors may influence the actual evolution of energy demand and emissions.

Finally, uncertainties associated with climate variability were not explicitly modeled in the energy supply subsystem. Extreme weather events, such as prolonged droughts, may alter electricity availability and indirectly affect fossil fuel use and emissions due to the significant role of hydropower in Ecuador's electricity generation.

Despite these limitations, the model provides a useful analytical tool for investigating long-term trends and examining the potential consequences of different policy pathways. Therefore, the results should not be interpreted as definitive predictions of the future development of Ecuador's energy system, but rather as indicators that support strategic planning.

4. Conclusions

Economic projections alone do not offer a favorable pathway for reducing emissions in Ecuador; therefore, targeted public policies are required to improve the quality of life while advancing environmental sustainability. At the same time, the scenario analysis suggests that, as renewable energy use increases alongside continued economic growth, the relationship between these variables becomes less tightly coupled over time than it has been historically.

Investment in scientific research focused on emerging technologies and mitigation strategies must become a state priority to ensure that economic growth generates positive environmental outcomes. This effort should include strengthening local capacities in smart grid management and demand digitalization, thereby enabling more efficient load management and reducing pressure on existing infrastructure.

Since the transport sector is the largest source of emissions and accounts for 34% of the consumption matrix under the projected trend, it is necessary to move beyond a passive policy of technological substitution toward one that actively promotes the electrification of public and heavy freight transport. The findings indicate that energy efficiency alone will not be sufficient to accommodate the sector's projected growth. Therefore, tax incentives should be implemented to directly support freight infrastructure, while fossil fuel subsidies should be gradually phased out and the corresponding resources reallocated to technological innovation funds.

The results also show that energy intensity in Ecuador remains high. Strengthening the National Energy Efficiency Plan through binding regulations for industry is therefore essential. In this regard, mandatory energy audits and the adoption of international standards are required. The ultimate objective should be genuine decoupling, allowing GDP to grow while energy demand stabilizes or declines, as observed in the ESCN2 scenario trajectories.

The vulnerability of the system to climate-related events, such as droughts that adversely affect hydropower generation, also highlights the need for rapid diversification toward non-conventional renewable energy sources, particularly wind and solar photovoltaic energy. The model indicates that increasing the combined share of hydropower and renewable energy to between 50% and 70% could significantly reduce emissions to a range of 15.03 to 27.36 MtCO2. To support this transition, specific auctions for microgrids and energy storage projects should be introduced to ensure supply stability without relying on backup thermal power plants fueled by diesel or fuel oil.

Contributor Roles

- **Flavio Arroyo-Morocho:** Conceptualization, data processing, research.
- **Dely Bravo-Donoso:** Conceptualization, data processing, research.
- **Abel Remache-Coyago:** Conceptualization, formal analysis, data curation.
- **Tatiana Freire-Rosero:** Visualization, writing – review and editing.

References

[1] El Mundo. (2016, Jan.) Alerta mundial por la contaminación en las ciudades de todo el planeta. ElMundo.es. Accessed: May 19, 2026. [Online]. Available: https://upsalesiana.ec/ing36ar5r1

[2] International Energy Agency (IEA), "CO_2 emissions in 2023," International Energy Agency, Paris, France, Tech. Rep., 2024, accessed: May 19, 2026. [Online]. Available: https://upsalesiana.ec/ing36ar5r2

[3] P. K. Wesseh and B. Lin, "Energy consumption, fuel substitution, technical change, and economic growth: Implications for CO_2 mitigation in Egypt," *Energy Policy*, vol. 117, pp. 340–347, 2018. [Online]. Available: https://doi.org/10.1016/j.enpol.2018.03.022

[4] M. Mirzaei and M. Bekri, "Energy consumption and CO_2 emissions in Iran, 2025," *Environmental Research*, vol. 154, pp. 345–351, Apr. 2017. [Online]. Available: https://doi.org/10.1016/j.envres.2017.01.023

[5] J. Emmerling, P. Andreoni, and M. Tavoni, "Global inequality consequences of climate policies when accounting for avoided climate impacts," *Cell Reports Sustainability*, vol. 1, no. 1, p. 100008, Jan. 2024. [Online]. Available: https://doi.org/10.1016/j.crsus.2023.100008

[6] S. Baik, J. F. Hines, and J. Sim, "Racial disparities in the energy burden beyond socio-economic inequality," *Energy Economics*, vol. 127, p. 107098, Nov. 2023. [Online]. Available: https://doi.org/10.1016/j.eneco.2023.107098

[7] M. K. Ardakani and S. M. Seyedaliakbar, "Impact of energy consumption and economic growth on CO_2 emission using multivariate regression," *Energy Strategy Reviews*, vol. 26, p. 100428, Nov. 2019. [Online]. Available: https://doi.org/10.1016/j.esr.2019.100428

[8] F. Arroyo and L. J. Miguel, "Analysis of energy demand scenarios in Ecuador: National government policy perspectives and global trend to reduce CO_2 emissions," *International Journal of Energy Economics and Policy*, vol. 9, no. 2, Mar. 2019. [Online]. Available: https://doi.org/10.32479/ijeep.7132

[9] International Energy Agency (IEA), "Renewables 2023: Analysis and forecast to 2028," International Energy Agency, Paris, France, Tech. Rep., 2024, accessed: May 19, 2026. [Online]. Available: https://upsalesiana.ec/ing36ar5r9

[10] Energy Institute, *Statistical Review of World Energy 2024*, 73rd ed. London, United Kingdom: Energy Institute, 2024, accessed: May 19, 2026. [Online]. Available: https://upsalesiana.ec/ing36ar5r10

[11] BP, *bp Statistical Review of World Energy 2022*, 71st ed. Whitehouse Associates, London, Jun. 2022, accessed: 2026-05-19. [Online]. Available: https://upsalesiana.ec/ing36ar5r73

[12] A. O. Acheampong and E. E. O. Opoku, "Environmental degradation and economic growth: Investigating linkages and potential pathways," *Energy Economics*, vol. 123, p. 106734, 2023. [Online]. Available: https://doi.org/10.1016/j.eneco.2023.106734

[13] F. R. Arroyo M. and L. J. Miguel, "The trends of the energy intensity and CO_2 emissions related to final energy consumption in Ecuador: Scenarios of national and worldwide strategies," *Sustainability*, vol. 12, no. 1, p. 20, Dec. 2019. [Online]. Available: https://doi.org/10.3390/su12010020

[14] Q. Li, W. Zhang, H. Li, and P. He, "CO_2 emission trends of China's primary aluminum industry: A scenario analysis using system dynamics model," *Energy Policy*, vol. 105, pp. 225–235, 2017. [Online]. Available: https://doi.org/10.1016/j.enpol.2017.02.046

[15] B. Muhammad, "Energy consumption, CO_2 emissions and economic growth in developed, emerging and Middle East and North Africa countries," *Energy*, vol. 179, pp. 232–245, 2019. [Online]. Available: https://doi.org/10.1016/j.energy.2019.03.126

[16] W. Xia, N. Apergis, M. F. Bashir, S. Ghosh, B. Doğan, and U. Shahzad, "Investigating the role of globalization, and energy consumption for environmental externalities: Empirical evidence from developed and developing economies," *Renewable Energy*, vol. 183, pp. 219–228, Jan. 2022. [Online]. Available: https://doi.org/10.1016/j.renene.2021.10.084

[17] M. A. González-Álvarez and A. Montañés, "CO_2 emissions, energy consumption, and economic growth: Determining the stability of the 3E relationship," *Economic Modelling*, vol. 121, p. 106195, Apr. 2023. [Online]. Available: https://doi.org/10.1016/j.econmod.2023.106195

[18] F. Ozturk, "Energy consumption–GDP causality in MENA countries," *Energy Sources, Part B: Economics, Planning, and Policy*, vol. 12, no. 3, pp. 231–236, Mar. 2017. [Online]. Available: https://doi.org/10.1080/15567249.2015.1072597

[19] E. Cifci and M. E. Oliver, "Reassessing the links between GHG emissions, economic growth, and the UNFCCC: A difference-in-differences approach," *Sustainability*, vol. 10, no. 2, p. 334, Jan. 2018. [Online]. Available: https://doi.org/10.3390/su10020334

[20] K. Saidi and S. Hammami, "The impact of CO_2 emissions and economic growth on energy consumption in 58 countries," *Energy Reports*, vol. 1, pp. 62–70, Nov. 2015. [Online]. Available: https://doi.org/10.1016/j.egyr.2015.01.003

[21] M. S. Shabbir, M. Shahbaz, and M. Zeshan, "Renewable and nonrenewable energy consumption, real GDP and CO_2 emissions nexus: A structural var approach in Pakistan," *Bulletin of Energy Economics (BEE)*, vol. 2, no. 3, pp. 91–105, 2014, accessed: May 19, 2026. [Online]. Available: https://upsalesiana.ec/ing36ar5r21

[22] M. Sterpu, G. Soava, and A. Mehedintu, "Impact of economic growth and energy consumption on greenhouse gas emissions: Testing environmental

curves hypotheses on EU countries," *Sustainability*, vol. 10, no. 9, p. 3327, 2018. [Online]. Available: http://doi.org/10.3390/su10093327

[23] Comisión Económica para América Latina y el Caribe (CEPAL), "La economía del cambio climático en el Ecuador, 2012," CEPAL, Santiago, Chile, Tech. Rep. LC/W.560, 2013, accessed: May 19, 2026. [Online]. Available: https://upsalesiana.ec/ing36ar5r23

[24] A. R. López, "Carbon emissions, energy consumption and sustainable development in Ecuador (1980–2025): System dynamics modelling, decomposition analysis and the environmental kuznets curve," Doctoral thesis, Universidad de Huelva, Huelva, Spain, 2014, accessed: May 19, 2026. [Online]. Available: https://upsalesiana.ec/ing36ar5r24

[25] R. A. Begum, K. Sohag, S. M. S. Abdullah, and M. Jaafar, "CO_2 emissions, energy consumption, economic and population growth in Malaysia," *Renewable and Sustainable Energy Reviews*, vol. 41, pp. 594–601, Jan. 2015. [Online]. Available: http://doi.org/10.1016/j.rser.2014.07.205

[26] L. J. Esso and Y. Keho, "Energy consumption, economic growth and carbon emissions: Cointegration and causality evidence from selected African countries," *Energy*, vol. 114, pp. 492–497, Nov. 2016. [Online]. Available: http://doi.org/10.1016/j.energy.2016.08.010

[27] J. C. Cárdenas Herrera, "Estudio de la reducción de emisiones de carbono en el Ecuador," Master's thesis, Escuela Politécnica Nacional, Quito, Ecuador, 2014, Repositorio Digital EPN. [Online]. Available: https://upsalesiana.ec/ing36ar5r27

[28] B. Lin, O. E. Omoju, and J. U. Okonkwo, "Impact of industrialisation on CO_2 emissions in Nigeria," *Renewable and Sustainable Energy Reviews*, vol. 52, pp. 1228–1239, Dec. 2015. [Online]. Available: http://doi.org/10.1016/j.rser.2015.07.164

[29] G. Mavromatidis, K. Orehounig, P. Richner, and J. Carmeliet, "A strategy for reducing CO_2 emissions from buildings with the Kaya identity – a Swiss energy system analysis and a case study," *Energy Policy*, vol. 88, pp. 343–354, Jan. 2016. [Online]. Available: http://doi.org/10.1016/j.enpol.2015.10.037

[30] X. Chen, G. Wang, X. Guo, and J. Fu, "An analysis based on SD model for energy-related CO_2 mitigation in the Chinese household sector," *Energies*, vol. 9, no. 12, p. 1062, Dec. 2016. [Online]. Available: http://doi.org/10.3390/en9121062

[31] A. Mardani, D. Streimikiene, F. Cavallaro, N. Loganathan, and M. Khoshnoudi, "Carbon dioxide (CO_2) emissions and economic growth: A systematic review of two decades of research from 1995 to 2017," *Science of The Total Environment*, vol. 649, pp. 31–49, Feb. 2019. [Online]. Available: http://doi.org/10.1016/j.scitotenv.2018.08.229

[32] J. Zhou, B. Jin, S. Du, and P. Zhang, "Scenario analysis of carbon emissions of Beijing-Tianjin-Hebei," *Energies*, vol. 11, no. 6, p. 1489, 2018. [Online]. Available: http://doi.org/10.3390/en11061489

[33] R. Arango-Miranda, R. Hausler, R. Romero-López, M. Glaus, and S. P. Ibarra-Zavaleta, "Carbon dioxide emissions, energy consumption and economic growth: A comparative empirical study of selected developed and developing countries. "The role of exergy"," *Energies*, vol. 11, no. 10, p. 2668, Oct. 2018. [Online]. Available: http://doi.org/10.3390/en11102668

[34] N. Antonakakis, I. Chatziantoniou, and G. Filis, "Energy consumption, CO_2 emissions, and economic growth: An ethical dilemma," *Renewable and Sustainable Energy Reviews*, vol. 68, pp. 808–824, Feb. 2017. [Online]. Available: http://doi.org/10.1016/j.rser.2016.09.105

[35] F. M. Mirza and A. Kanwal, "Energy consumption, carbon emissions and economic growth in Pakistan: Dynamic causality analysis," *Renewable and Sustainable Energy Reviews*, vol. 72, pp. 1233–1240, May 2017. [Online]. Available: http://doi.org/10.1016/j.rser.2016.10.081

[36] A. Giri and G. Mohapatra, "Energy consumption, economic growth and CO_2 emissions: Empirical evidences from India," *The Empirical Econometrics and Quantitative Economics*, vol. 4, pp. 17–32, 01 2015. [Online]. Available: https://upsalesiana.ec/ing36ar5r36

[37] P. Stamatiou and N. Dritsakis, *Dynamic Modeling of Causal Relationship Between Energy Consumption, CO_2 Emissions, and Economic Growth in Italy.* Springer International Publishing, 2017, pp. 99–109. [Online]. Available: https://doi.org/10.1007/978-3-319-48454-9_8

[38] S. H. Kang, F. Islam, and A. Kumar Tiwari, "The dynamic relationships among CO_2 emissions, renewable and non-renewable energy sources, and economic growth in India: Evidence from time-varying bayesian VAR model," *Structural Change and Economic Dynamics*, vol. 50, pp. 90–101, 2019. [Online]. Available: https://doi.org/10.1016/j.strueco.2019.05.006

[39] P. R. Tayupanta Caiza, "Análisis del impacto de las políticas energéticas relacionadas con el cambio de la matriz energética del Ecuador en el período 2007–2014 y sus perspectivas al 2020," Tesis de Maestría, Escuela Politécnica Nacional, Quito, Ecuador, 2017, consultado: 2026-05-19. [Online]. Available: https://upsalesiana.ec/ing36ar5r39

[40] M. Peláez-Samaniego, M. García-Pérez, L. Cortez, J. Oscullo, and G. Olmedo, "Energy sector in Ecuador: Current status," *Energy Policy*, vol. 35, no. 8, pp. 4177–4189, Aug. 2007. [Online]. Available: https://doi.org/10.1016/j.enpol.2007.02.025

[41] B. Dyson and N.-B. Chang, "Forecasting municipal solid waste generation in a fast-growing urban region with system dynamics modeling," *Waste Management*, vol. 25, no. 7, pp. 669–679, Jan. 2005. [Online]. Available: https://doi.org/10.1016/j.wasman.2004.10.005

[42] H. V. Coombs, "Case study research defined [White paper]," *Jurnal Kemanusiaan*, 2022. [Online]. Available: https://doi.org/10.5281/zenodo.7604301

[43] R. K. Yin, *Case Study Research and Applications: Design and Methods*, 6th ed. Thousand Oaks, CA, USA: SAGE Publications, 2018, accessed: 2026-05-19. [Online]. Available: https://upsalesiana.ec/ing36ar5r43

[44] J. Derbyshire and G. Wright, "Augmenting the intuitive logics scenario planning method for a more comprehensive analysis of causation," *International Journal of Forecasting*, vol. 33, no. 1, pp. 254–266, Jan. 2017. [Online]. Available: https://doi.org/10.1016/j.ijforecast.2016.01.004

[45] D. Sarpong and J. A. Amoah, "Scenario planning: 'ways of knowing', methodologies and shifting conceptual landscape," *International Journal of Foresight and Innovation Policy*, vol. 10, no. 2/3/4, p. 75, 2015. [Online]. Available: https://doi.org/10.1504/ijfip.2015.074397

[46] H. J. Duus, "Strategic scenario construction made easy," *International Journal of Foresight and Innovation Policy*, vol. 11, no. 1/2/3, p. 167, 2016. [Online]. Available: https://doi.org/10.1504/IJFIP.2016.078349

[47] M. Amer, T. U. Daim, and A. Jetter, "A review of scenario planning," *Futures*, vol. 46, pp. 23–40, Feb. 2013. [Online]. Available: http://doi.org/10.1016/j.futures.2012.10.003

[48] UN Environment, *Global Environment Outlook – GEO-6: Healthy Planet, Healthy People*. Cambridge University Press, May 2019. [Online]. Available: http://doi.org/10.1017/9781108627146

[49] MCSE, "Agenda energética nacional 2016–2040," Ministerio Coordinador de Sectores Estratégicos, Quito, Ecuador, Tech. Rep., 2016, consultado: 2026-05-19. [Online]. Available: https://upsalesiana.ec/ing36ar5r49

[50] ——, "Balance energético nacional 2013," Ministerio Coordinador de Sectores Estratégicos, Quito, Ecuador, Tech. Rep., 2013, consultado: 2026-05-19. [Online]. Available: https://upsalesiana.ec/ing36ar5r50

[51] ——, "Balance energético nacional 2014," Ministerio Coordinador de Sectores Estratégicos, Quito, Ecuador, Tech. Rep., 2014, consultado: 2026-05-19. [Online]. Available: https://upsalesiana.ec/ing36ar5r51

[52] Coordinating Ministry of Strategic Sectors, "National energy balance 2015," Coordinating Ministry of Strategic Sectors, Quito, Ecuador, Tech. Rep., 2015, accessed: 2026-05-19. [Online]. Available: https://upsalesiana.ec/ing36ar5r52

[53] MCSE, "Balance energético nacional 2016," Ministerio Coordinador de Sectores Estratégicos, Quito, Ecuador, Tech. Rep., 2016, accessed: 2026-05-19. [Online]. Available: https://upsalesiana.ec/ing36ar5r53

[54] MICSE, "National energy balance 2017," Coordinating Ministry of Strategic Sectors (MICSE), Quito, Ecuador, Tech. Rep., 2017, referenced in peer-reviewed studies on Ecuadorian energy planning. [Online]. Available: https://upsalesiana.ec/ing36ar5r54

[55] Ministry of Energy and Non-Renewable Natural Resources, "National energy balance 2017," Ministry of Energy and Non-Renewable Natural Resources, Quito, Ecuador, Tech. Rep., 2018, referenced in peer-reviewed energy studies on Ecuador. [Online]. Available: https://upsalesiana.ec/ing36ar5r55

[56] Minister of Electricity and Renewable Energy, "National energy efficiency plan 2016–2035," Minister of Electricity and Renewable Energy, Quito, Ecuador, Tech. Rep., 2017, accessed: 2026-05-19. [Online]. Available: https://upsalesiana.ec/ing36ar5r56

[57] MEER, "Plan maestro de electricidad 2016–2025," Ministerio de Electricidad y Energía Renovable, Quito, Ecuador, Tech. Rep., 2017, accessed: 2026-05-19. [Online]. Available: https://upsalesiana.ec/ing36ar5r57

[58] CONELEC, "Plan maestro de electrificación 2013–2022," National Electricity Council, Quito, Ecuador, Tech. Rep., 2013, accessed: 2026-05-19. [Online]. Available: https://upsalesiana.ec/ing36ar5r58

[59] INER, "Analysis of r&d&i opportunities in energy efficiency and renewable energies in ecuador," National Institute of Energy Efficiency and Renewable Energies, Quito, Ecuador, Tech. Rep., 2016, referenced in national energy planning studies of Ecuador. [Online]. Available: https://upsalesiana.ec/ing36ar5r59

[60] MAE, *Estrategia Nacional de Cambio Climático del Ecuador: ENCC 2012–2025*. Quito, Ecuador: Ministerio del Ambiente del Ecuador, 2012, accessed: 2026-05-19. [Online]. Available: https://upsalesiana.ec/ing36ar5r60

[61] R. Gomelsky, "Sustainable energy for all: Rapid assessment Gap analysis Ecuador," Ministry of Electricity and Renewable Energy (MEER), Quito, Ecuador, Tech. Rep., 2013, prepared within the Sustainable Energy for All (SE4ALL) initiative. Accessed: 2026-05-19. [Online]. Available: https://upsalesiana.ec/ing36ar5r61

[62] OER-LAC, "Renewable energy case of Ecuador," Organización Latinoamericana de Energía (OLADE), Brasilia, Brazil, Tech. Rep., Aug. 2011, final Report, Accessed: 2026-05-19. [Online]. Available: https://upsalesiana.ec/ing36ar5r62

[63] IPCC, *Global Warming of 1.5°C*. Geneva, Switzerland: World Meteorological Organization, Intergovernmental Panel on Climate Change, 2018, accessed: 2026-05-19. [Online]. Available: https://upsalesiana.ec/ing36ar5r63

[64] C. B. Field, V. Barros, T. F. Stocker, Q. Dahe, D. J. Dokken, K. L. Ebi, M. D. Mastrandrea, K. J. Mach, G.-K. Plattner, S. K. Allen, M. Tignor, and P. M. Midgley, *Managing the Risks of Extreme Events and Disasters to Advance Climate Change Adaptation*. Cambridge, United Kingdom and New York, NY, USA: Cambridge University Press, 2012, accessed: 2026-05-19. [Online]. Available: https://upsalesiana.ec/ing36ar5r65

[65] O. Edenhofer, R. Pichs-Madruga, Y. Sokona, E. Farahani, S. Kadner, K. Seyboth, A. Adler, I. Baum, S. Brunner, P. Eickemeier, B. Kriemann, J. Savolainen, S. Schlömer, C. von Stechow, T. Zwickel, and J. C. Minx, *Climate Change 2014: Mitigation of Climate Change*. Cambridge, United Kingdom and New York, NY, USA: Cambridge University Press, 2014. [Online]. Available: https://upsalesiana.ec/ing36ar5r66

[66] IRENA, "Renewable energy benefits: Measuring the economics," International Renewable Energy Agency (IRENA), Abu Dhabi, United Arab Emirates, Tech. Rep., Jan. 2016, accessed: 2026-05-19. [Online]. Available: https://upsalesiana.ec/ing36ar5r67

[67] IEA, *Energy Efficiency*. OECD, Oct. 2017. [Online]. Available: https://doi.org/10.1787/9789264284234-en

[68] ——, *World Energy Outlook*. Organisation for Economic Co-operation and Development, Nov. 2018. [Online]. Available: https://doi.org/10.1787/weo-2018-en

[69] ——, *Key World Energy Statistics*. Organisation for Economic Co-operation and Development, Oct. 2019. [Online]. Available: https://doi.org/10.1787/71b3ce84-en

[70] ——, *World Energy Balances*. Organisation for Economic Co-operation and Development, 2019. [Online]. Available: https://doi.org/10.1787/3a876031-en

[71] ——, *World Energy Statistics*. Organisation for Economic Co-operation and Development (OECD), 2019. [Online]. Available: https://doi.org/10.1787/2e828dea-en

[72] A. Azhaginiyal and G. Umadevi, "System dynamics simulation modeling of transport, energy and emissions interactions," *Civil Engineering and Architecture*, vol. 2, no. 4, pp. 149–165, Apr. 2014. [Online]. Available: http://doi.org/10.13189/cea.2014.020401

[73] A. Barisa and M. Rosa, "A system dynamics model for CO_2 emission mitigation policy design in road transport sector," *Energy Procedia*, vol. 147, pp. 419–427, Aug. 2018. [Online]. Available: http://doi.org/10.1016/j.egypro.2018.07.112

[74] J. Lemke and M. Małgorzata, "Validation of system dynamics models – a case study," *Journal of Entrepreneurship, Management and Innovation*, vol. 9, no. 2, pp. 45–59, 2013. [Online]. Available: http://doi.org/10.7341/2013923

[75] A. Maciąg, R. Pietroń, and S. Kukla, *Prognozowanie i symulacja w przedsiębiorstwie*, 1st ed. Warszawa: Polskie Wydawnictwo Ekonomiczne (PWE), 2013, accessed: 2026-05-19. [Online]. Available: https://upsalesiana.ec/ing36ar5r77

[76] M. Martis, "Validation of simulation based models: A theoretical outlook," *Electronic Journal of Business Research Methods*, vol. 4, 11 2006. [Online]. Available: https://upsalesiana.ec/ing36ar6r78

[77] J. Sterman, *Business Dynamics, System Thinking and Modeling for a Complex World*. McGraw-Hill Higher Education, 01 2000, vol. 19. [Online]. Available: https://upsalesiana.ec/ing36ar6r79

[78] R. C. a. Shreckengost, "Dynamic simulation models: how valid are they?" *PsycEXTRA Dataset*, 1985. [Online]. Available: http://doi.org/10.1037/e496952006-007

[79] Y. Barlas and K. Kanar, "A dynamic pattern-oriented test for model validation," *Boğaziçi University Research*, 01 1999. [Online]. Available: https://upsalesiana.ec/ing36ar6r81

[80] J. D. Sterman, "All models are wrong: Reflections on becoming a systems scientist," *System Dynamics Review*, vol. 18, no. 4, pp. 501–531, Dec. 2002. [Online]. Available: http://doi.org/10.1002/sdr.261

[81] ——, *Feedback complexity in integrated climate-economy models*. Massachusetts Institute of Technology, 1997. [Online]. Available: https://upsalesiana.ec/ing36ar6r83

[82] L. Režný and V. Bureš, "Energy transition scenarios and their economic impacts in the extended neoclassical model of economic growth," *Sustainability*, vol. 11, no. 13, p. 3644, 2019. [Online]. Available: https://doi.org/10.3390/su11133644

[83] C. Zou, Q. Zhao, G. Zhang, and B. Xiong, "Energy revolution: From a fossil energy era to a new energy era," *Natural Gas Industry B*, vol. 3, no. 1, pp. 1–11, Jan. 2016. [Online]. Available: https://doi.org/10.1016/j.ngib.2016.02.001

[84] F. V. Bekun, M. P. Fumey, M. W. Staniewski, L. Sun, and P. O. Agboola, "Energy intensive growth and the transition pathways: Insights into the role of renewable energy and open market conditions in developing countries," *Energy*, vol. 322, p. 135192, May 2025. [Online]. Available: https://doi.org/10.1016/j.energy.2025.135192

[85] K. Abbass, N. Amin, F. Khan, H. Begum, and H. Song, "Driving sustainability: The nexus of financial development, economic globalization, and renewable energy in fostering a greener future," *Energy & Environment*, Jan. 2025. [Online]. Available: https://doi.org/10.1177/0958305X241305374

[86] W. Zhao, X. Wang, and Y. Yan, "The substitution of fossil fuels for renewables in the electricity mix of China: From the perspectives of generation, capacity, and demand," *Energy*, vol. 315, p. 134364, Jan. 2025. [Online]. Available: https://doi.org/10.1016/j.energy.2025.134364

[87] A. Barragán-Ocaña, E. Cecilio-Ayala, P. Silva-Borjas, J. A. Cortés-Ruiz, and E.-Y. Hernández-Cardona, "Policies and sustainable energy transition in the global environment: Challenges for Latin America," *Heliyon*, vol. 11, no. 6, p. e42295, Mar. 2025. [Online]. Available: https://doi.org/10.1016/j.heliyon.2025.e42295

[88] A. J. Calderón Márquez, B. Smyth, A. F. Simões, and M. P. da Cunha, "Designing inclusive energy transitions: Insights from latin america's electricity sector," *Societal Impacts*, vol. 6, p. 100153, Dec. 2025. [Online]. Available: https://doi.org/10.1016/j.socimp.2025.100153

[89] P. Chavda and D. Mehta, "Assessing the impact of fossil fuel subsidies and environmental tax on renewable energy consumption of OECD countries: A panel quantile approach," *Next Energy*, vol. 8, p. 100313, 2025. [Online]. Available: https://doi.org/10.1016/j.nxener.2025.100313

[90] K. Bayramoğlu, M. Bayraktar, A. Seyhan, and O. Yuksel, "Evaluation of techniques to reduce carbon emissions from ships within the scope of revised greenhouse gas emission targets for 2030, 2040, and 2050," *Ocean Engineering*, vol. 334, p. 121605, Aug. 2025. [Online]. Available: https://doi.org/10.1016/j.oceaneng.2025.121605

Scientific Paper / Artículo Científico

UNIVERSIDAD POLITÉCNICA SALESIANA ECUADOR
INGENIUS
Revista de Ciencia y Tecnología
https://doi.org/10.17163/ings.n36.2026.06
pISSN: 1390-650X / eISSN: 1390-860X

Implementation of web accessibility in accordance with WCAG 2.1: perceptibility

Implementación de accesibilidad web según WCAG 2.1: perceptibilidad

Francisco Álvarez-Pineda[1,*], Yovin Urrego-Gómez[1], Pablo Ordóñez-Ordóñez[1], Hernán Torres-Carrión[1]

Received: 29-07-2025, Received after review: 09-03-2026, Accepted: 21-04-2026, Published: 01-07-2026

Abstract

The university web platform intended for individuals with visual impairments had significant accessibility limitations that restricted independent use. This Integrative Project aimed to implement the perceivability principle of the WCAG 2.1 standard, at conformance level AA, using the agile Rapid Application Development (RAD) methodology, which enabled rapid iterations of design, development, evaluation, and improvement. The main deficiencies identified included the absence of text alternatives, insufficient color contrast, poorly descriptive labels, and inadequate semantic structure. These issues were addressed by incorporating descriptive alt attributes, aria-label attributes, a hierarchical HTML5 structure, and CSS enhancements to improve visibility, focus indication, and keyboard navigation. The evaluation combined automated assessment using TAW, manual testing with the NVDA screen reader, and direct validation with users with visual impairments through Likert-type surveys. Quantitative results showed improvements of more than 2 points across all indicators, reaching scores above 4.4 out of 5, compared with the initial version, which did not exceed 2.5. Qualitative findings revealed a clearer, more structured, and more accessible user experience, with greater ease in identifying interface elements, navigating the platform, and using assistive technologies. These findings demonstrate that applying the perceivability principle not only fulfills the technical requirements of WCAG 2.1 but also has a tangible positive impact on digital inclusion and on the user experience of individuals with visual impairments.

Keywords: web accessibility, WCAG 2.1, perceptibility, visual impairment, accessibility assessment, RAD methodology

Resumen

La plataforma web universitaria para personas con discapacidad visual presentaba limitaciones significativas en accesibilidad, dificultando su uso autónomo. Este proyecto integrador tuvo como objetivo implementar el principio de perceptibilidad del estándar WCAG 2.1, nivel AA, utilizando la metodología ágil Rapid Application Development (RAD), que facilitó iteraciones rápidas de diseño, construcción, evaluación y mejora. Se identificaron deficiencias como la falta de alternativas textuales, bajo contraste de color, etiquetas poco descriptivas y una estructura semántica inadecuada. Estas se corrigieron mediante la incorporación de etiquetas alt, atributos aria-label, una jerarquía estructural en HTML5 y mejoras en CSS para optimizar la visibilidad, el foco y la navegación por teclado. La evaluación combinó herramientas automáticas (TAW), pruebas manuales con el lector NVDA y validación directa con usuarios con discapacidad visual a través de encuestas tipo Likert. Los resultados cuantitativos mostraron incrementos superiores a 2 puntos en todos los indicadores, alcanzando valores superiores a 4.4 sobre 5, en comparación con la versión inicial, que no superaba 2.5. Los resultados cualitativos reflejaron una experiencia más clara, estructurada y accesible, con mayor facilidad para identificar elementos, navegar y usar tecnologías asistivas. Estos hallazgos evidencian que la aplicación del principio de perceptibilidad no solo cumple con los requisitos técnicos del estándar WCAG 2.1, sino que también genera un impacto positivo real en la inclusión digital y en la experiencia de personas con discapacidad visual.

Palabras clave: accesibilidad web, WCAG 2.1, perceptibilidad, discapacidad visual, evaluación de accesibilidad, metodología RAD

[1,*]Universidad Nacional de Loja, Facultad de la Energía, Las Industrias y los Recursos Naturales No Renovables, Carrera de Computación, Loja, Ecuador. Corresponding author ✉: fjalvarez@unl.edu.ec.

Suggested citation: F. Álvarez-Pineda, Y. Urrego-Gómez, P. Ordóñez-Ordóñez and H. Torres-Carrión, "Implementation of web accessibility in accordance with WCAG 2.1: perceptibility," *Ingenius, Revista de Ciencia y Tecnología*, N.° 36, pp. 70-83, 2026, DOI: https://doi.org/10.17163/ings.n36.2026.06.

1. Introduction

Web accessibility constitutes a fundamental component of digital inclusion, particularly for individuals with visual impairments, who continue to face persistent barriers when using websites and online platforms. Despite the regulatory and technical efforts promoted by international organizations such as the W3C, numerous studies indicate that most digital environments still pose challenges related to navigation, visual interpretation, and access to information [1].

The Web Content Accessibility Guidelines (WCAG) 2.1, published by the World Wide Web Consortium (W3C), establish a set of guidelines organized around four fundamental principles: perceivable, operable, understandable, and robust. Among these, perceivability is particularly relevant for individuals with visual impairments, as it requires interface components and content to be presented in ways that users can perceive through different sensory channels [1]. This includes requirements such as appropriate alternative text, sufficient visual contrast, hierarchical headings, and compatibility with assistive technologies, including screen readers.

Recent studies have revealed significant gaps between the theoretical framework of the standard and its practical implementation. A systematic review published in Discover Computing showed that many digital platforms do not adequately meet the minimum accessibility criteria for individuals with low vision or blindness, particularly on mobile devices, where perceptual issues are more pronounced [2]. Similarly, an empirical evaluation of major e-commerce websites found that more than 60% of users with visual impairments reported frustration due to the absence of labels, coherent semantic structures, and accessible navigation [3].

In academic settings, studies such as the analysis of higher education institution websites in Finland have shown that compliance with the principle of perceivability varies considerably, even in contexts where digital accessibility is legally required [4]. Qualitative approaches based on the direct experiences of blind users have also highlighted that the limited participation of individuals with visual impairments in platform design and evaluation restricts the actual scope of accessibility [5].

In Ecuador, digital accessibility has increasingly gained recognition as a key component of social and technological inclusion. Regulatory frameworks, such as the Technical Standard on Disabilities, have established guidelines to ensure equitable access to digital platforms for individuals with disabilities, including those with visual impairments [6]. However, the effective implementation of these regulations remains limited. Despite institutional efforts, several studies indicate that many public and educational platforms in the country still present significant barriers for users with visual impairments, particularly in relation to the accessibility principles established by the WCAG [7].

In this context, this study focuses on analyzing the application of the perceivability principle of the WCAG 2.1 standard in a university web platform designed to facilitate access to digital content for individuals with visual impairments. One relevant example is the use of tools that convert text documents into audio, such as those employed in academic settings for assisted reading, which have proven to be key inclusion strategies when incorporated into accessible platforms from the design stage [8]. However, various studies indicate that many of these systems do not meet the minimum accessibility criteria established by the WCAG, which hinders both content perception and interaction through assistive technologies.

In response to this problem, the study addresses the following research question: To what extent does the application of the perceivability principle of the WCAG 2.1 standard in university web platforms improve accessibility for individuals with visual impairments? To this end, an agile Rapid Application Development (RAD) methodology was adopted, as this approach is widely used in the development of accessible solutions [9]. The process included an initial evaluation using the TAW Web Accessibility Test tool [10], the definition of technical requirements, the redesign of accessible interfaces through Figma prototypes, the progressive implementation of improvements, automated validation, manual testing, and final evaluation with real users. This approach seeks to demonstrate the impact of systematically integrating accessibility guidelines into the design and development of inclusive digital platforms in educational contexts [11].

2. Materials and Methods

2.1. Development Methodology

The implementation of accessibility improvements was carried out using the RAD approach. This methodology was selected because it enables short cycles of development, review, and continuous improvement, which is appropriate for an iterative process aimed at correcting accessibility barriers [12].

The RAD model enabled the work to be structured into four phases: requirements analysis, analysis and design, construction, and evaluation.

2.2. Tools and Materials

For the development and evaluation of the project, the following resources were used:

- **Automatic evaluation tool:** TAW (Web Accessibility Test), used for the initial and final

analysis of compliance with the WCAG 2.1 guidelines.

- **Assistive technology:** the NVDA screen reader, employed in manual evaluations of navigation and web content reading.
- **Reference standard:** the guidelines associated with the perceivability principle of the WCAG 2.1 standard, level AA.
- **Data collection instruments:** satisfaction questionnaires and semi-structured interviews to obtain qualitative feedback from end users.

Although TAW enabled initial and final automated evaluations of compliance with the criteria associated with the perceivability principle, its use involves methodological limitations that must be considered. In particular, automated tools cannot comprehensively assess aspects related to the quality of the user experience, the contextual interpretation of content, the clarity of instructions, the appropriateness of alternative texts, or actual interaction with assistive technologies. Likewise, elements classified as warnings or non-verifiable require manual review to determine whether they constitute real accessibility barriers. For this reason, the results obtained with TAW were complemented by manual testing with the NVDA screen reader and direct validation with users. Additionally, other evaluation tools, such as Axe and WAVE, may provide complementary assessments by detecting issues that a single automated platform may not identify in the same way.

2.3. Training Methods

The study consisted of two main stages: the implementation of accessibility improvements in accordance with the perceivability principle of WCAG 2.1 and the evaluation of their impact on the accessibility of the web platform.

Figure 1 shows the workflow followed during the implementation of the technical improvements.

The impact of the implemented improvements was then evaluated through five phases: planning, execution of automated tests, manual testing, validation, and delivery. This process enabled validation of the final version of the web platform. The tasks corresponding to each phase are detailed in Figure 2.

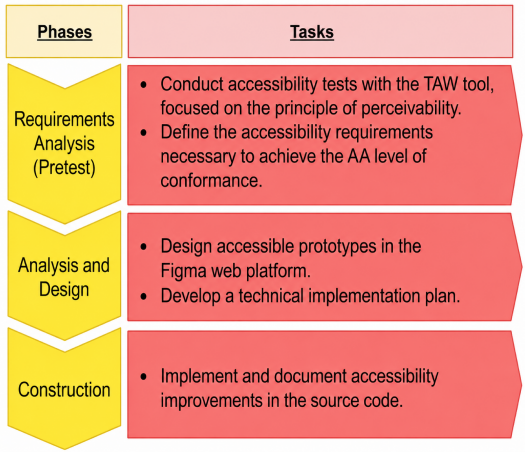

Figure 1. Procedure for implementing accessibility improvements.

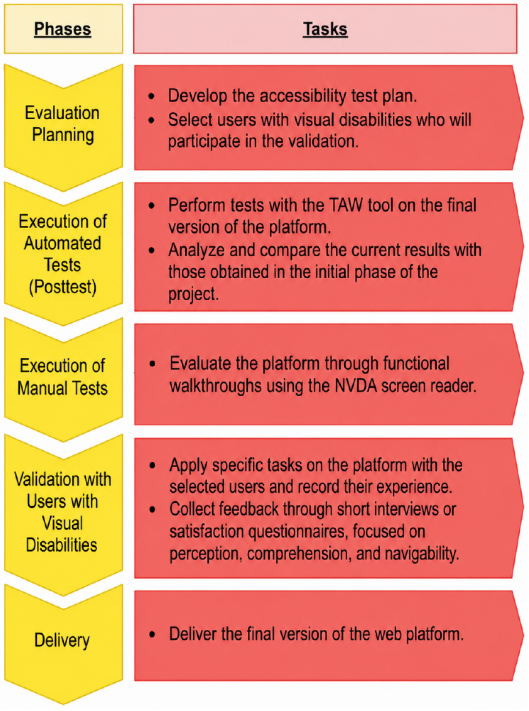

Figure 2. Procedure for the evaluation of the impact of the improvements.

2.4. Initial Evaluation (Pretest)

To conduct the initial accessibility evaluation based on the perceivability principle of WCAG 2.1, at conformance level AA, a specific development branch named "test" was created within the original web project. This version was adapted for automated evaluation by removing security layers, such as token-based authentication and performing a user data dump. This allowed the analysis tool to access each key section of the platform directly.

Subsequently, this version of the system was deployed on a virtual machine through the Azure portal, providing an internet-accessible testing environment. The URLs of the ten main pages of the web platform were then identified and collected, including the login, user registration, dashboard, global settings, content extractor, player, institutional information, user profile, password recovery, and new password request interfaces, as shown in Figure 3.

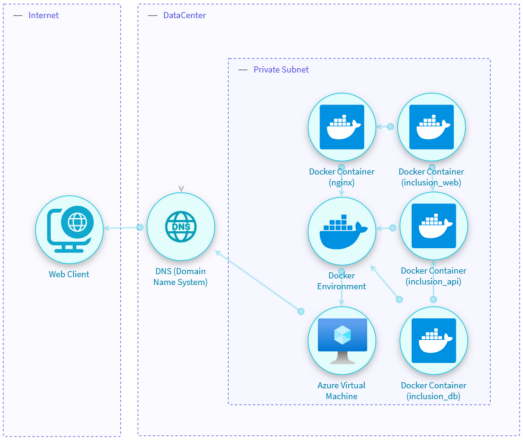

Figure 3. System deployment diagram.

Each URL was evaluated individually using the automated TAW tool. The evaluation focused exclusively on the criteria associated with the perceivability principle, extracting the corresponding results for detected issues, warnings, and elements that could not be automatically verified.

Given that automated tools have limitations when evaluating certain criteria that depend on the context of use and actual interaction with assistive technologies, these findings were considered an initial diagnostic baseline rather than an exhaustive verification of accessibility.

Based on these findings, the accessibility requirements needed to guide the redesign and improvement of the platform were defined, as described in the following section.

2.5. Design of Improvements

Based on the criteria established for AA conformance with the perceivability principle of WCAG 2.1, the functional and non-functional requirements guiding the platform modifications were defined. These requirements were grouped into two categories: general functional accessibility requirements, shown in Table 1, and non-functional requirements, shown in Table 2.

Table 1. Functional accessibility requirements related to perceivability

ID	WCAG Guideline	Description	Priority
REQ-001	1.1.1	Inclusion of meaningful alternative text for images and graphics.	High
REQ-002	1.3.1	Proper use of HTML5 and ARIA semantic labels.	High
REQ-003	1.4.3	Ensure a minimum contrast ratio of 4.5:1 between text and background.	High
REQ-004	1.4.4	Allow text resizing up to 200%, without loss of functionality.	High
REQ-005	1.4.5	Avoid the use of text images, except in exceptional cases.	High

Table 2. Non-functional requirements improving perceivability

ID	Category	Description	Priority
RNF-001	Usability	Ensure accessibility for users with visual impairments.	High
RNF-002	Performance	Maintain optimal load times after modifications.	Medium
RNF-003	Compatibility	Ensure proper functioning with screen readers.	High
RNF-004	Maintainability	Document all adaptations to facilitate future updates.	Medium

Once the requirements had been established, accessible prototypes were designed using the Figma platform, as shown in Figure 4. These prototypes incorporated inclusive design criteria, including:

- the correct semantic hierarchy of content through structured headings;
- institutional colors with sufficient contrast;
- the intuitive interface organization to facilitate assisted navigation;
- the reduction of distracting visual elements to promote simplicity;
- the inclusion of clear and visible labels in forms, buttons, and links.

Likewise, a technical implementation plan was developed in accordance with the RAD methodology. This plan specified:

- the specific tasks to be performed for each affected component;

- the prioritization of interventions according to the severity of the identified barriers;
- the technologies and best practices to be applied, including semantic HTML, ARIA, and accessible CSS;
- the development schedule organized into iterative cycles;
- the technical documentation of each intervention for validation and maintenance purposes.

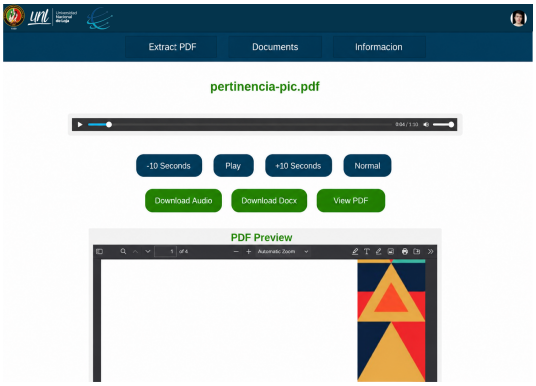

Figure 4. Accessible prototype of a key platform interface designed in Figma.

Additionally, as part of the development and validation process, a technical project repository was used to document the implemented modifications and design decisions, thereby supporting the reproducibility and validation of the results: https://github.com/Yovin001/inclusionLectora

2.6. Technical Implementation

Based on the defined functional and non-functional requirements, the source code of the main pages of the web platform was modified by applying the accessible design principles established in WCAG 2.1, at conformance level AA. The implemented improvements are summarized in Table 3.

To illustrate the impact of the implemented improvements, Figures 5 and 6 compare the original platform interface with the accessible version developed in this study. This comparison highlights changes in color contrast, visual organization, and the clarity of interactive components.

Although the platform's visual interface was not substantially modified, technical adjustments were made to improve its interpretation by assistive technologies. In particular, priority was given to accessible component labeling, semantic structural organization, and the proper definition of names, roles, and descriptions for interactive elements.

One of the most relevant aspects of the intervention was the improvement in accessible labeling for interface elements. Attributes such as aria-label, aria-describedby, along with appropriate semantic associations between labels and form fields, were incorporated to improve screen reader interpretation.

Table 3. Accessibility improvements implemented in the source code

Identified issue	WCAG 2.1 guideline not met	Solution applied
Images without text meaningful alternative text were added	1.1.1 Non-text content.	Descriptive alt attributes or aria-hidden="true" for decorative elements.
Icons without textual alternative	1.1.1 Non-text content.	Dynamic aria-label attributes were added, hidden with aria-hidden="true", or removed if unnecessary.
Use of color without sufficient contrast	1.4.3 Minimum contrast.	Colors in CSS styles were adjusted to achieve a minimum contrast of 4.5:1 in all states.
Buttons or links without accessible labels	4.1.2 Name, function, value.	aria-label attributes were added that clearly describe the function of each button or link.
Form fields without clear semantic relationships.	1.3.1 Information and relationships.	The attributes htmlFor, aria-describedby, and role="alert" were used to associate labels, inputs, and messages.
Headers without structure were reorganized	1.3.1 Information and relationships.	The tags <h1>, <h2>, and <h3> to reflect a clear, semantic hierarchy.
Controls without visible focus	2.4.7 Visible focus.	Custom styles were applied to the :focus state to ensure the focus is visible during keyboard navigation.
Elements defined by color alone	1.4.1 Use of color.	ARIA text or attributes were added that allow the purpose to be interpreted without relying exclusively on color.
Absence of the attribute lang in the document	3.1.1 Page language.	The Spanish language was declared in the root HTML using lang="es" for assistive technologies.
Status messages non-accessible	4.1.3 Status messages.	It was proposed to use role="alert" or aria-live="assertive" in message containers (in some cases, this remained pending).
Audio controls without text alternatives	1.2.1 Audio only (recorded).	It was recommended to add an accessible text transcript for users with hearing impairments.
Removed visual elements due to lack of functionality or accessibility	N/A	Elements that did not contribute and did not meet accessibility criteria were removed from the code.

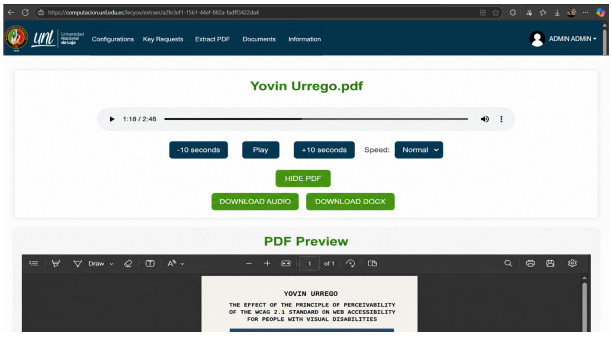

Figure 5. Original interface with accessibility barriers.

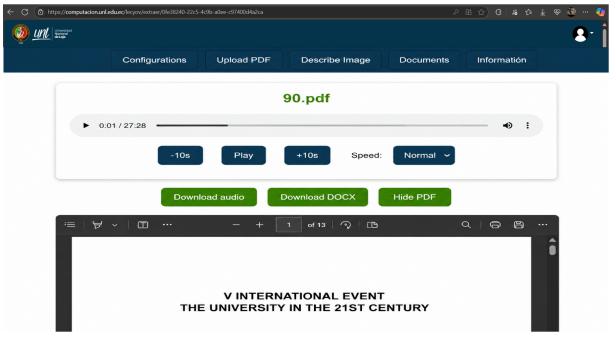

Figure 6. Accessible interface after implementing improvements based on the perceivability principle of WCAG 2.1.

To illustrate these technical changes, Figures 7, 8, and 9 present examples obtained using the browser's accessibility inspector. These captures show improvements in component labeling and accessible structure, enhancing screen reader reading and interpretation.

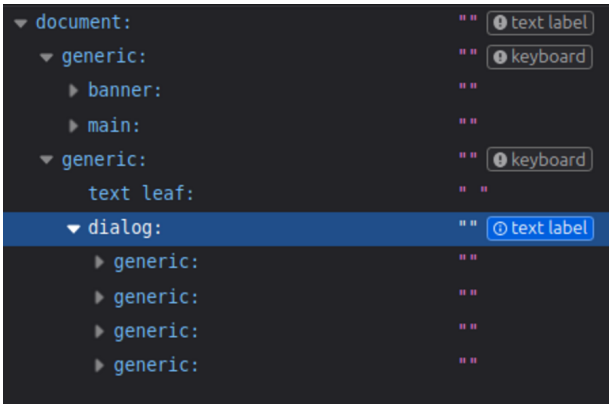

Figure 7. Accessible structure in the original version.

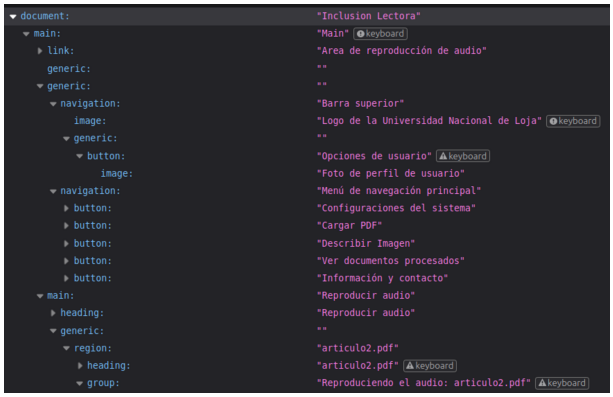

Figure 8. Accessible structure in the improved version (upper section).

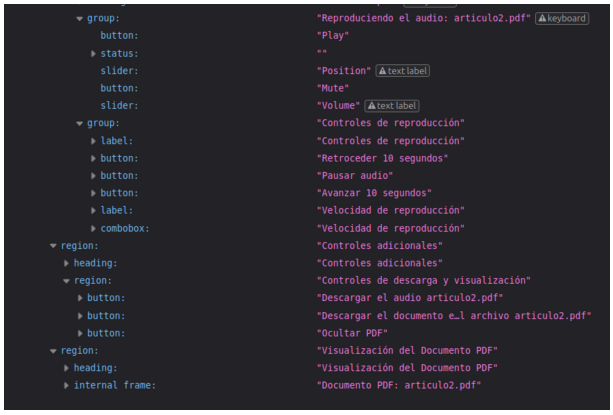

Figure 9. Accessible structure in the improved version (lower section).

2.7. Post-Evaluation (Posttest)

To measure the impact of the implemented improvements, a second automated evaluation was conducted using the same methodological approach as in the pretest [13]. A new project branch, named "posttest," was created, incorporating all modifications related to the perceivability principle.

This version was deployed in a testing environment equivalent to the initial one, and the same reference URLs of the platform were reused to ensure comparability of the results.

The TAW tool was used again to analyze each page according to the perceivability criteria. Data were collected on detected issues, warnings, and non-verifiable elements.

Consequently, the posttest results were interpreted together with the manual evaluation and user validation to avoid relying solely on an automated assessment of the level of accessibility achieved.

These results were compared with those obtained in the initial evaluation, allowing the specific effect of the interventions on platform accessibility to be estimated.

2.8. Manual Evaluation

Manual accessibility testing was carried out using the NVDA screen reader to validate compliance with Principle 1, Perceivability, of WCAG 2.1 at conformance level AA. The evaluations focused on key interface components, including form fields, buttons, links, menus, and navigation structures, through actions such as tab navigation, use of arrow keys, keyboard activation, and sequential reading.

To ensure objectivity in the process, an external evaluator outside the development team was included: a university student experienced in using the NVDA screen reader. Her participation made it possible to assess the platform's accessibility from a perspective closer to the real experience of users with visual impairments, identifying barriers that may go unnoticed in a technical self-evaluation [11].

2.9. User Validation

As part of the validation process, an in-person workshop was organized with users with visual impairments at the National University of Loja. Participants were selected based on their experience using assistive technologies, particularly screen readers such as NVDA.

From an initial population of 15 students with visual impairments enrolled in face-to-face programs, four participants were selected for the tests. The selection criteria included availability, prior experience with screen readers, and logistical constraints, such as academic schedule conflicts, mobility difficulties, or technological limitations. From a qualitative perspective, this reduced sample size is justified by the purposive sampling method, which is commonly used in exploratory accessibility studies [14].

Although the sample was small, its selection was consistent with the exploratory nature of the study and its purpose of identifying relevant accessibility barriers during an initial validation stage. In usability and accessibility research, small samples can detect frequent interaction issues when evaluations involve specific tasks and users experienced in assistive technologies. However, this methodological decision limits the inferential scope of the results; therefore, the findings should be interpreted as contextual evidence rather than as a statistical generalization applicable to the entire university population with visual impairments.

Additionally, according to Jakob Nielsen's model, four participants are estimated to be sufficient to identify approximately 75% of the most frequent usability problems. This estimate is based on the following formula:

$$P = N \times (1 - (1 - L)^n) \tag{1}$$

where P represents the detected problems, N the total number of problems, L the probability that a user detects a problem ($L \approx 0.31$), and n the number of evaluated users [15]. As Nielsen argues, even a single user can reveal a considerable proportion of critical issues, and as more users are added, the amount of new information decreases. This rationale supports the use of small samples in early stages, when the objective is to identify and address the most evident barriers.

During the workshop, users performed functional tasks representative of actual platform use, including registration flows, login, PDF file upload, and audio content playback. Each activity was carried out autonomously using the NVDA screen reader. When significant difficulties arose, the development team intervened promptly to allow the exercise to continue.

After participants completed the functional tasks in the first version of the platform, which did not include accessibility improvements, the validation instruments were applied to assess their perception of accessibility. The same process was then repeated with the second version, which had been modified according to the perceivability principle. Finally, a comparative interview was conducted between both versions. All participants completed the tests in both versions of the system, pretest and posttest, allowing for a direct comparison of the user experience under the same experimental conditions.

Instruments applied for the evaluation of accessibility

To evaluate the user experience from both quantitative and qualitative perspectives, the following instruments were designed and applied:

- A Likert-scale survey from 1 to 5, based on criteria associated with the perceivability principle of WCAG 2.1.
- Open-ended questions to collect detailed observations.
- A comparative interview between versions to validate perceived improvements.

Likert-type survey: This instrument assessed perceptions of accessibility in key aspects of the interface, including ease of reading, screen reader use, clarity of instructions, visibility of alerts, and accessibility of controls.

Table 4. Likert-type survey questions

Question	Associated WCAG criterion
Was it easy to perceive all text on the screen?	Text contrast / readability.
Did the screen reader correctly read all elements?	Text alternatives / accessible labels.
Were the instructions clear and perceptible?	Contextual hints / visible instructions.
Were alerts or errors easily perceived?	Audible and visual alerts.
Were buttons, fields, and controls distinguishable and visible when focused?	Visible focus / contrast / keyboard navigation.

Each question was rated on a scale from 1 (strongly disagree) to 5 (strongly agree) and applied separately after the use of each version of the platform.

Open-ended questions: To obtain deeper qualitative feedback, open-ended questions were administered after participants used each version. These questions helped identify perceived barriers, navigation difficulties, and specific suggestions from the user's perspective.

Comparative interview between versions: After the validation of both versions was completed, a comparative interview was conducted to identify perceived differences, observed improvements, and elements still requiring improvement. This activity helped validate the effectiveness of the interventions through a direct comparison of user experience.

Table 5. Open-ended questions for qualitative feedback

Question
Was it easy to read all the text on the screen?
Was there anything you couldn't read clearly in this version?
Which part did you find most difficult to identify or understand?
How would you improve this version?

Table 6. Comparative interview questions between versions

Question
Did you notice any differences between the first and second versions?
Which version was clearer or easier to use with your screen reader?
Where did you notice the biggest difference?
Were the messages, buttons, or alerts easier to perceive in the second version?
What would you improve in the accessible version?

2.10. Results Analysis

The results were analyzed through methodological triangulation, integrating quantitative and qualitative data from three sources: automated evaluation, manual evaluation using a screen reader, and validation with users with visual impairments.

Given the small sample size, the quantitative analysis was approached descriptively, and no inferential tests were performed. The results were interpreted using averages and observed trends between the evaluated versions.

For the automated evaluation, the reports generated by the TAW tool during the pretest and posttest phases were used. The extracted data were organized into comparative matrices for each evaluated page, classifying the findings into three categories: errors, warnings, and non-verifiable elements. Based on these matrices, bar charts were generated to visualize changes between versions, highlighting the reduction or persistence of issues related to the perceivability principle.

For the manual evaluation, the findings reported by the external evaluator during the functional walkthroughs were coded and grouped according to the type of barrier detected, namely visual, structural, or semantic, and the affected component, including forms, navigation, controls, and content. This coding enabled the construction of a barrier map, which was later compared with the implemented improvements.

The qualitative and quantitative data collected during user validation were analyzed at two levels. First, responses to the Likert questionnaires were processed using measures of central tendency, including means and standard deviations, to identify patterns of perception regarding accessibility, comprehension, and navigability. Second, a thematic analysis of the semi-structured interviews and open-ended questions was conducted, organizing the responses into emerging categories related to user experience, identified barriers, and improvement suggestions.

2.11. Ethical Considerations

All user validation activities were conducted in accordance with ethical principles for research involving human subjects. Written informed consent was obtained from all participants, ensuring voluntary participation, confidentiality of the collected data, and anonymity of responses in the dissemination of results.

3. Results and Discussion

3.1. Results of the Automated Evaluations

The initial evaluations identified accessibility barriers related to insufficient color contrast, absence of alternative texts, deficient semantic structures, and forms without descriptive labels.

After the implementation of improvements, the critical errors detected by TAW were reduced to zero on the evaluated pages, as shown in Table 7. The barriers initially identified included the following:

- **Insufficient color contrast,** which hindered readability.
- **Lack of alternative** texts in images and graphical elements.
- **Inadequate semantic structure,** affecting interpretation by assistive technologies.
- **Form-related issues,** such as the absence of descriptive labels.

As shown in Table 7, critical errors classified as "Issues" were completely eliminated, indicating a significant technical improvement. Likewise, warnings were reduced by 44.19%, reflecting progress in labels and descriptions, although these aspects still require further improvement.

The "non-verifiable" elements remained unchanged due to the limitations of automated tools such as TAW, which must be complemented by manual evaluation or user-based validation. These results demonstrate the positive impact of applying the perceivability principle of WCAG 2.1 through iterative approaches, including RAD, contributing to a more accessible web experience for individuals with visual impairments.

Table 7. Comparison of accessibility errors before and after the intervention

Category	Pre-test	Post-test	Reduction
Problems	32	0	100%
Warnings	43	24	44.19%
Unverified elements	40	40	0%

3.2. Results of the Manual Evaluation

The NVDA evaluation revealed several perceptual barriers, including errors in button activation, lack of confirmation for critical actions, incorrect labels, and conflicts between screen reader narration and audio playback. Most of these issues were corrected during the improvement process, as summarized in Table 8, where the main findings are grouped by test case and resolution status.

Table 8. Summary of the manual evaluation results with NVDA

Case test	Identified issues	Status
Login.	Typing errors, disabled button, resizing when displaying warnings.	Resolved
Registration	Incorrect password confirmation prompt, fields accepting letters, incorrect button order.	Partially resolved
Forgotten password	Button disabled with no feedback.	Resolved
Dashboard	The reader does not announce search results or confirm deletion.	Resolved
Player	Narration overlaps between reader and audio.	Unresolved
Extractor	Vague buttons, issues loading files.	Resolved
Global settings.	Unnecessary reading of warnings, incorrect messages when deletion fails.	Resolved
Profile and change password	Incorrect reading of password buttons and non-standard labels.	Resolved
All pages	Missing "skip to content" link and unintuitive order of save/cancel buttons.	Resolved

Manual testing confirmed that most of the initial barriers were eliminated, substantially improving the navigation experience with assistive technologies. However, some aspects requiring future review were identified, particularly in the audio component, where perceptual conflicts persist.

3.3. Results of User Validation

As part of the system accessibility validation process, tests were conducted with four participants with visual impairments, who completed all interaction flows in both versions of the system: the initial version and the accessible version. Subsequently, satisfaction surveys with Likert-type questions were administered, open-ended interviews were conducted to collect qualitative observations, and a comparative interview between versions was carried out to understand participants' overall perceptions.

3.3.1. Results of the Likert-type survey

The results obtained through the Likert scale show a substantial improvement in perceived accessibility in the accessible version of the system. Five key aspects related to the perceivability principle of WCAG 2.1, at conformance level AA, were evaluated: text readability, visibility of buttons and controls, perception of alerts, clarity of instructions, and document reading by the screen reader.

Table 9. Averages obtained for each item in both evaluated versions

Assessment criterion	Pre-test	Post-test
Contrast / text	3.00	4.50
Text alternatives	2.50	4.75
Instructions / contextual hints	2.00	4.75
Visual and auditory alerts	2.50	4.75
Visual focus / contrast / keyboard navigation	2.25	4.50

As shown in Table 9, all evaluated aspects improved significantly after the implementation of accessibility enhancements based on the perceivability principle of WCAG 2.1, at conformance level AA. Specifically, text contrast improved from 3.00 to 4.50; text alternatives from 2.50 to 4.75; instructions and contextual aids from 2.00 to 4.75; visible and auditory alerts from 2.50 to 4.75; visible focus, contrast, and keyboard navigation from 2.25 to 4.50; and proper document reading by the screen reader from 2.00 to 5.00. These results indicate that the implemented interventions were effective in improving interaction through assistive technologies.

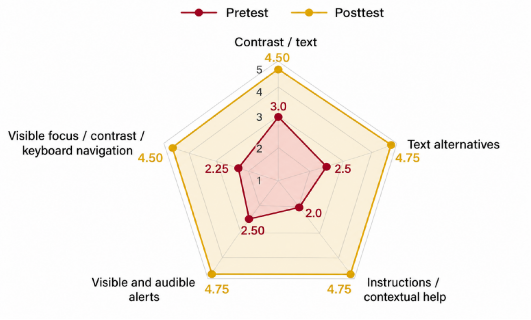

Figure 10. Graphical comparison of scores by evaluated criterion on a scale from 1 to 5.

3.3.2. Results of the open-ended interviews

The open-ended interviews provided a qualitative and detailed perspective on the user experience. The most relevant findings are summarized below, according to the categories of analysis.

Perception of visual elements: In the initial version, users reported difficulties distinguishing certain visual elements. Issues such as buttons with similar colors that did not clearly differentiate their functions, as well as dialogs that were difficult to perceive or poorly structured, were identified. In contrast, users reported a clearer experience in the accessible version, indicating that visual elements were more distinguishable and that the NVDA screen reader correctly interpreted dynamic interface changes, such as pop-up messages and focus transitions.

Comprehension and navigability: Navigation in the first version was confusing, particularly when users tried to identify the player buttons, complete the document upload process, and locate status messages. In the accessible version, these obstacles were notably reduced. Users reported that the organization of content and the screen reader response facilitated a more intuitive understanding of the system.

Suggestions for improvement: Among the suggestions collected, participants proposed incorporating an option to select the starting page for document reading, allowing the upload of .doc files, improving the wording of informational dialogs, and adding functions to jump to specific sections of the content. Several of these recommendations had already been implemented in the evaluated accessible version.

3.3.3. Results of the comparative interview between versions

In the final interview, users were asked to compare both versions of the platform. The responses reflected a clear preference for the accessible version (V2), highlighting substantial improvements in both interface design and compatibility with assistive technologies.

General perception: Users agreed that the accessible version offered a clearer and less confusing experience, with a more organized visual and semantic structure. Improvements in content presentation and a reduction in cognitive load during navigation were also highlighted.

Screen reader compatibility: Users reported smoother and more understandable navigation with the screen reader in the accessible version. Improvements in HTML structure, tab order, and the appropriate use of ARIA labels contributed to more effective interaction.

Areas with the greatest perceived improvement: The elements that showed the greatest improvement were buttons, navigation focus, contextual messages, and informational dialogs. Some users also noted that blank spaces and sections previously omitted by the screen reader could now be correctly identified.

Perception of messages and alerts: System messages, errors, and alerts were more clearly perceived in the accessible version, both visually and through screen reader interpretation. This contributed to a better understanding of system states and required actions.

Additional suggestions: Although the accessible version significantly improved the experience, users suggested continuing to incorporate features aimed at reading personalization, such as the ability to define specific starting points or jump to certain sections to facilitate navigation in long documents.

3.4. Discussion of the Findings

The results indicate that applying the perceivability principle of WCAG 2.1 has a positive and measurable impact on improving web accessibility for individuals with visual impairments in university environments. The technical implementation was based on the level AA criteria of this standard [1], through practices such as semantic tags, alternative attributes, adequate contrast, and ARIA roles, in line with the approaches was proposed by Miranda and Araujo [8] and Manu et al. [4].

First, the automated evaluations conducted using the TAW tool showed the complete elimination of critical errors after the intervention, with a reduction of 100%. This improvement is attributed to the systematic application of accessibility guidelines, particularly in aspects such as text contrast, the inclusion of text descriptions, and clear semantic structure. These results are consistent with previous studies that identify perceivability errors as key factors affecting the experience of users with visual impairments [7], [11], and have also been documented by Henkelmann and Fertig [5].

Likewise, warnings related to labels, descriptions, and relationships between elements were reduced by 44.19%. This result suggests that, although automated tools are useful for identifying perceptual barriers, they have significant limitations when evaluating certain aspects, such as text resizing or auditory feedback. Therefore, they must be complemented by manual evaluations and testing with real users [10], [16].

Manual testing with NVDA confirmed that most of the initial barriers were corrected, including incorrect button reading, focus issues, and lack of feedback. However, difficulties such as overlap between the screen reader voice and the audio player persisted, as also noted by Kerdar et al. [2]. This finding reinforces the idea that some perceptual conflicts cannot be resolved solely through technical adjustments but require a user-centered functional redesign.

The results of the Likert-type survey reflect a substantial improvement in all evaluated aspects, as shown in Table 9. Particularly notable were the increases in button visibility, clarity of instructions, and document reading, which reached the maximum score of 5.0. This finding is consistent with the W3C WAI recommendations [17], which emphasize the importance of ensuring that content is distinguishable and understandable both visually and auditorily to guarantee perceivability.

The qualitative interviews provided deeper insight into the user experience. Participants highlighted improvements in visual organization, element identification, and screen reader interpretation of content. Increased autonomy during navigation was also reported. These perceptions confirm the relationship between accessibility and usability described by Petrie and Kheir [3], as well as the importance of clear auditory feedback, as noted by Henkelmann and Fertig [5] and Laamanen et al. [4].

However, some recommendations provided by users were not strictly related to the perceivability principle, but rather to additional functionalities, such as the ability to select the starting page for reading or facilitate navigation between sections. These observations suggest that comprehensive accessibility should also consider the operability and understandability principles of WCAG 2.1 [1], and that its implementation requires an iterative and participatory approach, as proposed by Miranda and Araujo [8].

Furthermore, from critical perspectives on digital disability, accessibility is not limited to technical compliance; it also involves considering users' real experiences in specific social and technological contexts [18].

Although WCAG 2.1 constitutes a fundamental technical guide for improving web accessibility, compliance alone does not guarantee a fully accessible experience in real academic contexts. Aspects such as the contextual clarity of content, cognitive load during navigation, and interaction with dynamic components cannot always be adequately assessed through normative criteria or automated tools. Therefore, in complex university environments, the application of these guidelines must be complemented by manual evaluations, user validation, and a user-centered approach focused on real experiences of individuals with visual impairments.

However, the results should be interpreted with caution. Although significant improvements in perceived accessibility were evident, they were evaluated in a controlled context and with a limited sample, which restricts their generalization. Additionally, some aspects of accessibility, such as interaction with dynamic components and the management of multimedia content, remain challenging and were not fully addressed in this

study. Future work could therefore expand the analysis by incorporating other WCAG 2.1 principles and conducting evaluations in more diverse usage contexts.

In summary, the implementation of the perceivability principle significantly improved accessibility for individuals with visual impairments, from both a technical and a user-experience perspective. These findings provide an affirmative answer to the research question by demonstrating that the improvements not only contributed to regulatory compliance but also had a clear effect on user interaction, comprehension, and autonomy. Consequently, the study confirms that effective accessibility in university contexts requires not only technical adjustments but also continuous evaluation processes focused on real experiences of individuals with visual impairments.

4. Conclusions

The application of the perceivability principle of WCAG 2.1, at conformance level AA, had a significant impact on improving the accessibility of a university web platform for individuals with visual impairments by facilitating system comprehension, navigation, and autonomous use. The results obtained in this study showed increases of more than two points across all indicators of the Likert-type survey, with scores exceeding 4.4 out of 5, compared with the original version, whose scores did not exceed 2.5. These improvements were reflected in the complete elimination of critical errors detected through automated evaluation and in users' clear preference for the accessible version. Collectively, these findings demonstrate that the proper implementation of the perceivability principle has a positive effect on both the technical quality of the platform and the user experience.

The use of the RAD methodology enabled the application of the perceivability principle, facilitating the correction of previously identified accessibility deficiencies, such as the absence of textual alternatives, inadequate color contrast, incorrect use of labels, and insufficient semantic hierarchy. To address these deficiencies, technical solutions were incorporated, including aria-label attributes, alt tags in images, HTML5 structural elements, and CSS stylesheet adjustments to ensure visible focus and keyboard navigation.

The evaluations conducted with users confirmed a smoother experience, characterized by clearer feedback and greater compatibility with screen readers. The accessible version was rated as significantly more usable and understandable, reinforcing the effectiveness of applying the perceivability principle of WCAG 2.1 through a process that integrated automated evaluation, manual testing, and user validation.

The application of the perceivability principle in a university web platform for individuals with visual impairments enabled the creation of a digital environment that not only improves technical compliance with the criteria associated with WCAG 2.1 but also substantially enhances the experience of these users.

The combination of an agile methodology, specific technical interventions, and validation with end users supported compliance with accessibility requirements and contributed to a more inclusive, clear, and efficient experience, thereby improving the quality and usability of the university web platform for individuals with visual impairments.

Limitations of the Study

The study presents some limitations that should be considered when interpreting the results. First, the sample size was small, which is consistent with the exploratory nature of the research but limits the generalization of the findings to other populations.

Second, the same participants evaluated both versions of the system, pretest and posttest, which could introduce a learning bias that may influence the perceived improvement.

Likewise, the use of automated tools such as TAW presents inherent limitations, as these tools do not allow for a comprehensive evaluation of aspects related to user experience, contextual understanding of content, or interaction with assistive technologies.

Finally, the study focused solely on the perceivability principle ofWCAG 2.1; therefore, the principles of operability, understandability, and robustness were not comprehensively evaluated.

Acknowledgments

The National University of Loja is acknowledged for the institutional support provided during the development of this work and for facilitating the spaces and resources necessary to conduct the accessibility tests.

Special thanks are extended to the users with visual impairments who actively participated in the validation process. Their collaboration, feedback, and commitment were essential for identifying real barriers and guiding meaningful improvements to the developed platform.

Funding

This research is part of the outreach project entitled "Reading inclusion of students with visual impairments at the National University of Loja through technological innovation," code FEIRNNR-C-001, funded by the National University of Loja.

Contributor Role

- **Francisco Álvarez-Pineda:** Conceptualization, data curation, formal analysis, research, methodology, project management, supervision, validation, visualization, writing – review and editing.
- **Yovin Urrego-Gómez:** Conceptualization, data curation, formal analysis, research, methodology, software, validation, visualization, writing – original draft.
- **Pablo Ordóñez-Ordóñez:** Conceptualization, validation, visualization, writing – review and editing.
- **Hernán Torres-Carrión:** Conceptualization, validation, visualization, writing – revision and editing.

References

[1] W3C. (2018) Web content accessibility guidelines (WCAG) 2.1. World Wide Web Consortium. [Online]. Available: https://upsalesiana.ec/ing36ar6r1

[2] S. Hamideh Kerdar, L. Bächler, and B. M. Kirchhoff, "The accessibility of digital technologies for people with visual impairment and blindness: a scoping review," *Discover Computing*, vol. 27, no. 1, Aug. 2024. [Online]. Available: https://doi.org/10.1007/s10791-024-09460-7

[3] H. Petrie and O. Kheir, "The relationship between accessibility and usability of websites," in *Proceedings of the SIGCHI Conference on Human Factors in Computing Systems*, ser. CHI07. ACM, Apr. 2007, pp. 397–406. [Online]. Available: https://doi.org/10.1145/1240624.1240688

[4] M. Laamanen, T. Ladonlahti, H. Puupponen, and T. Kärkkäinen, "Does the law matter? an empirical study on the accessibility of finnish higher education institutions' web pages," *Universal Access in the Information Society*, vol. 23, no. 1, pp. 475–491, Nov. 2022.

[5] D. Henkelmann, "Exploring the link between accessible website design and user experience for humans with blindness and visual impairment: a quality study," 2023. [Online]. Available: https://doi.org/10.35011/IDIMT-2023-101

[6] D. Soliz Carrión, L. Cadena Minotta, and T. Rosero, *Norma Técnica de Discapacidades. Servicios para personas con discapacidad.* Ministerio de Inclusión Económica y Social del Ecuador, 2014. [Online]. Available: https://upsalesiana.ec/ing36ar6r6

[7] T. Acosta and S. Luján-Mora, "Análisis de la accesibilidad de los sitios web de las universidades ecuatorianas de excelencia," *Enfoque UTE*, vol. 8, no. 1, pp. 46–61, Feb. 2017. [Online]. Available: https://doi.org/10.29019/enfoqueute.v8n1.133

[8] D. G. Miranda and J. Araujo, "A framework for integrating web accessibility requirements in agile methodologies," *Universidade Nova de Lisboa*, 2020. [Online]. Available: https://doi.org/10.5281/zenodo.4618349

[9] V. Stray, A. Bai, N. Sverdrup, and H. Mork, *Empowering Agile Project Members with Accessibility Testing Tools: A Case Study.* Springer International Publishing, 2019, pp. 86–101. [Online]. Available: https://doi.org/10.1007/978-3-030-19034-7_6

[10] CTIC. (2024) Test de accesibilidad web. Fundación CTIC, Online Resource. [Online]. Available: https://upsalesiana.ec/ing36ar6r10

[11] Y. Yesilada and S. Harper, *Web Accessibility: A Foundation for Research.* Springer London, 2019. [Online]. Available: https://doi.org/10.1007/978-1-4471-7440-0

[12] W. S. Davis and D. C. Yen, *The Information System Consultant's Handbook: Systems Analysis and Design*, W. S. Davis and D. C. Yen, Eds. CRC Press, Apr. 2019. [Online]. Available: https://doi.org/10.1201/9781420049107

[13] D. T. Campbell and J. C. Stanley, *Experimental and Quasi-Experimental Designs for Research. Boston: Houghton Mifflin Company.* Houghton Mifflin Company, 1963. [Online]. Available: https://upsalesiana.ec/ing36ar6r13

[14] H. Boone and D. Boone, "Analyzing likert data," *Journal of Extension*, vol. 50, no. 2, Apr. 2012. [Online]. Available: https://doi.org/10.34068/joe.50.02.48

[15] J. Nielsen, *Usability Engineering.* San Francisco, CA, USA: Morgan Kaufmann Publishers, 1994. [Online]. Available: https://upsalesiana.ec/ing36ar6r15

[16] M. Snaprud, K. Rasta, K. Andreasson, and A. Nietzio, *Benefits and Challenges of Combining Automated and User Testing to Enhance e-Accessibility – The European Internet Inclusion Initiative.* Springer International Publishing, 2014, pp. 137–140. [Online]. Available: https://doi.org/10.1007/978-3-319-08596-8_20

[17] W3C. (2023) Web accessibility initiative (WAI). World Wide Web Consortium. [Online]. Available: https://upsalesiana.ec/ing36ar6r17

[18] National Library of Australia. (2026) National library of Australia catalog record. New Media. Rowman & Littlefield. Accessed: May14, 2026. [Online]. Available: https://upsalesiana.ec/ing36ar6r18

Scientific Paper / Artículo Científico

UNIVERSIDAD POLITÉCNICA SALESIANA ECUADOR
INGENIUS
Revista de Ciencia y Tecnología
https://doi.org/10.17163/ings.n36.2026.07
pISSN: 1390-650X / eISSN: 1390-860X

Influence of cabin temperature and compressor speed on the performance of an automotive air conditioning system

Influencia de la temperatura del habitáculo y la velocidad del compresor en el rendimiento del sistema de aire acondicionado automotriz

Iván M. Ashqui-Cuvi[1], Klever S. Morales-Morales[1], Daniela C. Vásconez-Núñez[2], Fernando M. Tello-Oquendo[3,*], Fabián C. Gunsha-Maji[3]

Received: 16-11-2025, Received after review: 09-03-2026, Accepted: 21-04-2026, Published: 01-07-2026

Abstract

This study examines the influence of compressor speed and cabin temperature on the performance of an automotive air conditioning system. An experimental test bench was developed with a compressor coupled to a variable-speed electric motor and equipped with pressure, temperature, and air velocity sensors, as well as a thermal chamber to regulate the temperature of the air entering the evaporator. A thermodynamic model was also implemented to calculate the compressor operating parameters and evaluate system performance. The results show that increasing the compressor speed from 900 to 2800 rpm raises the refrigerant mass flow rate and cooling capacity by up to 50.3 % and 22.4 %, respectively, thereby improving the cooling capacity. However, this increase also raises power consumption from 0.287 to 0.878 kW and nearly doubles fuel consumption, reaching 0.54 L/h at a cabin temperature of 45 °C. In addition, isentropic efficiency, volumetric efficiency, and the coefficient of performance decrease by up to 22.66%, 44%, and 61.27%, respectively, while the compressor discharge temperature exceeds 80 °C at high operating speeds. Finally, correlations are proposed to estimate compressor efficiencies, and fuel consumption is calculated considering the powertrain efficiencies of a gasoline-powered internal combustion engine vehicle.

Keywords: compressor speed, cabin temperature, volumetric efficiency, isentropic efficiency, coefficient of performance, air conditioning

Resumen

Este artículo analiza la influencia de la velocidad del compresor y la temperatura del habitáculo en el rendimiento del sistema de aire acondicionado automotriz. Para ello, se construyó un banco experimental con un compresor acoplado a un motor eléctrico de velocidad variable, equipado con sensores de presión, temperatura y velocidad del aire, así como una caja térmica para regular la temperatura del aire de entrada al evaporador. Además, se implementó un modelo termodinámico para calcular los parámetros de funcionamiento del compresor y el desempeño del sistema. Los resultados muestran que, al incrementar la velocidad del compresor de 900 a 2800 rpm, el flujo másico de refrigerante y la capacidad frigorífica aumentan hasta en un 50.3 % y un 22.4 %, respectivamente, lo que mejora la capacidad de enfriamiento. Sin embargo, también se incrementan la potencia consumida de 0.287 a 0.878 kW, y el consumo de combustible, que llega a duplicarse hasta 0.54 L/h a 45 °C de temperatura en el habitáculo. Asimismo, se observa una disminución de la eficiencia isentrópica del 22.66 %, de la eficiencia volumétrica del 44 % y del coeficiente de desempeño (COP) de hasta 61.27 %, junto con un incremento de la temperatura de descarga del compresor por encima de 80 °C a altas velocidades. Finalmente, se proponen correlaciones para el cálculo de las eficiencias del compresor y se estima el consumo de combustible considerando las eficiencias del tren motriz de un vehículo con motor de combustión interna a gasolina.

Palabras clave: velocidad del compresor, temperatura del habitáculo, eficiencia volumétrica, eficiencia isentrópica, coeficiente de desempeño, aire acondicionado.

[1]Investigador independiente, Ecuador.
[2]Grupo de investigación INVELECTRO, Carrera de Ingeniería Industrial, Facultad de Mecánica, Escuela Superior Politécnica de Chimborazo (ESPOCH), Riobamba, Ecuador.
[3,*]Grupo de investigación INVELECTRO, Carrera de Ingeniería Automotriz, Facultad de Mecánica, Escuela Superior Politécnica de Chimborazo (ESPOCH), Riobamba, Ecuador. Corresponding author ✉: fernando.tello@espoch.edu.ec.

Suggested citation: I. M. Ashqui-Cuvi, K. S. Morales-Morales, D.C. Vásconez-Núñez, F. M. Tello-Oquendo and F. C. Gunsha-Maji "Influence of cabin temperature and compressor speed on the performance of an automotive air conditioning system," *Ingenius, Revista de Ciencia y Tecnología*, N.° 36, pp. 84-97, 2026, DOI: https://doi.org/10.17163/ings.n36.2026.07.

1. Introduction

The automotive air conditioning (A/C) system removes heat from the air inside the vehicle to maintain thermal comfort, particularly under hot climate conditions. Thermal comfort refers to the state of physical and psychological satisfaction experienced under environmental conditions typically associated with temperatures between 20 and 40 °C and relative humidity levels ranging from 30% to 60% [1]. The A/C system operates according to the vapor-compression refrigeration cycle and comprises four thermodynamic processes undergone by the refrigerant, namely compression, condensation, expansion, and evaporation [2]. Under real operating conditions, the compressor is driven by a belt and pulley transmission system connected to the engine crankshaft, causing the compressor speed to vary continuously from approximately 950 rpm during engine idle conditions to 3000 rpm during on-road operation [3]. Consequently, compressor speed has a direct influence on the cooling capacity and energy consumption of the A/C system [4].

The compressor circulates the refrigerant through the A/C system and consumes energy to sustain the refrigeration cycle, thereby reducing the engine power available for vehicle propulsion. When the compressor is activated, the engine must increase its operating speed to meet the additional energy demand, which raises energy consumption by 3% to 20%, equivalent to approximately 0.2 to 1 L of fuel per 100 km in light-duty vehicles [5]. In compressors with a displacement of 210 cm^3, peak energy consumption can reach up to 6 kW [6].

The performance of automotive air conditioning systems is determined by the interaction among compressor type, refrigerant, lubricant, and system load conditions.

Santanu et al. [7] evaluated the effects of refrigerant charge, compressor speed, and evaporator airflow rate in an automotive A/C system using an experimental test bench operating with R-134a. The results showed that increasing the refrigerant charge raised the refrigerant mass flow rate and system pressure. Greater compressor speed increased the temperature and pressure in the compressor discharge region and improved the system cooling capacity. However, this also led to increased compressor power consumption, negatively affecting A/C system performance. Finally, they concluded that the optimal charge for the A/C system was 530 ±3 g of refrigerant, achieving greater cooling capacity at 1900 rpm and a higher COP at a compressor speed of 1600 rpm.

Macagnan et al. [8] studied the influence of refrigerant charge and compressor speed. The authors concluded that compressor speed can increase compressor work by up to 78% within the range of 1500 to 3500 rpm, while the COP tends to decrease as compressor revolutions increase. They also reported a slight increase in COP when the refrigerant charge in the system was increased.

Gomaa [9] conducted simulations to evaluate the performance of an automotive A/C system using several refrigerants proposed as alternatives to R-134a. The tests were performed at different compressor speeds, cabin temperatures, and condenser airflow rates. The results showed that a 5 °C increase in condenser air temperature decreased the cooling capacity by up to 27% when the system operated with R-134a. Increasing compressor speed raised the refrigerant mass flow rate in the evaporator and improved the cooling capacity. However, higher compressor speed is associated with greater friction and lower efficiency, which negatively affects the COP. The study also showed that R-1234ze has better thermal and environmental characteristics, while R-1234yf provides better thermal performance but requires system design modifications to compensate for reductions in COP and cooling capacity.

Lee et al. [10] conducted compressor design optimization studies using an experimental model and a simulation program to evaluate the effects of R-134a and R-1234yf within a compressor speed range of 1000 rpm to 4000 rpm, while controlling the evaporator temperature. The authors concluded that R-1234yf has a COP 5% lower than that of R-134a. By redesigning the compressor valves, the system improved its COP by up to 8% when the evaporator temperature was maintained at 5 °C. Increasing the compressor speed from 1000 to 2000 rpm enhanced the cooling capacity, whereas the COP decreased due to higher energy consumption. Within the speed range of 2000 to 4000 rpm, the COP decreased by 17%.

Alkan and Hosoz [11] compared fixed-displacement and variable-displacement compressors. They evaluated the compressors at different speeds and under different airflow rates through the evaporator and condenser. The results showed that the automotive A/C system with a fixed-displacement compressor, operating at 750 rpm, presented a cooling capacity that was 3.2% to 7.8% higher than that of the variable-capacity compressor. The system with a variable-capacity compressor had a lower COP at low rotational speeds, whereas at high speeds, it was more efficient than the system with a fixed-displacement compressor.

Shaker et al. [12] compared refrigerants intended to replace R-134a by implementing a test bench that simulated the operation of a single-stage heat pump at different compressor speeds. Pressure, temperature, and Coriolis-type flow sensors were installed, along with a frequency-controlled compressor operating at 35, 40, 45, and 50 Hz to simulate the behavior of R-1234yf and R-515B. The results showed that R-1234yf exhibited better cooling capacity performance. However, compressor work was also affected by the high

operating pressures. In addition, the operating temperatures of R-1234yf were 3 °C lower than those of R-515B, which may contribute to extending compressor life. Both refrigerants also had a lower global warming potential (GWP) than R-134a. For both refrigerants, increasing compressor speed enhanced cooling capacity because a greater amount of refrigerant circulated through the evaporator, which, in turn, implied higher compressor energy demand. Finally, R-515B offered lower cooling capacity but, due to its lower compressor work, maintained a COP that was 8% higher in cooling mode and 13% higher in heating mode than that of R-1234yf.

Alkan and İnan [13] conducted an experimental study showing that R-1234yf produced a 13.6% to 20.1% reduction in COP compared with R-134a in variable-capacity compressors, although it reduced exergy destruction in certain system components.

Zawawi et al. [14] demonstrated that lubricant selection is a determining factor in electric vehicle systems, since PAO-type oils provide greater efficiency, lower energy consumption, and higher cooling capacity than PVE and POE oils. Yusri et al. [15] analyzed the optimization of refrigerant volume and compressor oil in an automotive air conditioning system, demonstrating that these parameters directly influence system performance and dynamic behavior, and that efficiency can be improved through advanced statistical analysis and machine learning techniques. Overall, these results highlight the importance of integrating thermodynamic and operational variables into the design of automotive A/C systems to improve energy efficiency and performance.

The literature review reveals limited analysis of the influence of compressor speed on isentropic and volumetric efficiencies, which restricts the understanding of its effect on cooling capacity, energy consumption, and the performance of automotive A/C systems. Moreover, the experimental test benches used in previous studies do not control evaporator temperature, making it difficult to reproduce operating conditions similar to those of a real system. Finally, measurement limitations were identified due to physical factors, the limited number of measurement points, and the use of conventional sensors.

In the present work, an experimental test bench was developed to control compressor rotational speed and record temperature, pressure, and air velocity data through an automated real-time data acquisition system. The test bench includes a thermal chamber to control the inlet air temperature at the evaporator. In addition, the increase in fuel consumption associated with air conditioning operation is calculated, and correlations are proposed to estimate the compressor isentropic and volumetric efficiencies as functions of operating parameters such as rotational speed and pressure ratio.

2. Materials and Methods

2.1. Experimental Test Bench of the Automotive A/C System

The experimental test bench is a system designed to simulate and evaluate the operation of the automotive A/C system under controlled conditions. Figure 1 illustrates the experimental test bench, which consists of the refrigeration circuit, the compressor drive system, and the control and instrumentation system.

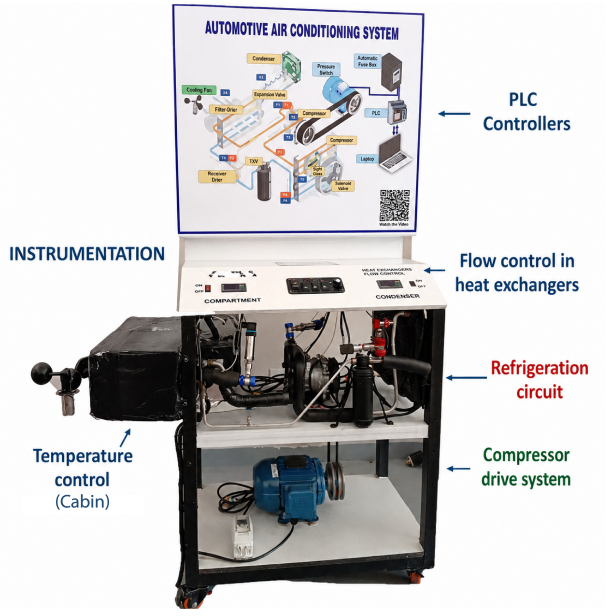

Figure 1. Experimental test bench of the automotive A/C system.

2.1.1. Refrigeration Circuit

The refrigeration circuit consists of an 87 cm^3 SD5H09 A/C compressor, a 3.5 m^2 evaporator with a cooling capacity of 12000 BTU (3.5 kW), a 7.2 m^2 condenser, a TI(E)1/20A5TR thermostatic expansion valve, a 515-3R external filter drier with switch, R-134a refrigerant, and PAG 100 compressor oil with a charge of 4.5 to 5 oz. The evaporator air blower is rated at 80 W and reaches 3800 rpm, controlled by a three-speed potentiometer, whereas the condenser fans are rated at 80 W and reach maximum speeds of 2250 rpm and 2100 rpm.

2.1.2. Compressor Drive System

Figure 2 shows the implementation of the compressor drive system. In internal combustion engine (ICE) vehicles, compressor speed depends on engine rotational speed, whereas in electric vehicles, it depends on the thermal demand of the cabin. In the experimental test bench, the compressor is driven by a 2.2 kW WEG-W22 three-phase electric motor through pulleys and

a V-belt with a tensioner. The electric motor speed is controlled by a KEWO-AD350 frequency inverter and SIEMENS LOGO 8 programmable logic controller (PLC) modules. Communication is performed through a 0 to 10 V analog reference signal sent by the PLC module, allowing the compressor speed to be controlled from a computer linked to the experimental test bench program.

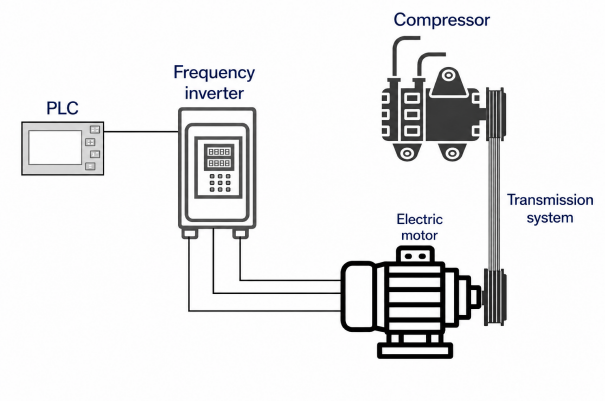

Figure 2. Compressor drive system.

The electric motor was sized by determining the compressor power consumption ($\dot{W}_m$) through an energy balance expressed in Equation (1), in which the isentropic compressor work, the isentropic efficiency (η_{iso}), and a heat loss coefficient to the environment (ϵ) due to natural convection in the compressor are considered [16].

$$\dot{W}_{comp} = \frac{\dot{m}(h_{2s} - h_1)}{\eta_{iso}(1 - \epsilon)} \tag{1}$$

The power supplied to the drive system ($\dot{W}_m$) is calculated considering the efficiencies of the electric motor (η_m) and the transmission system (η_p), as given in Equation (2) [16].

$$\dot{W}_m = \frac{\dot{W}_{comp}}{\eta_p * \eta_m} \tag{2}$$

Equation (3) expresses the dynamic analysis of the transmission system, where N_m is the rotational speed of the motor pulley, D_{pm} is the diameter of the motor pulley, N_c is the rotational speed of the compressor pulley, and D_{pc} is the diameter of the compressor pulley.

$$N_m * D_{pm} = N_c * D_{pc} \tag{3}$$

2.1.3. Instrumentation and Control System

The experimental test bench is designed to control compressor speed, cabin temperature, and airflow through the evaporator and condenser using the following systems.

Cabin Temperature Control

To simulate the temperature reached inside the cabin, a thermal chamber controlled by a PID controller was developed to activate and deactivate a direct-current electric resistance, generating up to 1000 W of power to heat the air entering the evaporator, as shown in Figure 1.

Airflow Control Through the Heat Exchangers

The airflow through the evaporator is controlled by a circuit that adjusts the electric fan speed across three levels, while the condenser airflow is controlled by a second fan activated by an STC 1000 PID controller when the condensation temperature configured in the test bench is reached.

Instrumentation and Data Acquisition

Four pressure sensors (P) were installed downstream of each component of the refrigeration circuit. Eight temperature sensors (T) were installed: four in the refrigeration circuit (1–4), one on the compressor casing (5), one at the evaporator air inlet (7), one at the evaporator air outlet (6), and one at the condenser air outlet (8). In addition, an anemometer was installed to measure the velocity of the air leaving the evaporator, as shown in Figure 3.

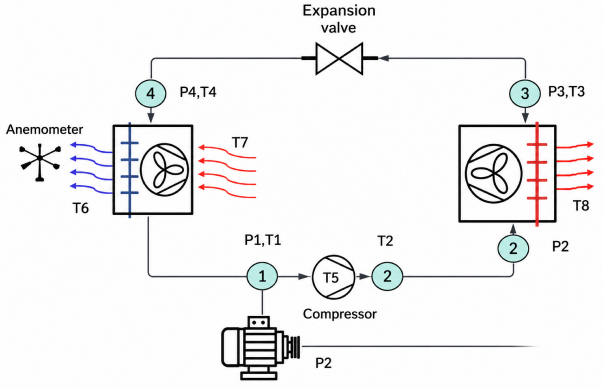

Figure 3. Sensors installed in the experimental test bench.

The PLC modules operate with analog and digital signals from 0 to 10 volts; therefore, the sensor signals must remain within the PLC operating range. The pressure sensors generate a 4 to 20 mA current signal, which is converted to a voltage range of 1.32 to 6.6 V through a 330 Ω resistance circuit.

The PT100 resistive temperature sensors change their resistance as a function of temperature and, when connected to an RTD transmitter, generate a 0 to 10 V signal. The anemometer is self-generating, does not require an external power supply, and produces a 0 to 2 V signal.

Monitoring, control, and data acquisition are performed using PLC modules (LOGO 8 12/24 RCE) and their corresponding expansion modules (AM2, AM2 AQ, AM2 RTD). The program was developed using LOGO Soft Comfort V8 software. In this program, the sensors were calibrated, analog signals were converted into measurement units, frequency inverter control was established, and data logging was configured. The monitoring interface was designed using LOGO Web Editor V1.1.0 (LWE) software [17]. This interface enables sensor monitoring, frequency inverter management, and data logging. Finally, the drive system equipment and sensors were calibrated and verified using equipment datasheets and reference instruments to ensure proper operation and result accuracy.

The uncertainty analysis of the measurements was performed according to the international ISO/IEC standard [18]. The combined (μ_c) and expanded (U_c) sensor uncertainties were evaluated, considering the uncertainty of each sensor (μ_s), the PLC uncertainty (μ_{PLC}) associated with the 10-bit ADC, and the repeatability uncertainty (μ_r) for 10 repetitions. Table 1 summarizes the sensor uncertainties.

Table 1. Sensor Uncertainties

Sensor	Tolerance	μ_s	μ_{PLC}	μ_r	μ_c	U_c
PT100 Temperature (-100°C–200°C)	± 0.3 °C	0.173 °C	0.085 °C	0.081 °C	0.209 °C	±0.418 °C
HK1100C pressure transducer (0–1.2 MPa)	± 1.5% FS ±0.018 MPa	0.0104 MPa	0.00034 MPa	0.00069 MPa	0.0104 MPa	±0.0208 MPa
DIY Anemometer (0–30 m/s)	±0.3 m/s	0.173 m/s	0.0085 m/s	0.068 m/s	0.186 m/s	±0.372 m/s

Sensor calibration was performed according to ISO/IEC Guide 99:2007 [19]. The PT100 sensors were calibrated in accordance with IEC 60751:2022 [20] by comparison with a reference standard thermometer (PIDMaxwell MLC-48) inside the thermal chamber, using two calibration points, 35 °C and 40 °C, which cover the operating range of the vehicle cabin. The maximum observed deviation was ±1 °C, within the specified class B tolerance. The HK1100C pressure sensors were calibrated according to IEC 62828-2:2017 [21], with a maximum observed deviation of ±0.021 MPa. Meanwhile, the DIY anemometer was calibrated by comparison with an Extech AN100-NIST anemometer, with a maximum observed deviation of ±0.25 m/s.

2.2. Experimental Campaign

The tests conducted on the experimental test bench represent real operating conditions of the A/C system in light-duty vehicles, as shown in Table 2.

Table 2. Test Matrix

Temperature in the passenger compartment (°C)	Compressor speed compressor (RPM)	Flow rate evaporator (m^3/h)	Flow rate condenser (m^3/h)
35–40–45	900–2800	313	496

Table 2 shows the parameters configured in the experimental test bench for testing and data collection. The cabin temperature varied from 35 to 45 °C, a range that can be reached in Riobamba [22, 23]. Under real operating conditions, the compressor rotational speed is 900 rpm under idling conditions, 1800 rpm during urban driving, and up to 3000 rpm on highways [3, 4]. In addition, the evaporator airflow was maintained at its maximum capacity, while the condenser airflow was generated by a single fan.

Cabin temperature control is performed using an STC-1000 PID temperature controller, as shown in Figure 4 (A). Control of the evaporator airflow and the compressor electromagnetic clutch is performed from the panel shown in Figure 4 (B), while condenser airflow control is achieved using an STC-1000 PID temperature controller, as shown in Figure 4 (C).

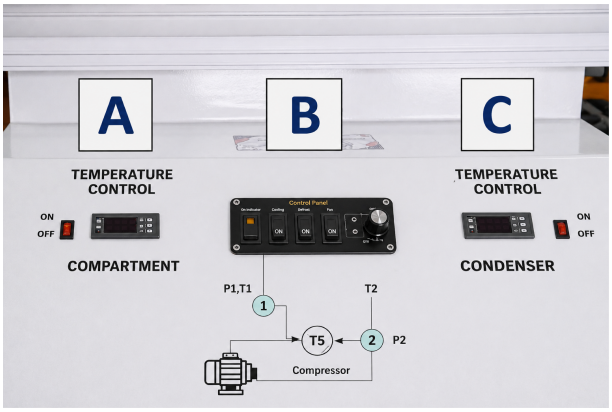

Figure 4. Experimental Test Bench Controls.

2.3. Thermodynamic Model of the Automotive A/C System

The data obtained from the experimental test bench sensors are recorded in a (.csv) file generated by LOGO

8 Soft Comfort software. To analyze the performance of the A/C system, the refrigerant mass flow rate delivered by the compressor, evaporator cooling capacity, compressor power consumption, and coefficient of performance (COP) must be calculated. To this end, a thermodynamic model was implemented considering energy transfers in the heat exchangers and compressor performance in terms of isentropic and volumetric efficiencies. The thermodynamic model is based on a steady-state analysis of an open system, assuming one-dimensional refrigerant flow and negligible variations in kinetic and potential energy. Heat losses to the surroundings are considered negligible, except in the heat exchangers and the compressor. Thermophysical properties are obtained from the NIST database [24]. The compressor is modeled using isentropic and volumetric efficiencies [16], while the heat exchangers are analyzed using energy balances based on the calorimetric method [25]. Isenthalpic expansion is assumed in the thermostatic expansion valve, and pressure losses in pipes and fittings are considered negligible compared with those of the main components.

The refrigerant mass flow rate was calculated through an energy balance in the evaporator, according to Equation (4) and based on the calorimetric method described in EN 13771-1 [25], where $\dot{m}_{ref}$ is the refrigerant mass flow rate, $\dot{m}_{air}$ is the air mass flow rate, ΔT_{6-7} is the temperature difference between the inlet and outlet air of the evaporator, as shown in Figure 3, Cp_{air} is the specific heat of air, and Δh_{1-4} is the refrigerant enthalpy difference between the inlet and outlet of the evaporator.

$$\dot{m}_{ref} = \frac{\dot{m}_{air} * Cp_{air} * \Delta T_{6-7}}{\Delta h_{1-4}} \tag{4}$$

The air mass flow rate is calculated from the volumetric airflow rate and air density, as given in Equation (5). The volumetric airflow rate is determined by multiplying the airflow passage area at the evaporator outlet (A_{air}), the density of the air leaving the evaporator (ρ_{air}), and the flow velocity ($\vec{V}_{air}$) measured by the anemometer, as shown in Figure 3 [2].

$$\dot{m}_{air} = \rho_{air} * A_{air} * \vec{V}_{air} \tag{5}$$

The evaporator cooling capacity ($\dot{Q}_{evap}$) is calculated using Equation (6) [16].

$$\dot{Q}_{evap} = \dot{m}_{ref} * (h_1 - h_4) \tag{6}$$

The volumetric efficiency (n_v) represents the relationship between the theoretical and actual capacity of the compressor to drive the refrigerant through the system. It is calculated using Equation (7) [16], [23], where $\dot{V}_s$ is the volumetric displacement of the compressor and ρ_{in} is the density of the refrigerant entering the compressor.

$$n_v = \frac{\dot{m}_{ref}}{\rho_{in} * \dot{V}_s} \tag{7}$$

The compressor isentropic efficiency (η_{iso}) represents the relationship between the ideal and actual energy required to compress the refrigerant. It is calculated using Equation (8) [16] [23], where h_1 is the refrigerant enthalpy at the compressor suction, h_{2s} is the discharge enthalpy during isentropic compression, and h_2 is the discharge enthalpy during actual compression.

$$\eta_{iso} = \frac{h_{2s} - h_1}{h_2 - h_1} \tag{8}$$

The energy consumed by the compressor is greater than the energy transferred to the refrigerant because of heat losses ($\dot{Q}_p$) caused by system irreversibilities. The heat rejected from the compressor to the surroundings is calculated using Equation (9) [26], where h_{amb} is the natural convection coefficient, A_c is the compressor surface area, T_s is the compressor casing temperature, and T_{amb} is the ambient temperature.

$$\dot{Q}_p = h_{amb} * A_c * (T_s - T_{amb}) \tag{9}$$

The work transferred to the refrigerant ($\dot{W}_{fluid}$) is determined using Equation (10).

$$\dot{W}_{fluid} = \dot{m}_{ref} * (h_2 - h_1) \tag{10}$$

The compressor heat rejection coefficient (ϵ_{Qp}) is calculated using Equation (11) [27].

$$\epsilon_{Qp} = \frac{\dot{Q}_p}{\dot{W}_{fluid} + \dot{Q}_p} \tag{11}$$

The compressor energy consumption is calculated using Equation (12).

$$\dot{W}_c = \frac{\dot{m}_{ref}(h_{2s} - h_1)}{\eta_{iso}(1 - \epsilon_{Qp})} \tag{12}$$

Finally, the system COP is used to evaluate the operating efficiency of the automotive A/C systemby relating the cooling capacity to the compressor energy consumption. It is calculated using Equation (13).

$$COP = \frac{\dot{Q}_{evap}}{\dot{W}_c} \tag{13}$$

Fuel consumption associated with air conditioning operation is estimated by considering the energy transformations in a gasoline-powered internal combustion engine (ICE) vehicle, as shown in Figure 5. This transformation begins in the internal combustion engine, which converts fuel energy into thermal energy and subsequently into mechanical energy at the crankshaft. These energy transformations have efficiencies between 27% and 30% [28]. Losses also occur in the transmission mechanisms connecting the crankshaft

to the compressor, with efficiencies between 80% and 93% [29].

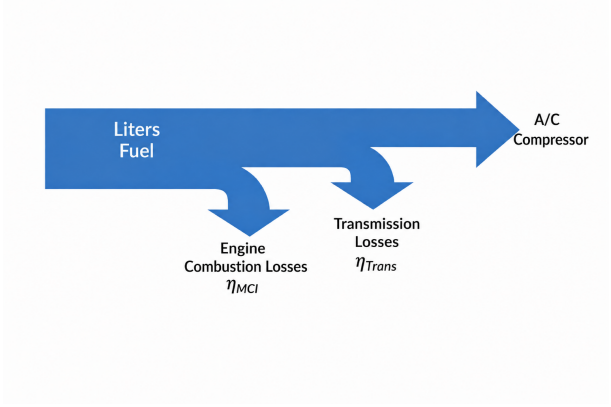

Figure 5. Energy transformation in an ICE vehicle for compressor operation [30].

The energy delivered by the fuel (E_{tot}) is calculated by dividing the energy consumed by the compressor (E) by the internal combustion engine efficiency (η_{MCI}) and the transmission efficiency (η_{trans}), as given in Equation (14).

$$E_{tot} = \frac{E}{\eta_{MCI} * \eta_{trans}} \tag{14}$$

Fuel consumption in liters (l_{fuel}) is obtained by dividing (E_{tot}) by the fuel lower heating value (PCI_{fuel}) and the fuel density (ρ_{fuel}), as given in Equation (15).

$$l_{fuel} = \frac{E_{tot}}{PCI_{fuel} * \rho_{fuel}} \tag{15}$$

An LHV of 46522.5 kJ/kg and a density of 739 kg/m^3 were used for gasoline [31].

3. Results and Discussion

A total of 60 experimental points were obtained according to the test matrix in Table 2 to analyze the influence of compressor speed and cabin temperature on compressor operation and automotive A/C system performance. To validate the results, the experimental values were compared with those predicted by the thermodynamic model. The percentage deviations were 1.66% for the COP, 4.85% for cooling capacity, 4.91% for compressor power, 4.86% for refrigerant mass flow rate, 3.08% for isentropic efficiency, and 9.83% for volumetric efficiency. Likewise, the overall energy balance showed a closure error of 6.05%. The observed differences are mainly attributed to measurement uncertainties, model simplifications and unaccounted thermal losses. Overall, these results demonstrate good agreement between the model and the physical behavior of the system.

3.1. Compressor Performance

3.1.1. Compressor Discharge Temperature

Figure 6 shows that the compressor discharge temperature rises as the compressor rotational speed increases. At a cabin temperature of 35 °C, the discharge temperature increases by 34.3%, from 58.16 °C to 78.13 °C, within the range of 900 to 2800 rpm. Similar results were also reported in [12].

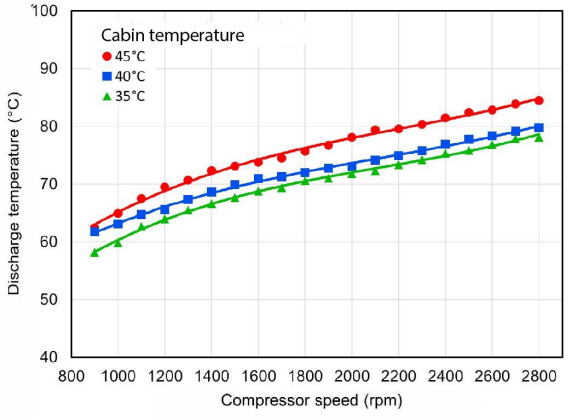

Figure 6. Discharge temperature as a function of compressor speed.

The compressor discharge temperature increases by 4.3 to 7.1 °C when the cabin temperature rises by 10 °C. However, the temperatures reached remain within the safe operating range, below 115 °C, preventing possible lubricating oil degradation that could compromise the mechanical integrity of the compressor.

This behavior occurs because increasing compressor speed raises the compression work and, consequently, the energy transferred to the refrigerant, thereby increasing the discharge temperature. In addition, greater process irreversibilities and limited heat dissipation to the surroundings contribute to the observed temperature rise.

3.1.2. Refrigerant Mass Flow Rate

Figure 7 shows that, at a cabin temperature of 35 °C, the mass flow rate increases by 50.3% as the compressor speed rises from 900 to 2800 rpm, because the compressor drives a greater amount of refrigerant per unit time.

When the cabin temperature increases from 35 to 40 °C, the refrigerant mass flow rate rises by 16.8% at 900 rpm, 21.0% at 1800 rpm, and 22.5% at 2800 rpm. This trend indicates that refrigerant circulation increases as cabin temperature rises. When the air passing through the evaporator is hotter, the refrigerant has a higher density at the compressor inlet because its temperature and pressure increase, which,

according to Equation (7), raises the mass flow rate. Similar results were reported in [32].

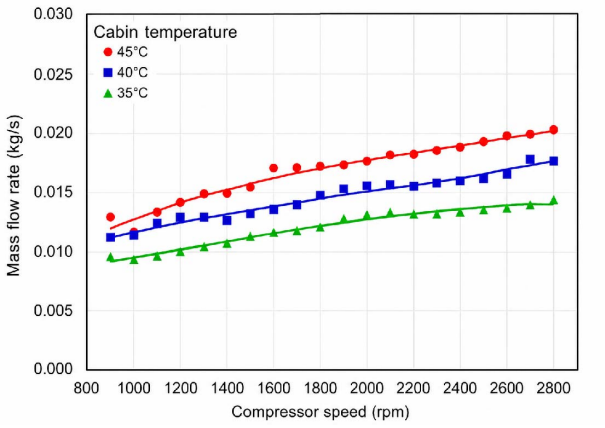

Figure 7. Refrigerant mass flow rate as a function of compressor speed.

From a physical perspective, the increase in refrigerant mass flow rate is directly related to the greater displaced volume per unit time and to variations in the thermodynamic properties of the refrigerant at the compressor suction, which increase refrigerant density and promote higher refrigerant circulation within the system.

3.1.3. Compressor Power Consumption

Figure 8 shows that as the compressor speed increases, a greater amount of energy is consumed. At a cabin temperature of 35 °C, the compressor power consumption increases from 0.287 kW to 0.878 kW when the speed rises from 900 to 2800 rpm. This increase is due to the greater amount of refrigerant driven by the compressor, as shown in Figure 7.

At high compressor speeds, the pressure ratio (PR) is greater, meaning that the compressor must reach a higher pressure in the high-pressure line, which increases the power required to compress the refrigerant. This behavior results from the higher pressure ratio, which raises the specific compression work, while the greater mass flow rate increases the total power requirement. Overall, these effects reflect increased irreversibilities and mechanical losses at high operating speeds.

When the cabin temperature increases from 35 to 40 °C, compressor power consumption also rises by 11.0%, 19.4%, and 20.6% at 900, 1800, and 2800 rpm, respectively. This increase becomes even more evident when the cabin temperature reaches 45 °C, because the cooling demand increases and a greater refrigerant mass flow rate must be compressed, as shown in Figure 7.

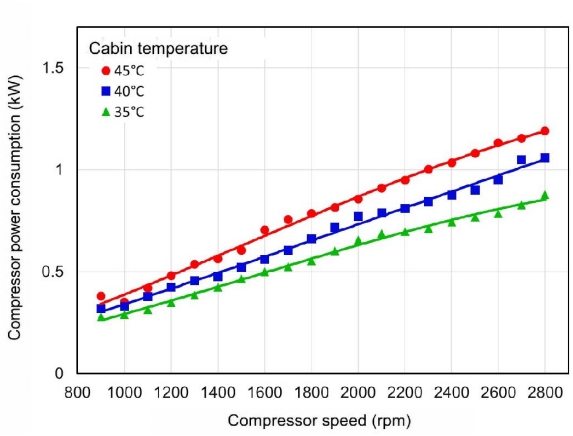

Figure 8. Compressor power consumption as a function of compressor speed.

3.1.4. Compressor Isentropic Efficiency

Figure 9 shows that isentropic efficiency decreases as compressor speed increases. At a cabin temperature of 35 °C, isentropic efficiency decreases by 22.66% when compressor speed rises from 1000 to 2800 rpm. Energy losses occur due to isenthalpic pressure drops in the suction valve, which generate flow turbulence, reduce compressor capacity, and increase energy consumption. This effect also occurs in the discharge valve [9]. Another contributing factor is the energy released by the compressor as heat. From a thermodynamic perspective, the decrease in isentropic efficiency is associated with increased internal irreversibilities, such as friction, turbulence, and thermal losses, which intensify as compressor operating speed increases.

When the cabin temperature increases from 40 to 45 °C, the efficiencies tend to decrease slightly, by 2.7% at 1000 rpm and 1% at 2800 rpm. As the temperature of the air passing through the evaporator increases, the refrigerant evaporation temperature and pressure also rise, increasing losses associated with pressure drops and heat transfer.

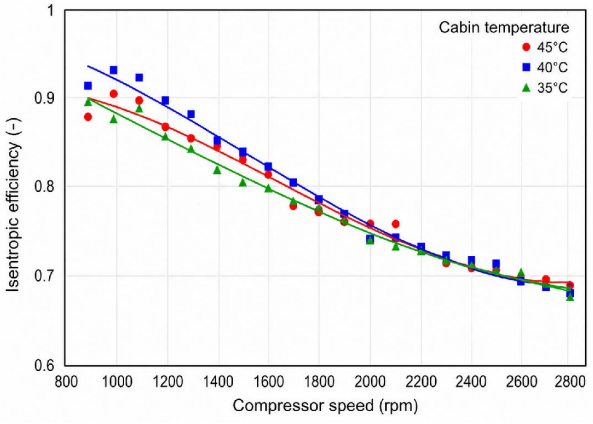

Figure 9. Isentropic efficiency as a function of compressor speed.

To provide a simple mathematical function for estimating compressor efficiency under different operating conditions, a linear regression was performed by correlating isentropic efficiency with compressor speed (ω_{comp}) and pressure ratio (PR), as given in Equation (16).

$$\eta_{iso} = 1.1905 + 0.000071\omega_{comp} - 0.1295PR \quad (16)$$

Figure 10 illustrates the comparison between the experimental isentropic efficiency values and those calculated using correlation (16). The results show a good fit for all points, with a maximum deviation of ±7% and a correlation coefficient r^2 of 0.914. The proposed correlation can be used to model compressor behavior in automotive A/C systems and predict compressor energy consumption.

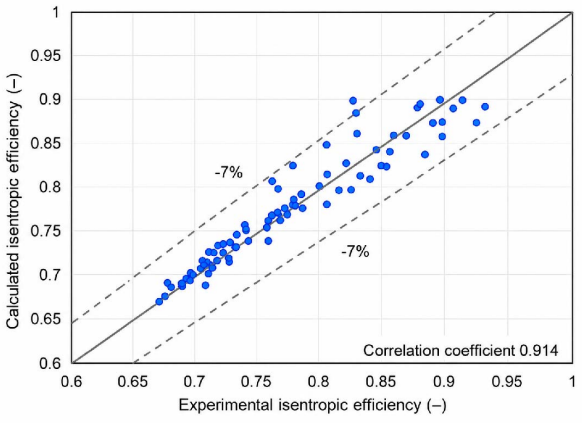

Figure 10. Comparison of the experimental and calculated values of compressor isentropic efficiency.

3.1.5. Compressor Volumetric Efficiency

Figure 11 shows that volumetric efficiency decreases as compressor rotational speed increases. At a cabin temperature of 35 °C, volumetric efficiency decreases by 44% within the range of 900 to 2800 rpm. Similar results were also reported in [33]. This behavior can be attributed to increased internal leakage, recirculation losses, and refrigerant compressibility effects, which become more significant at high speeds, reducing the effective suction capacity of the compressor.

An increase of 5 °C in cabin temperature results in a volumetric efficiency increase of 9.5% and 12.6% at 900 and 2800 rpm, respectively. This behavior occurs because the compressor heats up due to the refrigerant compression process and friction between the mechanical components. At higher compressor speeds, heat generation also increases. This heat is transferred to the compressor casing and to the suction and discharge ducts; consequently, the refrigerant expands reducing its density and decreasing the amount of refrigerant displaced by the compressor. In addition, compressors operate with a pressure difference between the suction and discharge sides, generating leakage of approximately 4.80% in the valve seating area [33]. This effect becomes more critical as the compressor rotational speed increases, since the pressure ratio (PR) also rises. Similarly, the pressure ratio produces greater pressure losses between the cylinder wall and the piston, negatively affecting volumetric efficiency [32]. Another factor influencing efficiency occurs during compression, when a small portion of the refrigerant tends to condense and then re-evaporate during suction, leading to the formation of liquid particles that increase the dead volume inside the cylinder. This effect is referred to as recirculating mass [33].

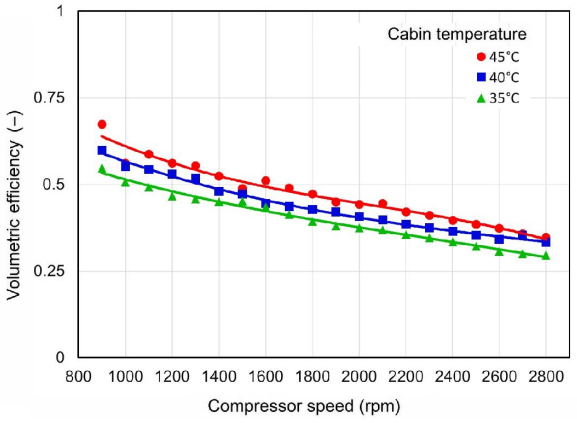

Figure 11. Volumetric efficiency as a function of compressor speed.

To determine a correlation for compressor volumetric efficiency, a regression was performed as a function of compressor speed (ω_{comp}), pressure ratio (PR), evaporation temperature ($T_{sat;evap}$), and refrigerant superheating at the evaporator outlet (SH), as given in Equation (17). The variables $T_{sat;evap}$ and SH are included in the correlation because refrigerant density changes at the compressor suction, directly affecting the displaced mass flow rate and, consequently, volumetric efficiency. When the system operates with high SH values, density varies at the same evaporation pressure. Therefore, considering only, the PR is insufficient, and SH and $T_{(sat;evap)}$ must also be included in the equation.

$$\begin{aligned}\eta_v = {} & 0.2576 + 0.000056\,\omega_{\text{comp}} - 0.0797\,PR \\ & + 0.01881\,T_{\text{sat,evap}} \\ & + 0.01908\,SH\end{aligned} \quad (17)$$

Figure 12 illustrates the comparison between the experimental volumetric efficiency values and those calculated using correlation (17).

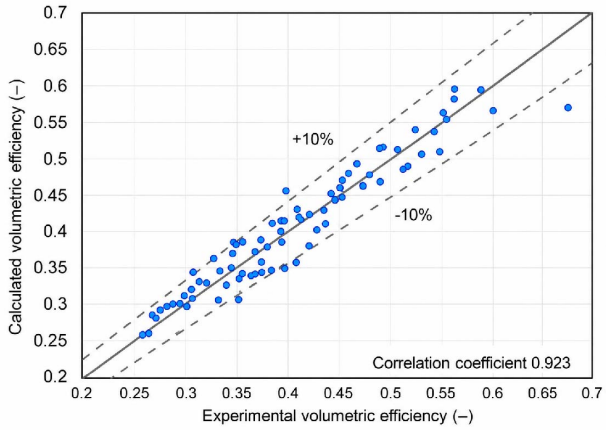

Figure 12. Comparison of the experimental and calculated values of compressor volumetric efficiency.

The results show a good fit for all points, with a maximum deviation of ±10% and a correlation coefficient r^2 of 0.923. The proposed correlation can be used to model compressor behavior in automotive A/C systems and predict the mass flow rate displaced by the compressor.

3.2. Performance of the Automotive A/C System

3.2.1. Cooling Capacity

Figure 13 shows that cooling capacity rises with increasing compressor rotational speed.

At a cabin temperature of 40 °C, increasing compressor speed from 900 to 2800 rpm raises the cooling capacity by 24.3%, whereas at 35 °C, the increase is 22.4%. Higher compressor speed leads to greater refrigerant circulation through the evaporator.

Cabin temperature also influences cooling capacity; greater cooling capacities are obtained as cabin temperature increases due to the higher mass flow rate as shown in Figure 7. Similar results were reported in [32] and [34].

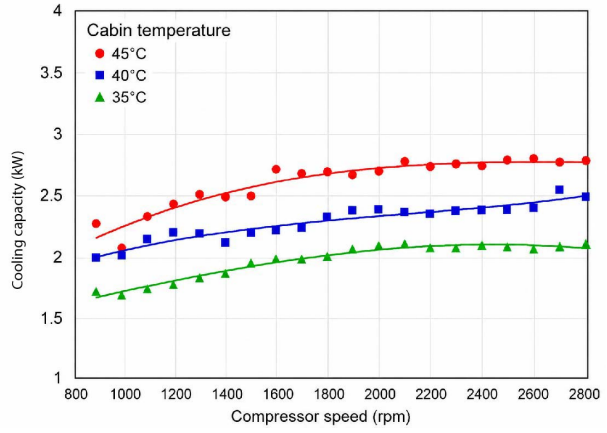

Figure 13. Cooling capacity as a function of compressor speed.

3.2.2. Coefficient of Performance (COP)

Figure 14 shows that, at a cabin temperature of 35 °C, the COP decreases by up to 61.27% as compressor rotational speed increases from 900 to 2800 rpm. Although the cooling capacity improves at higher compressor rotational speeds, power consumption also increases significantly, thereby reducing the system COP.

At higher speeds, greater energy losses occur due to friction in the moving components of the compressor, which reduces the COP [9]. When the cabin temperature increases from 40 °C to 45 °C, the COP decreases by 4.86% at 900 rpm and by 1.02% at 2800 rpm. However, cabin temperature has a smaller effect on the COP than on cooling capacity and compressor power consumption.

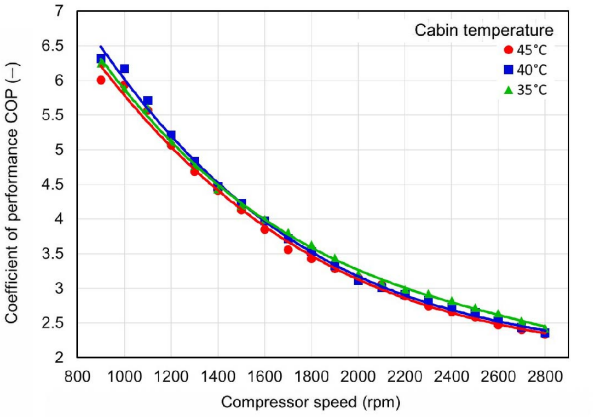

Figure 14. COP as a function of compressor speed.

3.2.3. Fuel Consumption

Figure 15 shows that fuel consumption rises when the engine operates at higher speed. At a cabin temperature of 45 °C, consumption increases by 213% from 900 to 2800 rpm because the compressor drives a greater amount of refrigerant.

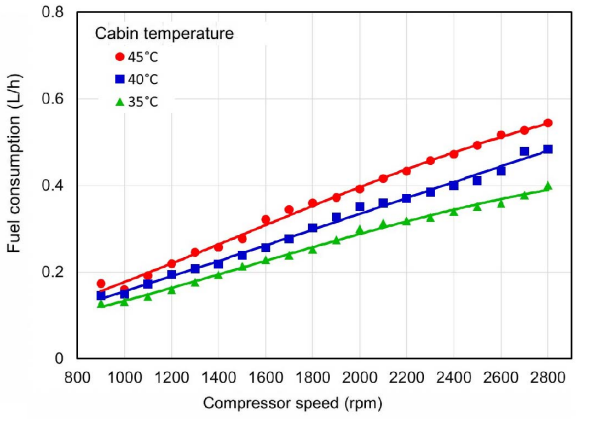

Figure 15. Fuel consumption of the automotive A/C system as a function of compressor speed.

As the cabin temperature increases, fuel consumption also rises. At 2800 rpm, corresponding to highway conditions, consumption increases from 0.40 L/h at 35 °C to 0.54 L/h at 45 °C. Similar results were reported in [35].

4. Conclusions

Increasing compressor speed raises the refrigerant mass flow rate, improving heat transfer capacity inside the vehicle. However, it also increases energy demand, leading to higher power and fuel consumption.

At a cabin temperature of 35 °C, increasing compressor speed from 900 to 2800 rpm raises the refrigerant mass flow rate by 50.3% and power consumption from 0.287 to 0.878 kW. Under the same conditions, compressor isentropic efficiency decreases by 22.66%, while volumetric efficiency decreases by 44%.

The compressor discharge temperature increases at higher rotational speeds, exceeding 80 °C. At a cabin temperature of 35 °C, increasing compressor speed from 900 to 2800 rpm raises the cooling capacity by 22.4%, whereas the system COP decreases by up to 61.27%. Although cooling capacity improves at higher compressor rotational speeds, power consumption also increases significantly, thereby reducing the system COP.

Fuel consumption doubles when compressor speed increases from 900 to 2800 rpm at a cabin temperature of 45 °C, reaching an instantaneous consumption of 0.54 L/h at 2800 rpm.

Contributor role

- **Iván M. Ashqui-Cuvi:** Data curation, formal analysis, validation, writing – original draft.
- **Klever S. Morales-Morales:** Data curation, formal analysis, validation, writing – original draft.
- **Daniela C. Vásconez-Núñez:** Conceptualization, research, methodology, supervision, writing – review and editing of results analysis.
- **Fernando M. Tello-Oquendo:** Conceptualization, research, methodology, supervision, writing – review and editing of results analysis.
- **Fabián C. Gunsha-Maji:** Data curation, formal analysis, and methodology.

References

[1] ANSI/ASHRAE, *ANSI/ASHRAE Standard 55-2017: Thermal Environmental Conditions for Human Occupancy*, ASHRAE Std., 2017, accessed: 2026-05-19. [Online]. Available: https://upsalesiana.ec/ing36ar7r1

[2] Y. A. Cengel, M. A. Boles, and M. Kanoglu, *Termodinámica*, 9th ed. Madrid: McGraw-Hill Education, 2019. [Online]. Available: https://upsalesiana.ec/ing36ar7r2

[3] R. Mcenaney, D. E. C. Boewe, J. M. Yin, Y. C. Park, C. Bullard, and P. S. Hrnjak, "Experimental comparison of mobile A/C systems when operated with transcritical CO_2 versus conventional R134A," in *Semantic Scholar*, 1998. [Online]. Available: https://upsalesiana.ec/ing36ar7r3

[4] Z. Diao, Y. Zhang, C. Li, X. Liu, and Z. Liu, "Dynamic characteristics of an automotive air-conditioning electromagnetic clutch," *Processes*, vol. 12, no. 1, p. 80, Dec. 2023. [Online]. Available: https://doi.org/10.3390/pr12010080

[5] S. Vashisht and D. Rakshit, "Recent advances and sustainable solutions in automobile air conditioning systems," *Journal of Cleaner Production*, vol. 329, p. 129754, Dec. 2021. [Online]. Available: https://doi.org/10.1016/j.jclepro.2021.129754

[6] NREL, "Significant fuel savings and emission reductions by improving vehicle air conditioning," National Renewable Energy Laboratory, Tech. Rep., 2004, presented at the 15th Annual Earth Technologies Forum and Mobile Air Conditioning Summit. [Online]. Available: https://upsalesiana.ec/ing36ar7r6

[7] S. P. Datta, P. K. Das, and S. Mukhopadhyay, "Effect of refrigerant charge, compressor speed and air flow through the evaporator on the performance of an automotive air conditioning system," *Proceedings of the International Refrigeration and Air Conditioning Conference (IRACC)*, 2014, paper No. 2399. [Online]. Available: https://upsalesiana.ec/ing36ar7r7

[8] M. Macagnan, J. Copetti, R. Souza, R. Reichert, and M. Amaro, "Analysis of the influence of refrigerant charge and compressor duty cycle in an automotive air conditioning system," in *Conference: 22nd International Congress of Mechanical Engineering (COBEM 2013)*, 12 2013. [Online]. Available: https://upsalesiana.ec/ing36ar7r8

[9] A. Gomaa, "Performance characteristics of automotive air conditioning system with refrigerant R134a and its alternatives," *International Journal of Energy and Power Engineering*, vol. 4, no. 3, p. 168, 2015. [Online]. Available: https://doi.org/10.11648/j.ijepe.20150403.15

[10] T. Lee, K.-H. Shin, J. Kim, D. Jung, and J.-H. Kim, "Design optimization of external variable displacement compressor with R1234yf for vehicle air conditioning system," *Applied Thermal Engineering*, vol. 198, p. 117493, Nov. 2021. [Online]. Available: https://doi.org/10.1016/j.applthermaleng.2021.117493

[11] R.-F. Horng, Y.-P. Chang, and S.-C. Wu, "Investigation on the production of hydrogen rich gas in a plasma converter for motorcycle applications," *Energy Conversion and Management*, vol. 47, no. 15-16, pp. 2155–2166, 2006. [Online]. Available: https://doi.org/10.1016/j.enconman.2005.12.010

[12] A. K. S. Al-Sayyab, J. Navarro-Esbrí, A. Barragán-Cervera, and A. Mota-Babiloni, "Effect of compressor speed on heat pump performance with climate-friendly refrigerants," *International Journal of Refrigeration*, vol. 177, pp. 296–304, 2025. [Online]. Available: https://doi.org/10.1016/j.ijrefrig.2025.05.027

[13] A. Alkan and M. S. İnan, "Experimental investigation of the effects of compressor types on the performance of an automobile air conditioning system using R1234yf," *International Journal of Refrigeration*, vol. 155, pp. 58–66, Nov. 2023. [Online]. Available: https://doi.org/10.1016/j.ijrefrig.2023.09.004

[14] N. N. M. Zawawi, A. R. M. Aminullah, W. H. Azmi, and H. M. Ali, "Performance comparison of electric vehicle air-conditioning system using R1234yf with various compressor lubricants," *Applied Thermal Engineering*, vol. 288, p. 129652, Mar. 2026. [Online]. Available: https://doi.org/10.1016/j.applthermaleng.2025.129652

[15] K. Zhang, D. Wu, K. Xu, and F. Zhan, "Design method for improving the electromagnetic and temperature performance of the four-way valve," *International Journal of Refrigeration*, vol. 154, pp. 19–32, Oct. 2023. [Online]. Available: https://doi.org/10.1016/j.ijrefrig.2023.07.018

[16] American Society of Heating, Refrigerating and Air-Conditioning Engineers, *ASHRAE Handbook—HVAC Systems and Equipment (SI Edition)*. Atlanta, GA, USA: ASHRAE, 2024. [Online]. Available: https://upsalesiana.ec/ing36ar7r16

[17] SIEMENS, *Ayuda en pantalla de LOGO Soft Comfort*, Siemens AG, 2022, software documentation / online help. [Online]. Available: https://upsalesiana.ec/ing36ar7r17

[18] ISO/IEC, *ISO/IEC Guide 98-1:2024 — Guide to the Expression of Uncertainty in Measurement — Part 1: Introduction*, ISO Std., 2024. [Online]. Available: https://upsalesiana.ec/ing36ar7r18

[19] ISO, *ISO/IEC Guide 99:2007: International Vocabulary of Metrology — Basic and General Concepts and Associated Terms (VIM)*, ISO Std., 2007, accessed: 2026-05-19. [Online]. Available: https://upsalesiana.ec/ing36ar7r19

[20] International Electrotechnical Commission (IEC), *IEC 60751:2022: Industrial Platinum Resistance Thermometers and Platinum Temperature Sensors*, IEC Std., 2022, accessed: 2026-05-19. [Online]. Available: https://upsalesiana.ec/ing36ar7r20

[21] ——, *IEC 62828-2:2017: Reference Conditions and Procedures for Testing Industrial and Process Measurement Transmitters – Part 2: Specific Procedures for Pressure Transmitters*, IEC Std., 2017, accessed: 2026-05-19. [Online]. Available: https://upsalesiana.ec/ing36ar7r21

[22] J. A. Chica Yuqui and M. P. Vinueza Cisneros, "Estudio de la influencia de la radiación solar en el calentamiento de vehículos tipo SUV," Riobamba, Ecuador, 2023. [Online]. Available: http://dspace.espoch.edu.ec/bitstream/123456789/19222/1/65T00497.pdf

[23] J. Trujillo Tello, C. Machado Solís, D. Vásconez Núñez, and F. Tello Oquendo, "Analysis of the thermal behavior of a vehicle cabin using a dynamic thermal model," *The Ecuadorian Journal of S.T.E.A.M.*, vol. 2, no. 4, pp. 1204–1217, 2021, accessed: 2026-05-19. [Online]. Available: https://doi.org/10.18502/espoch.v2i4.11747

[24] E. W. Lemmon, M. L. Huber, and M. O. McLinden, *NIST Standard Reference Database 23: Reference Fluid Thermodynamic and Transport Properties — REFPROP, Version 9.0*, National Institute of Standards and Technology, Gaithersburg, MD Std., 2010, accessed: 2026-05-19. [Online]. Available: https://upsalesiana.ec/ing36ar7r24

[25] European Committee for Standardization (CEN), *EN 13771-1:2017: Compressors and Condensing Units for Refrigeration — Performance Testing and Test Methods — Part 1: Refrigerant Compressors*, CEN Std., 2017, accessed: 2026-05-19. [Online]. Available: https://upsalesiana.ec/ing36ar7r25

[26] G. F. Nellis and S. A. Klein, *Heat Transfer*. New York, NY, USA: Cambridge University Press, 2009, accessed: 2026-05-19. [Online]. Available: https://upsalesiana.ec/ing36ar7r26

[27] E. Granryd, I. Ekroth, P. Lundqvist, Å. Melinder, B. Palm, and P. Rohlin, *Refrigerating Engineering*. Stockholm, Sweden: Royal Institute

of Technology (KTH), 2003. [Online]. Available: https://upsalesiana.ec/ing36ar7r27

[28] E. A. Llanes Cedeño, J. B. Carguachi-Caizatoa, and J. C. Rocha-Hoyos, "Evaluación energética y exergética en un motor de combustión interna ciclo Otto de 1.6l," *Enfoque UTE*, vol. 9, no. 4, pp. 221–232, Dec. 2018. [Online]. Available: http://doi.org/10.29019/enfoqueute.v9n4.365

[29] Megadyne, *Saving Energy with Efficient Belt Drives*. MegadyneGroup, 2025, e-book, Accessed: 2026-05-19. [Online]. Available: https://upsalesiana.ec/ing36ar7r29

[30] D. C. Vásconez Núñez, "Desarrollo de un modelo para el cálculo del consumo de climatización en vehículos de pasajeros urbanos." Ph.D. dissertation, Universitat Politecnica de Valencia, 2019. [Online]. Available: http://doi.org/10.4995/Thesis/10251/121133

[31] J. M. Mantilla González, B. J. Aguirre Junco, and S. P. L. Andrés, "Experimental evaluation of a spark-ignited engine using biogas as fuel," *Ingeniería e Investigación*, vol. 28, no. 2, pp. 131–141, 2008, accessed: 2026-05-19. [Online]. Available: https://upsalesiana.ec/ing36ar7r31

[32] J.M. Belman-Flores, J.M. Barroso-Maldondao, J.M. Mendoza-Miranda, A. Gallegos-Muñoz, J.M. Riesco Ávila, and C. Rubio-Maya, "Simulación energética de un aire acondicionado automotriz trabajando con refrigerantes R-1234yf y R-134a," *XIX Congreso Internacional Anual de la SOMIM*, 2013. [Online]. Available: https://doi.org/10.13140/2.1.2061.4725

[33] B. Tremeac, A. K. Datta, M. Hayert, and A. Le-Bail, "Thermal stresses during freezing of a two-layer food," *International Journal of Refrigeration*, vol. 30, no. 6, pp. 958–969, 2007. [Online]. Available: https://doi.org/10.1016/j.ijrefrig.2007.01.012

[34] J. Navarro-Esbrí, J. Mendoza-Miranda, A. Mota-Babiloni, A. Barragán-Cervera, and J. Belman-Flores, "Experimental analysis of R1234yf as a drop-in replacement for R134a in a vapor compression system," *International Journal of Refrigeration*, vol. 36, no. 3, pp. 870–880, May 2013. [Online]. Available: https://doi.org/10.1016/j.ijrefrig.2012.12.014

[35] C. Ding, T. Nie, and Y. Chen, "A distribution network solid-state DC circuit breaker with current limiting function," *Energy Reports*, vol. 8, pp. 986–994, Apr. 2022. [Online]. Available: https://doi.org/10.1016/j.egyr.2021.11.052

Scientific Paper / Artículo Científico

UNIVERSIDAD POLITÉCNICA SALESIANA ECUADOR
INGENIUS
Revista de Ciencia y Tecnología
https://doi.org/10.17163/ings.n36.2026.08
pISSN: 1390-650X / eISSN: 1390-860X

Neural inverse control of a rotary flexible link

Control neuronal por modelo inverso de un eslabón flexible rotatorio

Carlos Alberto Saldaña Enderica[1,2,*], José Ramón Llata[1,2], Carlos Torre-Ferrero[1,2]

Received: 11-11-2025, Received after review: 04-02-2026, Accepted: 28-04-2026, Published: 01-07-2026

Abstract

This paper presents a data-driven inverse-model control scheme for a rotary flexible-link (RFL) system, with θ denoting the base angular position and α the relative tip deflection. The plant is identified from experimental data and represented as a continuous-time fourth-order state-space model. On this basis, an inverse-model controller is designed and implemented using an artificial neural network (ANN) of the multilayer perceptron (MLP) type, trained on regressors composed of delayed states and inputs. Validation relies on quantitative error metrics, transient-response analysis, and an indirect discrete-time BIBO (Bounded Input–Bounded Output) stability certification obtained by identifying an equivalent closed-loop linear model. Six MLP architectures are compared under three reference scenarios. The selected configuration achieves the best trade-off between θ tracking and α vibration attenuation, with bounded closed-loop signals and competitive settling times. The work integrates, into a single workflow, data-driven identification of the RFL, systematic MLP architecture selection, and discrete-time BIBO stability analysis, providing a reproducible framework for designing and objectively comparing inverse-model neural controllers in subactuated flexible systems.

Keywords: rotary flexible-link system; data-driven inverse-model control; artificial neural networks; multilayer perceptron; system identification; vibration suppression; BIBO stability.

Resumen

Este trabajo presenta un esquema de control por modelo inverso basado en datos para un sistema rotatorio de eslabón flexible, en el que la posición angular de la base se denota por θ y la deflexión relativa de la punta por α. La planta, correspondiente a un sistema rotatorio de eslabón flexible (*rotary flexible link*, RFL), se identifica a partir de datos experimentales y se modela en espacio de estados continuo de cuarto orden. A partir de este modelo, se diseña un controlador por modelo inverso implementado mediante una red neuronal artificial (RNA) de tipo perceptrón multicapa (MLP), entrenada con regresores formados por estados y entradas retardadas. La validación incluye métricas cuantitativas de error, análisis de respuesta transitoria y una certificación indirecta de estabilidad BIBO en tiempo discreto, obtenida mediante la identificación de un modelo lineal equivalente en lazo cerrado. Se comparan seis arquitecturas MLP en tres escenarios de referencia. La configuración seleccionada muestra el mejor compromiso entre el seguimiento de θ y la mitigación de las oscilaciones en α. Además, el trabajo integra en un flujo único la identificación basada en datos, la selección sistemática de la arquitectura y el análisis de estabilidad.

Palabras clave: control por modelo inverso; eslabón flexible rotatorio; estabilidad BIBO; identificación de sistemas; perceptrón multicapa; redes neuronales artificiales; supresión de vibraciones

[1,*]Departamento de Tecnología Electrónica, Ingeniería de Sistemas y Automática, Universidad de Cantabria, España.
[2]Facultad de Sistemas y Telecomunicaciones, Universidad Estatal Península de Santa Elena, Ecuador.
Corresponding author ✉: cse386@alumnos.unican.es.

Suggested citation: C. A. Saldaña Enderica, J. R. Llata and C. Torre-Ferrero "Neural inverse control of a rotary flexible link," *Ingenius, Revista de Ciencia y Tecnología*, N.° 36, pp. 98-109, 2026, DOI: https://doi.org/10.17163/ings.n36.2026.08.

1. Introduction

Single-link flexible rotary manipulators constitute a representative case study in both real-world applications, such as lightweight robotics and deployable structures, and academic testbeds for advanced control. Their underactuated nature and inherent structural flexibility generate oscillations and dynamic couplings that hinder the synthesis of robust and precise controllers, particularly when information about the physical model of the system is incomplete or uncertain [1].

In this context, data-driven control is an attractive alternative to classical methods whose design relies on detailed parametric models. Rather than depending on high-fidelity analytical identifications, data-driven approaches design controllers directly from experimental or simulated data, which is particularly useful for complex and nonlinear systems [2]. Within this framework, inverse-model control schemes based on multilayer perceptron (MLP) artificial neural networks (ANNs) have demonstrated the ability to approximate the inverse dynamics of manipulators and other nonlinear systems with considerably less explicit modeling effort [3–5]. These networks can capture highly nonlinear input–output relationships from data and have demonstrated strong performance in trajectory-tracking tasks and in compensating for unmodeled dynamic effects [6].

Recent literature on data-driven control and model inversion can be organized into three main research lines. The first focuses on the design of optimal controllers without relying on an explicit physical model, using finite impulse response (FIR) structures combined with LASSO-type regularization and convex formulations for inverse control. Overall, these methods reduce the structural complexity of the controller without compromising performance, while providing formal guarantees of data-based optimality [7–9]. In this context, hyperparameter selection, the effective number of FIR coefficients, and the quality of the experimental data are critical factors for achieving good generalization.

The second line addresses model inversion through machine learning, particularly by using MLPs to approximate the direct or inverse dynamics of manipulators. MLPs can outperform classical methods, such as SVMs, in dynamic prediction when their hyperparameters are properly tuned, although their performance remains sensitive to the representativeness of the training data [10]. In addition, several approaches incorporate optimization and regularization through metaheuristic techniques to improve computational efficiency and reduce overfitting in neural networks used for control [11].

The third line focuses on the robust synthesis of fixed-order controllers and the integration of noisy, non-ideal data. Data-driven approaches enable the model-matching problem and robustness requirements to be addressed directly in the data space, but they also introduce new trade-offs among robustness to uncertainty, computational complexity, and ease of implementation [9]. For rotary systems with flexible links, recent experimental studies combine state-space identification with guided reinforcement learning techniques [12], using metrics related to tracking performance, vibration reduction, and disturbance rejection. However, comparability among studies remains limited by the lack of standardized testing protocols and benchmark scenarios.

Despite these advances, several specific gaps can still be identified in the state of the art:

- The lack of studies that systematically integrate the data-based identification of an RFL, the construction of a neural inverse model, and its quantitative validation under multiple reference scenarios.
- The limited integration of neural inversion with formal model order selection criteria, supported by metrics such as FPE, MDL, and percentage fit [9], which allow the selection of moderate-dimensional models to be justified over lower-order alternatives.
- The absence of detailed analyses of closed-loop BIBO stability when neural controllers are employed, beyond qualitative observations based on simulations.

In this context, this work aims to analyze and demonstrate the feasibility of a data-driven inverse-model control scheme for a rotary flexible-link system, using an MLP-type ANN to approximate the inverse dynamics. Specifically, the proposed workflow integrates: i) continuous state-space identification of the plant from experimental data, following the framework of [12]; ii) construction of a regressor set based on delayed states and inputs for inverse-model training; iii) synthesis and selection of the neural architecture according to objective metrics; and iv) evaluation of the inverse-controller performance in terms of tracking error, vibration suppression, and discrete BIBO stability.

The approach is not intended to compete with high-level techniques in terms of absolute performance, but rather to demonstrate the value of a clear and reproducible methodology for designing, training, and validating a neural inverse controller in rotary systems with flexible links. This methodology can be extrapolated to other complex dynamic systems characterized by difficult analytical modeling, structural couplings, and sensitivity to disturbances, and it is presented through a representative case study that facilitates replication in control laboratories.

2. Materials and Methods

This section describes the state-space model of the RFL, the acquisition of experimental data, and the design of the ANN-MLP inverse neural controller used in the simulations.

2.1. General Description of Inverse Model Control

Inverse model control is based on training an ANN to approximate the inverse dynamics of the plant from input-output data pairs

$$\big(\boldsymbol{\varphi}(k),\, u(k)\big), \tag{1}$$

where $\boldsymbol{\varphi}(k)$ is a regressor vector containing delayed outputs and inputs, and $u(k)$ is the associated control signal [13,14]. During the training phase, the plant is excited using step signals of different magnitudes and random application times to cover a wide operating range and obtain a truly representative dataset [15]. The resulting records are then divided into training, validation, and test sets to adjust the ANN parameters while simultaneously mitigating overtraining, thereby preserving adequate generalization capability [4], [16].

The Levenberg-Marquardt algorithm is employed for training because of its fast convergence and ability to achieve low errors in moderate-size networks [16,17]. Robustness is reinforced through data normalization, partitioning into training, validation, and test sets, and early stopping based on the validation error.

2.2. General Workflow of the Methodology

The development of the neural controller is structured into three main stages:

1. Continuous state-space identification of the RFL from experimental data, yielding a fourth-order (A, B, C, D) model.
2. Generation of synthetic data from this model to train the neural inverse model.
3. Design, evaluation, and selection of the most suitable MLP architecture based on tracking metrics and link oscillation amplitude.

The platform used is the Quanser QLabs Virtual Rotary Flexible Link environment, implemented in MATLAB/Simulink® R2022b and QUARC 2.15, according to the workflow described in [12].

2.3. Identification of the Rotary Flexible-Link System

A single rotary flexible-link system actuated at the base is considered. The following variables are used:

$$\begin{aligned} &\theta(t):\ \text{angular position of the base,}\\ &\alpha(t):\ \text{relative deflection at the tip,}\\ &u(t) \in [-10,\, 10]\ \text{V.} \end{aligned} \tag{2}$$

For the identification of the continuous model, experimental data obtained from the Quanser virtual environment were used. The angular position θ and the relative deflection α were recorded with a sampling time

$$T_s = 2\ \text{ms}, \tag{3}$$

sufficient to capture the low-frequency bending modes without aliasing, consistent with previous studies on the same prototype [12], [18]. The tests were performed while maintaining $\alpha(t)$ within the interval $[-5°,\, 5°]$ to operate in a quasi-linear regime [1].

To ensure persistence of excitation and cover the operating range of interest, a pseudo-random square voltage signal was applied to $u(t)$, with amplitude and frequency varying within the safe interval $[-10,\, 10]$ V. Throughout the entire process, the operating constraints defined for the virtual model were respected [19]. Subsequently, the data were divided into:

- an identification set, used to estimate the model parameters; and
- a validation set, reserved exclusively to evaluate the predictive capability of the model.

2.3.1. Identification Procedure and Order Selection

A fourth-order continuous state-space model with one input and two outputs is adopted:

$$\begin{aligned} \dot{x}(t) &= A\,x(t) + B\,u(t)\\ y(t) &= C\,x(t) + D\,u(t) \end{aligned} \tag{4}$$

Where

$$x(t) = \begin{bmatrix}\theta(t) & \alpha(t) & \dot{\theta}(t) & \dot{\alpha}(t)\end{bmatrix}^{\top}, y(t) = \begin{bmatrix}\theta(t) & \alpha(t)\end{bmatrix}^{\top}. \tag{5}$$

Prediction Error Methods (PEM) were applied to the previously described data for model identification. As a result, a fourth-order model was obtained with $D = 0$, since the inertia of the motor–link assembly and the structural flexibility prevent instantaneous changes in the outputs in response to variations in $u(t)$ [12], [19].

The selection of a fourth-order model is supported by the comparative analyses reported in [20]. In particular, lower-order models do not adequately represent the bending dynamics, and increasing the order does not lead to significant improvements in FPE, MSE, or percentage fit. However, it increases computational cost and the risk of overfitting.

2.3.2. Identified Continuous Model

By applying the procedure described above, the following fourth-order continuous state-space model with one input and two outputs was obtained. The identified matrices are:

$$A = \begin{bmatrix} 0.2629 & -0.6923 & 2.0550 & 1.0130 \\ -11.5200 & 23.9900 & -54.7900 & -30.0000 \\ -4.2910 & -10.4200 & -63.9600 & -20.6300 \\ -3.4710 & 77.0200 & 24.4800 & -10.1900 \end{bmatrix} \tag{6}$$

$$B = \begin{bmatrix} -0.05998 \\ 1.6080 \\ 7.1510 \\ -6.6660 \end{bmatrix} \tag{7}$$

$$C = \begin{bmatrix} 29.6200 & 0.7060 & 0.1893 & 0.1340 \\ -0.1510 & 0.8635 & -0.7005 & -0.5094 \end{bmatrix} \tag{8}$$

$$D = \begin{bmatrix} 0 \\ 0 \end{bmatrix} \tag{9}$$

This model reproduces the coupled dynamics between θ and α within the considered operating range. Previous studies using the same RFL prototype have shown that continuous models of this order adequately capture the system behavior in tracking and vibration-suppression tasks [12], [20].

2.4. Design of the Neural Inverse Model Controller

From the identified continuous model (A,B,C,D), a state-space simulation of the RFL was constructed using Euler discretization with a step size of $dt = 0.002s$. The input was a random step signal, with new levels assigned every 2 within the range

$$u(k) \in [-1.5,\ 1.5]\ \text{V}, \tag{10}$$

applied for 1000 s. In this way, persistent data for

$$\theta,\ \alpha,\ \dot{\theta},\ \dot{\alpha},\ y\ and\ u, \tag{11}$$

which constituted the basis for regressor construction and estimation of the neural inverse model.

Table 1 shows the configuration used for training the inverse model. The selection was made to promote stable convergence, avoid overfitting, and maintain an adequate balance between accuracy and generalization capability.

Table 1. Training Parameters of the Neural Network

Parameter	Value
Optimization algorithm	Levenberg-Marquardt (`trainlm`)
Maximum number of iterations	600
Error criterion (objective)	10^{-4}
Training set	85%
Validation set	10%
Data normalization	`mapminmax` on inputs and outputs

The diagram in Figure 1 summarizes the inverse identification process. This scheme provides a clear visualization of how the information flow is organized during ANN training, highlighting the relationship between the employed regressors and the control signal that the network must learn to predict.

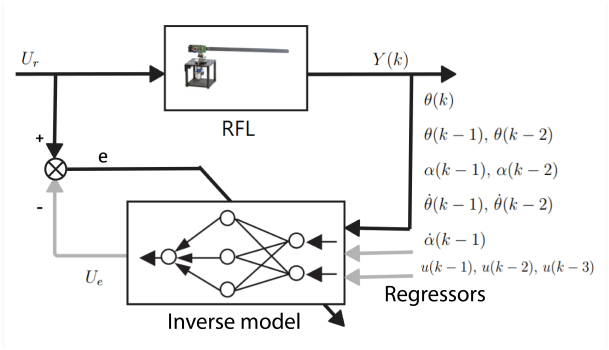

Figure 1. Scheme of the RFL inverse dynamics identification process.

2.4.1. Evaluated Architectures

Different MLP configurations are evaluated, varying in the number of neurons and hidden layers while maintaining a fixed linear activation function at the output. The configurations are detailed in Table 2.

Table 2. Evaluated Configurations for the MLP Neural Network

Conf.	Hidden layers	Activation functions
C1	[15]	*logsig–purelin*
C2	[20]	*logsig–purelin*
C3	[20, 10]	*logsig–logsig–purelin*
C4	[25, 15]	*logsig–logsig–purelin*
C5	[12, 2]	*logsig–logsig–purelin*
C6	[30, 20]	*logsig–logsig–purelin*

2.4.2. Inverse Model and Training

For each configuration in Table 2, a feedforward MLP neural network was trained using the Levenberg–Marquardt algorithm to approximate the control signal $u(k)$ from a regressor vector composed of current and delayed values of the measured variables. In NARX/NARMAX-type notation, this vector is defined as:

$$\boldsymbol{\varphi}(k) = \big[(I, q^{-1}, q^{-2})\,\theta(k),\ (q^{-1}, q^{-2})\,\alpha(k),\ (q^{-1}, q^{-2})\,\dot{\theta}(k),\ q^{-1}\dot{\alpha}(k),\ (q^{-1}, q^{-2}, q^{-3})\,u(k)\big]^{\top}. \tag{12}$$

where q^{-1} denotes the one-sample delay operator ($q^{-1}x(k) = x(k-1)$, $q^{-2}x(k) = x(k-2)$, etc.), and I is the identity operator.

Explicitly, the regressor vector can be expressed as

$$\boldsymbol{\varphi}(k) = \big[\theta(k),\ \theta(k-1),\ \theta(k-2),\ \alpha(k-1),\ \alpha(k-2),\ \dot{\theta}(k-1),\ \dot{\theta}(k-2),\ \dot{\alpha}(k-1),\ u(k-1),\ u(k-2),\ u(k-3)\big]^{\top}. \tag{13}$$

That is, the ANN receives as input a "time window" formed by the current and past samples of the base position θ, the tip deflection α, their corresponding velocities, and the control signal u over the three most recent sampling instants.

In the preliminary tests, regressor vectors with more delays were also considered, for example, including $\theta(k-3)$, $\alpha(k-3)$ or $u(k-4)$.

However, increasing the number of delays causes the dimension of $\boldsymbol{\varphi}(k)$ to grow without providing further relevant dynamic information, which worsens the conditioning of the training problem. In practice, the network tended not to converge, with the validation error remaining high, or stabilized at local minima with insufficient performance in reference tracking. For this reason, the regressor vector in (13) was adopted, as it provides an adequate compromise between temporal memory and learning capability.

The network output therefore approximates the inverse model of the plant:

$$u(k) = \mathcal{N}_{\boldsymbol{\psi}}\big(\boldsymbol{\varphi}(k)\big), \tag{14}$$

where $\mathcal{N}_{\boldsymbol{\psi}}(\cdot)$ represents the MLP parameterized by the weight vector $\boldsymbol{\psi}$.

2.4.3. Closed-Loop Implementation

To implement the neural controller based on the trained inverse model, the MLP ANN generates the control signal $u(k)$ required for the RFL system to follow the reference $\theta_{\text{ref}}(k)$. The conceptual scheme of the closed-loop controller is shown in Figure 2.

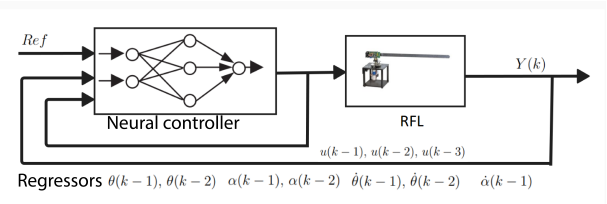

Figure 2. Diagram of the RFL neural inverse-model controller.

3. Results and Discussion

3.1. Results of the RFL Model Identification

For the validation set, the fourth-order continuous model provides:

- A time-domain fit for θ in the range of 99.85–96.95 % for one-step-ahead prediction and free-run simulation, with FPE $= 2.89 \times 10^{-13}$ and MSE $= 1.326 \times 10^{-6}$;
- A free-run simulation fit of 96.25 % for θ and 81.41 % for α, indicating that the coupled dynamics between the base rotation and the link flexure are reasonably captured within the considered operating range

In preliminary studies using the same platform, lower-order models ($n = 2, 3$) have been found to significantly degrade the prediction capability for α, whereas higher-order models do not provide significant improvements in FPE or MSE, but do increase complexity and sensitivity to noise [1], [20]. Therefore, the order $n = 4$ is adopted as a compromise between model fidelity and reasonable complexity, serving as the basis for the synthesis of the neural inverse-model controller developed in this article.

3.2. Characterization of the Training Set

Figure 3 summarizes the open-loop dataset used to train the neural inverse model. The upper subplot shows the control signal $u(k)$, whereas the lower subplot presents the inverse-model inputs, that is, the regressors constructed from delayed outputs and inputs.

The control signal $u(k)$ repeatedly and persistently spans its operating range, without prolonged steady-state intervals or clear signs of saturation. Consistently, the regressors exhibit smooth and bounded variations throughout the sample horizon, allowing dense coverage of the operating region around the operating point.

From an experimental perspective, this temporal distribution ensures sufficient excitation of the system within the domain of interest and avoids poorly

sampled regions of the state space. Consequently, the dataset illustrated in Figure 3 is suitable for the supervised training of the neural inverse model, as it provides representative examples of the dynamics relevant to subsequent closed-loop control.

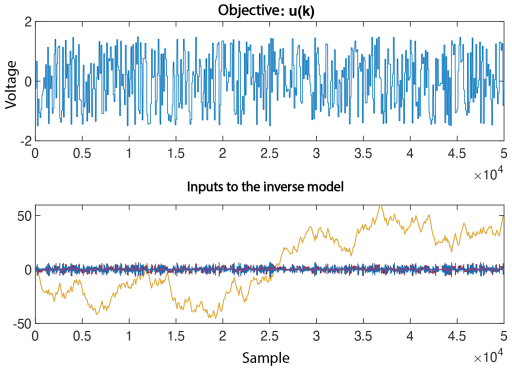

Figure 3. Training set used for the neural inverse model. Top: control signal $u(k)$; bottom: discrete-time regressors (delayed outputs and inputs) acting as inputs to the inverse model.

3.3. Training and Evaluation of the Neural Inverse Model

After training the neural inverse model using the configurations listed in Table 2, the mean squared error (MSE) curves corresponding to the architectures with the most representative behavior were obtained.

The comparison between the actual control signal $u(k)$ and that estimated by the trained ANN is presented in Figure 4. The two trajectories practically overlap over most of the validation horizon, with the visible discrepancies concentrated in the transients with the steepest slopes. This behavior is consistent with an adequate fit of the inverse model within the considered operating range.

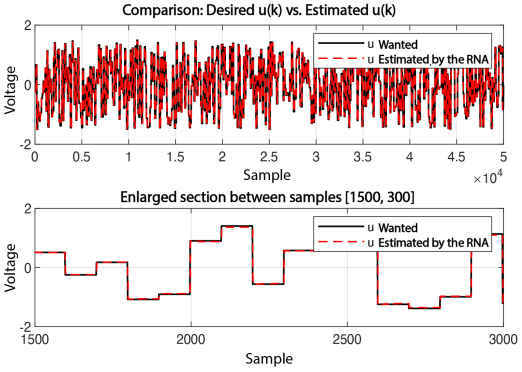

Figure 4. Comparison between the actual $u(k)$ and the $u(k)$ estimated by the ANN for the validation set.

Training stopped after 15 epochs after satisfying the early-stopping criterion based on validation performance. The best validation result was obtained at epoch 9, with a mean squared error (MSE) of 0.012968. For the training set, an MSE of 0.0163 (RMSE $\approx$ 0.128) was achieved, indicating a small error and reasonable ANN generalization capability.

Configuration C5 was selected for the closed-loop tests based on the previous results: low MSE, stable learning with no divergence in training or validation, and an estimated $u(k)$ that closely follows the reference without marked discrepancies.

3.4. Design Acceptance Criteria for Controlling the System

The following performance thresholds were established to evaluate the different neural architectures:

$$|e_{ss,\theta}| < 2^\circ, \tag{15}$$

$$t_{\text{est},\theta} < 6 \text{ s} \quad (\pm 2\%), \tag{16}$$

$$|\alpha|_{\text{peak}} < 0.15 \text{ rad } (\approx 8.6^\circ). \tag{17}$$

In practice, not all neural configurations can simultaneously satisfy the three thresholds under all test scenarios. Therefore, these thresholds are used to objectively compare architectures C1–C6 based on the quantitative metrics reported in the tables of this section.

3.5. Closed-Loop Evaluation: Influence of the MLP Architecture

For each MLP configuration in Table 2, a neural inverse model was trained using the same dataset, and its closed-loop performance was evaluated under three reference scenarios in θ: i) single step, ii) periodic step with variable amplitude, and iii) constant periodic step. The following metrics were used:

- Root mean squared error (RMSE);
- Integral indices IAE and ITAE;
- Overshoot and settling time for θ;
- Peak value of $|\alpha|$ as an indicator of tip vibration.

The results for each reference type are presented below, including the tables with the numerical metrics supporting the conclusions.

3.5.1. Single Step

Figure 5 shows the response of $\theta(t)$ to a single step for the six ANN configurations, while Figure 6 illustrates the behavior of the flexible link $\alpha(t)$.

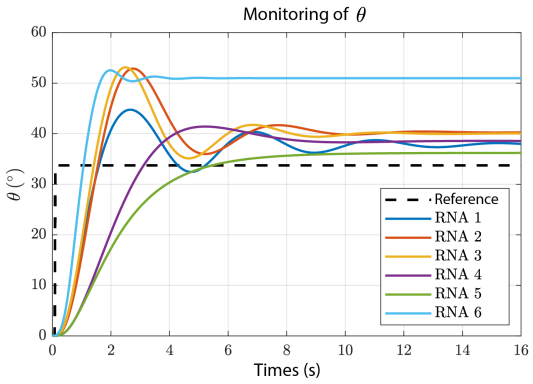

Figure 5. Comparison of the $\theta(t)$ response under a single-step reference for the six ANN configurations.

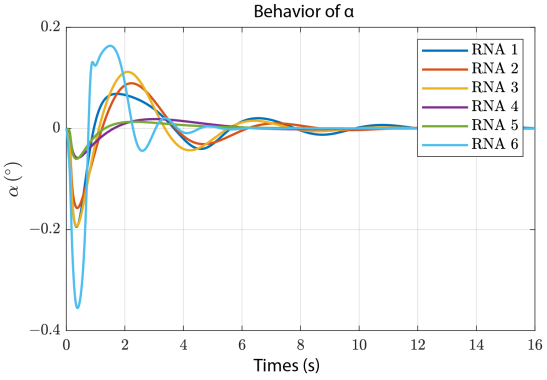

Figure 6. Behavior of $\alpha(t)$ for a single-step reference under the six ANN configurations.

The dynamic parameters extracted from these responses are summarized in Table 3, while the error metrics are presented in Table 4.

Table 3. Dynamic Parameters under a Single-Step Signal

Conf.	Overshoot [%]	t_{est} [s]	Range α [°]
C1	32.6	11.28	[−11.1, 3.9]
C2	56.7	8.52	[−9.0, 5.1]
C3	57.4	7.68	[−11.1, 6.4]
C4	22.7	7.48	[−3.3, 1.1]
C5	7.3	7.56	[−3.5, 0.8]
C6	55.7	2.20	[−20.4, 9.4]

Table 4. Error Metrics for Each Configuration (Single Step)

Conf.	RMSE	IAE	ITAE
C1	7.6990	109.4850	840.0724
C2	9.9954	164.9611	1349.4845
C3	9.5792	156.5936	1287.0993
C4	9.7163	142.9398	1030.5302
C5	9.1722	102.2241	529.4320
C6	17.4475	343.1674	3442.3005

From these figures, configuration C5 provides the most favorable compromise: it exhibits the lowest overshoot (7.3%) and one of the shortest settling times (7.56 s), with a highly contained tip-oscillation range of $\alpha \in [-3.5°, 0.8°]$. In addition, its aggregated errors are the lowest in the set, or close to the minimum values, with RMSE = 9.17, IAE = 102.22, and ITAE = 529.43. In contrast, C6 exhibits a pronounced overshoot (55.7%), a final value of 50.99°, clearly above the reference, and an α range of $[-20.4°, 9.4°]$. Furthermore, it records RMSE = 17.45, IAE = 343.17 and ITAE = 3442.30, values several times higher than those obtained with C5.

3.5.2. Variable Periodic Step

Figure 7 shows the θ response to a variable-amplitude periodic step reference for the six configurations, while Figure 8 illustrates the behavior of α.

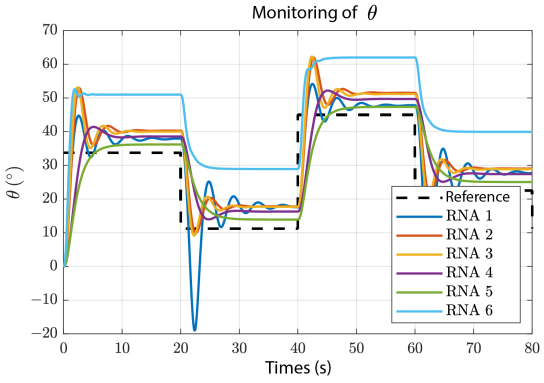

Figure 7. $\theta(t)$: response under a variable-amplitude periodic step reference for the six ANN configurations.

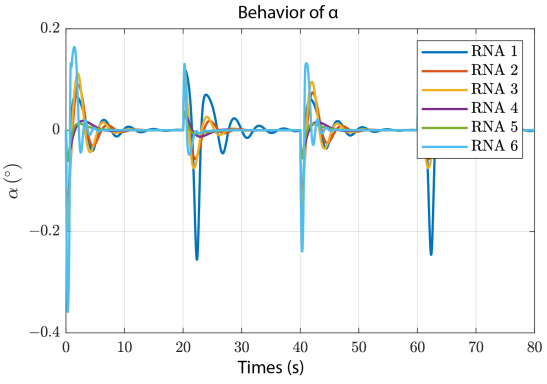

Figure 8. $\alpha(t)$: under a variable-amplitude periodic step reference.

From the results in Tables 5 and 6, configuration C5 again shows the most favorable compromise between θ tracking accuracy and damping of tip vibrations. The analysis focuses on the α flexion range and the accumulated errors.

In this scenario, C5 maintains the most contained tip flexure, with a range of $\alpha \in [-3.5°, 2.1°]$, noticeably smaller than those observed in the remaining configurations (C1–C4), whose intervals range approximately from $[-14.6°, 6.7°]$ to $[-3.4°, 2.0°]$ This indicates that, for the same reference signal, C5 consistently reduces the amplitude of tip oscillations without degrading the tracking of the angular profile $\theta(k)$. In contrast, C6 represents the most extreme case, concentrating the strongest vibratory behavior, reaching $\alpha \in [-20.5°, 9.4°]$ and exhibiting more pronounced deviations in $\theta(k)$ with respect to the desired trajectory.

In terms of accumulated error, C5 achieves the best performance, with RMSE = 8.39 and the lowest integral indices, IAE = 419.35 and ITAE = 14944.07. C1–C4 remain relatively close, with moderate increases but within the same order of magnitude.

For the variable periodic step input, C5 again proves to be the most robust alternative: it combines the lowest RMSE (8.39), the lowest integral errors (IAE = 419.35, ITAE = 14944.07), and the smallest tip flexure, with $\alpha \in [-3.5°, 2.1°]$. The remaining configurations exhibit a less favorable trade-off between accuracy and vibration, whereas C6 accumulates both the largest errors and the widest vibration range, with $\alpha \in [-20.5°, 9.4°]$.

Table 5. Tip-Flexure Range α Under a Variable-Amplitude Periodic Step Input

Conf.	Range α [°]
C1	$[-14.6°,\ 6.7°]$
C2	$[-9.1°,\ 5.3°]$
C3	$[-11.2°,\ 6.7°]$
C4	$[-3.4°,\ 2.0°]$
C5	$[-3.5°,\ 2.1°]$
C6	$[-20.5°,\ 9.4°]$

Table 6. Error Metrics Under a Variable-Amplitude Periodic Step Input

Conf.	RMSE	IAE	ITAE
C1	8.8691	522.1624	20022.8260
C2	9.1393	615.1249	23273.9122
C3	8.7681	589.7227	22370.7007
C4	8.9462	543.6551	20005.5536
C5	8.3926	419.3452	14944.0715
C6	18.3018	1432.3069	57311.4578

3.5.3. Constant Periodic Step

Finally, the system behavior was analyzed under a constant periodic step reference. Figure 9 shows the response of $\theta(t)$, while Figure 10 presents the response of $\alpha(t)$.

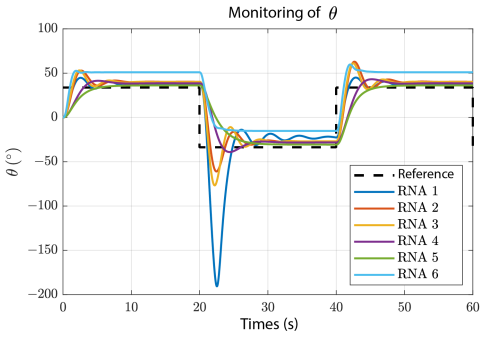

Figure 9. $\theta(t)$: response under a constant periodic step reference.

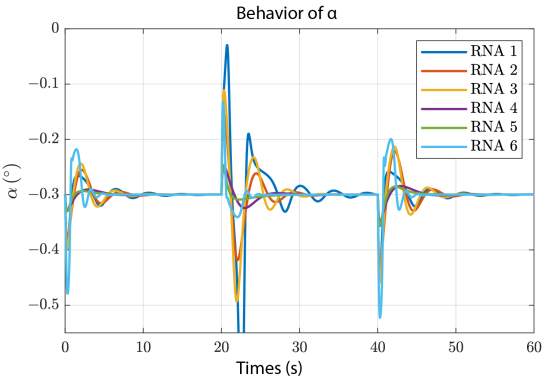

Figure 10. $\alpha(t)$: response under a constant periodic step reference.

In terms of flexure, configurations C4 and C5 provide the best containment of tip vibration, with very narrow ranges around −6°: $\alpha \in [-6.1°, -5.7°]$ and $\alpha \in [-6.5°, -6.1°]$ (C5). The remaining configurations exhibit significantly larger deflections: C2 and C3 remain within narrow bands but farther from the neutral axis (approximately between −16.5° and −22.1°), whereas C1 and C6 represent the worst cases, with extreme α ranges of $\in [-61.9°, -30.9°]$ and $\alpha \in [-25.5°, -19.2°]$, respectively. This indicates that, for the same periodic input, C4 and C5 are clearly the configurations that induce the smallest tip oscillations.

For this second evaluation, C5 achieves the best integral indices, with IAE = 752.84 and ITAE = 29147.57, followed closely by C4 (IAE = 774.76, ITAE = 29764.48). Although C2 and C3 report slightly lower RMSE values, 15.47 and 15.82, respectively, this specific advantage does not translate into better overall performance, as it is accompanied by larger integral errors and tip flexure farther from the neutral axis. At the opposite extreme, C1 and C6 continue to exhibit behaviors far from the desired performance.

Table 7. Tip-Flexure Range α Under a Constant Periodic Step Reference

Conf.	Range α [°]
C1	[−61.9, −30.9]
C2	[−16.5, −15.0]
C3	[−22.1, −21.6]
C4	[−6.1, −5.7]
C5	[−6.5, −6.1]
C6	[−25.5, −19.2]

Table 8. Error Metrics Under a Constant Periodic Step Reference

Conf.	RMSE	IAE	ITAE
C1	31.7209	1282.9760	54425.4854
C2	15.4694	834.2291	32438.9853
C3	15.8182	847.0670	33297.9880
C4	16.8459	774.7553	29764.4846
C5	17.7625	752.8363	29147.5748
C6	22.7026	1628.4212	65823.4133

3.6. Global Performance Comparison

Across the three test scenarios, configuration C5 emerges as the most robust option. It achieves substantially more contained tip-flexure ranges than most alternative configurations while consistently maintaining RMSE, IAE, and ITAE among the lowest values across the experiments. In contrast, configurations C1 and C6 concentrate the least favorable combinations of error and vibration, whereas C2–C4 achieve intermediate performance. These results support the selection of C5 as the reference architecture for inverse-model control in the tested flexible-link system.

3.7. Comparison with Baseline Approaches

Following the criterion in [18], three control approaches previously tested in RFL systems with similar dynamic characteristics are considered as references: a "classical" neural network trained directly in closed loop, a fuzzy controller, and the proposed ANN–C5 inverse-model architecture. Although the physical configurations are not strictly identical in terms of link length, inertia, and related parameters, the three solutions address the same θ-tracking task with tip-vibration limitation in α. Therefore, the reported figures are used as an indicative comparison of the order of magnitude of the performance.

Within this framework, ANN–C5 proves to be the fastest strategy, with $t_{\text{est}} \approx 7.56$ s, compared with the classical neural network (≈ 9 s)) and the significantly slower fuzzy controller (> 60 s). Regarding the peak value of $|\alpha|$, expressed in degrees, the fuzzy and NN approaches yield values of approximately 3.3°, whereas ANN–C5 reaches approximately 3.5°, corresponding to the maximum absolute value within the range [−3.5°, 0.8°].

Overall, ANN–C5 offers a clearly competitive settling time at the expense of a slightly larger peak in tip vibration, which is consistent with the design emphasis placed on inverse θ-tracking rather than on the explicit minimization of oscillations in α. These comparisons are not intended to provide an exhaustive study of controller performance, but rather to position ANN–C5 within the range of solutions already explored for similar RFL systems [18].

3.8. Discrete-Time BIBO Stability Analysis

The stability analysis of a dynamic system controlled by an artificial neural network (ANN) is commonly conducted through indirect procedures because neural networks generally do not allow a closed-form expression of the closed-loop model to be derived. In this work, system identification tools are used to obtain a discrete-time transfer function that approximates the effective dynamics of the $\theta_{\text{ref}} \to \theta$ channel when the RFL system is controlled by ANN–C5.

One of the most widely used approaches for evaluating the stability of discrete-time systems is the BIBO (bounded-input bounded-output) criterion, according to which a system is stable if every bounded input produces a bounded output. For discrete-time linear time-invariant (LTI) systems, this property is verified by analyzing the location of the poles of the transfer function in the z-plane. The system is described by:

$$G(z) = \frac{b_0 + b_1 z^{-1} + \cdots + b_m z^{-m}}{1 + a_1 z^{-1} + \cdots + a_n z^{-n}}, \tag{18}$$

where b_i and a_ii are real coefficients. Accordingly, the system is BIBO stable if and only if all poles, namely the roots of the denominator, lie strictly inside the unit circle:

$$|p_i| < 1, \quad \forall i. \tag{19}$$

3.8.1. Identification of the Closed-Loop Model

To perform this analysis, the reference (θ_{ref}) and output (θ) signals were recorded in response to a step input while the system operated under ANN–C5 control. Based on these data, the MATLAB System Identification Toolbox was employed to estimate a second-order discrete-time transfer function with a one-sample delay, representing the closed-loop behavior:

$$G(z) = \frac{0.0002971\, z^{-1}}{1 - 1.966\, z^{-1} + 0.9667\, z^{-2}}. \tag{20}$$

The system has a sampling time of $T_s = 0.002$ s. From this function, the poles and their corresponding magnitudes were obtained:

- Poles: $p_{1,2} = 0.9830 \pm 0.0203i$,
- Magnitudes: $|p_1| = |p_2| = 0.9832$.

Finally, since both identified poles satisfy $|p_{1,2}| < 1$, the closed loop with ANN–C5 is classified as locally BIBO stable, as all the roots of the denominator lie inside the unit circle. The fact that $|p_{1,2}|$ is close to 1 is consistent with slower settling dynamics but marked damping, in agreement with the times observed in the step responses.

This indirect mathematical stability assessment enables the neural controller performance to be evaluated without requiring explicit knowledge of the internal system model. It should be emphasized that the identified transfer function $G(z)$ represents a linear approximation of the closed-loop behavior around the operating point and for the dataset considered. Therefore, the BIBO stability conclusion obtained from the poles $|p_{1,2}| = 0.9832 < 1$ is valid within a local neighborhood of the operating conditions used, with small variations in the amplitude and frequency of the reference, but it does not imply global stability under severe saturations, large nonlinearities, or drastic changes in the dynamics of the RFL. This interpretation is consistent with the use of identified linear models for inherently nonlinear systems such as flexible manipulators [1] and complements the time-domain results presented in the previous subsections.

3.9. Discussion

3.10. Relationship with the Design Criteria

The acceptance criteria defined in (15) to (17) were established as particularly demanding targets. For the single-step input, no configuration satisfies all of them simultaneously; however, C5 comes closest. It maintains moderate overshoot, response times on the order of 7.6 s and a peak tip flexure of $|\alpha|_{\text{peak}} \approx 3.5°$, which is clearly below the design limit of (8.6°). For the periodic step inputs, both constant and variable, overshoot and settling time are no longer representative measures. In these cases, C5 preserves a reduced α range, on the order of $\pm 3.5°$, and yields the lowest integral errors. These results position C5 as the most favorable compromise between θ-tracking and vibration damping.

3.11. Influence of the MLP Architecture

The comparison among C1–C6 shows that neither small networks nor excessively deep architectures are suitable for this application. Configurations with a single layer and few neurons (C1–C2) do not adequately represent the inverse dynamics of the RFL, resulting in larger tip vibrations. At the other extreme, C6 may accelerate the response, but it systematically worsens RMSE, IAE, and ITAE, while increasing the α range. By contrast, the intermediate architecture C5, with two hidden layers [12, 2], provides a better balance: it achieves the best or second-best error values in all scenarios, keeps α bounded, and avoids extreme control efforts, thereby mitigating both insufficient capacity and overfitting.

3.12. Limitations and Scope

The results are based on simulations using an identified model with fits above 96% for θ and 80% for α. This enables the comparison of architectures but does not replace experimental validation, where nonlinear friction, backlash, noise, and saturation effects may arise. The discrete-time BIBO analysis confirms local stability ($|p_{1,2}| = 0.9832 < 1$),but it does not guarantee global behavior under extreme references or disturbances. Finally, the comparison with fuzzy controllers and conventional neural networks reported in [18] is only indicative, since it is based on similar but not identical prototypes. A conclusive evaluation would require implementing all strategies on the same test bench, which is therefore proposed as a direction for future work.

3.13. Future Work

Future work will focus on bridging the gap between simulation and experimental implementation while strengthening the robustness of the proposed scheme:

- Implement the ANN–C5 architecture on the real RFL prototype and measure RMSE, IAE, ITAE, and the α range under noise, saturation, and computation delays, directly comparing the results with those obtained in simulation.
- Analyze the sensitivity of the closed loop to moderate variations in system parameters, including mass, stiffness, and friction, and in the reference signal, including amplitude and frequency, to verify the margins within which the observed stability is maintained.
- Test, on the same test bench, at least one classical controller, such as PID or LQR, and one fuzzy or conventional neural controller to provide a direct quantitative comparison with ANN–C5.

4. Conclusions

This work demonstrated the feasibility of designing and evaluating a neural inverse-model controller for a rotary flexible-link system using experimental data from an identified model, without resorting to complex analytical modeling.

Starting from a state-space model with a good fit for θ and acceptable fit for α, closed-loop test scenarios were constructed and six MLP architectures were

trained. Among them, C5 [12, 2] provided the best compromise, maintaining $|\alpha|_{\text{peak}} < 8.59°$ and, for the three reference types considered, achieving the best RMSE, IAE, and ITAE values when compared with configurations with insufficient capacity (C1–C2) or excessive size (C6).

The discrete-time BIBO stability analysis locally confirmed the stability of the closed loop with ANN–C5, with pole magnitudes satisfying $|p_{1,2}| < 1$, in agreement with the time-domain responses obtained. In addition, the indicative comparison with fuzzy and neural solutions reported in the literature suggests that the proposed approach is competitive in terms of settling time and vibration level.

Overall, the results support three main conclusions. First, prior plant identification with acceptable fidelity is a key element for enabling neural inverse control. Second, a moderately sized MLP, together with an adequate regressor design, allows reference tracking and vibration suppression to be balanced. Finally, combining time-domain metrics with local stability verification provides a solid quantitative basis for advancing toward experimental validation, robustness analysis, and systematic comparison with reference controllers.

Contributor Roles

- **Carlos Alberto Saldaña Enderica:** conceptualization, methodology, software, formal analysis, investigation, data curation, writing – original draft.
- **José Ramón Llata:** methodology, validation, supervision, writing – review and editing.
- **Carlos Torre-Ferrero:** methodology, validation, supervision, writing – review and editing.

References

[1] D. Subedi, I. Tyapin, and G. Hovland, "Review on modeling and control of flexible link manipulators," *Modeling, Identification and Control: A Norwegian Research Bulletin*, vol. 41, no. 3, pp. 141–163, 2020. [Online]. Available: https://doi.org/10.4173/mic.2020.3.2

[2] W. Tang and P. Daoutidis, "Data-driven control: Overview and perspectives," in *2022 American Control Conference (ACC)*. IEEE, 2022, pp. 1048–1064. [Online]. Available: https://doi.org/10.23919/ACC53348.2022.9867266

[3] K. Narendra and K. Parthasarathy, "Identification and control of dynamical systems using neural networks," *IEEE Transactions on Neural Networks*, vol. 1, no. 1, pp. 4–27, Mar. 1990. [Online]. Available: https://doi.org/10.1109/72.80202

[4] S. Haykin, *Neural Networks and Learning Machines*, 3rd ed. Upper Saddle River, NJ, USA: Pearson Education, 2009, accessed: 2026-05-19. [Online]. Available: https://upsalesiana.ec/ing36ar8r4

[5] S. Shin, M. Kang, and J. Baek, "Dynamic model learning and control of robot manipulator based on multi-layer perceptron neural network," *Transactions of the Korean Society of Mechanical Engineers - A*, vol. 47, no. 12, pp. 945–957, Dec. 2023. [Online]. Available: https://doi.org/10.3795/KSME-A.2023.47.12.945

[6] M. Deja and A. P. Markopoulos, "Advances and trends in non-conventional, abrasive and precision machining," *Machines*, vol. 9, no. 2, p. 37, Feb. 2021. [Online]. Available: https://doi.org/10.3390/machines9020037

[7] M. Suzuki and O. Kaneko, "Data-driven control by using data-driven prediction and LASSO for FIR typed inverse controller," *Electronics and Communications in Japan*, vol. 106, no. 3, Aug. 2023. [Online]. Available: https://doi.org/10.1002/ecj.12405

[8] S. Yahagi and M. Suzuki, "Direct data-driven design for a sparse feedback controller based on VRFT and LASSO regression," *IFAC-PapersOnLine*, vol. 55, no. 25, pp. 229–234, 2022. [Online]. Available: https://doi.org/10.1016/j.ifacol.2022.09.351

[9] E. Garrabe, H. Jesawada, C. D. Vecchio, and G. Russo, "On convex data-driven inverse optimal control for nonlinear, non-stationary and stochastic systems," *Automatica*, vol. 173, p. 112015, Mar. 2025. [Online]. Available: https://doi.org/10.1016/j.automatica.2024.112015

[10] Marji, A. M. Widodo, Marjono, W. Firdaus Mahmudy, and A. Maulana Muhamad, "Comparison of multi-layer perceptron and support vector machine methods on rainfall data with optimal parameter tuning," *International Journal of Advanced Computer Science and Applications*, vol. 14, no. 7, 2023. [Online]. Available: https://dx.doi.org/10.14569/IJACSA.2023.0140745

[11] N. V. Thieu, S. Mirjalili, H. Garg, and N. T. Hoang, "Metaperceptron: A standardized framework for metaheuristic-driven multi-layer perceptron optimization," *Computer Standards & Interfaces*, vol. 93, p. 103977, Apr. 2025. [Online]. Available: https://doi.org/10.1016/j.csi.2025.103977

[12] C. Saldaña Enderica, J. R. Llata, and C. Torre-Ferrero, "Guided reinforcement learning with twin delayed deep deterministic policy gradient for a rotary flexible-link system," *Robotics*,

vol. 14, no. 6, p. 76, May 2025. [Online]. Available: https://doi.org/10.3390/robotics14060076

[13] J. G. Guarnizo Marin, N. Díaz Aldana, and C. Trujillo Rodríguez, "Design and implementation of an inverse neural network controller applied to VSC converter for active and reactive power flow, based on regions of work," *Revista Facultad de Ingeniería Universidad de Antioquia*, no. 72, pp. 20–34, Aug. 2014. [Online]. Available: https://doi.org/10.17533/udea.redin.15045

[14] V. A. Rodríguez-Toro, J. E. Garzón, and J. A. López, "Control neuronal por modelo inverso de un servosistema usando algoritmos de aprendizaje levenberg-marquardt y bayesiano," *arXiv*, 2011. [Online]. Available: https://doi.org/10.48550/arXiv.1111.4267

[15] M. Sasaki, M. Takeda, J. Muguro, and W. Njeri, "Trajectory control of flexible manipulators using forward and inverse models with neural networks," *Vibration*, vol. 8, no. 3, p. 48, Aug. 2025. [Online]. Available: https://doi.org/10.3390/vibration8030048

[16] M. T. Hagan, H. B. Demuth, M. H. Beale, and O. D. Jesús, *Neural Network Design*, 2nd ed. Stillwater, OK, USA: Martin Hagan, 2024, free eBook available online, Accessed: 2026-05-19. [Online]. Available: https://upsalesiana.ec/ing36ar8r16

[17] M. Hagan and M. Menhaj, "Training feedforward networks with the marquardt algorithm," *IEEE Transactions on Neural Networks*, vol. 5, no. 6, pp. 989–993, 1994. [Online]. Available: https://doi.org/10.1109/72.329697

[18] J. Capa López, *Control de un manipulador flexible de un único segmento.* Universidad de Cantabria, 2022. [Online]. Available: https://upsalesiana.ec/ing36ar8r18

[19] C. A. Saldaña Enderica, J. R. Llata, and C. Torre-Ferrero, "Optimization of Q and R matrices with genetic algorithms to reduce oscillations in a rotary flexible link system," *Robotics*, vol. 13, no. 6, p. 84, May 2024. [Online]. Available: https://doi.org/10.3390/robotics13060084

[20] Quanser. (2021) Rotary flexible link system identification and LQR design. MATLAB Central File Exchange. [Online]. Available: https://upsalesiana.ec/ing36ar8r20

Scientific Paper / Artículo Científico

UNIVERSIDAD POLITÉCNICA SALESIANA ECUADOR
INGENIUS
Revista de Ciencia y Tecnología
https://doi.org/10.17163/ings.n36.2026.09
pISSN: 1390-650X / eISSN: 1390-860X

Swarm algorithms for UAV route planning: a systematic review of characteristics, classification, and operational performance

Algoritmos de enjambre para planificación de rutas en UAV: Una revisión sistemática de características, clasificación y desempeño operativo

Marcelo Rea-Guamán[1,*], Andrea López-López [1], Andrés Almeida-Jara[1]

Received: 16-11-2025, Received after review: 23-03-2026, Accepted: 28-04-2026, Published: 01-07-2026

Abstract

Path planning for unmanned aerial vehicles (UAVs) using swarm algorithms is a central topic in autonomous robotics. However, the literature still lacks systematic reviews that jointly address algorithm classification, operational characteristics, and performance evaluation. This study proposes a five-category taxonomy, a domain-based frequency analysis, and a nine-metric evaluation framework. Following PRISMA guidelines, searches were conducted in IEEE Xplore, Scopus, ScienceDirect, and ACM Digital Library between November and December 2025. From an initial set of 2,761 records, 31 articles were included, comprising 25 primary studies and 6 systematic reviews. PSO, ACO, and ABC account for 66% of the 56 identified algorithm appearances, with prominent applications in defense, search and rescue, and agriculture. Hybrid methods emerged as the main research trend, while AI-based approaches show the greatest potential for scalability and autonomous adaptation. The reviewed literature prioritizes path length (96%) and convergence time (88%), whereas energy efficiency (56%) and area coverage (48%) remain comparatively underexplored.

Keywords: UAVs, swarm intelligence, path planning, metaheuristic optimization, PRISMA.

Resumen

La planificación de rutas para UAV mediante algoritmos de enjambre es clave en la robótica autónoma; sin embargo, faltan revisiones sistemáticas que integren clasificación, características operativas y desempeño. Este estudio propone una taxonomía de cinco categorías, un análisis de frecuencias por dominio y un marco de evaluación con nueve métricas. Siguiendo la metodología PRISMA, se revisaron las bases de datos IEEE Xplore, Scopus, ScienceDirect y ACM Digital Library entre noviembre y diciembre de 2025. De 2761 registros, se incluyeron 31 artículos: 25 estudios primarios y 6 revisiones. Los algoritmos PSO, ACO y ABC concentran el 66 % de las 56 implementaciones identificadas, con especialización en defensa, búsqueda y rescate, y agricultura. Los métodos híbridos constituyen la principal tendencia, mientras que la IA destaca por su potencial de escalabilidad y adaptación. La literatura prioriza la longitud de trayectoria (96 %) y el tiempo de convergencia (88 %), mientras que la eficiencia energética (56 %) y la cobertura de área (48 %) reciben menor atención.

Palabras clave: UAV, inteligencia de enjambre, planificación de rutas, optimización metahurística, PRISMA

[1,*]Departamento de Ciencias de la Computación. Universidad de las Fuerzas Armadas ESPE, Sangolquí, Ecuador.
Corresponding author ✉: amrea1@espe.edu.ec.

Suggested citation: M. Rea-Guamán, A. López-López and A. Almeida-Jara, "Swarm algorithms for UAV route planning: a systematic review of characteristics, classification, and operational performance," *Ingenius, Revista de Ciencia y Tecnología*, N.° 36, pp. 110-124, 2026, DOI: https://doi.org/10.17163/ings.n36.2026.09.

1. Introduction

1.1. Context and Motivation

Unmanned aerial vehicles (UAVs) have expanded rapidly across civil and military sectors because of their relatively low cost, operational flexibility, and ability to access remote or hazardous environments [1, 2]. They are now widely used in reconnaissance, precision agriculture, infrastructure inspection, disaster response, and emergency support, where rapid deployment and real-time information are essential for decision-making [3–5]. Technological advances have also enabled the development of UAV swarms, defined in this study as systems composed of two or more UAVs that coordinate through centralized or decentralized mechanisms to accomplish a shared mission [6]. Their scalability makes them particularly suitable for surveillance, search and rescue, environmental monitoring, and communication support in uncertain environments.

Path planning is a core challenge because UAVs must generate safe and efficient trajectories while satisfying constraints related to distance, threats, energy consumption, time windows, coverage, and admissible airspace [3], [7, 8]. In swarms, this becomes a coordination problem: vehicles must avoid collisions, route overlap, resource waste, and communication bottlenecks while acting cooperatively [6], [9].

Path-planning approaches comprise graph-based, swarm-based, and AI-based methods [5, 6]. Traditional algorithms, including Dijkstra and A*, perform well in structured settings, whereas swarm algorithms such as PSO, ACO, and ABC are better suited to dynamic multi-UAV optimization because they support population-based search, adaptability, and decentralized coordination [6], [10].

However, core swarm methods also have limitations: PSO may converge prematurely, ACO may scale poorly because of pheromone updates, and ABC may stagnate during exploitation [11]. These limitations explain the recent shift toward hybrid and AI-augmented approaches, underscoring the need for a structured synthesis of algorithm types, operational characteristics, and application-specific trade-offs.

1.2. Theoretical Framework and Related Work

Swarm intelligence is a computational paradigm inspired by decentralized biological systems in which local interactions generate adaptive collective behavior [12,13]. Its main principles include self-organization, local communication or stigmergy, feedback, and redundancy, which together provide robustness and adaptability in dynamic environments [13]. Among the foundational algorithms, ACO models pheromone-based foraging, PSO models flocking behavior, and ABC models bee foraging. These algorithms remain the principal reference methods in UAV path planning [14–16]. Later proposals, such as GWO, WOA, and SSA, have broadened the bio-inspired repertoire, particularly for high-dimensional optimization; however, the present review shows that these newer techniques remain less frequently validated in UAV-specific contexts [17–20].

Swarm algorithms are attractive because they explore multiple regions of the search space simultaneously, do not require gradient information, and adapt well to nonlinear or non-differentiable problems [21, 22]. These properties have supported applications in robotics, routing, and autonomous coordination and have encouraged recent work on hybridization with reinforcement learning and other AI methods for dynamic multi-agent settings [23–25].

Recent reviews address either general UAV path planning or swarm intelligence more broadly [26–29], but they do not jointly examine swarm-algorithm prevalence, taxonomic structure, operational characteristics, and comparative metrics for UAV path planning. This review addresses that gap by focusing on studies published between 2020 and 2025.

1.3. Problem Statement and Justification

Despite significant advances in the development of swarm algorithms for path planning, there remains a notable lack of systematic reviews that comprehensively integrate and classify algorithmic approaches, operational characteristics, and comparative performance across diverse application scenarios [30, 31].

Classical methods such as PSO, ACO, and ABC remain effective, but each has limitations in dynamic and complex scenarios [11]. This has driven the development of hybrid methods, yet the field still lacks unified evaluation metrics and common comparison protocols.

In this review, operational performance encompasses computational indicators, including convergence time, solution quality, and efficiency, as well as mission-level indicators, such as energy efficiency, area coverage, success rate, and threat exposure. This broader definition is necessary because UAV path planning must be evaluated beyond isolated optimization scores.

Accordingly, this PRISMA-based review synthesizes, classifies, and analyzes swarm algorithms for UAV path planning to support algorithm selection, identify research trends, and highlight future directions based on 25 primary studies and 6 prior reviews published between 2020 and 2025.

1.4. Research Objectives and Research Questions

Building on the gaps identified in the literature, this systematic review is structured around three interre-

lated research axes. The first seeks to determine which swarm algorithms are most frequently implemented in UAV path planning, using quantitative analysis to characterize the current landscape of the field and its dominant approaches. The second develops a grounded taxonomy that classifies these algorithms according to their theoretical foundations, optimization mechanisms, and coordination strategies, thereby providing an organizational framework for the diversity of existing approaches. Finally, the third examines the operational characteristics that define the behavior of these algorithms, ranging from multi-agent coordination to computational efficiency, and analyzes how these characteristics affect performance across different application contexts.

The main contributions of this work are threefold: (1) a five-category grounded taxonomy of swarm methods for UAV path planning, organized according to optimization and coordination strategies and developed empirically from patterns identified across 25 primary studies and theoretically from prior systematic reviews [26, 28, 27, 29] to provide an overarching organization of the diverse approaches found in the literature; (2) a quantitative assessment of 56 algorithm implementations across 25 studies, identifying the predominant methodologies used in each application domain, including defense (36.0%), search and rescue (32.0%), agriculture (20.0%), and inspection (8.0%), as well as their functional specialization; (3) a nine-metric evaluation framework for assessing swarm-method performance, with complete traceability to all reviewed studies, enabling systematic comparison across different approaches.

The remainder of this article is organized as follows: Section 2 details the PRISMA methodology employed; Section 3 presents the results and discussion; and Section 4 outlines the conclusions, limitations, and future research directions.

2. Materials and Methods

2.1. Systematic Review Strategy and Design

This systematic review follows the PRISMA (Preferred Reporting Items for Systematic Reviews and Meta-Analyses) guidelines to ensure transparency and replicability throughout the identification, selection, and analysis of studies [32].

Identification: The bibliographic search was conducted between November 15 and December 19, 2025, in four major academic databases selected for their relevance to robotics, artificial intelligence, and autonomous systems: ACM Digital Library, IEEE Xplore, ScienceDirect, and Scopus. The search was performed using the standardized search string defined in Section 2.2, with adaptations to the syntax requirements of each database interface while preserving semantic equivalence.

Screening: At this stage, duplicate records were identified through Mendeley Reference Manager's automatic detection feature based on DOI, title, and author matching. No duplicates were detected across the four databases, likely because of the specificity of the search string and the distinct coverage scope of each database. Subsequently, records with no direct relation to the research question, based on their title and abstract, were independently screened by the three authors, with disagreements resolved through discussion until consensus was reached. Reference management and bibliographic tracking were performed using Mendeley Reference Manager, while the screening matrix and data extraction were documented in shared spreadsheets using Google Sheets to ensure transparency and traceability.

Eligibility: Full-text assessment was applied to 51 preselected articles using the inclusion and exclusion criteria described in Section 2.3. Twenty studies were excluded mainly because they lacked swarm coordination, adequate metrics, temporal fit, or experimental/simulation-based validation.

Inclusion: The final selection comprised 31 articles that met all defined criteria. These studies were analyzed in depth to extract algorithmic implementations, operational characteristics, evaluation metrics, and application domains. The final corpus consisted of 25 primary studies on specific implementations of swarm algorithms and 6 systematic reviews that provided the theoretical framework for the proposed taxonomy.

2.2. Search String

A structured search string was developed by combining terms related to three main dimensions of the study: ("drone swarm" OR "swarm intelligence") AND ("route optimization" OR "path planning") AND ("algorithms" OR "optimization techniques").

The search string was designed to capture articles that simultaneously addressed three mandatory dimensions: (1) drone swarm systems, (2) route planning or optimization problems, and (3) algorithmic solutions. All searches were restricted to the 2020–2025 publication window and limited to journal articles and conference proceedings.

It is acknowledged that the search string may not capture all relevant studies, particularly those using nonstandard terminology such as "formation control," "cooperative navigation," or "multi-robot planning" without explicitly mentioning swarm intelligence. This limitation was partially mitigated through backward reference checking of the six included systematic reviews and forward citation tracking of highly cited primary studies.

2.3. Selection Criteria

Inclusion (IC) and exclusion (EC) criteria were established to delimit relevant articles and ensure the pertinence of the results.

The criteria considered are detailed in Table 1:

Table 1. Inclusion and exclusion criteria.

Inclusion Criteria	Exclusion Criteria
IC1: Studies must present swarm algorithms applied specifically to UAV path planning.	**EC1:** Exclusive focus on individual UAVs without swarm coordination or multi-agent cooperation.
IC2: Must describe at least three operational characteristics of the algorithms, such as drone cooperation, dynamic task distribution, energy	**EC2:** Applications unrelated to path planning (e.g., solely flight control, stabilization, or communication systems with no impact on trajectories).
IC3: Must include quantitative evaluation metrics or comparisons with other state-of-the-art algorithms.	**EC3:** Grey literature without peer review (technical reports, undergraduate theses, working papers).
IC4: Must be research articles, conference papers, or systematic reviews published in peer-reviewed academic sources.	**EC4:** Insufficient methodological information or absence of quantitative results.
IC5: Must be written in English or Spanish.	

The exclusion of grey literature (EC3) warrants specific justification. Technical reports, undergraduate theses, and working papers were excluded to ensure that all analyzed studies had undergone peer review, thereby providing a minimum quality baseline for the evidence synthesized in this review. Although this criterion may omit relevant industry implementations of UAV swarm technology, the decision was made to prioritize methodological rigor and reproducibility over exhaustive coverage. This limitation is explicitly acknowledged in Section 4.

2.4. Quality Assessment

Given the heterogeneous nature of the included studies, which spanned simulation-based experiments, comparative benchmarks, and algorithm proposals with varying levels of validation, a formal quality appraisal was conducted to contextualize the strength of evidence underlying the review's conclusions. Rather than applying a standardized tool designed for clinical or experimental research, such as the Cochrane Risk of Bias tool, which would be poorly suited to the computational optimization literature, a domain-appropriate quality assessment framework was developed based on five criteria:

(Q1) Algorithmic description: Does the study provide sufficient detail to understand and potentially reproduce the proposed algorithm?

(Q2) Experimental design: Does the study define clear test scenarios with specified parameters, such as map dimensions, obstacle density, UAV count, and iteration limits?

(Q3) Baseline comparison: Does the study compare the proposed method against at least one established baseline algorithm?

(Q4) Statistical reporting: Does the study report results across multiple independent runs with measures of central tendency and variability, such as mean and standard deviation?

(Q5) Metric coverage: Does the study evaluate performance using at least three of the nine metrics identified in this review?

Each criterion was evaluated as met (1) or not met (0), yielding a quality score from 0 to 5. The assessment was performed independently by two authors, with the third author resolving discrepancies. Two studies initially classified as primary (IEEE7 and IEEE8) were reclassified as systematic reviews during this process, as they scored 1/5 due to the absence of novel algorithmic proposals or experimental validation. Following this reclassification, the final set of 25 primary studies yielded a mean quality score of 4.3/5 (SD = 0.9), with 24 studies (96.0%) scoring 3 or higher. The most frequently unmet criterion was Q4, statistical reporting with variability measures, which was met by 52.0% of studies, followed by Q5, coverage of at least three evaluation metrics, which was met by 80.0%. No studies were excluded based on quality scores.

Performance claims in this review, particularly regarding the 15–50% improvements attributed to hybrid methods, are reported as stated by the original authors within their specific experimental contexts. Therefore, they should not be interpreted as generalizable findings across standardized benchmarks, which do not yet exist in this field. The absence of such benchmarks is identified as a critical limitation in Section 4.

2.5. Study Selection Process

The initial search, conducted between November 15 and December 19, 2025, using the defined search strings, identified 2,761 records across the four academic databases. ScienceDirect contributed the largest share, with 1,404 records (50.9%), followed by Scopus with 771 (27.9%), IEEE Xplore with 314 (11.4%), and

ACM Digital Library with 272 (9.9%). After title and abstract screening, 51 articles were assessed for full-text eligibility, of which 20 were excluded based on the criteria detailed in Section 2.1. Figure 1 presents the PRISMA flow diagram for each phase of the selection process.

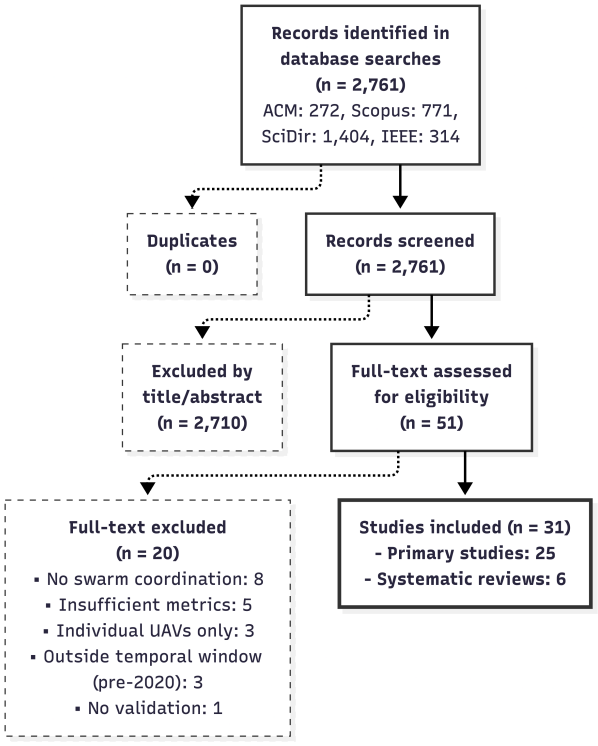

Figure 1. Flowchart of the selection process at each PRISMA phase.

The final sample comprised 25 primary studies and 6 systematic reviews. Only the primary studies were used for implementation counts, metric coverage, and comparative analysis. This distribution is shown in Table 2.

Table 2. Distribution of Articles by Source.

Source	Articles	Percentage	Year Range
Science Direct	7	22.60%	2020-2025
ACM Digital Library	6	19.40%	2021-2025
IEEE Xplore	9	29.00%	2020-2025
Scopus	9	29.00%	2021-2025
Total	**31**	**100%**	**2020-2025**

Each article was coded according to its source to facilitate traceability:

- SCI1–SCI7: ScienceDirect (7 articles)
- ACM1–ACM6: ACM Digital Library (6 articles)
- IEEE1–IEEE9: IEEE Xplore (9 articles)
- SCO1–SCO9: Scopus (9 articles)

Table 4 summarizes the 31 included articles by their ID, title, primary algorithm or study type, objective, and year of publication.

3. Results and Discussion

3.1. Data Extraction and Classification

The systematic analysis of the 25 primary studies enabled responses to the three research questions posed. Before presenting the findings, it is necessary to clarify an important methodological distinction between the two counting systems used in this analysis. Table 3 reports the total frequency of base algorithm appearances across all studies (n = 56), where a single study employing multiple algorithms, such as a hybrid combining PSO and ABC, contributes one count to each respective algorithm category. Table 3 presents the algorithmic building blocks of the field, while Table 5 summarizes the research contributions organized by methodological approach.

RQ1: Which algorithms are most commonly used in UAV path planning? The quantitative analysis reveals a clear dominance of three base algorithms in the UAV path-planning field. Table 4 summarizes the implementation frequency of the five most representative algorithm groups.

As the data indicate, PSO leads with 18 appearances (32.1%), followed by ACO with 11 (19.6%) and ABC with 8 (14.3%). GWO accounts for 7 appearances (12.5%), while other algorithms, such as GA, DE, and MPA, collectively contribute 12 additional cases (21.4%). Taken together, PSO, ACO, and ABC represent 66% of all identified algorithm appearances, consolidating their status as the fundamental reference algorithms in this domain. Figure 2 provides a visual representation of this distribution.

This predominance is not arbitrary: each algorithm has demonstrated specific strengths according to its operational context. PSO is widely used in defense scenarios requiring rapid convergence [33, 34]; ACO is prominent in search and rescue because of its route-optimization precision [35]; and ABC appears especially useful in agricultural settings, where energy efficiency is critical [36].

Table 3. Implementation Frequency of Base Algorithms

Algorithm	Implementations	Percentage
PSO	18	32.1 %
ACO	11	19.6 %
ABC	8	14.3 %
GWO	7	12.5 %
Others	12	21.4 %
Total	**56**	**100%**

Table 4. Complete Analysis of Included Articles Algorithms.

ID	Title	Primary Algorithm	Objetive	Year
SCI1	AUV path planning in a 3D marine environment	MCO (Multiple Swarm Co-Evolutionary)	Minimize distance, altitude, angle, currents	2024
SCI2	From PID to swarms: A decade of advancements	Systematic Review	Synthesize advances 2013–2023	2024
SCI3	Hybrid chaos game and grey wolf optimization	HCGO (GWO + CGO)	Minimize path length, threats, altitude	2025
SCI4	Large-scale UAV swarm path planning	PO-WMFDDPG	Maximize success rate and reward	2025
SCI5	MMPA: Modified marine predator algorithm	MMPA	Minimize multi-objective function	2024
SCI6	Novel task decomposed multi-agent TD3	TD-MATD3	Coordinate multiple UAVs	2024
SCI7	Path planning with online changing tasks	ORPFOA	3D routes for oil pipeline inspection	2020
ACM1	Enhanced Moth-Flame Optimization	EMFO	Optimize 3D path planning	2025
ACM2	Improved Particle Swarm Optimization Algorithms	DMSQPSO	Avoid premature convergence	2022
ACM3	AUV underwater 3D path planning based on particle swarm optimization	PSO-ASCS	Plan efficient underwater routes	2022
ACM4	Path Planning Methods for UAVs: Survey	Methods Review	Classify path planning techniques	2024
ACM5	UAV Path Planning with Improved PSO	PSO con Levy Flight	Avoid premature convergence	2024
ACM6	Swarm intelligence based robotic search in unknown maze-like environments	PSO + Bat Algorithm	Locate fixed target	2021
IEEE1	A Multigroups Cooperative Particle Swarm Algorithm	PSO multigroup	Improve accuracy in IoV	2024
IEEE2	A Survey on Swarm Intelligence Algorithms	SI Review	Classify SI techniques	2025
IEEE3	Artificial Hummingbird Algorithm	AHA	Optimize trajectories	2022
IEEE4	Distributed multi-UAV cooperation	NTVPSO-ADE	Distributed coordination	2022
IEEE5	Improved Bat Algorithm for UAV	IBA (BA + ABC)	Optimize 3D trajectories	2021
IEEE6	A Multi-UAV Formation Obstacle Avoidance Method	PSO	Maintain triangular formation	2025
IEEE7	Swarm Intelligence for UAV	SI Review	Analyze SI algorithms	2024
IEEE8	UAV Swarm Intelligence: Recent Advances	Multi-layer review	Synthesize SI architectures	2020
IEEE9	UCAV Path Planning Based on CPSO	CPSO	Minimize threats and fuel consumption	2020
SCO1	A Comparative Study of SI Algorithms	12 SI algorithms	Minimize combined cost	2021
SCO2	Multi-Strategy Enhanced MPA	MEMPA	Minimize multi-objective function	2025
SCO3	Bionic 3D Path Planning	Bionic-Krill	Minimize length, time, consumption	2024
SCO4	Intelligent Scheduling Technology	DQN-SISA	Minimize dynamic cost	2024
SCO5	Optimal path planning for drones	Improved ACO	Minimize distance and time	2022
SCO6	Path Planning via SI Algorithms	ABC vs PSO	Minimize total distance	2023
SCO7	Research on Unmanned Aerial Vehicle Path Planning	A* + BiLSTM	Minimize distance and time	2024
SCO8	Swarm intelligence: A survey of model classification and applications	Comprehensive review	Synthesize SI methods	2025
SCO9	UAV Path Planning Based on E-RRT	E-RRT	Minimize nodes and distance	2024

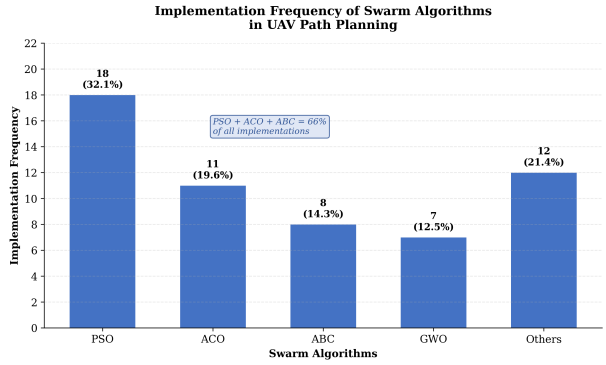

Figure 2. Implementation frequency of swarm algorithms in UAV path planning.

RQ2: How are swarm algorithms classified? The identified algorithms were organized into five taxonomic categories grounded in their theoretical foundations, optimization mechanisms, and coordination strategies. This classification was constructed bottom-up from the 25 primary studies and validated against the six systematic reviews that constitute the theoretical framework of the study. The categories are defined as follows: (1) Optimization Algorithms encompass classical metaheuristic methods that optimize objective functions through population-based search; (2) Hybrid Methods combine two or more distinct algorithmic approaches to overcome individual limitations; (3) Cooperative Control Algorithms specifically address multi-agent coordination through local behavioral rules; (4) Bio-inspired Algorithms simulate specific biological behaviors beyond classical swarm paradigms; and (5) AI-based Algorithms employ machine learning or deep learning for trajectory planning. These categories are mutually exclusive at the primary level; however, certain studies contribute to multiple categories when they present distinct methodological innovations, such as a cooperative control mechanism combined with a bio-inspired component. Table 5 presents the distribution.

Figure 3 complements the table by visualizing both the absolute count and the proportional weight of each category across the 36 classified implementations, making the structural hierarchy of the taxonomy immediately apparent.

Table 5. Distribution of Algorithms by Taxonomic Category.

Category	Count	Main Examples	Trend
Optimization Algorithms	13	PSO, ACO, GWO, ABC, DE, MPA	Stable
Hybrid Methods	10	MCO, HCGO, MMPA, PSO-ASCS, TD-MATD3	Growing
Cooperative Control Algorithms	6	Boids, UAV formations, multi-group coordination	Emerging
Bio-inspired Algorithms	4	AHA, Bat Algorithm, Bionic-Krill, EMFO	Emerging
AI-based Algorithms	3	PO-WMFDDPG, DQN-SISA, BiLSTM	Emerging

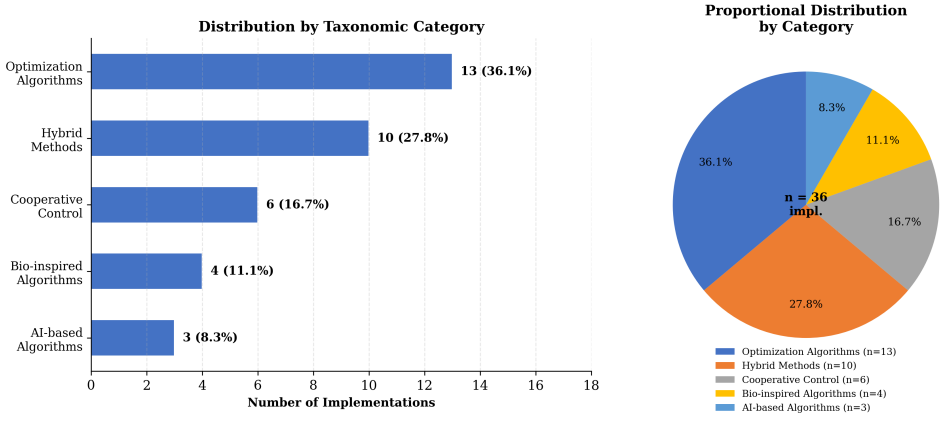

Figure 3. Distribution of swarm algorithm implementations by taxonomic category: absolute frequency (left) and proportional distribution (right).

The Optimization Algorithms category constitutes the foundation of the field, with 13 implementations of classical metaheuristic algorithms inspired by the collective animal behavior. Representative studies include ACM2 [37], ACM5 [38], IEEE1 [39], IEEE5 [40], IEEE6 [41], ACM6 [42], SCO6 [43], IEEE9 [34], SCO1 [44] ACM3 [45], and SCO5 [35].

Hybrid Methods emerge as the predominant research direction with 10 implementations, representing 27.8% of the total categories. These approaches

strategically combine multiple techniques to overcome the inherent limitations of individual algorithms. For instance, MCO integrates AOA with SSA through co-evolution, HCGO combines GWO with CGO by incorporating chaotic variation, and TD-MATD3 fuses multi-agent reinforcement learning with task decomposition. This category includes SCI1 [46], SCI3 [33], SCI5 [47], SCI6 [48], ACM3 [45], IEEE5 [40], SCO2 [49], SCO3 [36], SCI7 [50], and SCO9 [51].

Cooperative Control Algorithms, identified in 6 studies, specifically address multi-UAV coordination through local behavioral rules. The distinguishing characteristic of these methods is decentralized coordination: they require no central controller and operate exclusively through local communication between neighboring agents. These implementations are documented in IEEE1 [39], ACM6 [42], IEEE4 [52], IEEE6 [41], SCI6 [48], and SCO6 [43].

Bio-inspired Algorithms comprise 4 implementations that simulate specific behaviors of natural organisms beyond classical swarm paradigms: AHA (Artificial Hummingbird Algorithm), Bionic-Krill, EMFO (Enhanced Moth-Flame Optimization), and IBA. These studies report path-quality gains ranging from 1.1% to 17.5% in their respective comparisons [36], [53, 54]. The corresponding studies are IEEE3 [53], IEEE5 [40], SCO3 [36], and ACM1 [54].

Finally, AI-based Algorithms represent the most promising technological frontier, with 3 implementations, equivalent to 8.3% of the total. PO-WMFDDPG employs Deep Reinforcement Learning with mean-field theory, achieving success rates above 90% in swarms of up to 120 UAVs and latency below 0.05 seconds [55]. DQN-SISA uses a Deep Q-Network for dynamic algorithm selection, yielding 8–15% reductions in operational costs [56]. A*+BiLSTM integrates classical planning with bidirectional neural networks for trajectory prediction [57]. These methods stand out for their capacity to adapt dynamically to changing environments through continuous learning.

The trend analysis reveals significant patterns: classical optimization algorithms maintain a stable presence as the backbone of the field, hybrid methods show accelerated growth, and the three emerging categories, cooperative control, bio-inspired, and AI-based, collectively account for 36.1% of all classified implementations, evidencing the active diversification of the field toward increasingly sophisticated approaches.

RQ3: What are the operational characteristics and their impact? The qualitative analysis of the 25 primary studies identified 12 fundamental operational characteristics that define the behavior of swarm algorithms. These characteristics were systematically extracted through thematic analysis of the reported implementations and subsequently contrasted with the taxonomies proposed in six prior systematic reviews of the field: SCI2 [26], covering 2013–2023; ACM4 [27], a methods survey; IEEE2 [28], an SI survey; IEEE7 [58], a UAV SI analysis; IEEE8 [59], a review of SI architectures; and SCO8 [29], a comprehensive review. These reviews provide consolidated conceptual frameworks for classifying and evaluating swarm algorithms in path planning.

The 12 characteristics were grouped by function into four dimensions: coordination, including cooperation through information exchange, dynamic task distribution in the event of failures, and local communication without centralized infrastructure; optimization, including global minimization of distance, time, and costs, exploration–exploitation balance, and advanced methods such as PSO, GA, and ACO; safety, including collision avoidance through minimum separation and real-time adaptation to obstacles; and efficiency, including scalability while maintaining performance, real-time operation, energy management.

Performance was reported using nine main metrics, summarized in Table 6.

Table 6. Coverage of Evaluation Metrics Across Studies.

Metric	Studies	Coverage
Path Length	24	96%
Convergence Time	22	88%
Robustness	20	80%
Computational Efficiencyl	19	76%
Success Rate	18	72%
Threat Exposures	16	64%
Energy Efficiency	14	56%
Trajectory Smoothness	14	56%
Area Coverage	12	48%

Path length dominates with 96% coverage, reflecting the priority given to spatial efficiency in path-planning research. It is followed by convergence time (88%) and robustness (80%), both of which are essential for real-time applications. Notably, metrics that are critical for real-world deployment, such as energy efficiency (56%) and area coverage (48%), receive comparatively less attention, revealing a persistent gap between academic research priorities and actual operational requirements.

The relative importance of characteristics and metrics varies according to the application domain. As detailed in Section 3.3, military missions and search and rescue operations account for the largest shares of studies (36.0% and 32.0%, respectively), followed by precision agriculture (20.0%) and infrastructure inspection (8.0%). Each domain imposes distinct metric priorities that reflect its specific operational demands. Figure 4 illustrates this distribution.

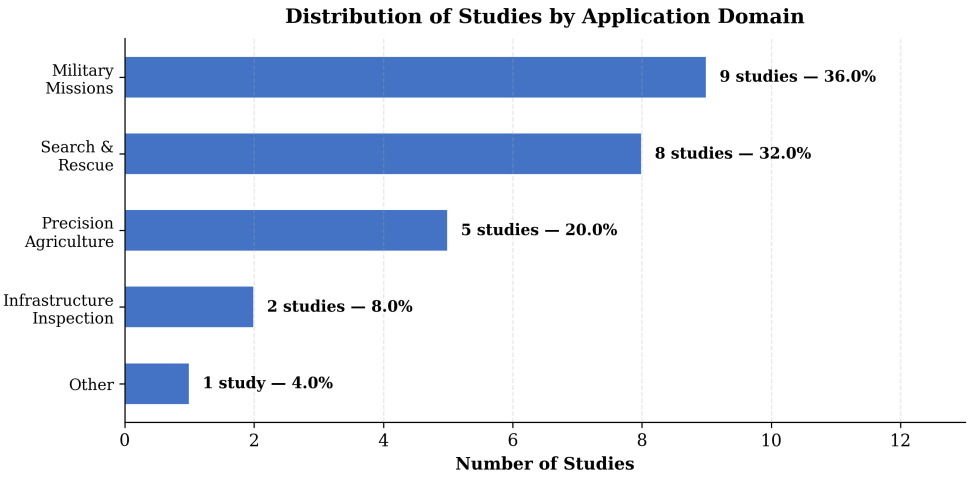

Figure 4. Distribution of studies by application domain.

3.2. Data Analysis

Comparative analysis was organized around convergence, solution quality, robustness, and computational complexity.

Because no standardized benchmarks exist, the reported figures must be interpreted as study-specific trends rather than direct head-to-head comparisons under identical conditions. Table 7 synthesizes the resulting performance profiles.

PSO generally converges faster than ACO and ABC, while hybrid methods tend to improve convergence, robustness, and adaptability in the reviewed experiments. ACO often favors solution quality, whereas AI-based methods provide the strongest dynamic adaptation in changing environments.

Table 7. Comparison of base versus hybrid algorithms.

Algorithm	Convergence	Quality	Robustness	Complexity
PSO	Medium	Alta	Medium	$O(n)$
ACO	Low	Very High	Alta	$O(n^2)$
ABC	Medium	Alta	Medium	$O(n)$
Híbridos	Very High	Very High	Very High	$O(n \log n)$

Computational complexity determines practical viability according to the operational context. PSO and ABC, with linear complexity O(n), are scalable for large-scale problems and real-time applications. ACO exhibits quadratic complexity $O(n^2)$ due to the iterative updating of the pheromone matrix, which limits its applicability in time-critical scenarios but justifies its use when solution quality is the priority. Hybrid methods, with O(nlogn) complexity, offer a balance between efficiency and performance.

Reported gains include path-length reductions of 1.1-17.5% and cost reductions of 10% to 13% in specific studies, while deep learning-based methods report inference times below 0.05 s [36], [49], [55].

A major limitation is the simulation-to-reality gap: none of the 25 primary studies validated results with physical UAV swarms. Most experiments involved 3 to 10 UAVs, with only one study testing scalability up to 120 units [55]. No systematic correlation between swarm size and path optimality could be established from the available data, as studies varied significantly in their experimental configurations, objective functions, and optimality criteria. Establishing such correlations would require standardized benchmarks that control for these confounding variables.

3.3. Analysis by Application Domain

The distribution of the analyzed studies by application domain reveals patterns of algorithmic specialization. As shown in Table 8, military missions account for 36.0% of studies, followed by search and rescue at 32.0%, agriculture at 20.0%, inspection at 8.0%, and other domains at 4.0%.

Table 8. Distribution of studies by application domain.

Domain	Studies	Percentage	Predominant Algorithms
Military missions	9	36.0 %	PSO, HCGO, CPSO
Search and rescue	8	32.0 %	ACO, PO-WMFDDPG
Agriculture	5	20.0 %	ABC, Bionic-Krill
Inspection	2	8.0 %	PSO-ASCS, Hybrid methods
Other (IoV)	1	4.0 %	Multi-group PSO
Total	**25**	**100%**	—

The military domain benefits particularly from PSO owing to its stability and rapid convergence, with variants such as HCGO [33] applied to threat minimization and CPSO [34] applied to fuel optimization. In search and rescue, ACO stands out for its precision in obstacle avoidance, while PO-WMFDDPG [55] achieves success rates above 90% while coordinating up to 120 UAVs. Agricultural applications favor ABC for its energy efficiency, complemented by Bionic-Krill [36], which achieves path-distance reductions of 1.1% to 17.5% relative to ACO and ABC. Inspection tasks favor hybrid methods such as PSO-ASCS [45] for their adaptability in variable environments.

It should be noted that the observed distribution may be influenced by publication bias, as military applications benefit from established funding streams and standardized problem formulations that facilitate academic publication, while civilian applications in logistics, environmental monitoring, and urban air mobility may be underrepresented due to proprietary constraints or the nascent state of regulatory frameworks. Additionally, the geographic distribution of research output was not analyzed in this review; regional preferences in research funding and journal accessibility may influence which algorithmic approaches receive greater attention in the indexed literature.

4. Conclusion

This review synthesized 31 studies published between 2020 and 2025, comprising 25 primary studies and 6 systematic reviews, to characterize swarm algorithms for UAV path planning following PRISMA guidelines. The evidence confirms the dominance of PSO, ACO, and ABC, which together account for 66% of the 56 identified algorithm appearances, while also showing that algorithm selection is strongly shaped by domain-specific demands.

The proposed five-category taxonomy indicates that classical optimization algorithms remain the backbone of the field, while hybrid methods constitute the main growth trend. Cooperative control, bio-inspired methods, and AI-based approaches suggest a shift toward more decentralized, adaptive, and learning-driven solutions. The nine-metric framework further shows that the literature prioritizes path length, convergence time, and robustness, while energy efficiency and area coverage remain comparatively underexplored.

Several limitations should be acknowledged. The reviewed studies are heterogeneous in scenario design, objectives, and reporting, which prevents strict meta-analysis and limits direct numerical comparison. In addition, all primary studies are simulation-based; therefore, issues such as latency, sensor noise, battery degradation, and aerodynamic interference remain insufficiently validated in real UAV swarms.

Future work should prioritize standardized benchmarks, stronger statistical reporting, public implementations, and physical validation with UAV swarms. Research opportunities are especially clear in AI-enhanced hybridization, extreme scalability, heterogeneous swarms, adversarial resilience, energy-aware replanning, and regulatory-compliant path planning. Overall, hybridization appears to be the most productive short-term direction, while artificial intelligence represents the most promising frontier for long-term scalability and autonomous adaptation.

Contributor role

- **Marcelo Rea-Guamán:** conceptualization, research, methodology, supervision, validation, writing – original draft and writing – reviewing and editing.
- **Andrea López-López:** conceptualization, formal analysis, research, methodology, supervision, validation and writing – reviewing and editing.
- **Andrés Almeida-Jara:** data curation, formal analysis, research, methodology, visualization and writing – reviewing and editing.

References

[1] H. A. Hashim, "Advances in UAV avionics systems architecture, classification and integration: A comprehensive review and future perspectives," *Results in Engineering*, vol. 25, p. 103786, Mar. 2025. [Online]. Available: https://doi.org/10.1016/j.rineng.2024.103786

[2] S. A. H. Mohsan, N. Q. H. Othman, Y. Li, M. H. Alsharif, and M. A. Khan, "Unmanned aerial vehicles (UAVs): practical aspects, applications,

open challenges, security issues, and future trends," *Intelligent Service Robotics*, vol. 16, no. 1, pp. 109–137, Jan. 2023. [Online]. Available: https://doi.org/10.1007/s11370-022-00452-4

[3] F. Outay, H. A. Mengash, and M. Adnan, "Applications of unmanned aerial vehicle (UAV) in road safety, traffic and highway infrastructure management: Recent advances and challenges," *Transportation Research Part A: Policy and Practice*, vol. 141, pp. 116–129, Nov. 2020. [Online]. Available: https://doi.org/10.1016/j.tra.2020.09.018

[4] Q. Wang, H. Zhu, G. Pan, J. Wei, C. Zhang, Z. Huang, and G. Ling, "Distributed decision making for unmanned aerial vehicle inspection with limited energy constraint," *Energy and AI*, vol. 18, p. 100429, Dec. 2024. [Online]. Available: https://doi.org/10.1016/j.egyai.2024.100429

[5] L. Mu, W. Liu, H. Wang, and Y. Zhang, "Research of UAV 3D path planning based on improved DWARF mongoose algorithm with multiple strategies," *Scientific Reports*, vol. 15, no. 1, 2025. [Online]. Available: https://doi.org/10.1038/s41598-025-11492-y

[6] K. Arshid, A. Krayani, L. Marcenaro, D. M. Gómez, and C. Regazzoni, "Toward autonomous UAV swarm navigation: A review of trajectory design paradigms," *Sensors*, vol. 25, no. 18, p. 5877, 2025. [Online]. Available: https://doi.org/10.3390/s25185877

[7] S. Aggarwal and N. Kumar, "Path planning techniques for unmanned aerial vehicles: A review, solutions, and challenges," *Computer Communications*, vol. 149, pp. 270–299, Jan. 2020. [Online]. Available: https://doi.org/10.1016/j.comcom.2019.10.014

[8] M. Jones, S. Djahel, and K. Welsh, "Path-planning for unmanned aerial vehicles with environment complexity considerations: A survey," *ACM Computing Surveys*, vol. 55, no. 11, pp. 1–39, Feb. 2023. [Online]. Available: https://doi.org/10.1145/3570723

[9] E. Dhulkefl, A. Durdu, and H. Terzioglu, "Dijkstra algorithm using UAV path planning," *Konya Journal of Engineering Sciences*, vol. 8, pp. 92–105, Dec. 2020. [Online]. Available: https://doi.org/10.36306/konjes.822225

[10] M. Dorigo, G. D. Caro, and L. M. Gambardella, "Ant algorithms for discrete optimization," *Artificial Life*, vol. 5, no. 2, pp. 137–172, Apr. 1999. [Online]. Available: https://doi.org/10.1162/106454699568728

[11] H. M. Zangana, Z. B. Sallow, M. H. Alkawaz, and M. Omar, "Unveiling the collective wisdom: A review of swarm intelligence in problem solving and optimization," *Inform : Jurnal Ilmiah Bidang Teknologi Informasi dan Komunikasi*, vol. 9, no. 2, pp. 101–110, May 2024. [Online]. Available: https://doi.org/10.25139/inform.v9i2.7934

[12] E. Bonabeau, M. Dorigo, and G. Theraulaz, *Swarm Intelligence: From Natural to Artificial Systems*. Oxford University Press, Oct. 1999. [Online]. Available: https://doi.org/10.1093/oso/9780195131581.001.0001

[13] S. Garnier, J. Gautrais, and G. Theraulaz, "The biological principles of swarm intelligence," *Swarm Intelligence*, vol. 1, no. 1, pp. 3–31, 2007. [Online]. Available: https://doi.org/10.1007/s11721-007-0004-y

[14] M. Dorigo and L. Gambardella, "Ant colony system: a cooperative learning approach to the traveling salesman problem," *IEEE Transactions on Evolutionary Computation*, vol. 1, no. 1, pp. 53–66, Apr. 1997. [Online]. Available: https://doi.org/10.1109/4235.585892

[15] J. Kennedy and R. Eberhart, "Particle swarm optimization," in *Proceedings of ICNN95 – International Conference on Neural Networks*, vol. 4. IEEE, 1995, pp. 1942–1948. [Online]. Available: https://doi.org/10.1109/ICNN.1995.488968

[16] D. Karaboga and B. Basturk, "A powerful and efficient algorithm for numerical function optimization: artificial bee colony (ABC) algorithm," *Journal of Global Optimization*, vol. 39, no. 3, pp. 459–471, Apr. 2007. [Online]. Available: https://doi.org/10.1007/s10898-007-9149-x

[17] S. Mirjalili, S. M. Mirjalili, and A. Lewis, "Grey wolf optimizer," *Advances in Engineering Software*, vol. 69, pp. 46–61, Mar. 2014. [Online]. Available: https://doi.org/10.1016/j.advengsoft.2013.12.007

[18] S. Mirjalili and A. Lewis, "The whale optimization algorithm," *Advances in Engineering Software*, vol. 95, pp. 51–67, May 2016. [Online]. Available: https://doi.org/10.1016/j.advengsoft.2016.01.008

[19] A. D. Boursianis, M. S. Papadopoulou, M. Salucci, A. Polo, P. Sarigiannidis, K. Psannis, S. Mirjalili, S. Koulouridis, and S. K. Goudos, "Emerging swarm intelligence algorithms and their applications in antenna design: The GWO, WOA, and SSA optimizers," *Applied Sciences*, vol. 11, no. 18, p. 8330, 2021. [Online]. Available: https://doi.org/10.3390/app11188330

[20] C. Li, B. Yan, C. Zhu, X. Zhou, and Y. Jia, "Swarm intelligence–optimized deep neural network for intelligent diagnosis of lithium-ion battery state of health," *Scientific Reports*, vol. 16, no. 1, Dec. 2025. [Online]. Available: https://doi.org/10.1038/s41598-025-34022-2

[21] M. Clerc, *Particle Swarm Optimization*. Hoboken, NJ, USA: John Wiley & Sons, 2010, accessed: 2026-05-19. [Online]. Available: https://upsalesiana.ec/ing36ar9r21

[22] A. G. Gad, "Particle swarm optimization algorithm and its applications: A systematic review," *Archives of Computational Methods in Engineering*, vol. 29, no. 5, pp. 2531–2561, Apr. 2022. [Online]. Available: https://doi.org/10.1007/s11831-021-09694-4

[23] R. Ghanbarzadeh and S. Mirjalili, "A structured review of large language models in metaheuristic optimisation," *Decision Analytics Journal*, vol. 15, p. 100587, 2025. [Online]. Available: https://doi.org/10.1016/j.dajour.2025.100587

[24] Y. Qiu, X. Yang, and S. Chen, "An improved gray wolf optimization algorithm solving to functional optimization and engineering design problems," *Scientific Reports*, vol. 14, no. 1, 2024. [Online]. Available: https://doi.org/10.1038/s41598-024-64526-2

[25] Y. Ji, Q. Liu, C. Zhou, Z. Han, and W. Wu, "Hybrid swarm intelligence and human-inspired optimization for urban drone path planning," *Biomimetics*, vol. 10, no. 3, p. 180, Mar. 2025. [Online]. Available: https://doi.org/10.3390/biomimetics10030180

[26] B. Cetinsaya, D. Reiners, and C. Cruz-Neira, "From PID to swarms: A decade of advancements in drone control and path planning - a systematic review (2013–2023)," *Swarm and Evolutionary Computation*, vol. 89, p. 101626, Aug. 2024. [Online]. Available: https://doi.org/10.1016/j.swevo.2024.101626

[27] X. Chen, J. Tang, Y. Ruan, and J. Zhan, "Path planning methods for UAVs: A survey," in *Proceedings of the 3rd International Conference on Computer, Artificial Intelligence and Control Engineering*, ser. CAICE 2024. ACM, Jan. 2024, pp. 894–903. [Online]. Available: https://doi.org/10.1145/3672758.3672905

[28] C. Y. Jie, M. B. Jasser, S.-S. M. Ajibade, H. N. Chua, R. T. Wong, A. S. Rafsanjani, and A. P. A. Majeed, "A survey on swarm intelligence algorithms for optimizing path planning," in *2025 21st IEEE International Colloquium on Signal Processing & Its Applications (CSPA)*. IEEE, Feb. 2025, pp. 283–288. [Online]. Available: https://doi.org/10.1109/CSPA64953.2025.10933006

[29] C. Wang, S. Zhang, T. Ma, Y. Xiao, M. Z. Chen, and L. Wang, "Swarm intelligence: A survey of model classification and applications," *Chinese Journal of Aeronautics*, vol. 38, no. 3, p. 102982, Mar. 2025. [Online]. Available: https://doi.org/10.1016/j.cja.2024.03.019

[30] G. E. M. Abro, A. M. Abdallah, F. Zahid, and S. Ahmed, "A comprehensive review of next-gen uav swarm robotics: Optimisation techniques and control strategies for dynamic environments," *Intelligent Automation & Soft Computing*, vol. 40, no. 1, pp. 99–123, 2025. [Online]. Available: https://doi.org/10.32604/iasc.2025.060364

[31] M. Kaur, A. Kaur, and P. Singh, "Uav swarm clustering and trajectory planning: A taxonomy, systematic review, current trends and research challenges," *Computers and Electrical Engineering*, vol. 128, p. 110697, Dec. 2025. [Online]. Available: https://doi.org/10.1016/j.compeleceng.2025.110697

[32] M. J. Page, J. E. McKenzie, P. M. Bossuyt, I. Boutron, T. C. Hoffmann, C. D. Mulrow, L. Shamseer, J. M. Tetzlaff, E. A. Akl, S. E. Brennan, R. Chou, J. Glanville, J. M. Grimshaw, A. Hróbjartsson, M. M. Lalu, T. Li, E. W. Loder, E. Mayo-Wilson, S. McDonald, L. A. McGuinness, L. A. Stewart, J. Thomas, A. C. Tricco, V. A. Welch, P. Whiting, D. Moher, J. J. Yepes-Nuñez, G. Urrútia, M. Romero-García, and S. Alonso-Fernández, "Declaración PRISMA 2020: una guía actualizada para la publicación de revisiones sistemáticas," *Revista Española de Cardiología*, vol. 74, no. 9, pp. 790–799, 2021. [Online]. Available: https://doi.org/10.1016/j.recesp.2021.06.016

[33] J. Yang, F. Yan, J. Zhang, and C. Peng, "Hybrid chaos game and grey wolf optimization algorithms for uav path planning," *Applied Mathematical Modelling*, vol. 142, p. 115979, 2025. [Online]. Available: https://doi.org/10.1016/j.apm.2025.115979

[34] P. Wu, T. Li, and G. Song, "Ucav path planning based on improved chaotic particle swarm optimization," in *2020 Chinese Automation Congress (CAC)*. IEEE, Nov. 2020, pp. 1069–1073. [Online]. Available: https://doi.org/10.1109/CAC51589.2020.9326556

[35] R. A. Saeed, M. Omri, S. Abdel-Khalek, E. S. Ali, and M. F. Alotaibi, "Optimal path planning for drones based on

swarm intelligence algorithm," *Neural Computing and Applications*, vol. 34, no. 12, pp. 10 133–10 155, Apr. 2022. [Online]. Available: https://doi.org/10.1007/s00521-022-06998-9

[36] N. Xu, H. Zhu, and J. Sun, "Bionic 3D path planning for plant protection UAVs based on swarm intelligence algorithms and krill swarm behavior," *Biomimetics*, vol. 9, no. 6, p. 353, 2024. [Online]. Available: https://doi.org/10.3390/biomimetics9060353

[37] C. Li and D. C. Coster, "Improved particle swarm optimization algorithms for optimal designs with various decision criteria," *Mathematics*, vol. 10, no. 13, p. 2310, 2022. [Online]. Available: https://doi.org/10.3390/math10132310

[38] X. Deng, J. Chen, C. Chen, Y. Zhang, and Z. Zhang, "UAV path planning with improved PSO algorithm based on levy flight," in *Proceedings of the 2024 6th International Conference on Control and Computer Vision*, ser. ICCCV 2024. ACM, 2024, pp. 86–91. [Online]. Available: https://doi.org/10.1145/3674700.3674714

[39] Y. Wang, F. Hu, H. Xu, and J. Zeng, "A multigroups cooperative particle swarm algorithm for optimization of multivehicle path planning in internet of vehicles," *IEEE Internet of Things Journal*, vol. 11, no. 22, pp. 35 839–35 851, Nov. 2024. [Online]. Available: https://doi.org/10.1109/JIOT.2024.3367328

[40] X. Zhou, F. Gao, X. Fang, and Z. Lan, "Improved bat algorithm for UAV path planning in three-dimensional space," *IEEE Access*, vol. 9, pp. 20 100–20 116, 2021. [Online]. Available: https://doi.org/10.1109/ACCESS.2021.3054179

[41] B. Ma, Y. Ji, and L. Fang, "A multi-UAV formation obstacle avoidance method combined with improved simulated annealing and an adaptive artificial potential field," *Drones*, vol. 9, no. 6, p. 390, May 2025. [Online]. Available: https://doi.org/10.3390/drones9060390

[42] K. A.-R. Youssefi and M. Rouhani, "Swarm intelligence based robotic search in unknown maze-like environments," *Expert Systems with Applications*, vol. 178, p. 114907, 2021. [Online]. Available: https://doi.org/10.1016/j.eswa.2021.114907

[43] M. Cosar, "Path planning via swarm intelligence algorithms in unmanned aerial vehicle population," *The Eurasia Proceedings of Science Technology Engineering and Mathematics*, vol. 26, pp. 439–450, Dec. 2023. [Online]. Available: https://doi.org/10.55549/epstem.1411059

[44] H. Zhu, Y. Wang, Z. Ma, and X. Li, "A comparative study of swarm intelligence algorithms for ucav path-planning problems," *Mathematics*, vol. 9, no. 2, p. 171, Jan. 2021. [Online]. Available: https://doi.org/10.3390/math9020171

[45] L. Wang, J. Li, J. Qi, and J. He, "Auv underwater 3d path planning based on particle swarm optimization-adaptive step-size cuckoo search algorithm," in *Proceedings of the 2022 11th International Conference on Networks, Communication and Computing*, ser. ICNCC 2022. ACM, Dec. 2022, pp. 215–225. [Online]. Available: https://doi.org/10.1145/3579895.3579929

[46] Z. Liu, D. Ning, J. Hou, F. Zhang, and G. Liang, "Auv path planning in a three-dimensional marine environment based on a novel multiple swarm coevolutionary algorithm," *Applied Soft Computing*, vol. 164, p. 111933, Oct. 2024. [Online]. Available: https://doi.org/10.1016/j.asoc.2024.111933

[47] L. Lyu and F. Yang, "Mmpa: A modified marine predator algorithm for 3D UAV path planning in complex environments with multiple threats," *Expert Systems with Applications*, vol. 257, p. 124955, Dec. 2024. [Online]. Available: https://doi.org/10.1016/j.eswa.2024.124955

[48] Y. Zhou, X. Kong, K.-P. Lin, and L. Liu, "Novel task decomposed multi-agent twin delayed deep deterministic policy gradient algorithm for multi-UAV autonomous path planning," *Knowledge-Based Systems*, vol. 287, p. 111462, Mar. 2024. [Online]. Available: https://doi.org/10.1016/j.knosys.2024.111462

[49] Z. Wang, Y. Zhang, J. Yu, Y. Gao, G. Zhao, E. H. Houssein, and R. Zhong, "Multi-strategy enhanced marine predator algorithm: performance investigation and application in intrusion detection," *Journal of Big Data*, vol. 12, no. 1, Feb. 2025. [Online]. Available: https://doi.org/10.1186/s40537-025-01080-2

[50] K. Li, F. Ge, Y. Han, Y. Wang, and W. Xu, "Path planning of multiple UAVs with online changing tasks by an ORPFOA algorithm," *Engineering Applications of Artificial Intelligence*, vol. 94, p. 103807, 2020. [Online]. Available: https://doi.org/10.1016/j.engappai.2020.103807

[51] H. Zhang, M. Wang, Y. Ping, C. Wu, J. Qi, W. Wu, and E. Zhou, "UAV path planning based on expert experience strategy RRT algorithm," in *2024 43rd Chinese Control Conference (CCC)*. IEEE, 2024, pp. 2124–2129. [Online]. Available: https://doi.org/10.23919/CCC63176.2024.10662062

[52] Y. Wang, K. Li, Y. Han, and X. Yan, "Distributed multi-UAV cooperation for dynamic target tracking optimized by an SAQPSO algorithm," *ISA Transactions*, vol. 129, pp. 230–242, Oct. 2022. [Online]. Available: https://doi.org/10.1016/j.isatra.2021.12.014

[53] W. Zhao, L. Wang, and S. Mirjalili, "Artificial hummingbird algorithm: A new bio-inspired optimizer with its engineering applications," *Computer Methods in Applied Mechanics and Engineering*, vol. 388, p. 114194, Jan. 2022. [Online]. Available: https://doi.org/10.1016/j.cma.2021.114194

[54] S. Sharma, A. Bhardwaj, A. Singh, and V. Singh, "Enhanced moth flame optimization algorithm entropy-based centroid svm-based software defect prediction," *Journal of Electronic Testing*, vol. 41, no. 5-6, pp. 631–649, Nov. 2025. [Online]. Available: https://doi.org/10.1007/s10836-025-06203-4

[55] Y. Zhan, M. Ding, Y. Yuan, J. Zhang, Q. Yang, G. Shi, and J. Jiang, "Large-scale UAV swarm path planning based on mean-field reinforcement learning," *Chinese Journal of Aeronautics*, vol. 38, no. 9, p. 103484, 2025. [Online]. Available: https://doi.org/10.1016/j.cja.2025.103484

[56] Z. Meng, D. Li, Y. Zhang, and H. Yan, "Intelligent scheduling technology of swarm intelligence algorithm for drone path planning," *Drones*, vol. 8, no. 4, p. 120, Mar. 2024. [Online]. Available: https://doi.org/10.3390/drones8040120

[57] J. Luo, Y. Tian, and Z. Wang, "Research on unmanned aerial vehicle path planning," *Drones*, vol. 8, no. 2, p. 51, Feb. 2024. [Online]. Available: https://doi.org/10.3390/drones8020051

[58] T. Volovoda, "Swarm intelligence for UAV," in *2024 IEEE 7th International Conference on Actual Problems of Unmanned Aerial Vehicles Development (APUAVD)*. IEEE, Oct. 2024, pp. 313–316. [Online]. Available: https://doi.org/10.1109/APUAVD64488.2024.10765878

[59] Y. Zhou, B. Rao, and W. Wang, "UAV swarm intelligence: Recent advances and future trends," *IEEE Access*, vol. 8, pp. 183 856–183 878, 2020. [Online]. Available: https://doi.org/10.1109/ACCESS.2020.3028865

Scientific Paper / Artículo Científico

UNIVERSIDAD POLITÉCNICA SALESIANA ECUADOR
INGENIUS
Revista de Ciencia y Tecnología
https://doi.org/10.17163/ings.n36.2026.10
pISSN: 1390-650X / eISSN: 1390-860X

Applied comparative study of existing methods for state-of-charge estimation in lithium-ion batteries

Estudio comparativo aplicado de métodos existentes para estimación del estado de carga en baterías de iones de litio

Edwin Paccha-Herrera[1,2,*], Ángel Recalde[1,3], Francisco Jaramillo-Montoya[4], Darwin Tapia-Peralta[2]

Received: 16-11-2025, Received after review: 23-03-2026, Accepted: 28-04-2026, Published: 01-07-2026

Abstract

Estimating the state of charge (SOC) of lithium-ion batteries is crucial for the operation of various electrical and electronic devices and equipment. This work presents the implementation of models based on a Bayesian approach using linearized Kalman filtering and particle filtering (PF) to estimate the SOC in lithium-ion batteries. state equation of the Bayesian models incorporates battery resistance as an artificial evolution parameter. Two models based on machine learning algorithms, random forest and K-nearest neighbors (KNN), are also implemented by fitting the parameters of an equivalent electric circuit model to electrochemical impedance spectroscopy measurements. A cylindrical LCO 26650 cell was employed in this study. The results show high performance in SOC estimation for the Bayesian filters, with PF exhibiting the best metrics, including an R^2 adjustment factor of 0.9968.

Keywords: Bayesian filtering, EIS, machine learning, SOC

Resumen

Estimar el estado de carga (SOC) de las baterías de iones de litio es crucial para la operación de diversos dispositivos y equipos eléctricos y electrónicos. Este trabajo presenta la implementación de modelos basados en un enfoque bayesiano mediante el filtro de Kalman linealizado y el filtro de partículas (PF) para estimar el SOC en baterías de iones de litio. La ecuación de estado de los modelos bayesianos incorpora la resistencia de la batería como un parámetro de evolución artificial. De igual manera, se implementan dos modelos basados en algoritmos de aprendizaje automático: random forest y KNN, mediante el ajuste de parámetros de un circuito eléctrico equivalente a las curvas de mediciones de espectroscopía de impedancia electroquímica. Se utilizó una batería cilíndrica LCO tipo 26650. Los resultados muestran un alto desempeño en la estimación del SOC para los filtros bayesianos, entre los cuales el PF presenta las mejores métricas, con un coeficiente de determinación R^2 de 0.9968.

Palabras clave: aprendizaje de máquinas, EIS, filtro bayesiano, SOC

[1,*]Facultad de Sistemas y Telecomunicaciones, Universidad Estatal Península de Santa Elena, Ecuador.
[2]Facultad de Energía, Universidad Nacional de Loja, Ecuador.
[3]Facultad de Ingeniería Eléctrica e Informática, Escuela Superior Politécnica del Litoral, Ecuador.
[4]Departamento de Ingeniería Eléctrica, Universidad de Chile, Chile.
Corresponding author ✉: edwin.paccha@unl.edu.ec.

Suggested citation: E. Paccha-Herrera, A. Recalde, F. Jaramillo-Montoya and D. Tapia-Peralta "Applied comparative study of existing methods for state-of-charge estimation in lithium-ion batteries," *Ingenius, Revista de Ciencia y Tecnología*, N.° 36, pp. 125-136, 2026, DOI: https://doi.org/10.17163/ings.n36.2026.10.

1. Introduction

Lithium-ion batteries are critical components in a wide range of electrical and electronic systems, including household appliances, medical devices, laptops, electric vehicles, and energy storage systems [1]. Due to their high energy density, long lifespan, excellent efficiency, and environmentally friendly operation, Li-ion batteries have become one of the most competitive and promising energy storage technologies [2]. The state of charge (SOC) is a key parameter that provides an indirect measure of the battery's remaining usable capacity. To ensure safe and efficient operation, lithium-ion batteries rely on Battery Management Systems (BMS), which continuously monitor essential variables such as voltage, current, temperature, and capacity to estimate both the SOC and the State of Health (SOH) [3]. Monitoring these variables enables the BMS to protect the battery against overcharging, over-discharging, extreme temperatures, and overcurrents, all of which can lead to physical degradation and significantly reduce battery lifespan [4].

Several direct SOC measurement methods are available, including Coulomb counting, open-circuit voltage (OCV), electrochemical impedance spectroscopy (EIS), and internal resistance methods. In addition, indirect estimation methods predict the battery SOC using mathematical models and algorithms, generally achieving higher accuracy than direct measurement methods. Indirect estimation methods can be classified into five subgroups: model-based, adaptive filter-based, adaptive artificial intelligence-based, advanced algorithm-based, and other approaches. Model-based methods rely on algorithms that create a mathematical representation of the battery's electrical behavior and characteristics. This approach includes the electrical circuit model (ECM) and the electrochemical model (EChM), which are widely used for SOC estimation and serve as the basis for various battery modeling techniques [5]

In [6], the author proposes a model employing a polynomial algorithm-based fitting approach. This approach does not require a thermal model and provides a means of correcting temperature-induced errors. The study in [7] reports that fractional-order models can achieve higher accuracy than their integer-order counterparts, although this improvement comes at the cost of increased complexity. Moreover, physical parameters can be considered in SOC estimation. For instance, the dependence of SOC estimation on the battery's internal resistance can be exploited to obtain more accurate results [8]. Temperature effects can also cause inconsistencies in the SOC estimation of a battery pack [9].

Electrochemical Impedance Spectroscopy (EIS) is a powerful technique for battery characterization. The EIS experiment is based on the application of an alternating signal across a range of frequencies. The resulting current and voltage data are correlated to identify impedances, which provide insight into electrochemical processes in the battery, such as charge transfer kinetics, ion diffusion, and interfacial reactions [10]. The EIS approach can be employed to improve SOC and SOH estimation [11]. One disadvantage of EIS is that it requires specific testing equipment and environmental temperature control to obtain more reliable results.

On the other hand, data-driven models are based on battery data, including temperature, voltage, and current measurements. These models may use simpler formulations or even operate without an explicit model, although their accuracy decreases when the input data are noisy or incomplete. However, they are more flexible because they do not require a specific battery model and demand fewer resources. The data-driven SOC estimation process comprises three key stages: data collection, model training, and SOC estimation. Some widely used techniques include Artificial Neural Networks (ANNs), Support Vector Regression (SVR), Support Vector Machines (SVMs), and Fuzzy Logic [2].

This article explores and compares different SOC estimation methods, with particular emphasis on the influence of internal resistance on SOC. The understanding and implementation of linear, nonlinear, and artificial intelligence-based models provide a new perspective for exploring the limitations of current methods and improving their robustness and adaptability under various operating conditions. Both direct and indirect models are presented. The direct approach is based on EIS measurements, where SOC is predicted using RF and KNN algorithms. The proposed indirect approaches are the linearized Kalman filter and particle filter, where a driving-cycle current profile is employed to estimate the battery SOC. By comparing different SOC estimation methods, it is possible to identify the most suitable and robust model for each operating condition, thereby improving BMS decision-making. This study paves the way for optimizing the performance and extending the lifetime of lithium-ion batteries, benefiting multiple industries and contributing to the development of more sustainable and efficient technologies.

This paper is structured as follows. The Introduction presents an overview of SOC estimation. The Materials and Methods section describes the techniques employed to estimate the SOC of the Li-ion battery under study. The Results and Discussion section presents the main findings and compares the metrics computed for each SOC estimation approach. Finally, the Conclusions section summarizes the main contributions and provides recommendations for future work.

1.1. Related work

The most common approaches applied to SOC estimation are the Coulomb counting method, also known as ampere-hour integration, the OCV method, data-driven approaches, and model-based methods [12]. The Coulomb counting method has been employed to estimate heat generation in a single Li-ion cell [13]. The authors in [14] affirm that a long short-term memory (LSTM) neural network model achieves high accuracy in estimating the SOC of a group of batteries compared with other neural network models. The LSTM-based algorithm can be improved by integrating clustering based on K-means and fuzzy C-means techniques [15]. In addition, an LSTM-based model can consider different temperatures and aging conditions to estimate SOC more accurately [16].

To address the cumulative error of the Coulomb counting method, [17] formulated an extended Kalman filter using the ampere-hour definition of SOC and a Thevenin model. This model can be improved using a nonlinear formulation based on the particle filter (PF). For instance, [18] employed a PF enhanced by an H-infinity filter to estimate SOC in an electric vehicle. Standard driving cycles were used.

Moreover, equivalent circuit models (ECMs) are commonly used with EIS measurements by combining electrical components and adjusting their parameters to minimize the discrepancy between collected data and modeled impedance spectra [19]. For example, [20] performed battery SOC estimation using an ECM based on EIS measurements combined with machine learning algorithms. Seven parameters were employed, including fractional-order elements. This approach reduces training time and is suitable for online SOC estimation.

2. Materials and methods

2.1. State of Charge definition

The SOC of a battery represents the relationship between the residual capacity Q_t and the nominal capacity Q_n and can be formulated as follows:

$$SOC(t) = \frac{Q_t}{Q_n} \times 100 \tag{1}$$

Furthermore, the SOC can be expressed as [21]:

$$SOC(t) = SOC_0 - \frac{\eta \int_{t_o}^{t} i(\tau) d\tau}{Q_n} \tag{2}$$

where SOC_0 is the initial value, and $I(t)$ is the real-time current, with $I(t) < 0$ for charging and $I(t) > 0$ for discharging. The parameter η denotes the Coulomb efficiency, defined as the ratio of the total charge removed from the battery to the total charge supplied during a complete cycle.

This study aims to compare direct and indirect methods for estimating the SOC in Li-ion batteries. The direct method was established based on EIS experiments. The indirect methods were based on Bayesian algorithms, namely the Kalman filter (KF) and particle filter (PF). A 26650 lithium-cobalt oxide (LCO) battery with a capacity of 4 Ah was employed.

2.2. SOC estimated based on Electrochemical impedance spectroscopy (EIS)

Results from EIS experiments are commonly presented using Nyquist diagrams, as shown in Figure 1. An ECM can be formulated for the corresponding EIS spectra. The pure ohmic resistance R_e is the value at the intersection of the curve with the horizontal axis [22]; the inductance L models the electromagnetic phenomena in the battery. The mid-frequency zone represents the charge transfer region, including the charge transfer resistance R_{ct} and double-layer capacitance C_{dl}. The R_{ct} reflects the resistance associated with lithium-ion movement between the electrode and the electrolyte [23]. Finally, the low-frequency zone represents the lithium-ion diffusion process, modeled by the constant phase element Q_{dl}, where the exponent n_{dl} varies between 0, corresponding to a resistor, and 1, corresponding to a capacitor. The ECM in Figure 1 is characterized by the impedance given by [24]:

$$Z(\omega) = R_e + \frac{1}{j\omega C_{dl}} + \left[\frac{1}{Q_{dl}(j\omega)^{-n}} + R_{ct}\right]^{-1} + j\omega L \tag{3}$$

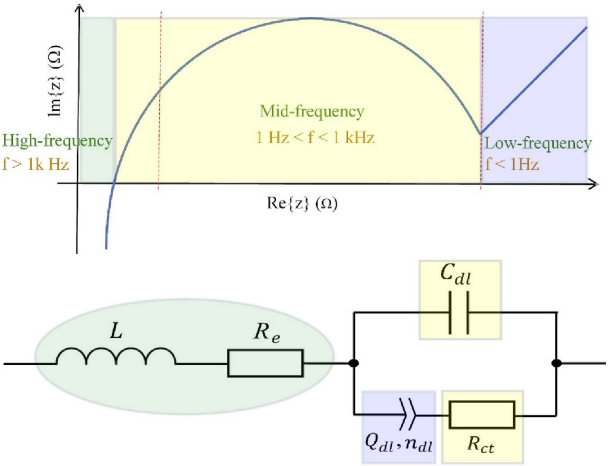

Figure 1. Nyquist plot based on EIS test of a battery and its equivalent circuit model. Adapted from [24].

In this study, SOC prediction based on EIS measurements was carried out using PGSTAT302N testing equipment. EIS was performed from 5% SOC to 100% SOC using a 4 Ah LCO 26650 Li-ion cell. A sinusoidal

current signal with an amplitude of 0.05 A was applied to the battery. Selected EIS profiles are shown in Figure 2

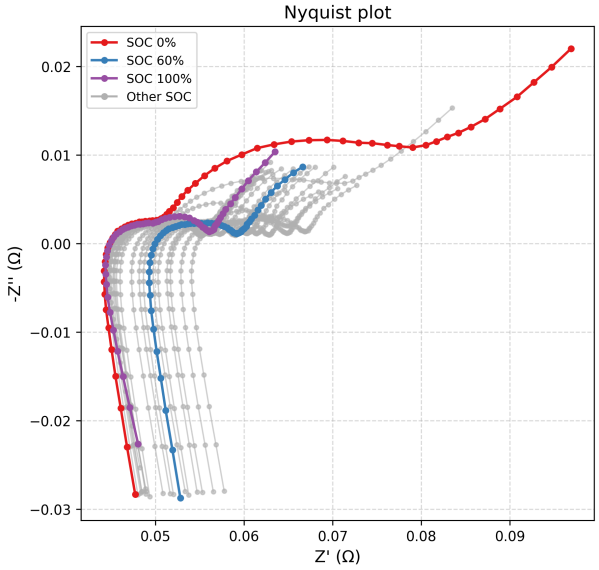

Figure 2. Nyquist plot from EIS test of the LCO 26650 battery at different SOC.

SOC estimation based on EIS measurements was performed by fitting the ECM parameters from the EIS curve and the battery terminal voltage, as illustrated in Table 1. These parameters were then used to train the RF and KNN algorithms to predict the battery SOC. Since SOC was predicted for each EIS measurement, the ECM parameters had to be fitted for each SOC measurement as well.

Table 1. Fitted parameters for the ECM at SOC 0.6.

Parameter	Value
C_{dl} (F)	0.1
L (H)	5.191×10^{-7}
n_{dl}	0.5
Q_{dl} ($\Omega^{-1}s^{n_{dl}}$)	1×10^{-5}
R_{ct} (Ω)	0.01
R_e (Ω)	0.06662

RF was implemented using 100 estimators, or trees. KNN was developed using $k = 2$ nearest neighbors. In both cases, k-fold validation was performed using 5 splits and a random state of 42.

2.3. SOC estimation based on Linearized Kalman Filter

2.3.1. Linearized Kalman Filter

The Linearized Kalman Filter (LKF) is an estimation method used for nonlinear systems whose dynamics can be accurately approximated by a first-order expansion around a known reference trajectory. This approach is widely described in the classical filtering literature [25, 26].

Consider the nonlinear system:

$$x_{k+1} = f(x_k, u_k) + w_k, \tag{4}$$

$$z_k = h(x_k) + v_k, \tag{5}$$

where x is the state-space vector, u denotes the input, z is the measurement vector, k is the time instant, w_k and v_k are zero-mean noises with covariances Q and R, respectively. The LKF assumes the existence of a nominal trajectory $\bar{x}_k$ satisfying

$$\bar{x}_{k+1} = f(\bar{x}_k, u_k), \tag{6}$$

which represents the expected evolution in the absence of disturbances.

The error variables are defined as

$$\delta x_k = x_k - \bar{x}_k, \qquad \delta z_k = z_k - h(\bar{x}_k), \tag{7}$$

and the system is linearized around $\bar{x}_k$ using the Jacobians:

$$F_k = \left.\frac{\partial f(x, u_k)}{\partial x}\right|_{x=\bar{x}_k}, \tag{8}$$

$$H_k = \left.\frac{\partial h(x)}{\partial x}\right|_{x=\bar{x}_k}. \tag{9}$$

This yields the linear error-state model:

$$\delta x_{k+1} = F_k\, \delta x_k + w_k, \tag{10}$$

$$\delta z_k = H_k\, \delta x_k + v_k, \tag{11}$$

which defines a linear time-varying (LTV) system suitable for Kalman filtering.

The main feature of the KF is that it enables recursive estimation of a system's internal, unmeasurable states, including the SOC in the case of a battery. This is achieved by using prior knowledge, model-based predictions, and noisy measurements. The prediction and update steps are outlined below [26]:

Prediction:

$$\delta\hat{x}_{k|k-1} = F_{k-1}\, \delta\hat{x}_{k-1|k-1}, \tag{12}$$

$$P_{k|k-1} = F_{k-1} P_{k-1|k-1} F_{k-1}^T + Q_{k-1}. \tag{13}$$

Update:

$$K_k = P_{k|k-1}H_k^T(H_kP_{k|k-1}H_k^T + R_k)^{-1}, \quad (14)$$

$$\delta\hat{x}_{k|k} = \delta\hat{x}_{k|k-1} + K_k(\delta z_k - H_k\,\delta\hat{x}_{k|k-1}), \quad (15)$$

$$P_{k|k} = (I - K_kH_k)\,P_{k|k-1}, \quad (16)$$

where K_k is the Kalman gain matrix, P_k is the error covariance, and I is the identity matrix. The actual state estimate is then reconstructed as:

$$\hat{x}_{k|k} = \bar{x}_k + \delta\hat{x}_{k|k}. \quad (17)$$

Compared with the Extended Kalman Filter (EKF), the LKF linearizes the system only around a predefined nominal trajectory, making it suitable when this trajectory is known a priori and deviations remain small [27].

2.3.2. SOC implementation based on LKF

For this study, the state-space vector is written as:

$$x_k = \begin{bmatrix} x_{1,k} \\ x_{2,k} \end{bmatrix}, \quad (18)$$

where $x_{1,k}$ is the component associated with the internal resistance of the cell and $x_{2,k}$ is the SOC at time instant k.

The Bayesian approach requires a measurement equation. In this study, this equation corresponds to the battery voltage v_0 linearized around the point $x_0 = [x_{1,0}\ x_{2,0}]^T$ and i_0 [28]:

$$v_0 = v_L + (v_{OC} - v_L)\,e^{\gamma(x_{2,0}-1)} + \alpha v_L + (x_{2,0} - 1) + (1-\alpha)\,v_L\left(e^{-\beta} - e^{-\beta\sqrt{x_{2,0}}}\right) - i_0x_{1,0} \quad (19)$$

The discharging current i is the input parameter in the model, and, v_{OC} is the open-circuit voltage at 100% SOC. The parameters v_L, α, β, and γ are estimated offline and were taken from [28].

The matrices used to solve the LKF algorithm are formulated as:

$$F_k = \begin{bmatrix} 1 & 0 \\ -\dfrac{\Delta t}{E_{\text{crit}}}i_0\dfrac{\partial v_0}{\partial x_1} & 1 - \dfrac{\Delta t}{E_{\text{crit}}}i_0\dfrac{\partial v_0}{\partial x_2} \end{bmatrix}, \quad (20)$$

$$H_k = \begin{bmatrix} \dfrac{\partial v_0}{\partial x_1} & \dfrac{\partial v_0}{\partial x_2} \end{bmatrix}, \quad (21)$$

where E_{crit} is the critical energy, defined as the total expected energy supplied by the battery.

2.4. SOC estimation based on Particle Filter

2.4.1. Particle filter (PF)

The particle filter (PF), like the LKF, recursively estimates the *posterior* probability density function (PDF) of the unknown state vector $\mathbf{x}_k$, given the measurements $\mathbf{z}_{1:k}$, where $k \in \mathbb{N}$ denotes the time instant [29]. The PF represents the *posterior* PDF $p(\mathbf{x}_k|\mathbf{z}_{1:k})$ at time k using particles, defined as a set of N_p random samples with their respective weights, described in Equation (22) [30].

$$\{\mathbf{x}_k^{(i)}, w_k^{(i)}\}_{i=1}^{N_p}, \quad \sum_{i=1}^{N_p} w_k^{(i)} = 1 \quad (22)$$

To formulate the *posterior* PDF at each time instant, the PF sequentially samples the N_p particles from an alternative PDF $q(\cdot)$, known as the *importance density* [31]. Therefore, $p(\mathbf{x}_k|\mathbf{z}_{1:k})$ can be modeled as [29]:

$$p(\mathbf{x}_k|\mathbf{z}_{1:k}) \approx \sum_{i=1}^{N_p} \mathbf{w}_k^{(i)}\delta(\mathbf{x}_k - \mathbf{x}_k^{(i)}), \quad (23)$$

where the weight of each particle can be updated as follows:

$$\mathbf{w}_k^{(i)} = \mathbf{w}_{k-1}^{(i)}\frac{p(\mathbf{z}_k|\mathbf{x}_k^{(i)})p(\mathbf{x}_k^{(i)}|\mathbf{x}_{k-1}^{(i)})}{q(\mathbf{x}_k^{(i)}|\mathbf{x}_{0:k-1}^{(i)}, \mathbf{z}_{1:k})}. \quad (24)$$

Two considerations should be taken into account. The first concerns the approximation given by Equation (23), which converges to the true *posterior* PDF $p(\mathbf{x}_k|\mathbf{z}_{1:k})$ when $N_p \to \infty$. The second concerns the design and performance of the PF implementation, which depend on the appropriate choice of the *importance density* $q(\cdot)$. For instance, in PF implementations, the following formulation is frequently proposed [32]:

$$q(\mathbf{x}_k|\mathbf{x}_{k-1}^{(i)}, \mathbf{z}_k) = p(\mathbf{x}_k|\mathbf{x}_{k-1}^{(i)}), \quad (25)$$

where $q(\cdot)$ PDF is equal to the *prior* PDF, allowing the weight vector $\mathbf{w}_k^{(i)}$ to be updated using the likelihood function, as detailed in Equation (26):

$$\mathbf{w}_k^{(i)} = \mathbf{w}_{k-1}^{(i)}p(\mathbf{z}_k|\mathbf{x}_k^{(i)}). \quad (26)$$

2.4.2. Artificial evolution for online parameter estimation

Artificial evolution is a strategy for joint state and parameter estimation within a particle filtering framework [33]. It is particularly useful when some model parameters are unknown or vary slowly over time [34]. This approach is implemented by augmenting the state vector to include the parameter vector, which is treated as an additional state variable whose evolution is described by a random-walk process [34]. Under this

formulation, the augmented process model can be expressed as follows:

$$\mathbf{x}_k = \boldsymbol{f}_k\left(\mathbf{x}_{k-1}, \boldsymbol{\theta}_{k-1}, \mathbf{u}_{k-1}, \boldsymbol{\omega}_{k-1}\right), \tag{27a}$$
$$\boldsymbol{\theta}_k = \boldsymbol{\theta}_{k-1} + \boldsymbol{\eta}_{k-1}. \tag{27b}$$

The variance of the random-walk process must be carefully selected, as an inappropriate choice can significantly affect the posterior PDF estimates [35]. To address this issue, the literature reports several techniques for adjusting the random-walk variance according to specific criteria. Examples include *kernel smoothing* [33] and *outer feedback correction loops* (OFCL) [36], which have been adopted in PF-based implementations relying on artificial parameter evolution.

2.4.3. SOC implementation based on PF

First, the state-transition model is defined as follows [28]:

$$x_1(k+1) = x_1(k) + \omega_1(k) \tag{28}$$

$$x_2(k+1) = x_2(k) - v(k)\cdot i(k)\cdot \Delta t\cdot E_{\text{crit}}^{-1} + \omega_2(k). \tag{29}$$

where x_1 represents the battery internal resistance, treated as an unknown parameter to be estimated, and x_2 denotes the SOC. The PF implementation considered in this study uses the following voltage measurement model:

$$\begin{aligned} v(k) = {} & v_L + (v_{OC} - v_L)\cdot e^{\gamma\cdot(x_2(k)-1)} + \\ & \alpha\cdot v_L\cdot(x_2(k)-1) + \\ & (1-\alpha)\cdot v_L\cdot\left(e^{-\beta} - e^{-\beta\sqrt{x_2(k)}}\right) - \\ & i(k)\cdot x_1(k) + \eta(k) \end{aligned} \tag{30}$$

Process noise (ω_1 and ω_2) and measurement noise (η) are considered in the state-space formulation.

In the PF implementation, the initial conditions (x_1 and x_2), the process noise terms (ω_1 and ω_2), and the measurement noise (η), are modeled using Gaussian distributions, i.e., $x_1(0) \sim \mathcal{N}(\mu_1, \sigma_1^2)$, $x_2(0) \sim \mathcal{N}(\mu_2, \sigma_2^2)$, $\omega_1 \sim \mathcal{N}(0, \sigma_{\omega_1}^2)$, $\omega_2 \sim \mathcal{N}(0, \sigma_{\omega_2}^2)$, and $\eta \sim \mathcal{N}(0, \sigma_\eta^2)$. In addition, a population of $N_p = 300$ particles was used, with each particle i initially assigned a weight $W_i = 1/N_p$. The PF parameter configuration is summarized in Table 2.

Table 2. Particle filter parameter configuration.

Parameter	Symbol	Value
Number of particles	N_p	300
Initial internal resistance mean	μ_1	$0,12\ \Omega$
Initial SOC mean	μ_2	1,00
Initial internal resistance std. dev.	σ_1	0,005
Initial SOC std. dev.	σ_2	0,02
ω_1 std. dev.	σ_{ω_1}	$0,001\ \Omega$
ω_2 std. dev.	σ_{ω_2}	0,0001
Measurement noise std. dev.	σ_η	0,001 V

2.5. Case study

To estimate the battery SOC using KF and PF, an HFWET driving cycle was employed. A scaled discharge current profile for this cycle was applied to the 26650 lithium-ion battery with LCO chemistry, as shown in Figure 3. This profile was selected because it exhibits variable behavior, whereas a constant current profile is not adequate for characterizing the battery's SOC.

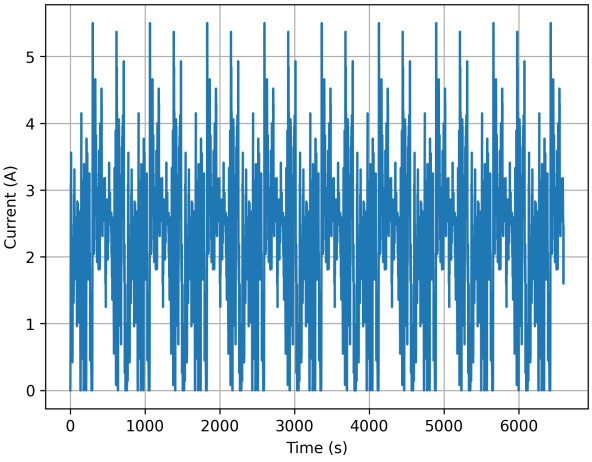

Figure 3. HWFET current profile scaled for a 4 Ah LCO battery [13].

3. Results and discussion

This section presents the results obtained from applying the SOC estimation approaches. Figures 4, 5, 6, and 7 show the SOC estimates obtained using the Kalman filter, particle filter, random forest, and KNN approaches, respectively. The last two approaches show lower fitting quality because they require more training data. Moreover, model hyperparameters could be implemented using other techniques, such as hybrid models. The PF algorithm shows robust performance due to its ability to capture nonlinear behavior and perform online estimation simultaneously. Furthermore, Bayesian algorithms are more complex to implement,

and their robustness depends on several factors, such as the process equation and the process and measurement noise terms.

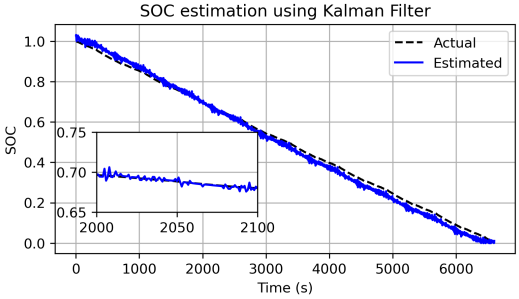

Figure 4. SOC estimation by Kalman Filter using HWFET driving profile.

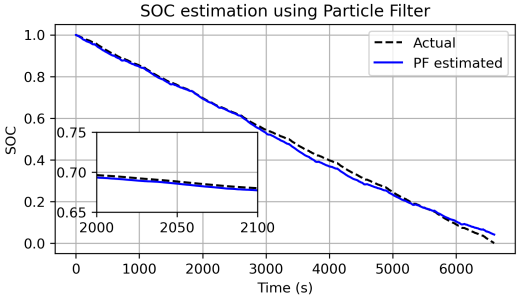

Figure 5. SOC estimation by Particle Filter using HWFET driving profile.

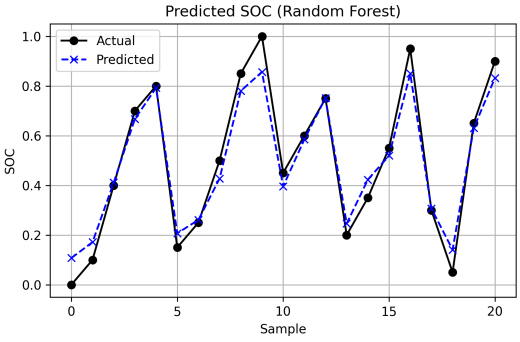

Figure 6. SOC estimation by Random Forest based on EIS.

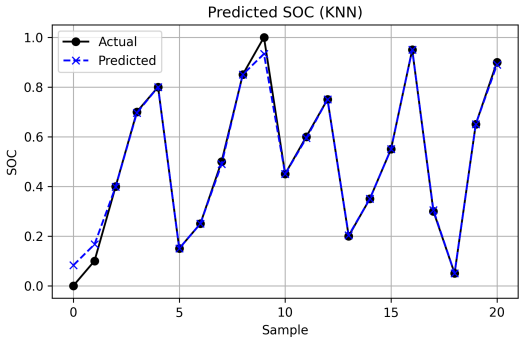

Figure 7. SOC estimation by KNN based on EIS.

Furthermore, Figure 8 and 9 show the voltage estimates obtained using the Kalman filter and particle filter, respectively. The PF provides a better fit between the real and estimated voltage.

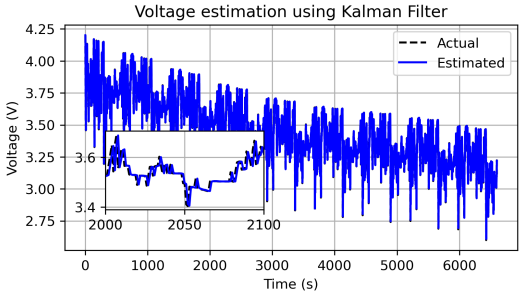

Figure 8. Voltage estimation by Kalman Filter using HWFET driving profile.

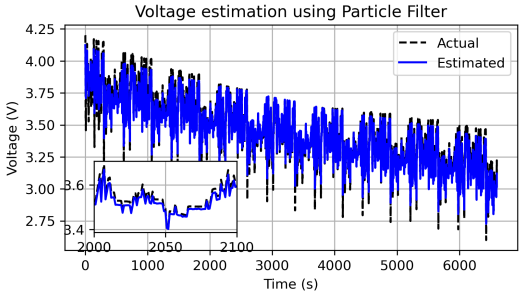

Figure 9. Voltage estimation by Particle Filter using HWFET driving profile.

One advantage of using artificial evolution for the battery resistance parameter is that its initial value is continuously adapted within the PF model, as shown in Figure 10.

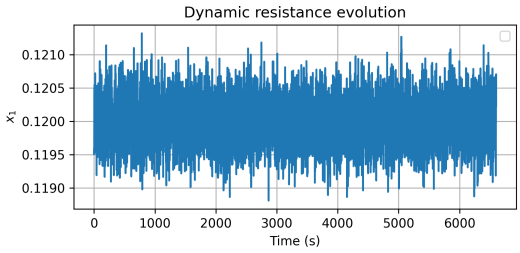

Figure 10. Artificial evolution of the battery resistance (in ohms).

A general comparison of the developed models was performed in terms of RMSE and R^2 metrics as shown in Table 3. Overall, the Bayesian approaches achieve better performance than EIS-based methods. Due to the discrete nature of EIS measurements, the RF and KNN models predict SOC only at the specific operating points where impedance spectra were acquired, rather than providing a continuous estimation over time. PF presents the best metrics due to its non-linear structure, which better captures SOC variations.

Table 3. RMSE and R^2 for SOC estimation.

Algorithm	RMSE	R^2
KF	0.0187	0.9891
PF	0.0164	0.9968
RF	0.0644	0.9548
KNN	0.0276	0.9917

The comparative analysis of state-of-charge (SOC) estimation methods for lithium-ion batteries highlighted key advantages and limitations of each approach. The Kalman Filter (KF) demonstrated reliable performance in linear estimation scenarios but exhibited sensitivity to model inaccuracies and noise, which could lead to errors over extended operating periods. By contrast, the Particle Filter (PF) was robust in handling nonlinearities and uncertainties, making it particularly suitable for real-time SOC estimation in dynamic environments. However, its computational complexity remains a challenge, requiring optimized implementations for practical deployment in battery management systems (BMS). In the present approach, the PF formulation, including the process and measurement equations, and the battery parameters were adopted from [28]. That study achieved higher accuracy in SOC estimation by performing offline parameter estimation for the process equation. Another technique that could be considered to capture nonlinear behavior is the EKF, which is used in electric vehicles to provide real-time SOC estimation under different operating conditions, leading to improved BMS performance [37]. Other operating conditions and parameters that should be explored include additional driving cycles, temperature, battery aging effects, regenerative braking, and different process equations in the model.

On the other hand, machine learning-based approaches, namely RF and KNN, are less practical than Bayesian approaches. RF and KNN predict SOC using EIS measurements, but these experiments require complex equipment and are not suitable for online implementation. The results are restricted to the SOC values for which experimental EIS data are available. Moreover, machine learning algorithms require the tuning of several parameters. Similar metrics to those shown in Table 3 for RF and KNN SOC prediction were reported in [24].

The results indicate that model-based approaches, such as KF and PF, remain essential because of their maturity and real-time applicability, whereas machine learning-based techniques have potential for further refinement. Future work should explore hybrid methodologies that combine the strengths of both approaches by integrating online correction techniques with deep learning models to achieve robust and adaptive SOC estimation.

Figure 11 shows the RMSE of the SOC estimation as a function of the scale factor applied individually to each noise parameter. Each parameter was varied by multiplying its nominal value by different scale factors, while all remaining parameters were kept at their nominal configuration. The PF shows low sensitivity to σ_{ω_1} and σ_η, with RMSE remaining stable at approximately 0.016–0.019 across the full range evaluated. The SOC process noise σ_{ω_2} shows the highest sensitivity: values below the nominal configuration cause RMSE to exceed 0.059, as an overly constrained state transition prevents adequate particle diversity. Similarly, the likelihood kernel variance σ_v^2 degrades estimation accuracy at both extremes. Overall, the nominal configuration, corresponding to a scale factor of 1.0 with the selected parameters, yields the lowest RMSE across all parameters.

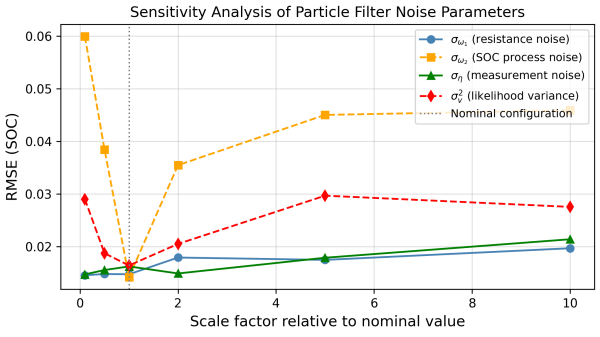

Figure 11. Sensitivity analysis of PF noise parameters.

Considering that this study is mainly applicable to battery BMS, some important aspects of this system are discussed. Table 4 presents the computational cost and embedded feasibility of the different approaches used to estimate the battery SOC. Estimators based

on the KF algorithm stand out because of their accuracy, low-to-medium memory consumption, and high feasibility for integration into embedded systems. On the other hand, EIS-based machine learning models are not sufficiently developed for implementation in embedded systems, despite their high accuracy.

Table 4. Comparative analysis of computational cost and embedded feasibility for SOC estimation methods.

Method	Typical Accuracy	Computational Cost	Memory Usage	Inference Time	Embedded Feasibility	Validated Platform
LKF	High (≤2%)	Low–Medium	Low–Medium	<1 ms	High	STM32, ARM Cortex-M [38, 39]
PF	Very High (≤1%)	Very High	High	10–100 ms (per particle)	Low	FPGA, STM32F4 [40, 41]
KNN (EIS-based)	High	High	Very High	Variable (dataset size)	Low	Offline only
RF (EIS-based)	High (≤3%)	Medium	Medium–High	1–10 ms	Medium	Offline only

4. Conclusions

This study demonstrates that state-of-charge (SOC) estimation methods differ significantly in accuracy, computational implementation, and adaptability to the nonlinear battery behavior induced by the applied driving cycle. The KF approach provides reliable estimates under linear assumptions but faces challenges associated with nonlinear models and noise. Nevertheless, the KF method shows high feasibility for implementation in embedded systems for SOC prediction. The PF algorithm demonstrates robustness under dynamic conditions. By contrast, because of their dependence on specific equipment, the EIS-based machine learning algorithms applied in this study are not capable of predicting online SOC behavior.

Future research should focus on optimizing hybrid SOC estimation models that integrate traditional filtering techniques with other machine learning approaches. Additionally, efforts should be made to enhance computational efficiency for real-time applications and expand training datasets to improve the generalization capability of data-driven models. Validation under real operating conditions in electric vehicles and energy storage systems is essential to confirm the practical applicability and reliability of these estimation and prediction methods.

Contributor role

- **Edwin Paccha-Herrera:** conceptualization, methodology, software, writing – original draft.
- **Ángel Recalde:** conceptualization, formal analysis, writing – review and editing.
- **Francisco Jaramillo-Montoya:** methodology, validation, writing – review and editing.
- **Darwin Tapia-Peralta:** formal analysis, visualization, resources.

References

[1] R. Hema and M. J. Venkatarangan, "Advancing sustainable development: Introducing a novel fast charging technique for li-ion batteries with supercapacitor integration," *Computers and Electrical Engineering*, vol. 120, p. 109810, 2024. [Online]. Available: https://doi.org/10.1016/j.compeleceng.2024.109810

[2] D. V. S. R. Sesidhar, C. Badachi, and R. C. Green II, "A review on data-driven SOC estimation with Li-ion batteries: Implementation methods & future aspirations," *Journal of Energy Storage*, vol. 72, p. 108420, 2023. [Online]. Available: https://doi.org/10.1016/j.est.2023.108420

[3] Y. Tavakol-Moghaddam, M. Boroushaki, and M. Astaneh, "Reinforcement learning for battery energy management: A new balancing approach for Li-ion battery packs," *Results in Engineering*, vol. 23, p. 102532, 2024. [Online]. Available: https://doi.org/10.1016/j.rineng.2024.102532

[4] O. Demirci, S. Taskin, E. Schaltz, and B. Acar Demirci, "Review of battery state estimation methods for electric vehicles - Part I: SOC estimation," *Journal of Energy Storage*, vol. 87, p. 111435, 2024. [Online]. Available: https://doi.org/10.1016/j.est.2024.111435

[5] Q. Wang, J. Wang, P. Zhao, J. Kang, F. Yan, and C. Du, "Correlation between the model accuracy and model-based SOC estimation," *Electrochimica Acta*, vol. 228, pp. 146–159, 2017. [Online]. Available: https://doi.org/10.1016/j.electacta.2017.01.057

[6] A. Tabine, E. M. Laadissi, H. Mastouri, A. Elachhab, S. Bouzaid, and A. Hajjaji, "A novel fitting polynomial approach for an accurate SOC estimation in Li-ion batteries in view of temperature variations," *Results in Engineering*, p. 103962, 2025. [Online]. Available: https://doi.org/10.1016/j.rineng.2025.103962

[7] C. Zou, L. Zhang, X. Hu, Z. Wang, T. Wik, and M. Pecht, "A review of fractional-order techniques applied to lithium-ion batteries, lead-acid batteries, and supercapacitors," *Journal of Power Sources*, vol. 390, pp. 286–296, 2018. [Online]. Available: https://doi.org/10.1016/j.jpowsour.2018.04.033

[8] C. Xu, T. Cleary, and H. K. Fathy, "Improving Li-S battery SOC estimation using an SOC-dependent resistance model," *IFAC-PapersOnLine*, vol. 56, no. 3, pp. 439–444, 2023, 3rd Modeling, Estimation and Control Conference MECC 2023. [Online]. Available: https://doi.org/10.1016/j.ifacol.2023.12.063

[9] H. Ren, L. Jia, L. Yin, C. Dang, and Z. Chen, "Research on battery pack SOC consistency based on the electric-thermal-fluid coupling model," *Journal of Energy Storage*, vol. 97, p. 112924, 2024. [Online]. Available: https://doi.org/10.1016/j.est.2024.112924

[10] A. C. Lazanas and M. I. Prodromidis, "Electrochemical impedance spectroscopy—A tutorial," *ACS Measurement Science Au*, vol. 3, no. 3, pp. 162–193, 2023. [Online]. Available: https://doi.org/10.1021/acsmeasuresciau.2c00070

[11] H. Mustafa, C. Bourelly, M. Vitelli, F. Milano, M. Molinara, and L. Ferrigno, "SOC estimation on Li-ion batteries: A new EIS-based dataset for data-driven applications," *Data in Brief*, vol. 57, p. 110947, 2024. [Online]. Available: https://doi.org/10.1016/j.dib.2024.110947

[12] C. Wang, M. Yang, X. Wang, Z. Xiong, F. Qian, C. Deng, C. Yu, Z. Zhang, and X. Guo, "A review of battery SOC estimation based on equivalent circuit models," *Journal of Energy Storage*, vol. 110, p. 115346, 2025. [Online]. Available: https://doi.org/10.1016/j.est.2025.115346

[13] E. Paccha-Herrera, W. R. Calderón-Muñoz, M. Orchard, F. Jaramillo, and K. Medjaher, "Thermal modeling approaches for a $LiCoO_2$ lithium-ion battery—A comparative study with experimental validation," *Batteries*, vol. 6, no. 3, 2020. [Online]. Available: https://doi.org/10.3390/batteries6030040

[14] E. Almaita, S. Alshkoor, E. Abdelsalam, and F. Almomani, "State of charge estimation for a group of lithium-ion batteries using long short-term memory neural network," *Journal of Energy Storage*, vol. 52, p. 104761, 2022. [Online]. Available: https://doi.org/10.1016/j.est.2022.104761

[15] M. K. Al-Alawi, A. Jaddoa, J. Cugley, and H. Hassanin, "A novel enhanced SOC estimation method for lithium-ion battery cells using cluster-based LSTM models and centroid proximity selection," *Journal of Energy Storage*, vol. 97, p. 112866, 2024. [Online]. Available: https://doi.org/10.1016/j.est.2024.112866

[16] G. Chen, W. Peng, and F. Yang, "An LSTM-SA model for SOC estimation of lithium-ion batteries under various temperatures and aging levels," *Journal of Energy Storage*, vol. 84, p. 110906, 2024. [Online]. Available: https://doi.org/10.1016/j.est.2024.110906

[17] Z. Cui, W. Hu, G. Zhang, Z. Zhang, and Z. Chen, "An extended Kalman filter based SOC estimation method for Li-ion battery," *Energy Reports*, vol. 8, pp. 81–87, 2022, iCPE 2021 - The 2nd International Conference on Power Engineering. [Online]. Available: https://doi.org/10.1016/j.egyr.2022.02.116

[18] Y. Chen, R. Li, Z. Sun, L. Zhao, and X. Guo, "SOC estimation of retired lithium-ion batteries for electric vehicle with improved particle filter by H-infinity filter," *Energy Reports*, vol. 9, pp. 1937–1947, 2023. [Online]. Available: https://doi.org/10.1016/j.egyr.2023.01.018

[19] N. Meddings, M. Heinrich, F. Overney, J.-S. Lee, V. Ruiz, E. Napolitano, S. Seitz, G. Hinds, R. Raccichini, M. Gaberščček, and J. Park, "Application of electrochemical impedance spectroscopy to commercial Li-ion cells: A review," *Journal of Power Sources*, vol. 480, p. 228742, 2020. [Online]. Available: https://doi.org/10.1016/j.jpowsour.2020.228742

[20] E. Buchicchio, A. De Angelis, F. Santoni, P. Carbone, F. Bianconi, and F. Smeraldi, "Battery SOC estimation from EIS data based on machine learning and equivalent circuit model," *Energy*, vol. 283, p. 128461, 2023. [Online]. Available: https://doi.org/10.1016/j.energy.2023.128461

[21] Y. Miao and Z. Gao, "Estimation for state of charge of lithium-ion batteries by adaptive fractional-order unscented Kalman filters," *Journal of Energy Storage*, vol. 51, p. 104396, 2022. [Online]. Available: https://doi.org/10.1016/j.est.2022.104396

[22] A. Barai, K. Uddin, W. D. Widanage, A. McGordon, and P. Jennings, "A study of the influence of measurement timescale on internal resistance characterisation methodologies for lithium-ion cells," *Scientific Reports*, vol. 8, no. 1, pp. 1–13, 2018. [Online]. Available: https://doi.org/10.1038/s41598-017-18424-5

[23] H. Thomas and M. H. Weatherspoon, "Capacity and state-of-health prediction of lithium-ion batteries using reduced equivalent circuit models," *Batteries*, vol. 11, no. 4, 2025. [Online]. Available: https://doi.org/10.3390/batteries11040162

[24] X. Zhang, L. Zhang, J. Wu, W. Bai, H. Dai, H. Lin, F. Zhang, and Y. Yang, "SOC estimation of lithium-ion batteries using equivalent circuit model and Nyquist plots from EIS data: A machine learning approach," *Journal of Electroanalytical Chemistry*, vol. 987, p. 119093, 2025. [Online]. Available: https://doi.org/10.1016/j.jelechem.2025.119093

[25] D. Simon, *Optimal State Estimation: Kalman, H-Infinity, and Nonlinear Approaches*. John Wiley & Sons, 2006. [Online]. Available: http://doi.org/10.1002/0470045345

[26] P. Zarchan and H. Musoff, *Fundamentals of Kalman Filtering: A Practical Approach*, 4th ed. American Institute of Aeronautics and Astronautics, Inc., 2015. [Online]. Available: https://doi.org/10.2514/4.102776

[27] M. S. Grewal and A. P. Andrews, *Kalman Filtering: Theory and Practice Using MATLAB*, 3rd ed. John Wiley & Sons, 2008. [Online]. Available: https://doi.org/10.1002/9780470377819

[28] D. Pola, H. Navarrete, M. Orchard, R. Rabie, M. Cerda, B. Olivares, J. Silva, P. Espinoza, and A. Perez, "Particle-filtering-based discharge time prognosis for lithium-ion batteries with a statistical characterization of use profiles," *IEEE Transactions on Reliability*, vol. 64, pp. 1–11, 2015. [Online]. Available: https://doi.org/10.1109/TR.2014.2385069

[29] M. S. Arulampalam, S. Maskell, N. Gordon, and T. Clapp, "A tutorial on particle filters for online nonlinear/non-Gaussian Bayesian tracking," *IEEE Trans. Signal Process.*, vol. 50, no. 2, pp. 174–188, 2002. [Online]. Available: https://doi.org/10.1109/78.978374

[30] C. Díaz, V. Quintero, A. Pérez, F. Jaramillo, C. Burgos-Mellado, H. Rozas, M. E. Orchard, D. Sáez, and R. Cárdenas, "Particle-filtering-based prognostics for the state of maximum power available in lithium-ion batteries at electromobility applications," *IEEE Trans. Veh. Technol.*, vol. 69, no. 7, pp. 7187–7200, 2020. [Online]. Available: https://doi.org/10.1109/TVT.2020.2993949

[31] M. Zając, "Online fault detection of a mobile robot with a parallelized particle filter," *Neurocomputing.*, vol. 126, pp. 151–165, 2014. [Online]. Available: https://doi.org/10.1016/j.neucom.2012.11.049

[32] M. Sami Fadali, *Introduction to random signals, estimation theory, and Kalman filtering*, 1st ed. Springer Singapore, 2024. [Online]. Available: https://doi.org/10.1007/978-981-99-8063-5

[33] A. Tulsyan, B. Huang, R. Bhushan Gopaluni, and J. Fraser Forbes, "On simultaneous on-line state and parameter estimation in non-linear state-space models," *J. Process Control.*, vol. 23, no. 4, pp. 516–526, 2013. [Online]. Available: https://doi.org/10.1016/j.jprocont.2013.01.010

[34] Z. Hong, L. Xu, and J. Chen, "Artificial evolution based cost-reference particle filter for nonlinear state and parameter estimation in process systems with unknown noise statistics and model parameters," *J. Taiwan Inst. Chem. Eng.*, vol. 112, pp. 377–387, 2020. [Online]. Available: https://doi.org/10.1016/j.jtice.2020.04.009

[35] Y. Hu, P. Baraldi, F. Di Maio, and E. Zio, "Online performance assessment method for a model-based prognostic approach," *IEEE Trans. Reliab.*, vol. 65, no. 2, pp. 718–735, 2016. [Online]. Available: https://doi.org/10.1109/TR.2015.2500681

[36] M. E. Orchard, F. A. Tobar, and G. J. Vachtsevanos, "Outer Feedback Correction Loops in Particle Filtering-based Prognostic Algorithms: Statistical Performance Comparison," *Stud. Informatics Control.*, vol. 18, no. 4, pp. 295–304, 2009. [Online]. Available: https://upsalesiana.ec/ing36ar10r36

[37] M. O. Oloyede, G. A. Akpakwu, H. C. Myburgh, A. De Freitas, and T. Kunatsa, "A review on state-of-charge estimation methods, energy storage technologies and state-of-the-art simulators: Recent developments and challenges," *World Electric Vehicle Journal*, vol. 15, no. 9, 2024. [Online]. Available: https://doi.org/10.3390/wevj15090381

[38] A. Valade, P. Acco, P. Grabolosa, and J.-Y. Fourniols, "A study about kalman filters applied to embedded sensors," *Sensors*, vol. 17, no. 12, 2017. [Online]. Available: https://doi.org/10.3390/s17122810

[39] G. Nishanth, M. M. Krishnan, B. Parandhaman, and J. Harinarayanan, "Hardware implementation of EKF based SOC estimate for lithium-ion batteries in electric vehicle applications," *Scientific Reports*, vol. 15, no. 1, p. 15551, 2025. [Online]. Available: https://doi.org/10.1038/s41598-025-99931-8

[40] J. Michalski, M. Retinger, P. Kozierski, and J. Zietkiewicz, "Temperature control unit—modeling and implementation of a particle filter on a microcontroller," *Applied Sciences*, vol. 12, no. 15, 2022. [Online]. Available: https://doi.org/10.3390/app12157631

[41] J. Schönefeld and D. Möller, "Mathematical aspects of the implementation of particle filters on FPGA," *IFAC Proceedings Volumes*, vol. 45, no. 2, pp. 1243–1248, 2012, 7th Vienna International Conference on Mathematical Modelling. [Online]. Available: https://doi.org/10.3182/20120215-3-AT-3016.00220

UNIVERSIDAD POLITÉCNICA SALESIANA ECUADOR
INGENIUS
Revista de Ciencia y Tecnología
pISSN: 1390-650X / eISSN: 1390-860X

Guidelines for publication in Ingenius Journal

1. General Information

Ingenius is a scientific publication of the *Universidad Politécnica Salesiana* of Ecuador, published since January 2007, with a fixed biannual periodicity, specialized in Mechanical Engineering, Electrical Engineering, Electronics, Computer Science and its integration in what is now known as Mechatronics; these lines of action strengthen areas such as automation, control, robotics, among others..

It is a scientific journal, which uses the peer-review system, under double-blind review methodology, according to the publication standards of the Institute of Electrical and Electronics Engineers (IEEE). Compliance with this system allows authors to guarantee an objective, impartial and transparent review process, which facilitates the publication of their inclusion in reference databases, repositories and international indexing.

Ingenius is indexed in the directory and selective catalog of the Regional Online Information System for Scientific Journals of Latin America, the Caribbean, Spain and Portugal (Latindex), in the Directory of Journals of Open Access DOAJ, In the Information Matrix for the Analysis of Journals, MIAR, In the Ibero-American Network of Innovation and Scientific Knowledge, REDIB and in repositories, libraries and specialized catalogs of Latin America.

The journal is published in a double version: printed (ISSN: 1390-650X) and digital (e-ISSN: 1390-860X), in Spanish, each work being identified with a DOI (Digital Object Identifier System. The articles sent to Ingenius magazine must comply with the following criteria:

2. Scope and policy

2.1. Theme

Original contributions in Mechanical Engineering, Electrical and Electronic Engineering, Computer Science and its integration in what is now known as Mechatronics, as well as related areas: Automation, Control, Domotics, Robotics in their different fields of action and all those related disciplines with the same central theme.

All the work carried out by national or foreign researchers may be published once they meet the required scientific quality criteria.

2.2. Contributions

Ingenius Journal preferably publishes articles related to empirical research, and also reports of technological development, proposals for models and innovations, products for the elaboration of graduate and postgraduate thesis that contribute to the field of science and technology, as well as select revisions of literature. (state-of-the-art).

- **Research:** 5,000 to 6,500 words of text, including title, abstracts, descriptors, charts and references.
- **Reports:** 5,000 to 6,500 words of text, including title, abstracts, charts and references.
- **Reviews:** 6,000 to 7,000 words of text, including charts and references. Current, selective and justified references, would be specially valued from among 40 works

The Ingenius Journal publishes original and unpublished works written in Spanish and English, they may not have been published

through any printed or electronic media, nor be in the process of arbitration or publication.

Every article will be subjected to a rigorous arbitration process; the evaluation of the article will be made according to criteria of originality, relevance, relevance, contributions, scientific rigor and compliance with established editorial guidelines.

Being an arbitrated publication, the Editorial Board approves its publication based on the concept of specialized pairs. The reception of a document does not imply commitment of publication.

It is essential to present a letter of presentation and grant of rights which can be downloaded from: <
urlhttps://goo.gl/ZNkMRD>.

Contributions must be exclusively sent and through the OJS (Open Journal System) <`https://goo.gl/JF7dWT`>. In which all authors must previously register as a user. For any consultation of the procedure you should contact:

<revistaingenius@ups.edu.ec>,
<jcalle@ups.edu.ec> ó
<mquinde@ups.edu.ec>.

To promote diversity in publications, the author(s) may not publish more than one (1) article per issue, nor in consecutive issues. In order for the author(s) to submit their research again to Ingenius, a minimum of 3 published issues must have elapsed.

3. Presentation and structure of the manuscripts

For those works that are empirical investigations, the manuscripts will follow the IMRDC structure (Introduction, Materials and Methods, Results and Discussion and Conclusions), being optional the Notes and Supports. Those papers that, on the contrary, deal with reports, studies, proposals and reviews may be more flexible in their epigraphs, particularly in material and methods, analysis, results, discussion and conclusions. In all typologies of works, references are mandatory.

Articles may be written on Microsoft Word (.doc or .docx) or LaTeX(.tex). The template to be used can be downloaded from the journal's website, a, <`https://goo.gl/gtCg6m`>, while for LaTeX in <`https://goo.gl/hrHzzQ`>, it is necessary that the file be anonymised in Properties of File, so that the author(s) ID is not displayed.

Figures, Graphs and/or Illustrations, as well as Charts shall be numbered sequentially including an explanatory description for each. The equations included in the article must also be numbered; the figures, charts and equations must be cited in the text.

Use space after point, commas and question marks.

Use "enter" at the end of each paragraph and title heading. Do not use .enter.anywhere else, let the word processor program automatically break the lines.

Do not center headings or subheadings as they should be aligned to the left.

Charts must be created in the same program used for the document body, but must be stored in a separate file. Use tabs, not spaces, to create columns. Remember that the final size of printed pages will be 21 x 28 cm, so the tables must be designed to fit the final print space.

3.1. Structure of the manuscripts

3.1.1. Presentation and cover letter

1. **Título (español) / Title (inglés):** Concise but informative, in Spanish on the front line and in English on the second, when the article is written in Spanish and vice versa if it is written in English.

2. **Authors and affiliations:** Full name and surname of each author, organized by order of priority and their institutional affiliation with reference to the end of the first sheet, where it must include: Dependency to which belongs within the institution, Institution to which he/she belongs, country, ORCID. A maximum of 5 authors will be accepted, although there may be exceptions justified by the complexity and extent of the topic.
3. **Abstract (Spanish) / Abstract (English):** It will have a maximum extension of 230 words, first in Spanish and then in English. : 1) Justification of the topic; 2) Objectives; 3) Methodology and sample; 4) Main results; 5) Main conclusions.
4. **Keywords (Spanish) / Keywords (English):** 6 descriptors must be presented for each language version directly related to the subject of the work. The use of the key words set out in UNESCO's Thesaurus will be positively valued.
5. **Presentation (Cover Letter):** A statement that the manuscript is an original contribution, not submission or evaluation process in another journal, with the confirmation of the signatory authors, acceptance (if applicable) of formal changes in the manuscript according to the guidelines and partial assignment of rights to the publisher, according to the format established in: <https://goo.gl/ZNkMRD>

3.1.2. Manuscript

1. **Título (español) / Title (inglés):** Concise but informative, in Spanish on the front line and in English on the second, when the article is written in Spanish and vice versa if it is written in English.
2. **Authors and affiliations:** Full name and surname of each author, organized by order of priority and their institutional affiliation with reference to the end of the first sheet, where it must include: Dependency to which belongs within the institution, Institution to which he/she belongs, country, ORCID. A maximum of 5 authors will be accepted, although there may be exceptions justified by the complexity and extent of the topic.
3. **Abstract (Spanish) / Abstract (English):** It will have a maximum extension of 230 words, first in Spanish and then in English. : 1) Justification of the topic; 2) Objectives; 3) Methodology and sample; 4) Main results; 5) Main conclusions.
4. **Keywords (Spanish) / Keywords (English):** 6 descriptors must be presented for each language version directly related to the subject of the work. The use of the key words set out in UNESCO's Thesaurus will be positively valued.
5. **Introduction:** It should include the problem statement, context of the problem, justification, rationale and purpose of the study, using bibliographical citations, as well as the most significant and current literature on the topic at national and international level.
6. **Material and methods:** It must be written so that the reader can easily understand the development of the research. If applicable, it will describe the methodology, the sample and the form of sampling, as well as the type of statistical analysis used. If it is an original methodology, it is necessary to explain the reasons that led to its use and to describe its possible limitations.
7. **Analysis and results:** It will try to highlight the most important observations, describing, without making value judgments, the material and methods used. They will appear in a logical sequence

in the text and the essential charts and figures avoiding the duplication of data.

8. **Discussion and Conclusions:** It will summarize the most important findings, relating the observations themselves to relevant studies, indicating contributions and limitations, without adding data already mentioned in other sections. It should also include deductions and lines for future research.
9. **Supports and acknowledgments (optional):** The Council Science Editors recommends the author (s) to specify the source of funding for the research. Priority will be given to projects supported by national and international competitive projects.
10. **The notes (optional):** will go, only if necessary, at the end of the article (before the references). They must be manually annotated, since the system of footnotes or the end of Word is not recognized by the layout systems. The numbers of notes are placed in superscript, both in the text and in the final note. The numbers of notes are placed in superscript, both in the text and in the final note. No notes are allowed that collect simple bibliographic citations (without comments), as these should go in the references.
11. **References:** Bibliographical citations should be reviewed in the form of references to the text. Under no circumstances should references mentioned in the text not be included. Their number should be sufficient to contextualize the theoretical framework with current and important criteria. They will be presented sequentially in order of appearance, as appropriate following the format of the IEEE.

3.2. Guidelines for Bibliographical references

Journal articles:

[1] J. Riess, J. J. Abbas, "Adaptive control of cyclic movements as muscles fatigue using functional neuromuscular stimulation". IEEE Trans. Neural Syst. Rehabil. Eng vol. 9, pp.326–330, 2001. [Onine]. Available: https://doi.org/10.1109/7333.948462

Books:

[1] G. O. Young, "Synthetic structure of industrial plastics" in Plastics, 2nd ed., vol. 3, J. Peters, Ed. New York: McGraw–Hill, 1964, pp. 15–64.

Technical reports:

[1] M. A. Brusberg and E. N. Clark, "Installation, operation, and data evaluation of an oblique–incidence ionosphere sounder system," in "Radio Propagation Characteristics of the Washington–Honolulu Path," Stanford Res. Inst., Stanford, CA, Contract NOBSR–87615, Final Rep., Feb. 1995, vol. 1

Articles presented in confeences (unpubished):

[1] Vázquez, Rolando, Presentación curso "Realidad Virtual". National Instruments. Colombia, 2009.

Articles of memories of Conferences (Published):

[1] L. I. Ruiz, A. García, J. García, G. Taboada. "Criterios para la optimización de sistemas eléctricos en refinerías de la industria petrolera: influencia y análisis en el equipo eléctrico," IEEE CONCAPAN XXVIII, Guatemala 2008.

Thesis:

[1] L.M. Moreno, "Computación paralela y entornos heterogéneos," Tesis doctoral, Dep. Estadística, Investigación Operativa y Computación, Universidad de La Laguna, La Laguna, 2005.

Guidelines:

[1] IEEE Guide for Application of Power Apparatus Bushings, IEEE Standard C57.19.100–1995, Aug. 1995.

Patents:

[1] J. P. Wilkinson, "Nonlinear resonant circuit devices," U.S. Patent 3 624 125, July 16, 1990.

Manuals:

[1] Motorola Semiconductor Data Manual, Motorola Semiconductor Products Inc., Phoenix, AZ, 1989.

Internet resources:

[1] E. H. Miller, "A note on reflector arrays" [Online]. Available. https://goo.gl/4cJkCF

3.3. Epigraphs, Figures and Charts

The epigraphs of the body of the article will be numbered in Arabic. They should go without a full box of capital letters, neither underlined nor bold. The numbering must be a maximum of three levels: 1. / 1.1. / 1.1.1. At the end of each numbered epigraph will be given an enter to continue with the corresponding paragraph.

The charts must be included in the text according to order of appearance, numbered in Arabic and subtitled with the description of the content, the subtitle should go at the top of the table justified to the left.

Figures can be linear drawings, maps or black and white halftone or color photographs in 300 dpi resolution. Do not combine photographs and line drawings in the same figure.

Design the figures so that they fit eventually to the final size of the journal 21 x 28 cm. Make sure inscriptions or details, as well as lines, are of appropriate size and thickness so that they are not illegible when they are reduced to their final size (numbers, letters and symbols must be reduced to at least 2.5 mm in height After the illustrations have been reduced to fit the printed page). Ideally, the linear illustrations should be prepared at about a quarter of their final publication size.

Different elements in the same figure should be spelled a, b, c, etc.

Photographs should be recorded with high contrast and high resolution. Remember that photographs frequently lose contrast in the printing process. Line drawings and maps should be prepared in black.

The text of the figures and maps must be written in easily legible letters.

If the figures have been previously used, it is the responsibility of the author to obtain the corresponding permission to avoid subsequent problems related to copyright.

Each figure must be submitted in a separate file, either as bitmap (.jpg, .bmp, .gif, or .png) or as vector graphics (.ps, .eps, .pdf).

4. Submission process

The manuscript must be sent through the OJS system of the journal, <`https://goo.gl/JF7dWT`>,the manuscript should be uploaded as an original file in .pdf without author data and anonymized according to the above; In complementary files the complete manuscript must be loaded in .doc or .docx (Word file), that is to say with the data of the author (s) and its institutional ascription; Also the numbered figures should be uploaded in independent files according to the corresponding in the manuscript (as bitmap .jpg, .bmp, .gif, or .png or as vector graphics .ps, .eps, .pdf). It is also obligatory to upload the cover letter and grant of rights as an additional file.

All authors must enter the required information on the OJS platform and only one of the authors will be responsible for correspondence.

Once the contribution has been sent the system will automatically send the author for correspondence a confirmation email of receipt

of the contribution.

5. Editorial process

Once the manuscript has been received in OJS, a first check by the editorial team of the following points:

- The topic is in accordance with the criteria of the journal.
- Must have the IMRDC structure.
- Must be in the INGENIUS format.
- Must use the IEEE citation format.
- All references should be cited in the text of the manuscript as well as charts, figures and equations.
- The manuscript is original; for this, software is used to determine plagiarism.

The assessment described above can take up to 4 weeks.

If any of the above is not complete or there is inconsistency, an email will be sent to the author to make the requested corrections.

The author will make the corrections and resend the contribution through an email in response to the notification and will also upload the corrected manuscript into OJS supplementary files.

The editorial team will verify that the requested corrections have been incorporated, if it complies, the manuscript will start the second part of the process that may be followed by the author through OJS, otherwise the author will be notified and the manuscript will be archived.

The second phase of the process consists of the evaluation under the methodology of double-blind review, which includes national and foreign experts considering the following steps:

- The editor assigns two or more reviewers for the article.
- After reviewing the article, the reviewers will submit the evaluation report with one of the following results.
  - Publishable
  - Publishable with suggested changes
  - Publishable with mandatory changes
  - Non publishable
- The editor once received the evaluation by the reviewers will analyze the results and determine if the article is accepted or denied.
- If the article is accepted, the author will be notified to make corrections if required and the corresponding editorial process will be continued.
- If the article is denied, the author will be notified and the manuscript will be archived.
- In the two previous cases the result of the evaluation of the reviewers and their respective recommendations will be sent.

The second phase of the process lasts at least 4 weeks, after which they will be notified to the author giving instructions to continue with the process.

6. Publication

The INGENIUS Journal publishes two issues per year, on January 1st and July 1st, so it is important to consider the dates for sending the articles and their corresponding publication. Articles received until October will be considered for the January publication and those received until April for the July publication.

7. Information on the Use of Artificial Intelligence

Should artificial intelligence be used at any stage of the research presented in the article, authors are required to clearly highlight this in the cover letter associated with the article, specifying the section or sections where artificial intelligence has been used. The purpose

of this requirement is to inform readers about the sections where this technology has been employed, providing greater transparency and understanding of its application in the presented research.

INGENIUS, Revista de Ciencia y Tecnología, recognizes the importance of maintaining high ethical standards in scientific research, particularly in the use of artificial intelligence (AI).

The decision to accept a publication that has utilized artificial intelligence rests at the discretion of the editorial team.

UNIVERSIDAD POLITÉCNICA SALESIANA DEL ECUADOR
Juan Cárdenas Tapia, sdb,
Rector

Turuhuayco 3-69 y Calle Vieja
Postal code 2074
Cuenca, Ecuador
Teléfono: (+593 7) 205 00 00
Fax: (+593 7) 408 89 58
Email: srector@ups.edu.ec

Exchange

Exchange with other periodicals is accepted.

Address:
Secretaría Técnica de Comunicación
Universidad Politécnica Salesiana
Turuhuayco 3-69 y Calle Vieja
Postal code 2074
Cuenca, Ecuador
Phone: (+593 7) 205 00 00 Ext. 1182
Fax: (+593 7) 408 89 58
Email: rpublicas@ups.edu.ec
www.ups.edu.ec
Cuenca – Ecuador

Ingenius, Journal Science of Technology,
Issue 36
july/december 2026
John Calle Siguencia, Editor in chief
revistaingenius@ups.edu.ec

Printed
Centro Gráfico Salesiano: Antonio Vega Muñoz 10-68 y General Torres.
Phone: (+593 7) 283 17 45
Cuenca – Ecuador
Email: centrograficosalesiano@lns.com.ec

OTHER PERIODIC PUBLICATIONS OF THE UNIVERSITY

UNIVERSITAS, Journal of Social and Human Sciences.

LA GRANJA, Journal of the Sciences.

ALTERIDAD, Journal of Education.

RETOS,Journal of Administration Sciences and Economics.

UTOPÍA, University Youth Ministry Magazine.

SOPHIA, Collection of Philosophy of Education.

ABYA YALA | UNIVERSIDAD POLITÉCNICA SALESIANA

ECUADOR SALESIANOS DON BOSCO